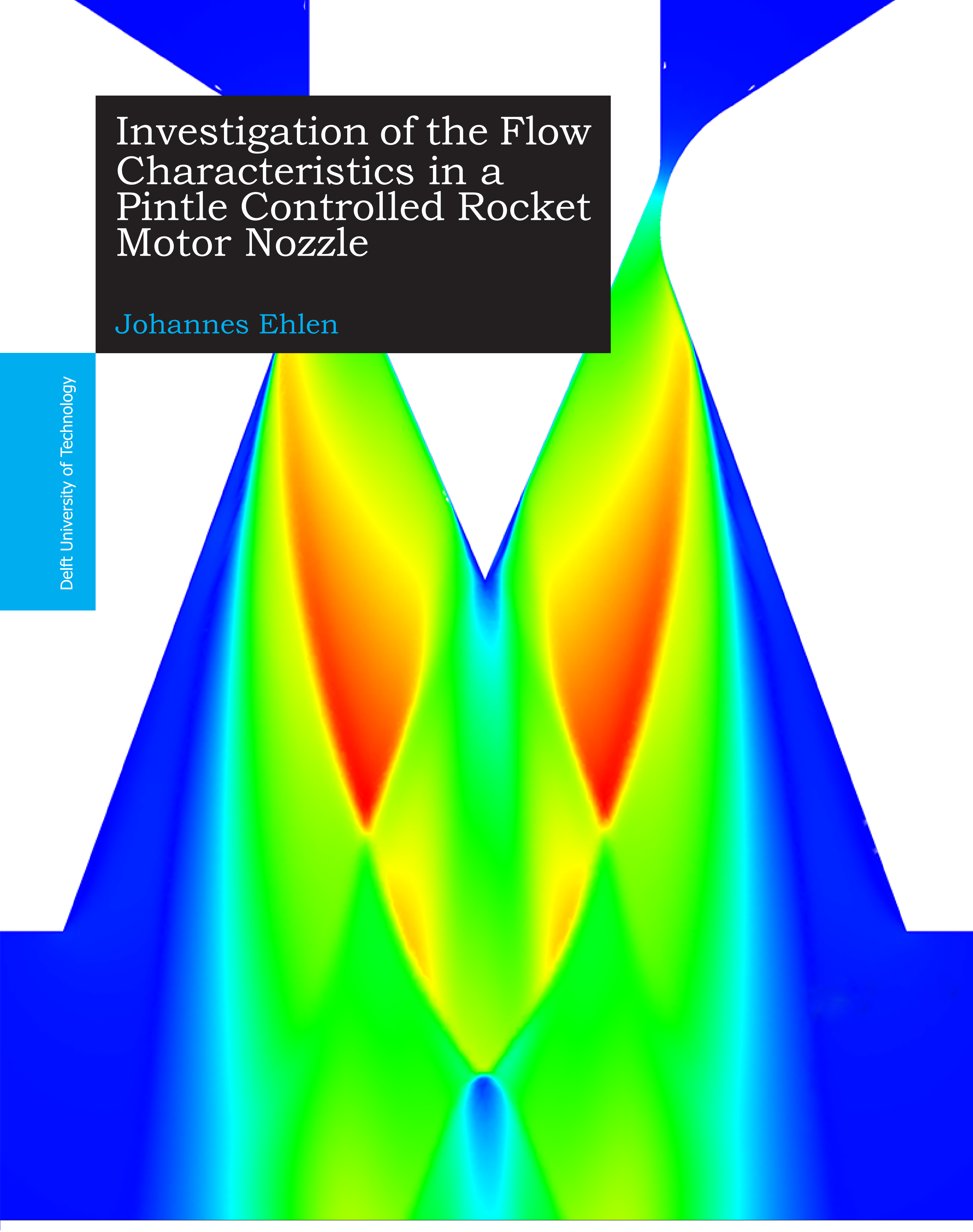

Investigation of the Flow Characteristics in a Pintle Controlled Rocket Motor Nozzle

Johannes Ehlen

Delft University of Technology

TU Delft Delft University of Technology

Challenge the future

Investigation of the Flow Characteristics in a Pintle Controlled Rocket Motor Nozzle

by

Johannes Ehlen

in partial fulfilment of the requirements for the degree of

Master of Science

in Aerospace Engineering

at the Delft University of Technology,

to be defended publicly on Thursday January 11, 2018 at 01:00 PM.

Student number:	4158334	
Supervisors:	Dr. A. Cervone,	TU Delft
	Dipl.Ing. A. Krenik,	MBDA Germany
	Dipl.Ing. Y. Metsker,	TU München
Thesis committee:	Prof. Dr. E.K.A. Gill,	TU Delft
	Dr. A. Cervone,	TU Delft
	Ir. M.C. Naeije	TU Delft

Preface

This master thesis project was conducted as part of the Spaceflight Master of Science track at the Faculty of Aerospace Engineering of the TU Delft. Prior to the thesis project I performed an extensive but separate literature study. This literature study is the foundation of this thesis projects. Thesis and literature study were both conduct in cooperation with MBDA Germany. The overall topic and direction of both has been set by MBDA Germany, these were than fitted in the frame work of a graduation topic at the TU Delft. The actual work has been conducted at the MBDA facility Schrobenhausen in Germany.

During the course of this project I received a lot of help and support. I would like to use this opportunity here and express my gratitude to everyone: First of all I would like to thank Dr. Angelo Cervone, from the TU Delft Faculty of Aerospace Engineering at the TU Delft, for the academic supervision of this thesis project. Thanks go to MBDA Germany for supporting me in my studies, especially to the people in my department and to the people from the HR Student Team. Most notably my two company supervisors Alex and Yuriy should be mentioned. I would also like to thank the head of department Dr. Jürgen Engel for his support and for making this thesis project possible. Moreover, I would especially like to thank Roland for all his professional help in all aspects of CFD and for doing his utmost in keeping alive the computer infrastructure required for all my long calculations. For their professional help and support I would also like to thank Jörg, Klaus, Mark and Michael. A thank you also goes to all my office colleagues and all the other MBDA student employees for providing such an excellent working atmosphere. From these I would especially like to thank Stefan for his assistance in solving all the calculation-data evaluation issues and to Mareike and Monty for providing me with excellent and prompt feedback for this thesis report.

Finally, I would like to express my highest gratitude to my parents and my family for their contines love, help and support throughout my entire student career.

J. Ehlen

Schrobenhausen (Germany), December 29, 2017

Contents

List of Abbreviations

Abbreviation	**Definition**	**First page**
1D	one-dimensional	4
ACS	Attitude Control System	1
AUSM	Advection Upstream Splitting Method	12
CEA	Chemical Equilibrium with Applications	94
CFD	Computational Fluid Dynamics	4
DACS	Divert and Attitude Control System	2
DES	Detached Eddy Simulation	12
DLR	Deutsches Zentrum für Luft- und Raumfahrt, German Aerospace Center	27
DNS	Direct Numerical Simulation	12
FVM	Finite Volume Method	11
KKV	Kinetic Kill Vehicle	2
LAS	Launch Abort System	2
LES	Large Eddy Simulation	12
MoC	Method of Characteristics	7
MPCV	Multi-Purpose Crew Vehicle	2
MUSCL	Monotonic Upwind Scheme for Conservation Laws	12
n/a	Not-Available	22
PCC	Post Combustion Chamber	1
PEPS	Pintle Escape Propulsion System	2
RANS	Reynolds-Averaged Navier-Stokes	12
SM-3	Standard Missile-3 (RIM-161)	2
TOP	Thrust Optimised Parabolic	8

List of Symbols

Symbol	**Definition**	**Unit**	**First page**
A	Area	m^2	5
C_F	Thrust Coefficient	-	6
F_{pin}	Axial Pintle Force	N	20
F_{thrust}	Nozzle Thrust	N	6
H	Enhtalpy	J	10
I_{sp}	Specific Impulse	s	6
M	Mach Number	-	5
Q	Source Term	-	11
R	Universal gas constant	J/kmol K	6
T	Temperature	K	6
U	Time dependent Scalar Variable	-	11
V	Velocity Vector $(u, v, w)^T$	m/s	10
Γ	Vandenkerckhove function	-	6
$\dot{m}$	Massflow	kg/s	6
γ	Specific Heat-Ratio	-	5
$\mathbf{F}$	Flux Vector	-	11
$\mathbf{S}$	Surface Vector	m^2	11
$\mathscr{V}$	Volume	m^3	11
μ	Dynamic Viscosity	Pa·s	13
ν	Kinematic Viscosity	m^2/s	13
ω	Specific Dissipation Rate	1/s	13
ρ	Density	kg/m^3	6
τ	Shear-Stress	N/m^2	10
ε	Turbulence Dissipation Rate	J/(kg · s)	13
a	Speed of Sound	m/s	12
c^*	Rocket Motor Characteristic Velocity	m/s	6
g_0	Mean Gravitational Acceleration at Sea Level (9.81)	m/s^2	6
k	Turbulence Kinetic Energy	J/kg	13
k	Thermal Conductivity	W·m^{-1}·K^{-1}	10
p	Pressure	Pa or bar	6
q	Heat Flux	W/m^2	10
t	Time	s	10
u	x-Velocity Component	m/s	5
v_e	Exit velocity	m/s	6
x	Position Vector or Value	m	10
y^+	Dimensonless Wall Distance	-	14

List of Figures

List of Tables

1. Introduction

Actively varying the thrust of a liquid rocket engine is done by changing the propellant massflow that is fed into the combustion chamber. If a hypergolic propellant combination is used, a thruster can be ignited and stopped simply by turning the propellant flow on and off, without the need for any additional system such as an ignition system. These properties make liquid rocket thrusters the ideal candidate for any active and non-aerodynamic Attitude Control System (ACS) for both civil and military applications. However, the common storable liquid hypergolic propellants, which are used for such systems, are both highly reactive and toxic. Thus, their application is very hazardous for the handling personnel and the environment. Therefore, increasing efforts are made into the development of new ACS approaches which no longer make use of such hazardous propellants. The most common approach is to replace the current storable liquid propellants by alternative propellants which are less hazardous.

An approach less common is to switch to a solid rocket propelled system. Unlike a liquid propulsion system it is not possible to actively throttle the overall combustion of a solid rocket motor. It is however possible to alter the thrust of an individual thruster by varying its throat area. This will alter the massflow expelled through the nozzle of the respective thruster and thus would change its thrust. The throat area can be altered by inserting a pintle of a conical or other shape into the nozzles throat. A schematic drawing of such a thrust concept is displayed in Figure 1.1.

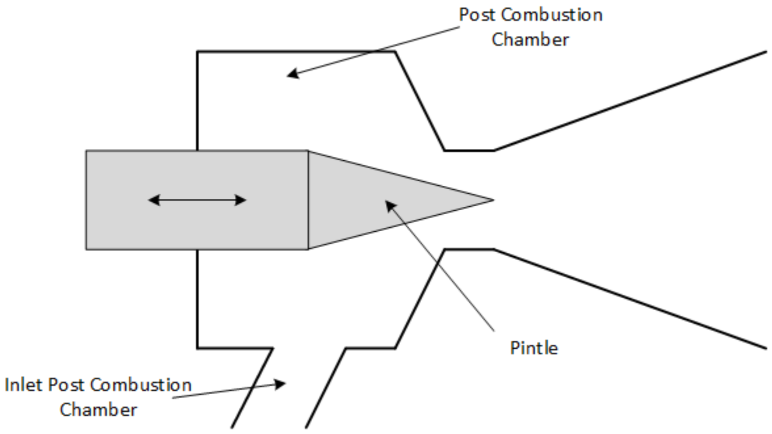

Figure 1.1: Pintle Controlled Rocket Motor Nozzle Concept

A thruster consists out of a Post Combustion Chamber (PCC) with a classical convergent-divergent nozzle. The PCC features a single or multiple inlets through which the combustion gases are fed in. The PCC does not contain any combusting solid propellant, hence the name *Post Combustion Chamber*. The PCC also houses the pintle which by means of an actuator (electromagnetic, hydraulic or pneumatic) can be inserted and retracted into the nozzle throat.

Any system utilising this thruster concept will feature multiple thrusters (at least two), which are arranged opposite of each other. All thrusters will be connected to the same combustion chamber. The net moment or force for a certain axis is the thrust difference for the opposing thruster set. Figure 1.2 shows a schematic cut through such an ACS system for a rocket or missile. The sample system shown here features four thrusters, with individually actuated pintles. Figure 1.2a, shows the system in idle configuration. All pintles are at the same position, the net thrust and moment will thus be zero. In Figure 1.2b, the thruster T2 is set to its minimum position and the opposing thruster T4 to the maximum position. The other two thruster T1 and T3 are unchanged and both at their mid positions. Therefore, there will be a net force in positive z-direction, which creates a moment around the y-axis. In the given case the actual combustion chamber would be situated below or above the actual thrusters. The run time of such a system is limited by the burn time of the solid propellant inside the combustion chamber. The number of cycles is limited to the amount of propellant charges stored in the combustion chamber. In theory it would also be possible to couple the pintles for the opposing thruster set, this would save two actuators. However, this would make it difficult to house all four thrusters on the same level. Usually the pintle positions would be chosen as such that the total massflow of the entire system remains constant. This way the pressure inside the combustion chamber remains constant and the propellant burn rate, to which most solid rocket motors are very sensitive, is not influenced.

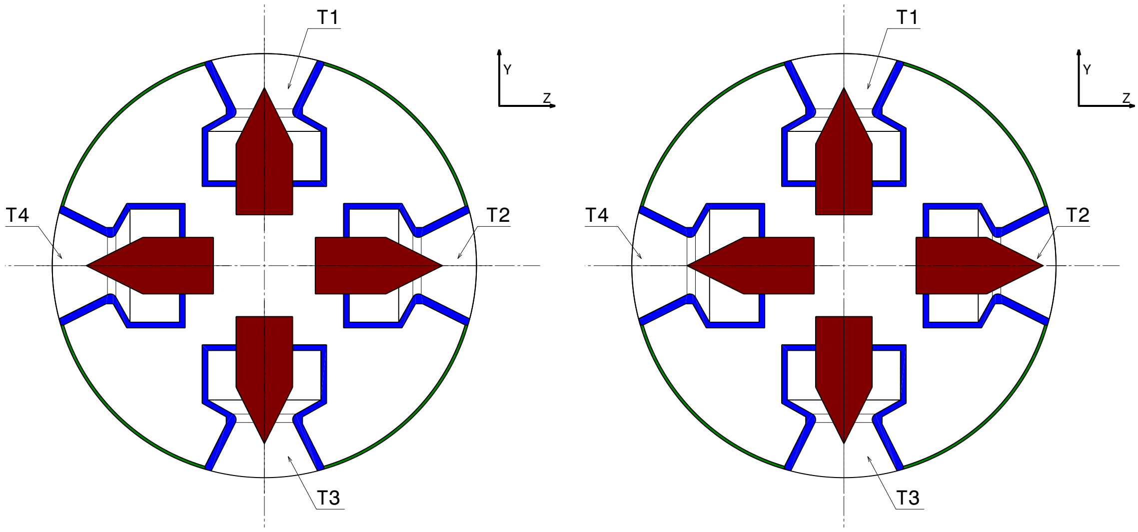

(a) Case 1

(b) Case 2

Figure 1.2: Application Concept using four Thrusters, each with an independently actuated Pintle

The pintle controlled rocket motor nozzle concept is not new. In fact it was already described in the early literature about rocket propulsion from the 1950's, such as the book of Barrere et al. [1]. However, so far there exists surprisingly little public research about these concepts and only three actual applications were found that make use of the concept. Here a short overview will be given of all three, for details see Ref. [2]:

- The new Launch Abort System (LAS) of the Orion Multi-Purpose Crew Vehicle (MPCV) uses an ACS that makes use of the pintle controlled rocket motor nozzle concept. However, instead of using only four thrusters it uses eight. The system is used to control the attitude of the capsule and the escape tower during a possible launch escape. A picture of the ACS system during a hot-fire test is shown in Figure 1.3a. Each thruster features an independently electromagnetically actuated pintle each capable of producing up to 7000 lbf (31.1 kN) of thrust, see Jones et al. [3]. The operating duration is max. 35 s. A detailed description of the whole LAS can be found in the publication of Bocem et al. [4] and for the system operations see Williams-Hayes [5].
- The Divert and Attitude Control System (DACS) of the new Standard Missile-3 (RIM-161) (SM-3) also makes use of pintle controlled rocket motor nozzles. A picture of the SM-3 DACS is shown in Figure 1.3b. The SM-3 is a mainly naval based air-defence missile used mainly for missile defence. The DACS is an integral part of the SM-3's Kinetic Kill Vehicle (KKV), which is mounted on top of the missiles third stage. After that has burned out the KKV separates and independently engages the enemy missile. For this the DACS features four high thrust divert thruster at the front and six smaller thruster for attitude control mounted at the rear. The systems development started in the early 1990's with a first concepts published by Coon and Yasuhara [6]. More information can be found in the publications of Robinson [7], Prins et al. [8] and Cover and Drendel [9].
- In the 1990's McDonald Douglas (now Boeing) developed a new type of ejection seat that also made use of the concept. The new seat featured a so called Pintle Escape Propulsion System

(PEPS). The system propelled the seat up- and forwards and provided attitude control. It consisted out of H-type rod structure mounted to the rear of the seat. The hollow rods contained the solid rocket propellant. At each of the four tips of the H-structure one pintle thruster was mounted. The thrust level of each thruster could be varied between 0 - 13 kN. The burn time was only 1.2 s, for reference see Rock et al. [10]. The PEPS system was successfully tested, however it was never used on any series production ejection seat. A detailed report about the system and all tests conducted, was published by McDonald [11].

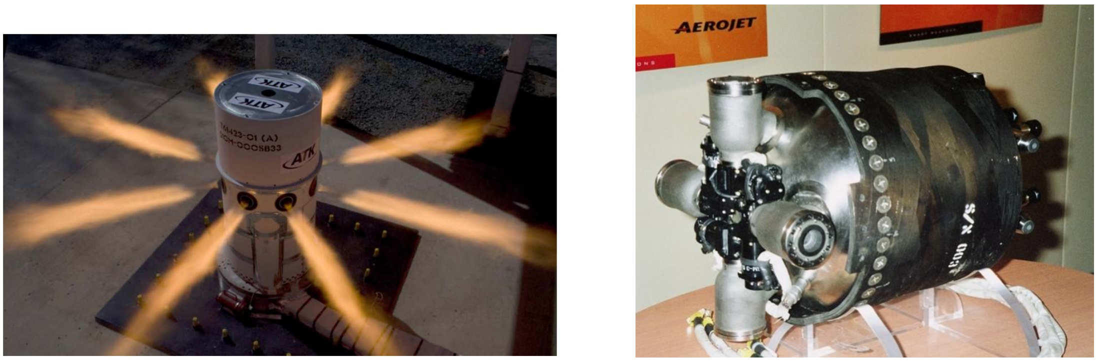

(a) Orion Capsule LAS Attitude Control Motor, from Ref. [3]

(b) SM-3 KKV DACS Show Model, from Ref. [12]

Figure 1.3: Application Examples for Pintle-Controlled Thurster

Over the last couple of years several papers have been published that present a flow analysis of different pintle controlled rocket motor nozzle concepts, with somewhat different results. Note, the following three paragraphs are an almost literal copy form the original project proposal which was presented in Ref. [2]. Initial calculations, by the author, on a generic pintle/ nozzle configuration have indicated that when the pintle is retracted (opened) the thrust will initially increase in a linear fashion. At the pintles 50 % position the slope starts to slowly decrease and is no longer linear. Similar results have been obtained for the axial load on the pintle, except that the initial linear bit of the slope is much shorter. The slope decrease is faster, but never becomes zero. A similar behaviour is observed by Dumortier [13], who performed calculations on such a setup. This is also confirmed by CFD results published by Lafond [14]. It should however be pointed out that there are some differences, which might be attributed to the different pintle shapes, but the general indication is the same.

All previously mentioned results were static simulations, the dynamic behaviour of such a system might look completely different. It is suspected that the actual movement of the pintle changes the results significantly. First of all it is suspected to cause short term pressure transients, due to its movement and change of throat area. Moreover, there might occur hysteresis effects when inserting and retracting the pintle, similar to an airfoil/ wing that is operated near the separation or stall point. Hence, pressure and thrust curve might have totally different shapes, depending on whether the pintle is retracted or inserted. The paper by Heo et al. [15], which also simulates the dynamic effects, confirms this suspicion. It both shows pressure and thus thrust transients and the hysteresis effects. In return, the test results published by Rock et al. [10] show no such effects.

Because of the unclarities mentioned above and in order to get a better understanding of the behaviour of such a thruster it was decided to research this in detail and to setup multiple different simulations of such a thruster. The main objective of this project is as follows:

To develop the capability of analysing the flow field in a pintle controlled rocket thruster, by developing a three-dimensional CFD simulation of the thruster, which is validated by experimentally obtained test results.

The objective was split up into multiple sub-objectives. A more detailed list of objectives can be found in the original project proposal in Ref. [2]:

1. Create a simple one-dimensional simulation model based upon Ideal Rocket Theory.
2. Develop a generic 3D model of a thruster that can be used by the solver.
3. Develop the three-dimensional CFD stationary/static simulation of the thruster.
4. Verify both simulations with each other and validate them using (external) test results.
5. Repeat points 2 and 3 for a hot-fire case and verify the results using the model in point 1.
6. Develop the three-dimensional CFD in-stationary/dynamic simulation of the thruster.

This research was conducted in close cooperation with Chair of Turbomachinery and Flight Propulsion at the TU Munich, where the general aspects of implementing the concept into a rocket or missile was studied by Metsker [16]. He also created a cold-gas static test setup for a single thruster. The results of some of those tests were used for the validation in point 4 above.

The above objectives were supposed to provide an answer to the following research question:

How do different positions of the pintle influence the flow characteristics inside and downstream of the pintle controlled thruster?

Also the research question was split into multiple sub-question. A more detailed list can again be found in the original project proposal in Ref. [2]:

1. What are the performance characteristics of the thruster at different pintle settings?
2. What are the different characteristics of the flow field (flow separation, shocks, sub-/supersonic boundary), do they occur and how do they change with different pintle settings?
3. What are the transient effects of the pintle moving inside the thruster?

The above research objectives and questions are dealt with in the following report. Chapter 2 summarises the necessary scientific knowledge which was used as part of this project. The following Chapter 3 discusses the setup and results of the simple one-dimensional (1D) Matlab simulation. The next Chapter 4, which can be considered the main part of this report, describes the setup and results of all Computational Fluid Dynamics (CFD) simulations conducted within this project. Chapter 5 briefly describes the test setup and results of the cold-gas test, that were used for the validation of the simulation results. The verification and validation and a detailed analysis of the simulation results is presented in Chapter 6. Finally, Chapter 7 concludes on all results and gives recommendations for future steps to be taken.

2. Fundamentals

The following chapter outlines the scientific and mathematical fundamentals for this project. The first section deals with the fundamentals of ideal rocketry and rocket nozzle flow. The second section describes the basics of the numerical and CFD method applied throughout this thesis. Note, prior to this project an extensive literature study has been conducted, see Ref. [2]. The information presented in this chapter is essentially a concise summary of the relevant parts of this literature study.

2.1. Rocket Propulsion and Rocket Nozzles

This section presents the fundamentals of rocket nozzle flow. These fundamentals have been used to construct the 1D simulation presented in Chapter 3. They are further considered essential for the understanding of the general principals of this project.

2.1.1. Quasi-1D Nozzle Flow

The flow through any diffuser, duct or nozzle and the behaviour of any rocket engine can be simplified by the following assumptions. These assumptions are the basis of ideal rocket theory and form the basis of this section:

1. The flow is assumed to be quasi-one-dimensional and continues. For such flow the general continuity equation reduced to $d\left(\rho u A\right) = 0$. Where ρ resembles the density, u is the velocity in x-direction and A is the cross-sectional area.
2. The flow is assumed to be steady and inviscid. Therefore, momentum equation reduces to $dp = -\rho u \, du$. Where the variable p stands for the pressure.
3. It is assumed that the flow is adiabatic and that no shocks occur. From this follows $dp/d\rho = a^2$, where a represents the speed of sound.
4. The exhaust gases composition is assumed to be homogeneous and frozen (no chemical reactions). Therefore the specific gas-constant R does not vary.
5. It is assumed that the exhaust gases can be treated as an ideal gas ($p = \rho R T$) with a constant specific heat ratio γ.

From relations one to three above Eq. 2.1 can be derived. For the full derivation see Anderson [17]. The aim of any rocket nozzle is to maximise the exit velocity. According to Eq. 2.1 this is achieved by a decreasing area ratio for subsonic flow ($M < 1$) and by an increasing area ratio for supersonic flow ($M > 1$). Hence the typical convergent-divergent shape of a conventional rocket nozzle.

$$\frac{dA}{A} = \left(M^2 - 1\right) \frac{du}{u} \tag{2.1}$$

From the above relations it is possible to derive an equation relating the area ratio and the velocity (Mach number) of a nozzle, see Eq. 2.2. Where A_{th} is the nozzle throat area and γ is the specific heat ratio. The full derivation can be found in Anderson [17].

$$\left(\frac{A}{A_{th}}\right)^2 = \frac{1}{M^2}\left[\frac{2}{\gamma+1}\left(1+\frac{\gamma-1}{2}M^2\right)\right]^{(\gamma+1)/(\gamma-1)} \tag{2.2}$$

Eq. 2.2 can be rewritten using the isentropic flow relations and the help variable Γ, which is defined in Eq. 2.4 and sometimes also referred to as the Vandenkerckhove function. This results into Eq. 2.3, which directly relates the local pressure and area/expansion ratio ε. The initial, combustion or reservoir pressure at the nozzle inlet is defined by p_c. The derivation of Eqs. 2.3 and 2.4 can be found in the works of Zanbergen [18] or Barrere et al. [1].

$$\varepsilon = \frac{A}{A_{th}} = \frac{\Gamma}{\sqrt{\left(\frac{2\gamma}{\gamma-1}\right) \cdot \left(\frac{p}{p_c}\right)^{\left(\frac{2}{\gamma}\right)} \left(1 - \left(\frac{p}{p_c}\right)^{\left(\frac{\gamma-1}{\gamma}\right)}\right)}} \tag{2.3}$$

$$\Gamma = \sqrt{\gamma} \cdot \left(\frac{2}{\gamma+1}\right)^{\frac{\gamma+1}{2(\gamma-1)}} \tag{2.4}$$

Using the above equations it is possible to predict the flow properties throughout any nozzle as long as the nozzle contour (area ratio function), the initial conditions and the ideal gas properties (specific heat ratio and gas constant) are known. These principals are later applied in the 1D simulation to calculate the pintle pressure distribution and the nozzle exit conditions, see Chapter 3.

$$F_{thrust} = \dot{m} \cdot v_e + (p_e - p_a)\, A_e \tag{2.5}$$

The thrust of any nozzle is defined by Eq. 2.5.The thrust is comprised of two components: The momentum thrust (massflow $\dot{m}$ at an exit velocity v_e) and the pressure thrust caused by the difference between nozzle exit pressure p_e and ambient pressure p_a. The latter term is zero for an adapted nozzle, which is designed such that exit and ambient pressure are equal.

$$\dot{m} = \rho_{th} \cdot A_{th} \cdot v_{th} = \frac{\Gamma \cdot p_c \cdot A_{th}}{\sqrt{R \cdot T_c}} = \frac{p_c \cdot A_{th}}{c^*} \tag{2.6}$$

The general definition of any internal massflow is $\dot{m} = \rho A v$. In case of a nozzle it is convenient to evaluate this equation in the throat, as there the Mach number is known ($M = 1$). This leads to Eq. 2.6. Assuming an ideal gas and an isentropic expansion it can be reformulated, such that the massflow can be obtained for any given throat area as long as the initial conditions (T_c and p_c) are known.

$$v_e = \sqrt{\frac{2\gamma}{\gamma-1} \cdot R \cdot T_c \cdot \left[1 - \left(\frac{p_e}{p_c}\right)^{\left(\frac{\gamma-1}{\gamma}\right)}\right]} \tag{2.7}$$

The nozzle exit velocity can be calculated using Eq. 2.7. It is derived using the first law of thermodynamics (conservation of energy/ enthalpy or $h_{tot} = h + 1/2 \cdot v^2$ is constant). Further assumptions are an isentropic expansion and that the initial velocity in the chamber is zero. The full derivation can be found in the Zandbergen [18].

$$v_e = I_{sp} \cdot g_0 = C_F \cdot c^* \tag{2.8}$$

Moreover, a number of coefficients and performance parameters for a rocket motor or nozzle can be derived, such as the thrust coefficient C_F, the characteristic velocity c^* and the specific impulse I_{sp}. These three parameters are related through Eq. 2.8, where v_e is the exit velocity and g_0 is the standard sea level gravitational acceleration.

$$c^* = \frac{p_c \cdot A_{th}}{\dot{m}} = \frac{1}{\Gamma} \cdot \sqrt{R \cdot T_c} \tag{2.9}$$

The characteristic velocity c^* is a performance measure for the combustion efficiency of a rocket motor. It is dependent on the propellant combination used and the combustion chamber. It does not depend in anyway on the nozzle design and is thus only of secondary relevance for this project. The characteristic velocity is defined, in both forms, in Eq. 2.9.

$$C_F = \frac{F}{p_c \cdot A_{th}} \tag{2.10}$$

The dimensionless thrust coefficient C_F is defined according to Eq. 2.10. It is a parameter for the efficiency of the nozzle. It is a measure of the amplification of the thrust compared to the case where the chamber pressure would act over the throat area only. The thrust coefficient for any nozzle is thus usually greater than one. For details see Ref. [18].

Using Eqs. 2.5, 2.6 and 2.7 the definition of the thrust coefficient, as presented in Eq. 2.10, can be rewritten. This results into Eq. 2.11. The actual thrust coefficient can be split into two components, the momentum thrust coefficient C_F^0 and the pressure term.

$$C_F = C_F^0 + \left(\frac{p_e}{p_c} - \frac{p_a}{p_c}\right) \cdot \frac{A_e}{A_{th}} = \Gamma \cdot \sqrt{\frac{2\gamma}{\gamma - 1} \cdot \left[1 - \left(\frac{p_e}{p_c}\right)^{\left(\frac{\gamma-1}{\gamma}\right)}\right]} + \left(\frac{p_e}{p_c} - \frac{p_a}{p_c}\right) \cdot \frac{A_e}{A_{th}} \tag{2.11}$$

The thrust coefficient for a nozzle can be calculated in case the specific heat ratio γ, the ambient pressure p_a, the nozzle pressure ratio p_e/p_c and the area ratio A_e/A_{th} are know. The pressure ratio is directly related to the area ratio and can be obtained by Eq. 2.3.

$$F_{thrust} = C_F \cdot \dot{m} \cdot c^* = C_F \cdot p_c \cdot A_{th} \tag{2.12}$$

Thereafter, the actual thrust can be calculated using Eq. 2.12 assuming the actual combustion pressure p_c and throat area A_{th} are known. The procedure outlined above is used to calculate the thrust for each pintle position in the 1D simulation.

2.1.2. Multidimensional Nozzle Flow

In the previous section it was shown how the flow inside a nozzle can be approximated as quasi-one-dimensional flow. This gives a good approximation to the actual flow, as it is axis-symmetric. However, real flow is not quasi-one-dimensional, but fully three-dimensional. These effects will be briefly touched up in the following. For the details regarding three dimensional nozzle flow see Ref. [2].

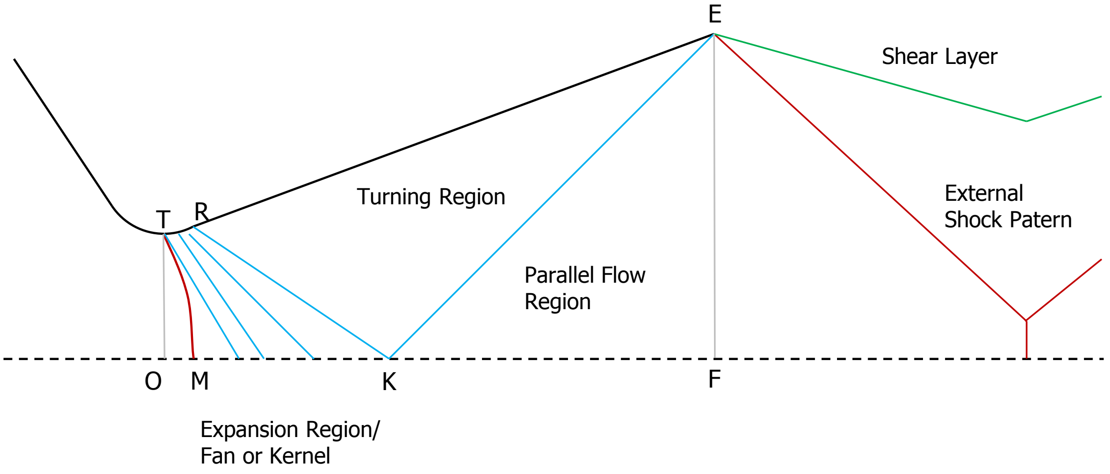

Figure 2.1: Schematic Layout of a Conical Nozzle Flow

Figure 2.1 shows the schematics of a multidimensional conical nozzle flow. The nozzle contour follows the points *TRE*, where *TR* forms the initial radial expansion contour. The smallest cross-section or throat is the line *TO* and the nozzle exit is formed by the line *EF*. Note, the following explanation makes use of the so called characteristic lines, which is part of the Method of Characteristics (MoC): "A characteristic line is defined as a line at which the velocity component that is exactly perpendicular to the line is sonic, thus they are equivalent to the so called Mach lines.",see Ref. [2]. The MoC is not explained here, for details see Ref. [2] or the book of Anderson [19].

The first significant multidimensional effect is that the flow $M = 1$ or sonic line is not in the smallest cross-section *TO* nor is it a straight line. The actual sonic line is slightly curved and usually a little downstream of the geometrical throat, see red line *TM* in Figure 2.1. There are numerous approaches to approximate the shape of this line, an overview can be found in Ref. [2]. A reasonable simple and straight forward approximation is the method developed by Sauer [20], who approximates the sonic line by a first order power series expansion of the potential flow equation. For details see Ref. [2] or Sauer [20].

Downstream of the sonic line the flow expands along the radial contour *TR*. From this the expansion lines,so called right running characteristic lines, are emitted towards the nozzle axis. Together these lines form a expansion fan, sometimes also referred to as kernel. The expansion region *TRKM* is limited by the last right running characteristic *RK*.

The region defined by the points *REK* is the so called turning region, where the flow is turned into a uniform flow in axial direction. This region is limited by the last left running characteristic line *KE*. Note, there are many right running characteristic line. However, to maintain clarity, only the most downstream or last one is depicted in Figure 2.1.

Downstream of the nozzle exit (line *EF*) the flow will come into contact with the ambient air, which is at a certain pressure, temperature and velocity. For the schematics in Figure 2.1 it is assumed that the velocity and or the pressure are lower than the respective exit value. This means that the flow, leaving the nozzle is, decelerated and/or the pressure must be increased. This is only possible by means of a shock wave. Such a shock would naturally occur as an oblique shock, that is emitted from the nozzle wall at the exit. In case a larger pressure and/or velocity difference has to be overcome, the oblique shock might partially or fully develop into a normal shock. This is shown by the red lines in Figure 2.1. Further downstream the shock will cross itself and might develop into shock train with the distinctive Mach diamonds visible at the intersection points. The green line in Figure 2.1 represents the shear layer that naturally forms between viscous flows of different velocity.

The situation described above is representative for the case where exit pressure p_e and ambient pressure p_a do not differ significantly. In case the nozzle is under-expanding the flow, thus if $p_e \gg p_a$, the flow will continue to expand rapidly after it leaves the nozzle. Therefore the shock and shear layer pattern will look substantially different and the shock pattern might disappear all together. In case the the flow is over-expanding, thus if $p_e \ll p_a$ the shock pattern will get stronger, move upstream and will develop more into normal shock. Usually flow separation inside the nozzle at the nozzle wall will occur, thus also the flow pattern inside the nozzle will be altered. The effects of flow separation will be briefly discussed in the following sub-section.

2.1.3. Nozzle Flow Separation

For viscous flow the velocity at and near the nozzle wall is zero. This means for a nozzle with strong over-expansion ($p_e \ll p_a$) that flow from the outside can potentially travel upstream into the nozzle along its wall. Therefore causing the actual nozzle flow to separate from the nozzle wall. The separation is usually accompanied by an oblique shock wave directed towards the nozzle exit. The whole effect is called free-shock separation and is displayed in Figure 2.2a.

Besides the free-shock separation there also exists the so called restricted-shock separation. In this case the flow first separates from the nozzle wall but reattaches a little further downstream followed by a series of smaller oblique shocks. The reattachment is caused by a natural internal shock which occurs further upstream of the first separation point. This is outlined in Figure 2.2b. The restricted-shock separation can only occur in a nozzle geometry that naturally features this internal shock in the nozzle turning region. An example for a contour is the Thrust Optimised Parabolic (TOP) contour first described by Rao [21]. Therefore, this phenomena will not be observed in any ideal or conical nozzle as these are naturally shock free until the exit. For an overview of different nozzle contour types see Ref. [2]. The restricted-shock separation has only recently been investigated in more detail, for details see Frey and Hagemann [22].

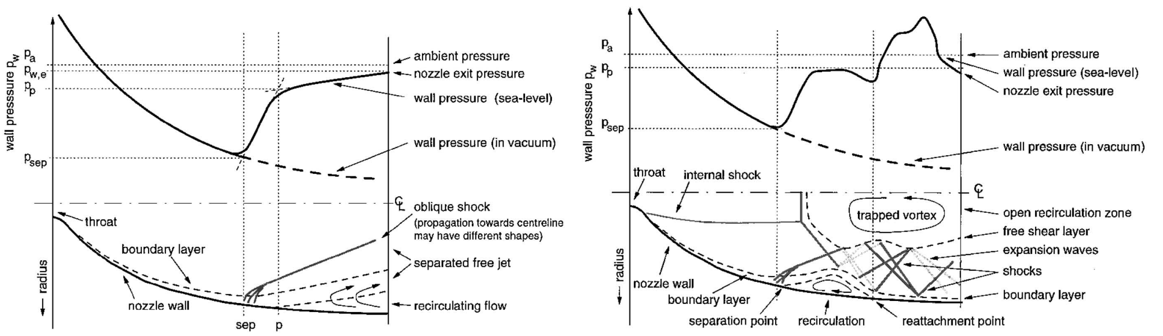

(a) Free-Shock Separation (b) Restricted-Shock Separation

Figure 2.2: Types of Flow Separation in an Overexpanded Rocket Nozzle, compression wave/ shock: ——, expansion waves: ···, boundary/ shear layer edge: − − −, Figures obtained from Frey and Hagemann [22]

Flow separation is generally considered undesirable. It causes a reduction in performance and the oblique shock puts high strains on the nozzle wall. The separation point is often not the same throughout the nozzle and the shock therefore is unsymmetrical. This can cause large off-axis loads which can potentially destroy the nozzle and in consequence the engine and the whole vehicle. The whole phenomena and its side effects have been described in detail by Hagemann et al. [23].

As flow separation is so undesirable, numerous criteria have been developed that predict when flow separation will occur, such that it can be prevented at an early design stage. The first work in this field has been done by Summerfield et al. [24], who published an empirical criterion at which flow separation might occur. The criterion is usually referred to as the Summerfield criterion. It states that flow separation occurs below a pressure ratio of $p_{sep}/p_a = 0.35 \cdots 0.4$. Here p_{sep} represents the pressure below which the flow separates. If p_e is designed as such that it is always above p_{sep} flow separation will not occur inside the nozzle.

$$\frac{p_{sep}}{p_a} = \left(1.88 \cdot M_{sep} - 1\right)^{-0.64} \tag{2.13}$$

Another well known criterion for flow separation is the Schmucker criterion, developed by Schmucker [25]. The criterion is described by Eq. 2.13 and relates the separation pressure p_{sep} and Mach number M_{sep} to the ambient pressure p_a. There are a large number of criteria that predict flow separation an overview can be found in the paper of Stark [26].

2.2. Computational Fluid Dynamics (CFD)

The following section describes all Computational Fluid Dynamics (CFD) related fundamentals, starting with the governing equations, their numerical solution and a description of the applied turbulence model. Thereafter the concept of adapted grids is outlined and finally the so called Chimera or Overset Grid Method is explained. Note, the theory outlined here is, except for the last two topics, a summary from the Literature Study [2].

2.2.1. Fundamental Equations

The fundamental or governing equations for any viscous CFD calculation are the Navier-Stokes Equations. These are derived from the three fundamental principals of conservation of mass, momentum and energy, which will result in the continuity equation, three momentum equations and the energy equation. There are four general versions of these equations. There is a conservation and a non-conservation form, where the term conservation refers to the fact that that the form directly conserves the mass. Each of the two afore forms can also be written in the integral (volume) form or the differential (infinitesimal element) form. Thus, there are a total of four forms. For the derivation and the exact differences see Anderson [27].

$$\frac{\partial \rho}{\partial t} + \frac{\partial}{\partial x_j}\left(\rho V_j\right) = 0 \tag{2.14}$$

$$\frac{\partial}{\partial t}\left(\rho V_i\right) + \frac{\partial}{\partial x_j}\left(\rho V_i V_j\right) = -\frac{\partial p}{\partial x_i} + \frac{\partial \tau_{ij}}{\partial x_j} \tag{2.15}$$

$$\frac{\partial}{\partial t}\left(\rho H\right) + \frac{\partial}{\partial x_j}\left(\rho V_j H\right) = \frac{\partial p}{\partial t} + \frac{\partial}{\partial x_j}\left(V_j \tau_{ij} - q_j\right) \tag{2.16}$$

The Navier-Stokes equations in the conservation and differential form are given above. Where Eq. 2.14 represents the continuity equation, Eq. 2.15 is the momentum equation and Eq. 2.16 the energy equation. Note, for conciseness they have been written in much shorter Einstein notation. This does not only shorten the respective equation, but also compresses the momentum equations, normally three, such that it looks like a single equation, see Eq. 2.15. The equations have been obtained from the book of Cebeci [28].

$$\tau_{ij} = \lambda \delta_{ij} \frac{\partial V_l}{\partial x_l} + \mu \left(\frac{\partial V_i}{\partial x_j} + \frac{\partial V_j}{\partial x_i} \right) \tag{2.17}$$

$$q_j = -k \frac{\partial T}{\partial x_j} \tag{2.18}$$

$$H = h + \frac{1}{2} V_i \cdot V_i \tag{2.19}$$

The shear stress tensor τ_{ij} in the momentum and energy equation (Eqs. 2.15 and 2.16) is defined by Eq. 2.17. The heat transfer q is defined by Eq. 2.18 and the total enthalpy H is given in Eq. 2.19.

$$p = \rho \cdot R \cdot T \tag{2.20}$$

The above set of equations has to be completed by an additional equation or relation which relates the pressure p, density ρ and temperature T. An example for such a relation is the ideal gas law, see Eq. 2.20, which is used for all CFD calculation except for the hot-gas cases presented in Chapter 4.5.

2.2.2. Numerical Solution

The system of equations presented in the previous section needs to be solved numerically for each grid point. This is done by the respective CFD solver. For this project the DLR TAU-Code was used. In this section only the basic principles and methods are outlined, for further details see Ref. [2] or the TAU-Code documentation [29].

Like most modern CFD solvers the TAU-Code is a Finite Volume Method (FVM) solver and therefore solves the Navier-Stokes equations in their integral form. For details on the finite volume discretisation see Hirsch [30]. Each of the Navier-Stokes equations can be converted into a general form, which is shown in Eq. 2.21.

$$\frac{\partial}{\partial t}\oint_{\mathscr{V}} U\, d\mathscr{V} + \oint_{\mathscr{S}} \mathbf{F}\cdot\mathbf{dS} = \oint_{\mathscr{V}} Q\, d\mathscr{V} \tag{2.21}$$

In Eq. 2.21 variable U represents the time dependent scalar variable integrated over the cell volume, which in case of the continuity equation (Eq. 2.14) would be the density ρ. $\mathbf{F}$ stands for the flux vector, which is integrated over cells boundary surface. For the continuity equation $\mathbf{F} = \rho\mathbf{V}$. Q represents a sum of the respective source terms. In case of the continuity equation $Q = 0$ for the other equation Q represents what is written on the right hand side.

$$\frac{\partial}{\partial t}\left(U_j \mathscr{V}_j\right) + \sum_{faces} \mathbf{F}\cdot\Delta\mathbf{S} = Q_J \mathscr{V}_j \tag{2.22}$$

Eq. 2.21 can be discretised for a specific cell j, this results in Eq. 2.22. The source term on the right hand side is usually evaluated as an average over the respective control volume $(Q\mathscr{V})_i = \mathbf{Q}\left(\mathbf{U}_i\right)\mathscr{V}_i$.

The left term on the left hand side of Eq. 2.22 must be discretised over the time domain. There are implicit and explicit time stepping schemes. As an implicit time scheme TAU features a first-order Backward Euler scheme. Discretising the 1D version of the continuity equation as an example using a Backward Euler scheme results in Eq. 2.23. Here superscript n represents the time step and subscript i indicates the cell. The equation cannot be solved on its own, but must be solved as a system of equations or matrix including the neighbouring cells. Thus solving any implicit time scheme includes inversion of a very large matrix for each time step. For details see Ref. [2].

$$\frac{\rho_i^{n+1} - \rho_i^n}{\Delta t} = \frac{-u}{\Delta x}\left(\rho_i^{n+1} - \rho_{i-1}^{n+1}\right) \tag{2.23}$$

As an explicit alternative TAU features a higher order Runge-Kutta scheme, where the coefficient and thus the order can be defined by the user. For details on the Runge-Kutta scheme, see Hirsch [30] or Ref. [2].

The right term of the left hand side governs the flux over the cell boundaries and is discretised over space. The convective and viscous fluxes are usually split and evaluated separately. Only the former will be elaborated here, for further details for both methods see Blazek [31]. When considering spatial discretisation methods one usually differs between central schemes (up- and downwind neighbouring cells are taken into account) and upwind schemes (only neighbouring cells situated upwind are included). The former are generally unstable for supersonic flow and will thus not be considered here, for further details see Ref. [2].

$$\left(\mathbf{F}_c \Delta S\right)_{i+1/2} \approx f_{Flux}\left(\mathbf{W}_L,\, \mathbf{W}_R,\, \Delta S_{i+1/2}\right) \tag{2.24}$$

Most modern schemes to determine the flux over a cell boundary, at $i + 1/2$ (both upwind and central) can be described by Eq. 2.24. Where the vector $\mathbf{W}$ stands for the individual flow variables (velocities u, v, w, pressure p, density ρ, temperature T and enthalpy H). The indices L and R stand for the left and right side of the boundary face $i + 1/2$.

$$W_R = W_{i+1} - \frac{\epsilon}{4}\left[(1+\kappa)\,\Delta_- + (1-\kappa)\,\Delta_+\right]\ W_{i+1} \tag{2.25a}$$

$$W_L = W_i + \frac{\epsilon}{4}\left[(1+\kappa)\,\Delta_- + (1-\kappa)\,\Delta_+\right]\ W_i \tag{2.25b}$$

$$\Delta_+ W_i = W_{i+1} - W_i \tag{2.26a}$$

$$\Delta_- W_i = W_i - W_{i-1} \tag{2.26b}$$

A general approach to interpolate the flow variables on the right and left hand side is shown in Eq. 2.25. The Delta Operators $\Delta_\pm$ are defined in Eq. 2.26. The coefficients ϵ and κ determine the exact scheme. Setting $\epsilon = 0$ will result in a first order upwind scheme and setting $\kappa = -1$ and $\epsilon = 1$ will lead to a second order upwind scheme. The above two equations form the basis for most modern upwind schemes and have first been published by van Leer [32] as part of his Monotonic Upwind Scheme for Conservation Laws (MUSCL).

$$(\mathbf{F}_c)_{i+1/2} = (M_n)_{i+1/2} \begin{bmatrix} \rho a \\ \rho a u \\ \rho a v \\ \rho a w \\ \rho a H \end{bmatrix}_{L/R} + \begin{bmatrix} 0 \\ n_x p \\ n_y p \\ n_z p \\ 0 \end{bmatrix}_{i+1/2} \tag{2.27}$$

The exact upwind scheme used for this project is the so called AUSMDV or AUSM D/V scheme, developed by Wada and Liou [33]. The scheme is considered a hybrid scheme featuring aspects of both Flux-Difference and Flux-Vector splitting scheme, hence the abbreviation D/V. The scheme is based upon the original Advection Upstream Splitting Method (AUSM) developed by Liou and Steffen [34]. This is a Flux-Vector splitting scheme, where the convective flux is split into velocity (Mach number) component and a pressure component, see Eq. 2.27. An overview of the most common upwind schemes including the AUSM D/V scheme can be found in the book of Blazek [31]. A summary of all available upwind schemes in the TAU-Code, including an explanation about the particular choice for AUSM D/V scheme, is presented in the Literature Study [2], which was conducted in preparation to this project.

$$Res_\rho^n = \sqrt{\sum_{i=1}^{N_{no}} \frac{\left[\mathbf{F}_\rho\,(i)\,/\mathscr{V}\,(i)\right]^2}{N_{no}}} \tag{2.28}$$

To asses the convergence of CFD simulations the residuals of the governing equations are monitored. The global residual Res for a certain time step n for a single equation is defined as the root mean square of the residual for each cell or node. The residual for a single cell or node is defined as the flux $\mathbf{F}$ over the cell/node boundary divided by the volume $\mathscr{V}$. This is shown for the density residual, which is the residual for the continuity equation (Eq. 2.14), is shown in Eq. 2.28. With N_{no} being the total number of nodes or cells and $\mathbf{F}_\rho\,(i)$ the density component of the flux vector for node i.

2.2.3. RANS Turbulence Modelling

In the Literature Study [2] it was concluded, that directly or partly simulating the turbulent flow through Direct Numerical Simulation (DNS) or Large Eddy Simulation (LES)/Detached Eddy Simulation (DES) respectively is not feasible. DNS and LES are too expensive from a computational point of view and the TAU-Code is also not capable of DNS. DES is computationally somewhat less demanding, however its improvements in accuracy compared to modelling the turbulent flow would in the given case be negligible. Moreover, both LES and DES have not been developed for highly compressible flow through a nozzle, but to simulate the flow over a wing. Therefore, it was decided to model the turbulent flow using classical Reynolds-Averaged Navier-Stokes (RANS) approach.

Modelling turbulent flow is based on the principal of averaging. First an average over time is assumed, this stipulates that the flow can be split into two components a mean component, which is constant over time, and a fluctuating component. Time averaging is usually referred to as Reynolds averaging, as the concept was first published by Osborne Reynolds [35]. However, purely averaging the Navier-Stokes equation over time will lead to a couple of undesirable terms that cannot easily be solved. These terms drop out if the equations are also averaged over the density (or mass). This concept was first applied by Favre [36]. Therefore, the time and density averaged Navier-Stokes equations are sometimes referred to as Favre/Reynolds-Averaged Navier-Stokes Equations. However, in most modern literature the name Favre is omitted and they are simply called Reynolds-Averaged Navier-Stokes Equations (RANS). A detailed summary of the two averaging concepts can be found in the Literature Study [2] and the full derivation can be found in the book of Cebeci [28].

$$\frac{\partial \bar{\rho}}{\partial t} + \frac{\partial}{\partial x_j}\left(\bar{\rho}\tilde{V}_j\right) = 0 \tag{2.29}$$

$$\frac{\partial}{\partial t}\left(\bar{\rho}\tilde{V}_j\right) + \frac{\partial}{\partial x_j}\left(\bar{\rho}\tilde{V}_i\tilde{V}_j\right) = \frac{\partial \bar{p}}{\partial x_i} + \frac{\partial}{\partial x_j}\left(\bar{\tau}_{ij} - \overline{\rho V_i' V_j'}\right) \tag{2.30}$$

$$\frac{\partial}{\partial t}\left(\rho\bar{\tilde{H}}\right) + \frac{\partial}{\partial x_j}\left(\bar{\rho}\tilde{H}\tilde{V}_j\right) = \frac{\partial \bar{p}}{\partial t} + \tilde{V}_j\frac{\partial \bar{p}}{\partial x_j} + \overline{V_j'\frac{\partial p}{\partial x_j}} + \frac{\partial}{\partial x_j}\left(-q_j - \overline{\rho h' V_j'}\right) + \overline{\tau_{ij}\frac{V_i}{\partial x_j}} \tag{2.31}$$

The RANS equations written in Einstein notation are displayed above in Eq. 2.29 to 2.31. Where the overhead-bar represents a mean time averaged variable, the overhead-tilde indicates a mean density average variable and the $'$ is fluctuating density component. The fluctuating time component would be denoted by a $''$, however they all cancel out in the derivation. For the full derivation, see Cebeci [28].

$$\tau_{ij} = -\overline{\rho V_i' V_j'} = 2\tilde{\mu}_T\left(\tilde{S}_{ij} - \frac{1}{3}\frac{\partial \tilde{V}_k}{\partial x_k}\delta_{ij}\right) - \frac{2}{3}\bar{\rho}K\delta_{ij} \tag{2.32}$$

$$\tilde{S}_{ij} = \frac{1}{2}\left(\frac{\partial \tilde{V}_i}{\partial x_j} + \frac{\partial \tilde{V}_j}{\partial x_i}\right) \tag{2.33}$$

$$K = \frac{1}{2}\left(\tilde{V}_i' \cdot \tilde{V}_i'\right) \tag{2.34}$$

The RANS equations presented above contain one unknown, this is the so called Reynolds stress tensor $\overline{\rho V_i' V_j'}$. The term represents the fluctuations in the momentum of the flow due to turbulence. This term needs to be modelled using a turbulence model. Most turbulent models make use of the eddy-viscosity or Boussinesq hypothesis. This hypothesis states that the turbulent shear stress is linearly related to the mean strain rate $\tilde{S}_{ij}$ through the turbulent dynamic viscosity μ_T. The exact relation is shown in Eq. 2.32. The strain rate is defined by Eq. 2.33 and K is given in Eq. 2.34. The turbulent dynamic viscosity μ_T is a component of the overall fluid viscosity $\mu = \mu_L + \mu_T$. The other component is the regular laminar viscosity μ_L, which is temperature dependent and can be determined using the Sutherland law.

Each turbulence model approximates the turbulent dynamic viscosity in a different manner. Usually one, two or even more differential equations are solved. This results in a respective equal amount of variables out of which the turbulent dynamic viscosity is calculated. Different turbulence models are classed according to the number of differential equations and the variable they use. An example for a one-equation model is the Spalart Allmaras model [37], where a single equation for the kinematic eddy viscosity $\tilde{\nu}$ is solved. From which the turbulent dynamic viscosity μ_T is determined. Well known two-equation models are the $k - \varepsilon$ by Jones and Launder [38] or the $k - \omega$ model of Wilcox [39]. A description of these models and their equations can be found in Cebeci [28] and detailed description including verification and validation cases for most turbulent models has been collected by NASA [40].

A detailed overview of the different models available in TAU can be found in the Literature Study [2].

The model that was chosen for this project is the Menter-SST model, see Menter [41]. The Menter-SST model is a derivative of the original $k-\omega$ model of Wilcox [39]. It solves for k (turbulent kinetic energy) and ω (specific dissipation rate) using a modified version of the two-equation system of the Wilcox model. However, it also features aspects from the $k-\varepsilon$ of Jones and Launder [38]. Using this approach it combines the advantages of both models, namely: Robust, cheap and good approximation of wall bounded flows and improved prediction of free-shear layer flows and flows subjected to adverse gradients and flow separation. Therefore, the model was chosen as the default model for this project. A more detailed comparison and description (including all equations) of the model can be found in the Literature Study [2]. The full Menter-SST model is also described in Ref. [40].

2.2.4. Grid Adaptation

The solution based adaptation of the grid or mesh has become a common practice in CFD. It refers to the modification of the mesh, meaning a shifting or resizing of cells or the increase or decrease of the number of cells, based on the results of an initial steady state solution or an older time-step generated with the original mesh. The method is used to refine the mesh in regions of strong gradients (e.g. shocks) and to assure the mesh is resolved sufficiently to capture the flows boundary layer. Two distinctive types of adaptation have been used throughout this project, both are presented separately below.

y^+ Adaptation

This adaptation type deals exclusively with the refinement of the structured grid in the boundary layer. It only changes the size (height) of the cells and shifts them in wall-normal (y) direction. No cells are removed or created. It increases the cell concentration and decreases cell height in the regions of strong velocity gradients, which is usually near the wall. As an indicator for the objective function the dimensionless wall distance y^+ is used. Hence, this type of adaptation is often referred to as $y+$ Adaptation.

$$u_\tau = \sqrt{\frac{\bar{\tau}_{wall}}{\rho}} \tag{2.35}$$

$$\delta_v = \frac{\nu}{u_\tau} \tag{2.36}$$

$$y^+ = \frac{y}{\delta_v} = \frac{y u_\tau}{\nu} \tag{2.37}$$

The dimensionless wall distance y^+ is defined as the ratio between the physical wall distance y and the wall layer thickness δ_v, see Eq. 2.37. The wall layer thickness δ_v is defined by Eq. 2.36, where ν is the kinematic viscosity and u_τ is the so called friction velocity. The latter is defined as the square root of the ratio of the wall shear-stress $\bar{\tau}_{wall}$ and the density ρ. A detailed derivation can be found in the book of Schlichting and Gersten [42].

The concept of the dimensionless wall distance y^+ is part of the so called *Universal Laws of the Wall*, which is derived from the *Couette Flow* model (a wall-bounded or channel flow where the top wall is moving with the local flow velocity u). For details see the book of Schlichting and Gersten [42]. The law divides the boundary layer into three sections: The pure viscous sublayer ($0 \leqslant y^+ < 5$), the buffer layer ($5 < y^+ < 70$) and the overlap (or log-law) layer ($70 < y^+$).

The y^+ adaptation tries to optimise the structured grid such that the the first cell height is at $y^+ \approx 1$. This assures sufficient resolution of the first part of the boundary layer (viscous sublayer) where the viscous shear forces τ_v are dominant compared to the turbulent shear forces τ_t. In fact, per definition of the law of the wall $\tau_t = 0$ for $y^+ = 1$, see Schlichting and Gersten [42]. For details regarding implementation of this principle into CFD algorithm, see Ref. [29].

Full Adaptation
A full adaptation deals with the full grid and not only the structured part at the boundary layer. Moreover, it may in- or decrease the number of cells of the mesh. It increases the the number of cells based on the gradient of certain flow variables. The gradient is defined as the difference of a flow variable between two grid points, divided by the distance between the two points. In areas with heigh gradients cells are added into the mesh, at areas with low gradients cells can also be removed. The amount of cells to be added is defined by the user, also the indicator variables are user defined. Typical regions with strong gradients are areas with strong expansion or compression (shock-waves) and free shear layers between regions of different velocity. Typically the number of cells is increase in these areas. Whether or not cells are also removed in regions with a low gradient is defined by the user. For details regarding implementation of this principle into CFD algorithm, see Ref. [29]. An example of two fully adapted grids can be found in Chapter 4.2.3 in Figure 4.8.

2.2.5. Chimera Grid Method

The chimera grid method, sometimes also referred to as the overset or overlapping grid method, is a CFD technique using multiple combined grids on top of each other. The method was amongst other developed by Benek, Steger and Dougherty [43, 44]. Its application is advantageous when dealing with complex and possibly multi-body geometries. Specific parts can than be meshed in detail without increasing the number of cells of the overall grid too much. Moreover, it is easier to replace or re-mesh certain parts of the geometry. This greatly increases the flexibility. However, the biggest advantage of this technique is that the the individual grids can be moved with respect to each other during the simulation. This enables the simulation of geometries in relative motion without deforming the grid, which would only allow limited motion, or without having to regenerate the grid for each time step, which would be extremely laborious and computationally intensive. Dougherty, Benek and Steger [45] first applied their own method to simulate the store separation from an aircraft. Another famous application is the simulation of booster and tank separation from the Space Shuttle, by Meakin and Suhs [46]. A detailed description of the method itself can be found in the work of Hadžić [47].

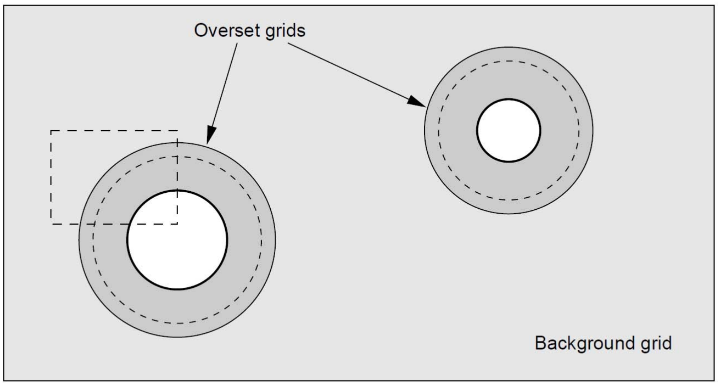

Figure 2.3: Chimaera Grid System Layout, Figure obtained from Hadžić [47]

The basic layout of a chimera grid system is depicted in Figure 2.3. The system displayed features a rectangular 2D background grid. Laid over the background grid are two circular bodies each surrounded by their own individual overset grid.

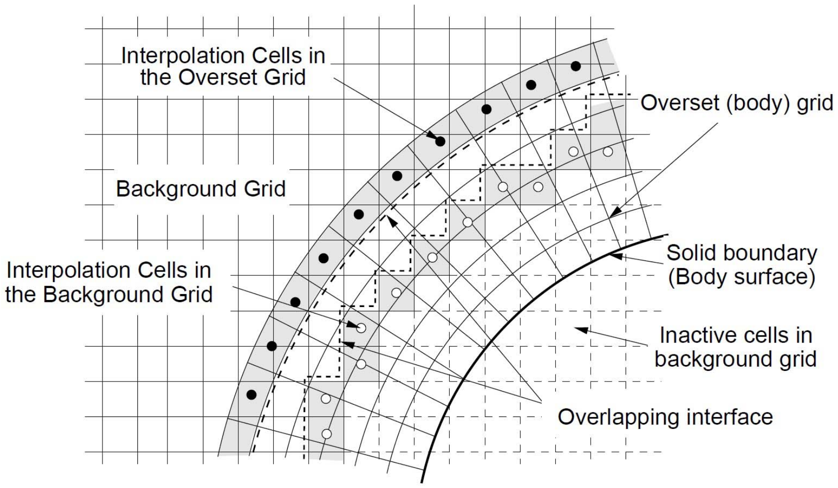

Figure 2.4: Chimaera Grid Overlapping Region, Figure obtained from Hadžić [47]

The interaction between the overset and background grid is outlined in Figure 2.4. Compared to an ordinary grid a chimera grid requires two additional steps:

Hole Cutting: The term hole cutting referrers to the exclusion or deactivation of cells that should not be part of the calculation. This exclusion is achieved by cutting a hole in the respective grid, hence the term hole cutting. There are multiple reasons why a cell should be excluded from the calculation domain:

1. The presence of a body. The body is usually contained within the respective overset grid. Therefore, the cells in the background at the location body must be deactivated. This is shown in Figure 2.4, by the dashed cells.
2. The presence of another grid. If two grids overlay each other the calculation should only be performed on one of the two grids. Usually the overset grid is used, meaning the respective cells in the background grid are deactivated. However, it is necessary to keep of a couple of cells of the background grid active, such that there is a sufficiently large overlap zone. The overlapping zone or interface is required for inter grid communication (see below). See Figure 2.4 for reference.
3. Out of limits of the background grid. If an overset grid is in parts or completely out if the limits defined by the background grid the respective cells are usually deactivated, unless this is otherwise specified. This case is not shown in any Figure. However, it should be kept in mind, as it occurs in both forms in this project, see Chapter 4.4.1.
4. Overlapping overset grids. If the two bodies shown in Figure 2.3 come to close too each other, their respective grids or even the two bodies would overlap. In this case both the cells in background grid and in one of the two overset grids must be deactivated. Therefore, a priority amongst the different overset grids must be specified.

The locations of the holes can be specified by the user or alternatively can be determined automatically by an algorithm, which is part of the solver. An automatic algorithm for that purpose was developed by Nakahashi et al. [48]. The DLR TAU-Code allows for two different user specified methods, and since version 2016.2.0 also features an automatic algorithm. As the choice of method is inherently coupled to the specific case which is to be simulated, these methods will be discussed in the respective case setup, see Chapter 4.4.1. For more details regarding the hole cutting procedure, see Hadžić [47].

Donor Searching and Interpolation: Information between the different grids needs to be communicated. This is done through interpolation from donor cells. For each pair of grids that overlay each other two interpolation boundaries exist. One transferring information from the background grid to the overset grid, this is always situated at the outer boundary of the overset grid, which is assigned a special chimera boundary condition. This is shown by the • in Figure 2.4. The other boundary transfers information from the overset grid back onto the background grid. This occurs at the hole boundary in the background grid, see ◦ in Figure 2.4.

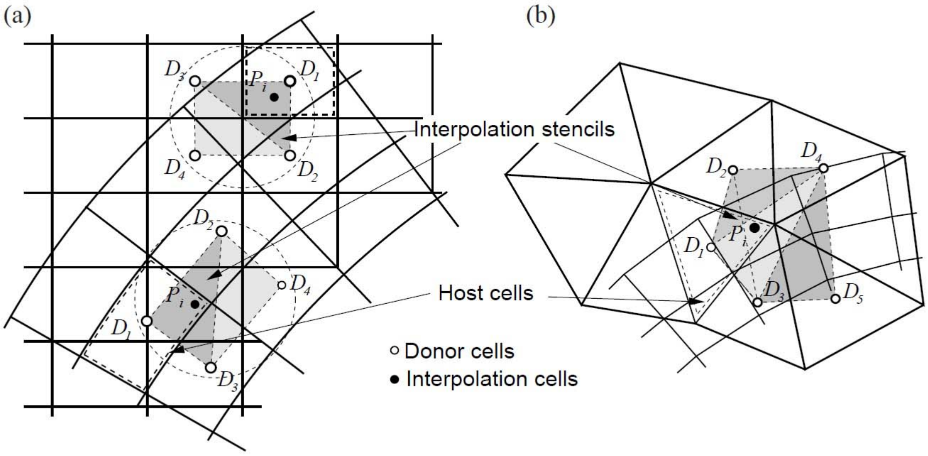

Figure 2.5: Chimaera Grid Interpolation, for a structured grid (a) and an unstructured grid (b), Figure obtained from Hadžić [47]

For each interpolation cell a main donor (host) cell needs to be found on the respective other grid. This is essentially a geometric optimisation problem. There exist multiple methods to solve such a problem. For example a Neighbour-to Neighbour Search, used by Hadžić [47] or the Alternating-Digital-Tree, developed by Bonet and Peraire [49]. The latter option is used by the TAU-Code. Once the host donor has been found an interpolation stencil can be constructed that uses the surrounding neighbours of the host cell as additional donors. This is shown for a structured and an unstructured grid in Figure 2.5. For an unstructured grid it is important that the interpolation cell lies within the stencil formed by the donors. If only the direct neighbours D_2 and D_3 of the host D_1 and the host itself would be used, this would not be the case. Therefore, more donors need to be included. The conservative variables transferred to the other grid are interpolated from all donor cells using linear interpolation. More details on the donor search and interpolation can be found in the work of Hadžić [47].

If the overset grid is in motion, the above steps need to be executed prior to any new time step. First the holes need to be re-cut and than the donor cells and interpolation stencil needs to be determined for each interpolation boundary point. The motion of a grid also needs to be governed by the separate dedicate function, this will be discussed during the chimera setup, see Chapter 4.4.1.

This concludes the general description of the Chimera or Overset Grid Method. Here only a brief overview of the principles could be given, for a more detailed description of the method used in a modern FVM solver see the work of Hadžić [47] or the paper of Nakahashi et al. [48].

3. 1D Nozzle-Pintle Simulation

This chapter outlines the 1D Simulation, that models the flow through a Nozzle-Pintle configuration in a simplified manner. The simulation was developed prior to the CFD calculations. The chapter first describes the setup of the simulation followed by the obtained results.

3.1. Simulation Setup

The main objective of the 1D Simulation was to provide a quick first order estimate for the thrust and pintle-load as a function of the pintle position of a particular Pintle-Nozzle configuration and geometry at predefined, constant gas (combustion) parameters. The general setup and structure of the simulation code is outlined in the following section.

3.1.1. General Setup

The simulation has been developed using Matlab, as it is both simple and well known amongst the engineering community. The simulation relies on a number of simplifying assumptions, which are listed below:

1. The gas/ combustion parameter in the post combustion chamber (upstream of the convergent section of the configuration) are said to be constant. Hence p_c, T_c, R and γ are constant and independent of the current pintle position.
2. The gas is modelled as an ideal gas. Hence $p = \rho RT$ is valid.
3. The flow is assumed to be compressible and inviscid.
4. The flow is assumed to be quasi-one-dimensional. Hence any flow properties varies in x-direction only (e.g. $p = p(x)$ or $u = u(x)$). Note, the "quasi" as the cross-sectional area varies with x only.
5. The flow is assumed to be continues, hence $\rho_1 u_1 A_1 = \rho_2 u_2 A_2$.
6. The flow is assumed to be isentropic.
7. The throat, $M = 1$ line, for a specific pintle position, is assumed to be located at the min. cross-section of the current configuration.

The above assumptions and simplifications mean that the problem reduces to solving Eq. 2.3 many times for different expansion ratios for each pintle position and for the thrust equation once per pintle position. The remainder of the simulation is mostly solving the geometrical problems. These are outlined in Figure 3.1. A flow chart of the whole simulation is depicted in Figure 3.2. Using both these figures the simulation is explained step by step, below:

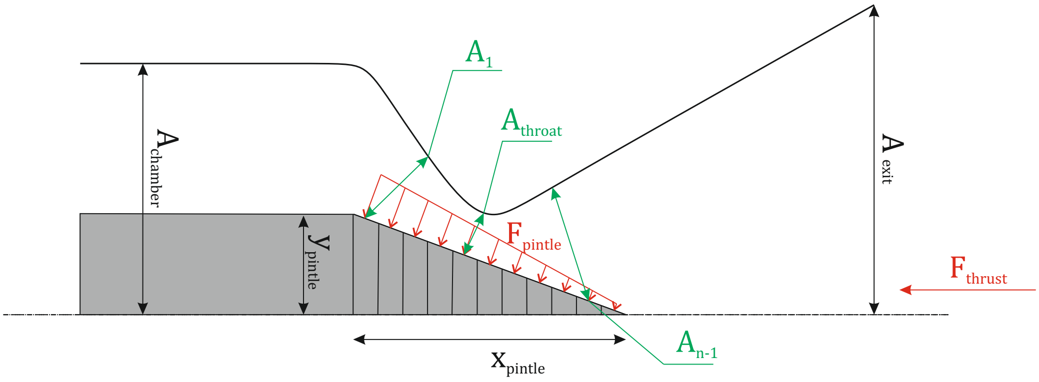

Figure 3.1: Principles of the 1D Nozzle-Pintle Simulation

The initial steps of the simulation code define all required inputs. The different input types are displayed as the orange diamonds in the flow chart, see Figure 3.2. Starting with the combustion/gas parameters: The pressure and temperature, the specific gas constant R, the specific heat ratio γ and the operational altitude. From these values the dependent parameters like c^* and the ambient pressure are calculated.

Secondly, the nozzle geometry is defined. Currently, the code is setup to use conical geometry with radii in the nozzle throat and between the chamber and divergent section (see Figure 3.1). However, the simulation in theory accepts any lists of non-equidistant x and y points. In its current setup the nozzle is defined using the throat radius, the chamber radius, the expansion ratio, the half angles of the convergent and divergent section and the three radii of curvature (between chamber and convergent section, between convergent section and throat and between throat and divergent section). From these values the cross-sectional areas, the length of the convergent and divergent sections and the lists with x and y coordinates for the full contour are calculated. The contour is calculated as such that it is fully continuous.

The pintle definition is very similar to the nozzle. Currently the simulation code accepts a simple conical shape, without any round corners. It is defined via the length x and height y of the conical part, see Figure 3.1. The final input required is the definition of the pintle displacement. This is done via the min. and max. position and a step size. These values are then used to setup the for-loop, with each loop iteration being one pintle position, see Figure 3.2. In order to decrease the total run time the simulation has the option of executing the for-loop in parallel, for this the Matlab Parallel Computing Toolbox is used.

At the start of each iteration the relative pintle coordinates are calculated with respect to the nozzle. Thereafter the pintle is discretised into n segments or slices, as visualised in Figure 3.1. For each segment the mid point coordinates and the circumferential surface area are calculated. Further the minimum distance between each segment mid point and the nozzle contour is calculated. For this complex geometric operation an already existing external function from the Matlab File Exchange was used, for details see [50]. The function was verified by applying it to a test case which yielded successful results. From the minimum distance the minimum cross-sectional area for each mid point is calculated. The smallest one is defined to be the throat area. Dividing the min. cross-sectional area for each mid point by the throat area results into a list with the expansion ratio for each mid point.

Note, in an older (more simplified) version of the tool the minimum cross-sectional area for each segment was assumed to be on the vertical line. The minimum throat area was assumed to be on the line perpendicular to the pintle surface which intersected the nozzle throat corner. The older version also did not a allow the definition of a curved throat, instead the throat was simplified as a horizontal line with a finite length. However, these assumptions led to a significant error in both thrust and pintle force prediction. This was especially true for positions where the pintle is almost fully inserted as then a small error in the throat area will have a large influence on the expansion-ratios. The relative differences in pintle force prediction for the two version was 3% for the full thrust position, 15% for the mid position and 85% for the minimum thrust position. The relative differences in thrust were less significant.

To obtain the pressure acting on each segment Eq. 2.3 has to be solved. This is only possible with a numerical approach, for this the *vpasolve* Matlab function is used. Each expansion-ratio Eq. 2.3 yields two solutions for the pressure, one sub and one supersonic solution. Thus if the mid point is located upstream of the throat the subsonic solution is assigned and for locations downstream of the throat the supersonic solution is used (see Assumption No. 7 in the above list).

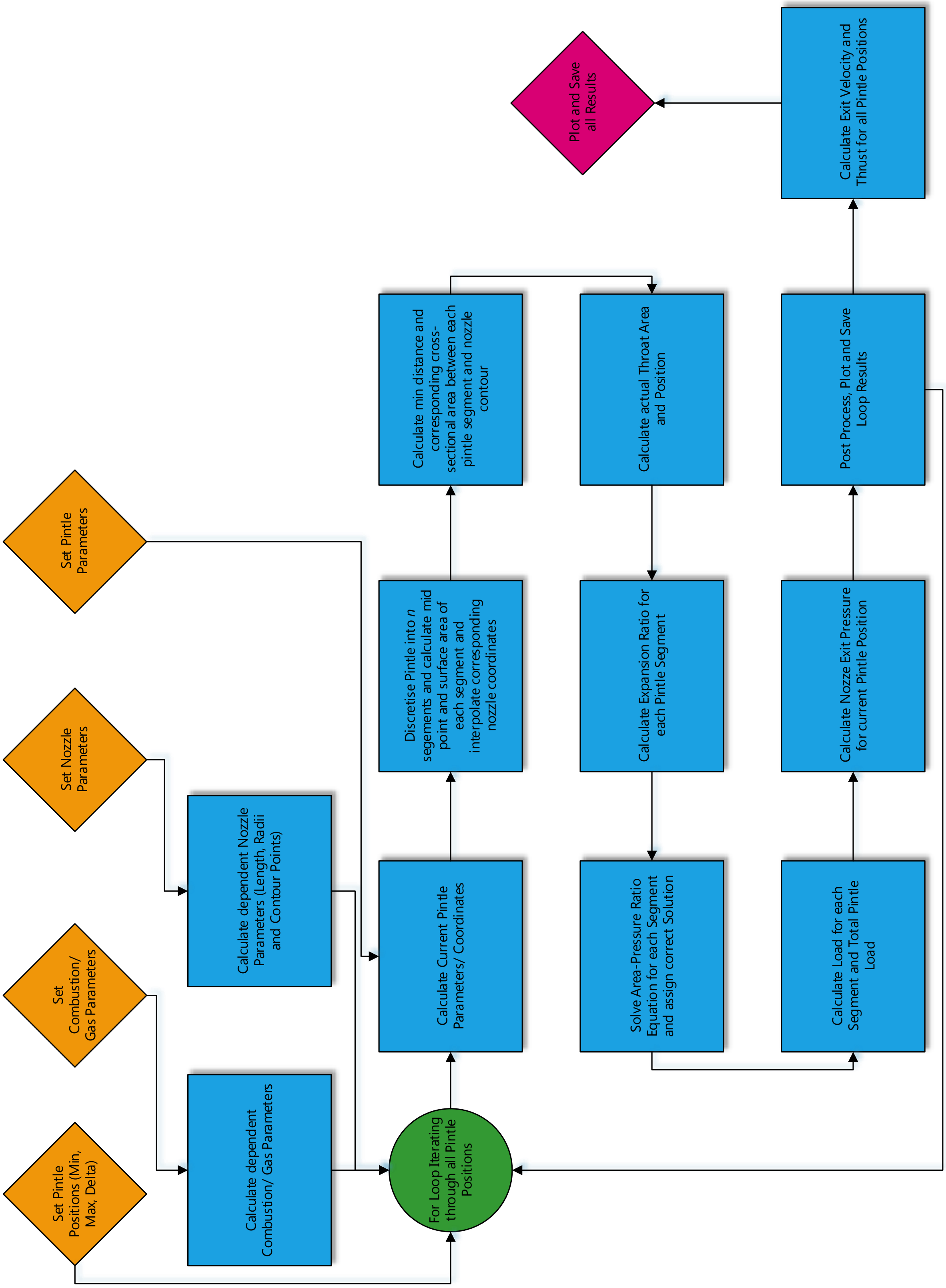

Figure 3.2: Flow Diagram of the 1D Nozzle-Pintle Simulation

$$F_{pin} = \sum_{i=1}^{i=n} \left[p_i \cdot S_i \cdot \sin(\alpha) \right] \tag{3.1}$$

The pintle load can then be calculated using Eq. 3.1, where p_i is the pressure for a single segment i with the surface area S_i and the angle α is the conical half angle of the pintle. This yields into the pintle force in x-direction, the force in y-direction cancels out for a symmetric pintle. The final calculation step of each iteration is to determine the nozzle exit pressure for the current pintle position. For this Eq. 2.3 needs to be solved again. At the end of each loop results are saved and plotted.
After the for-loop is complete the exit velocity and thrust are calculated from the exit pressure, using Eqs. 2.8, 2.11 and 2.12. Finally the summarised results are again plotted and saved.

3.1.2. Initial and Boundary Conditions

The above pages describe the general setup for the 1D Simulation, the specific setup for the given case is outlined below. Please note, that the absolute dimensions and initial conditions cannot be mentioned in this report. Values have been made dimensionless using certain reference values these or are marked as Not-Available (n/a), whenever the value shown is the reference value. Details and the reason for this are described in Appendix A. As a propellant gas Nitrogen was used. The initial (combustion) and nozzle exit conditions are summarised in Table 3.1.

Table 3.1: Initial and exit conditions of the 1D Simulation

Condition:	**Value:**
Specific gas constant R	$296 \quad [J/(kg \cdot K)]$
Specific heat ratio γ	$1.5 \quad [-]$
Combustion pressure p_c	$n/a \quad [Pa]$
Combustion temperature T_c	$n/a \quad [K]$
Exit conditions	*Ambient at:* $0.0 \quad [km]$

The nozzle and pintle geometry is equivalent to the geometry that was used for the simulation at that was also tested. Details on the test setup can be found in Chapter 5.1. The geometry is outlined in Figure 4.1 in the following chapter and can also be found in Metsker [16]. It should be noted the pintle closed position is not equivalent to zero thrust, hence the throat is never fully blocked. The geometry was designed in such a way that at the closed position the system produces approximately 5% of its max. design thrust.

3.2. Simulation Results

The second part of this chapter presents and discusses the results of the 1D Simulation. All results are displayed as graphs. Note, also here the actual/absolute performance values cannot be displayed. Instead all performance values have been made non-dimensional, using a reference value. For example by dividing by the max. thrust in case of forces. Details can be found in Appendix A. The performance values that are of most interest are the thrust and the pintle load, these are displayed in Figure 3.3.

Both thrust and pintle force increase the further the pintle is opened/retracted. They both initially increase roughly linear, starting from approximately the same value of force, while the increase in thrust is somewhat steeper than the pintle load. At about 40% of the relative pintle position the gradient starts to slowly level of. The thrust gradient eventually reaches zero. This is expected as the throat area stays constant once the pintle is fully retracted. While the force on the pintle should keep increasing, as the pressure distribution over the pintle keeps increasing to p_c, until the pintle is completely upstream of the convergent nozzle section. The max. pintle load is approximately 65% of the max. thrust, both are reached at the final and fully open pintle position.

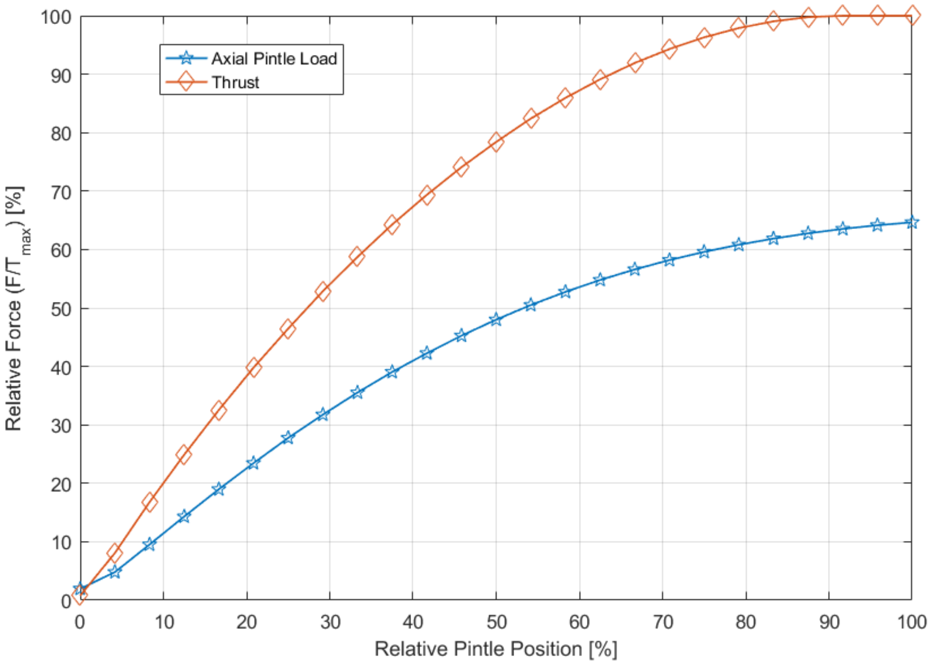

Figure 3.3: Thrust and Pintle Load as function of Pintle Position as predicted by the 1D Simulation (Values have been made dimensionless according to Table A.1))

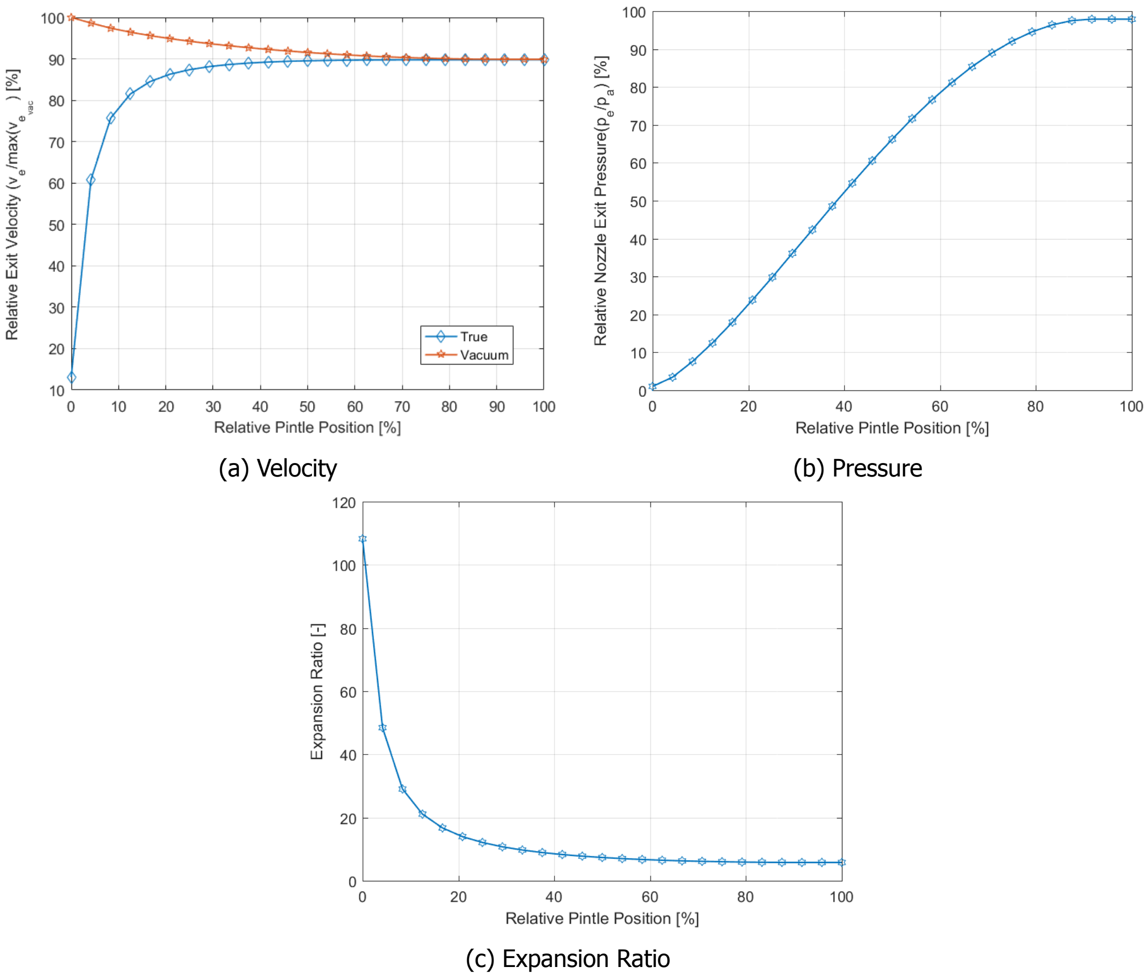

(a) Velocity

(b) Pressure

(c) Expansion Ratio

Figure 3.4: Nozzle Exit Conditions as function of Pintle Position as predicted by the 1D Simulation (Values have been made dimensionless according to Table A.1)

Figure 3.4a shows the vacuum and true exit velocity of the nozzle. The vacuum exit velocity is max. at the closed pintle position at which the the true exit velocity is zero. The vacuum exit velocity slowly levels off to about 90% of its max. value. The true exit velocity makes a steep rise in the first 15% of the pintle movement and than slowly approaches the same value as the vacuum value. This behaviour is as expected as the expansion ratio $\varepsilon = A_e/A_t$ at the closed pintle position is very large due to the very small throat area A_t, while the exit area A_e remains constant. This effect is depicted in Figure 3.4c. Here it can be seen that the initial expansion ratio is more than twenty times the final expansion ratio, which is the same as the expansion ratio of only the nozzle. Moreover, it becomes eminent that the expansion ratio behaves inversely proportional to the true exit velocity. Therefore, the flow is over-expanded to a very high velocity and thus extremely low pressure (see Figure 3.4b). The ambient pressure p_a is thus much higher than the exit pressure p_e. Therefore, reducing the true exit velocity to a value very close to zero. In reality it is highly likely that flow separation, see Chapter 2.1.3, and backflow into the nozzle will occur at the lower pintle positions. As the 1D Simulation does not treat any viscous effects these effects are neglected here. However there are a couple of criteria, which are based on empirical data and can predict flow separation, for details see Ref. [2]. The simplest one is the so called Summerfield criterion, see Chapter 2.1.3 or Summerfield [24]. This states that flow separation occurs below a pressure ratio of $p_{sep}/p_a = 0.35 \cdots 0.4$. Thus according to the Summerfield criterion flow separations would occur for all relative pintle positions below approximately 31.5%. However it should be kept in mind that the Summerfield criterion and all similar criteria are based on empirical data from conventional nozzles, hence it remains to be seen whether they can be applied to this particular nozzle configuration.

Figures 3.5, 3.6 and 3.7 show the simulation at three different pintle postions. The left plot shows the configuration of each loop. The blue curve shows the nozzle contour, the orange curve shows the pintle in its current position and the black line indicates the location of the smallest cross-sectional area, hence the throat. The right plot shows the corresponding pressure distribution over the discretised pintle.

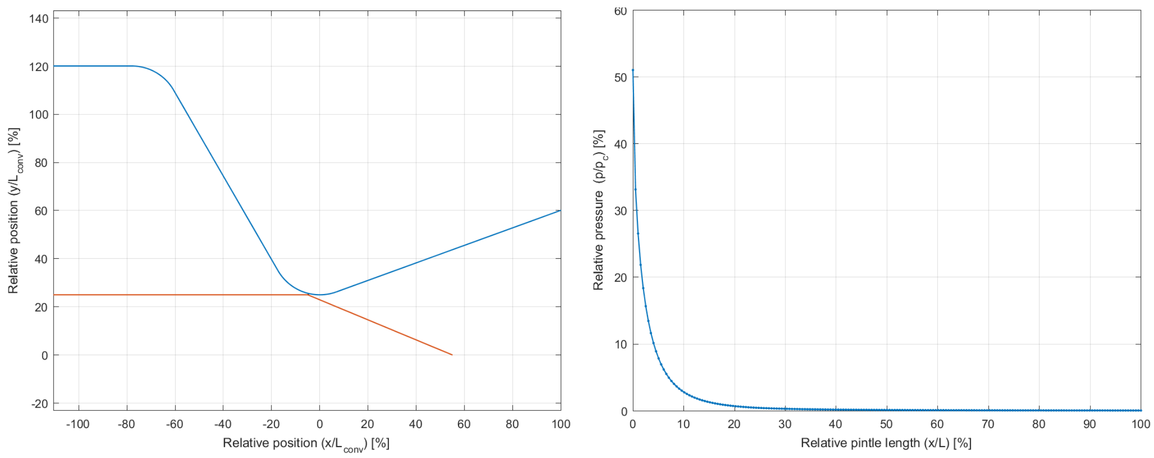

(a) Configuration (b) Pressure Distribution

Figure 3.5: 1D Simulation at Pintle Fully Closed Position (Position values have been made non-dimensional with the length of the divergent nozzle section L_{div} and pressure values have been made non-dimensional by the combustion pressure p_c)

Figure 3.5 shows the simulation at the 0% pintle fully closed position. Note the black line or dot representing the throat is hardly visible. The pressure over the pintle starts at 60% of the combustion pressure p_c at the pintle and rapidly drops to zero. Such a sharp pressure drop again indicates flow separation. Therefore, it is likely that for the closed position flow separation will occur both on the nozzle wall and on the pintle.

Figure 3.6 shows the simulation at the 50% (mid) pintle position. The pressure curve in Figure 3.6b looks like a typical curve showing the expansion through a nozzle. The flow expands from almost 100% of the combustion pressure to a value slightly below 10% of p_c. The discontinuity at 50% of the pintle

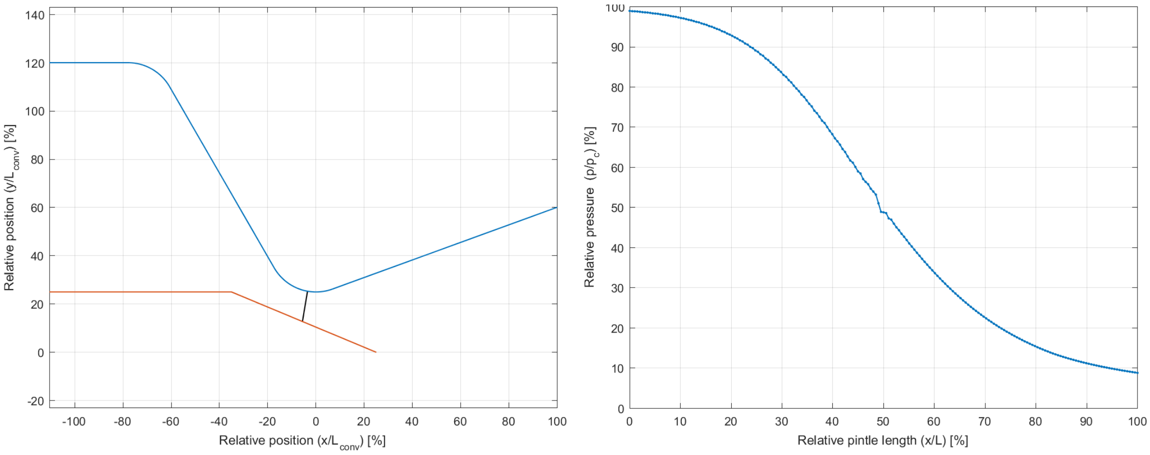

(a) Configuration (b) Pressure Distribution

Figure 3.6: 1D Simulation at Pintle Mid Closed Position (Position values have been made non-dimensional with the length of the divergent nozzle section L_{div} and pressure values have been made non-dimensional by the combustion pressure p_c)

length is not attributed to a shock, but to an error in the calculation of the cross-sectional areas of each segment. This error is caused by the discretisation of the pintle into a finite number of segments.

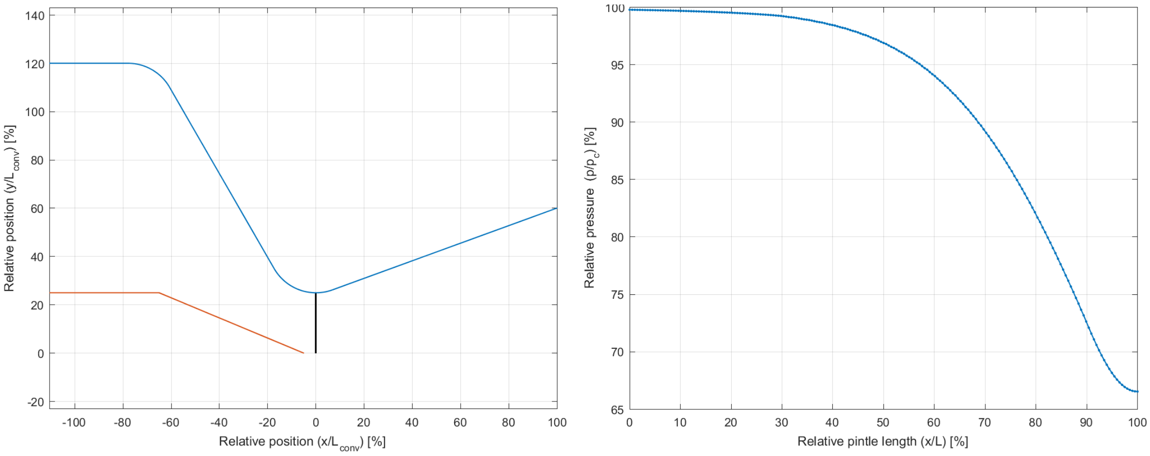

(a) Configuration (b) Pressure Distribution

Figure 3.7: 1D Simulation at Pintle Fully Open Position (Position values have been made non-dimensional with the length of the divergent nozzle section L_{div} and pressure values have been made non-dimensional by the combustion pressure p_c)

Figure 3.7 shows the simulation at the fully open (retracted) position. The black line in Figure 3.7a, representing the throat position, indicates that the pintle does not influence the flow downstream of the flow anymore. The throat area is equivalent to the nozzle only geometry. The pressure distribution over the pintle is depicted in Figure 3.7b. The flow is expanded from 100% to about 67% of the combustion pressure. The curve has a typical shape of the subsonic/convergent expansion curve of a nozzle.

This concludes the presentation of the 1D simulation and its results. The simulation seems to be meeting its requirements in providing a rapid estimate of the thrust, pintle force, etc. of a nozzle-pintle given fixed inlet conditions. Thus it is covering the first (sub) objective (see Chapter 1) of this project. The results presented here will be directly compared to the respective CFD results in the following chapter and will be analysed in further detail in Chapter 6.

4. CFD Simulation

This chapter deals with the CFD simulations that were performed in the course of this project. The chapter starts with a section describing the general setup of all CFD simulations. Thereafter the initial reference or test case is outlined, followed by the static Nozzle-Pintle simulation. The hot-gas static simulations and the dynamic chimera simulations are also presented in dedicated sections.

4.1. General Setup

This sections describes the general setup, which is roughly equivalent for all the CFD simulations. The respective specifics are explained in the dedicated section later in the chapter.

All CFD simulations have been made using the DLR TAU-Code, which employs the Finite Volume Method. During the project different versions of the code were used, this should not have any influence on the comparability of the results, but nevertheless will be highlighted in the respective sections. "The DLR TAU code is actually not one code but a modern software system for the prediction of viscous and inviscid flows about complex geometries from the low subsonic to the hypersonic flow regime, employing hybrid unstructured grids." Ref. [51] The tools main and intended application area is to simulate flow over a body, such as aircrafts, cars or rockets, hence it is a tool mainly for external aerodynamic flows and not for an internal flow problem simulated here. In theory this should not make much of a difference, but the fact should always be kept in mind. In practice this leads to some minor problems in the solver setup, which can be circumvented by applying a number of tricks. These will be highlighted later on. The TAU-Code has been developed in house by the Deutsches Zentrum für Luft- und Raumfahrt, German Aerospace Center (DLR). It is not an open source code and is not publicly available, like for example OpenFOAM. In theory it is possible to purchase the code from DLR and some larger companies like Airbus and MBDA use the code. However, in many aspects the code is not comparable to the classic commercial codes as for instance ANSYS (Fluent, CFX) or COMSOL. It is less robust than commercial codes and little documentation or support is publicly available.

4.1.1. Geometry, Domain and Boundary Calculation

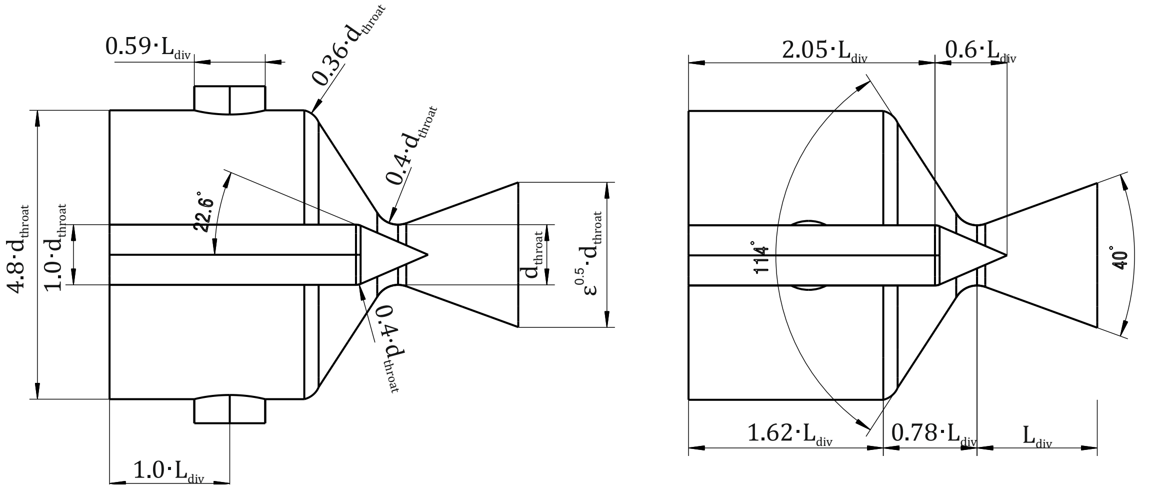

Figure 4.1: CFD Nozzle Geometry, based on Nozzle Geometry in Test Setup described in Ch. 5

Figure 4.1 above shows the thruster geometry that is to be simulated here. Downstream of the post combustion chamber the geometry is equivalent to the 2D geometry used in the 1D simulation (see previous Chapter 3). Figure 4.1 shows a cut-view of the actual geometry, the right view is rotated by 90° with respect to the left view. Note, the absolute dimension of the geometry cannot be disclosed in this report. The dimensions in Figure 4.1 are given as a function of the length of the divergent nozzle section L_{div} or the throat diameter d_{throat}. The left view shows the different diameters of the thruster, the radii between the different sections. Also the size and position of the cylindrical inlets are shown. Note, when creating the mesher geometry a minor error occurred. In the actual test geometry and in the 1D simulation the radius of curvature at the throat and between post combustion chamber and convergent section are equal. As this is a very minor error, which should not have any significant influence on the over all flow field and as it was only noticed very late in the course of the project, it was neglected. The right view shows all dimensions in x-direction, plus the angles of the nozzle.

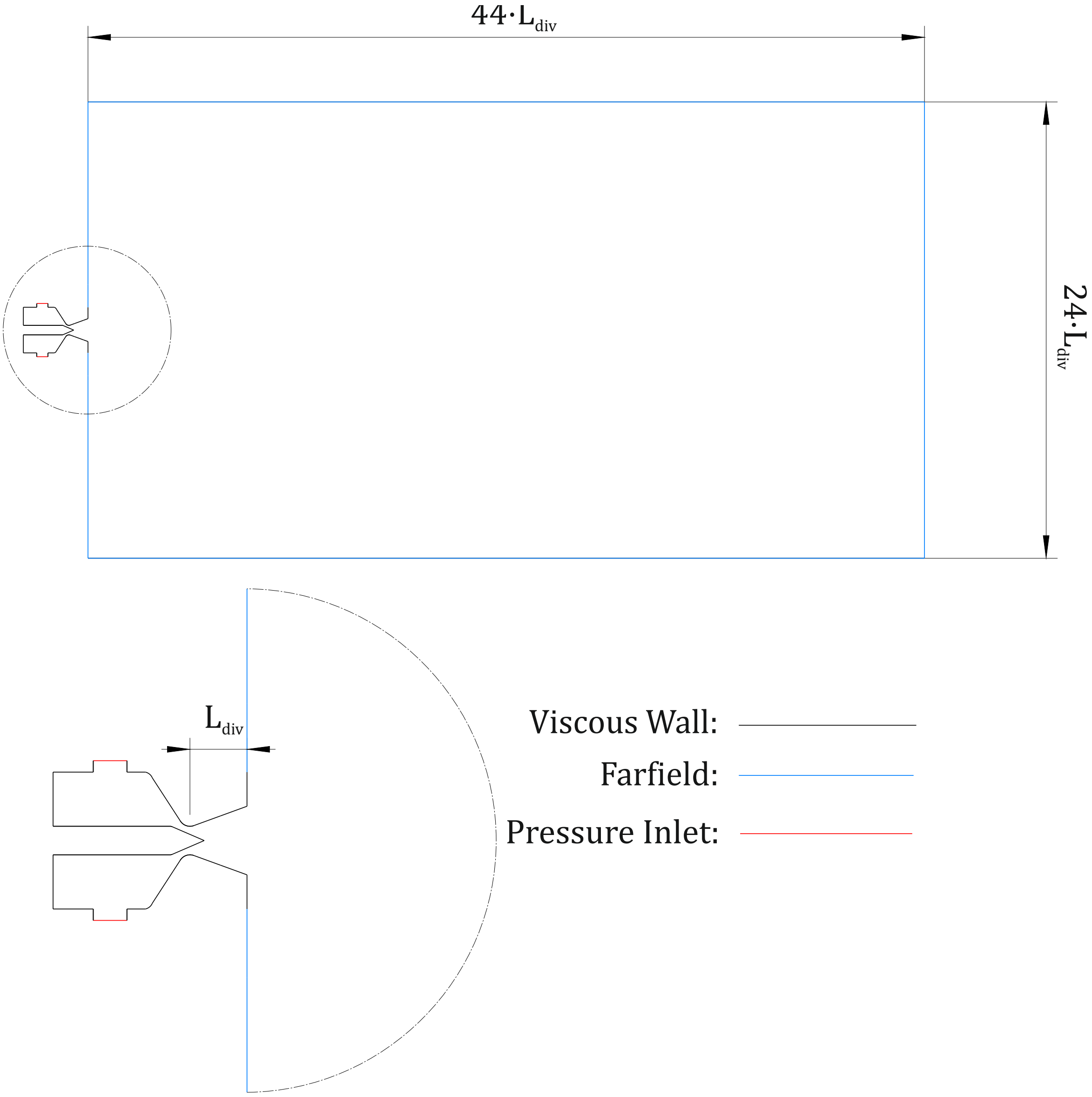

Figure 4.2: CFD Boundary Condition and Domain Layout

Figure 4.2 shows the layout of the full domain and the boundary layers. As the flow field downstream of the nozzle is also to be investigated the domain has to be extended accordingly. This is done by a cylindrical domain with a farfield boundary condition (blue lines in Figure 4.2). The dimensions of the farfield domain have to be chosen sufficiently large in order to avoid interferences between the farfield boundary condition and the relevant parts of the flowfield. The dimensions of the farfield domain are given as a function of the length of the divergent nozzle section L_{div}, see Figure 4.2. The farfield boundary has been set to ambient conditions at sea-level. The red lines in Figure 4.2 represent the inlet boundary condition. For this a so called *reservoir-pressure inflow* condition was chosen. This is defined as "... an inflow boundary for internal flow with prescribed constant total pressure and total density. The inflow direction is by default perpendicular to each boundary face, or it can be set to a desired direction." Ref. [29]. All remaining boundaries are defined as adiabatic viscous walls, see black lines in Figure 4.2. This means that per definition the velocity at the wall must be zero and that no heat transfer occurs between the fluid and the wall.

The TAU-Code requires as a mandatory input in combination with a farfield boundary condition a so called *Reference Velocity* or *Reference Mach number*. This value is used for initialisation of the flowfield and as a velocity for farfield boundary conditions. The latter means that fluid is streaming into the farfield with the given reference velocity from left to right at a given angle of attack (here 0°). The reference velocity must be unequal to zero, this would lead to division by zero. However, here any farfield velocity other than zero would induce an error in the physical solution. On the other hand, to initialise the flowfield a high reference velocity would be desirable. Parts of the solution are expected to be in the hypersonic speed range, therefore initialising the flowflield at a zero or very low velocity, would increase the calculation time and slow down convergence, but should not lead to an error in the solution, as initial conditions and final solution should be independent. For an aerodynamic problem, like the flow over an aircraft, the whole setup is well suited, as the aircraft would be surrounded by the farfield and the reference velocity would simply be the desired free-stream velocity. In this case however the particular setup does not make sense and is one of the minor issues of the TAU-Code mentioned and the beginning of this section. To minimise the error in the flowfield the reference velocity should be kept as low as possible. After some initial trials it was decided to perform all calculations with a reference Mach number of $M_{ref} = 0.01$.

4.1.2. Mesh Generation

The TAU-Code uses 2D or 3D hybrid unstructured cell-vertex meshes, but does not include a mesh generation tool. To generate the mesh any software that can export a hybrid unstructured cell-vertex mesh in the *Centauer*, *ICEM* or *FLOWer* format can be used, see Ref. [29]. For this project an in house tool developed by Airbus was used, see Ref. [52].

The meshing tool is fully script based and does not have a graphical-user-interface. A diagram showing the working principal of the tool is shown in Figure 4.3. The geometry to be meshed is defined as a *step* file. The step file must already include the named geometric groups (grouped lines and surfaces), that are relevant to the meshing process. It must also include a possible farfield boundary. All other inputs are script based. Starting with the logical model that connects the different CAD groups with the groups in the mesher. The mesher starts with meshing the surface of the geometry, it first rasters the geometry and connects all points to a surface mesh. The second step is to construct the structures boundary layer.

$$n_{lay} = \ln\left(\frac{h_{BL}}{h_{L_1}}\right) / \ln\left(GR\right) \tag{4.1}$$

The construction of the structured boundary layer is defined via the first layer height h_{L_1}, the total number of layers n_{lay} and the growth rate per layer GR. These three parameters are related to the total boundary layer height h_{BL} by Eq. 4.1. Typically the number of layers lies between 30 and 40, here $n_{lay} = 36$ was chosen. The growth rate usually is in the order of 1.3, here $GR = 1.32$ was used for all meshes. When selecting the total boundary layer one has to make sure to capture the actual boundary layer of the flow. Usually, the boundary layer inside a regular nozzle is not very large, usually in the order of a couple of percent of the throat radius, for details on nozzle boundary layers see Ref. [2]. However, as this project deals with rather unconventional nozzle shapes, a conservative estimate was made and $h_{BL} = 0.1 \cdot d_{th}$ was selected. Using Eq. 4.1 the first layer height can be calculated, resulting in a first layer height of approximately 0.04 ‰ of the total boundary layer height. When constructing the structured boundary layer, another aspect is important. The aspect ratio of the last layer should

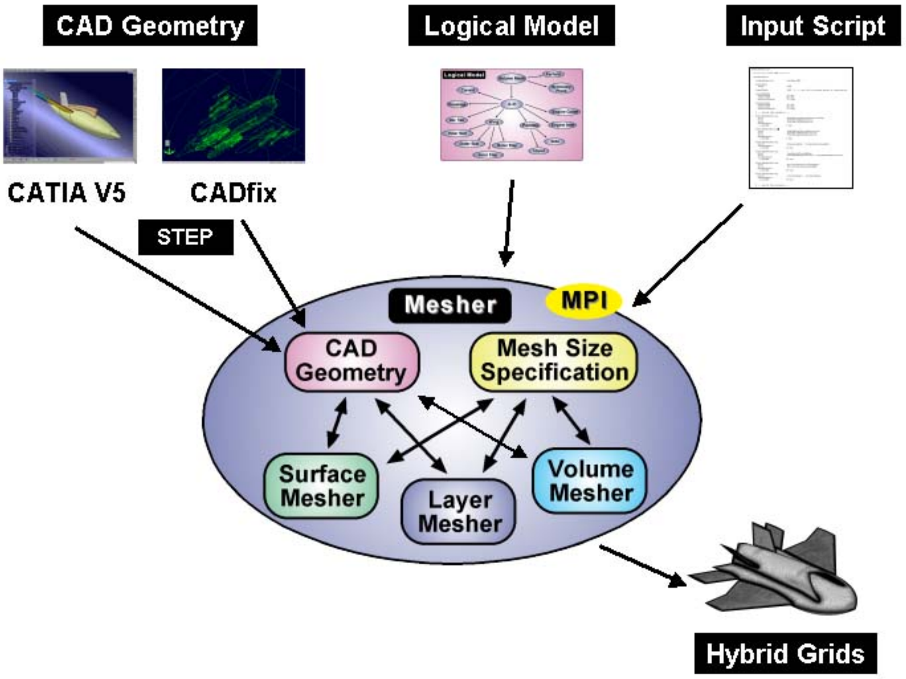

Figure 4.3: Overview of the in-house Meshing Tool, from Ref. [52] (Image Credit: Airbus Defence & Space)

be close to one, hence the cell is cube. Moreover, it should have roughly the same aspect ratio as the first/ neighbouring unstructured cell. This can be achieved by modifying the growth rate or the number of layers. The last step of the mesher is to create the unstructured volume mesh.

The level of mesh refinement can be steered in two ways: The first one is the raster script, which defines how edges and faces of the geometry are rasterised. For the given problem nozzle pintle problem the faces and edges in the curved throat area are the most refined, with a max. arc length of $0.02 \cdot d_{th}$. The faces and edges of the inlet, the divergent nozzle section and the conical part of the pintle have a max. arc length of $0.04 \cdot d_{th}$, the convergent nozzle section of $0.12 \cdot d_{th}$ and the remainder of the post combustion chamber of $0.12 \cdot d_{th}$. The edges of the farfield boundary have a max. arc length $3.0 \cdot d_{th}$ and a min. arc length of $0.60 \cdot d_{th}$. All these refinements directly effect the surface mesh only, the volume mesh is only indirectly effected. To directly influence the volume mesh it is possible to make use of local refinement sources in the volume, for this a dedicated source script is used. There are two types of sources: A point source, which is defined by its position its refinement level/spacing and its sphere of influence, which is defined by two radii. A line source, which is essentially two connected point source forming a cylindrical or conical shape. In the given geometry a couple of sources where used: A line source connecting the two inlet, to refine the region where the fluid is streaming into the combustion chamber and stagnate on the pintle. A line source connecting the start of the convergent section and the throat, which gets smaller and finer towards the throat. Another line source connecting throat and nozzle exit, which gets coarser and wider towards the exit. And a final line source refining the exhaust plume, which ranges approximately 2/3 down the total farfield length and is 1/3 in width. For cases where the pintle is inserted very far into the throat, the space between nozzle and pintle wall becomes very small, therefore an additional very fine point source was placed into the throat. This leads to a significant increase in the number of nodes and an increased calculation time for these meshes.

The respective meshes ar not presented in this section, but can be found in their respective sections further down the chapter. The mesh of the reference nozzle case can be found in Figure 4.4 in Section 4.2, selected meshes of the nozzle-pintle configuration can be found in Section 4.3, Figures 4.9, 4.11 and 4.13.

Note, the meshes shown in the above mentioned figures are not the exact the same meshes as generated by the mesher. It is the mesh, that has been modified using the TAU-Code $y+$ adaptation algorithm. Here the structured part of the boundary layer is modified, based on a stationary solution using the original mesh, to fit the actual boundary layer. In this procedure no new cells are added or removed from the mesh. The structured cells only change there spacing and width with respect to each other. After the $y+$ adaptation, the calculation is restarted with the new mesh and run until its has converged. This procedure is standard for CFD calculations to make sure all boundary layer effects have be properly captured and has been done throughout this project for all static CFD calculations. The basic principles behind the adaptation method are outlined in Chapter 2.2.4.

4.1.3. Solver Setup

The TAU-Code solver is mainly setup via two scripts, hence it does not posses a graphical-user-interface. One script is used to define and assign the different boundary conditions, these were already discussed in Section 4.1.1. The second script contains all the actual solver settings.

At the top of the script the preprocessing is defined. During the preprocessing the primary mesh is partitioned into multiple domains for later parallel calculations. Here the primary mesh was split into 64 domains. Furthermore, it is possible to apply so called multigrid levels, where each domain is created multiple times with different and consecutively lower refinement. This way it is possible to decrease the amount of iterations that are required for convergence and to prevent oscillation in the solution. It can however also make the computation less stable, especially in case of supersonic flow containing discontinuities. During initial trial calculations for this project, different multigrid levels and settings were tested, as expected, non yielded satisfactory results. Therefore, a standard singlegrid method was used.

As a spatial solver a 2nd order upwind method was used. During the literature study [2], that was performed prior to this project, different spatial discretisation methods were discussed. A summary of the most important aspects can be found in Chapter 2.2.2. In the literature study [2] it was concluded that only an upwind type method is suitable for supersonic flow. Further different types of upwind methods were discussed during the literature study, it was found that the *AUSMDV* method would likely be most suitable, but others like the *AUSM van Leer*, *MAPS* and *Roe* scheme should also be considered. Throughout the initial trial calculation this was confirmed, as the *AUSMDV* scheme converged to a fully stable solution. Other schemes took much longer to converge and or their final solution was still oscillating around a fixed value. During the trial calculations it was also discovered that starting a calculation from the initial conditions with 2nd order upwind immediately was not feasible. Convergence would take very long and required very low CFL numbers or the solution would not converge at all. Therefore, a first order fully converged solution was generated first using this the second order calculations was initialised. First order schemes are numerically much more diffusive than second order schemes, hence they are more stable but less accurate. As the standard *van Leer* scheme is more robust than the *ASUMDV* it was further decided to use it to generate the first order initial solution.

The TAU-Code employs two different time discretisation schemes, the implicit first order Backward Euler scheme and the higher order implicit Runge-Kutta scheme. For the latter scheme the coefficients and order can be defined by the user, with the default being a three stage/ order scheme. For details, see Ref. [2]. The Backward Euler scheme is usually more stable and also faster, the latter because it is only a first order scheme and the former as implicit schemes tend to be more stable than explicit ones. However, it is also less accurate. The standard scheme chosen for this project was therefore the Backward Euler scheme. The Runge-Kutta scheme was also tried in a couple of cases, to see if it would give better (more convergent) results. This was not the case in all cases performance was at most equal usually worse. Moreover, the calculation time was increased by around 50 $\%$ compared to the Backward Euler scheme. Therefore, it was decided to keep the Backward Euler scheme, as the default.

As all calculations are both viscous and turbulent a turbulence model must be specified. The TAU-Code features three types of turbulence models, RANS, LES and DES. During the previous literature study [2] all three types were discussed and it was concluded that only a RANS type model would be feasible, as the other two approaches are computationally too expensive and/or not worth the extra effort. A short overview of RANS turbulent models can be found in Chapter 2.2.3, for details see Ref. [2]. During the literature study [2] is was concluded, that out of the many different type of RANS models available in the TAU-Code, the *Menter-SST* would probably be the most suitable. Moreover, it was already successfully applied in nozzle flow problems, see Refs. [53] and [54]. Later into the project it was tested whether using the more simple one-equation *Spalart-Allmaras* model would yield to a better convergence of the solution. This was not the case, therefore the Menter-SST model was kept in place.

Further settings include the definition of the fluid used for the calculation. Here nitrogen N_2 was used, which was also used to perform the test described in Chapter 5. However, during the test the nozzle expands into an ambient atmospheric conditions, the CFD simulations expands into a nitrogen environment at atmospheric sea-level temperature and pressure. This will lead to a very small error in the overall CFD simulation. The error is considered negligible as the atmosphere is largely comprised out of nitrogen. Moreover, does this assumption greatly simplify the CFD calculation, as otherwise a real gas model with multiple components/elements would have had to be used. This would have also greatly increased the calculation time. It was further assumed that nitrogen behaves like an ideal gas in this temperature range. To model the temperature dependency of the viscosity of nitrogen Sutherlands law was used. An overview of the constants defining the fluid can be found in Table 4.1.

Table 4.1: Nitrogen N_2 Fluid definition for CFD calculations assuming an Ideal/ Perfect Gas

Condition:	**Value:**
Specific gas constant R	296 $[\mathrm{J}/(\mathrm{kg}\cdot\mathrm{K})]$
Specific heat ratio γ	1.5 [-]
Prandtl number Pr	0.72 [-]
Sutherland constant C	107 [K]
Sutherland reference viscosity μ_0	$1.6629\cdot10^{-5}$ $[\mathrm{Pa}\cdot\mathrm{s}]$
Sutherland reference temperature T_0	273 [K]

As reference values, which are also used to initialise the flow field, sea-level atmospheric conditions were used. The issue of the reference velocity/ Mach number, which was set to $M = 0.01$ was already addressed in Section 4.1.1. As a reference length and area, the nozzle exit radius and area were used respectively. The origin of the whole calculation domain was set to be in the centre of the nozzle throat. To monitor the convergence of the following values were used: Total force and moment vectors, the static inlet pressure and the massflow at inlet and over the farfield. Further the global continuity/ density residual was monitored. Monitoring of these values were not automated, but manually assessed on a calculation by calculation basis by the user. All other relevant settings will not be discussed here, but in the respective case section, as they differ from case to case.

4.2. Reference Nozzle CFD Simulation

The reference nozzle case, presented in this section, was setup to perform the initial trial calculations to get more familiar with the mesher and the solver, to find the optimal solver settings and to create a CFD solution for the reference nozzle. The reference solution will later be compared to the static nozzle-pintle simulation, which are presented in the following Section 4.3.

4.2.1. Reference Nozzle Setup

The geometry and the boundary conditions are the same as presented in Figures 4.1 and 4.2 in Section 4.1.1, with the exception that the pintle is missing. The post combustion chamber is empty and closed of at the end. The mesh was generated, as described in Section 4.1.2. A cut of the ZX-plane of the full mesh is depicted in Figure 4.4b. Here the nozzle itself is only visible as a black area, due the very fine resolution of the mesh. Nicely visible is the resolution of the farfield domain, with the line source refining the likely area of the exhaust plume with the resolution decreasing with the distance from the nozzle exit. The more relevant part of the mesh can be found in Figure 4.4a. Here the resolution in the post combustion chamber, with the two line sources connecting both inlets and resolving the convergent part of the nozzle. Also visible is the structured part of the mesh resolving the boundary layer. The divergent nozzle area is again only visible as a black surface due to its fine resolution, it can be seen in detail in Figure 4.4c. The mesh displayed here has a total of 7,552,102 nodes. This is in general quite high especially for such a small geometry. However, as a high speed flow is expected, with strong pressure gradients, including shocks and expansion waves, it was deemed necessary to accurately resolve these phenomena.

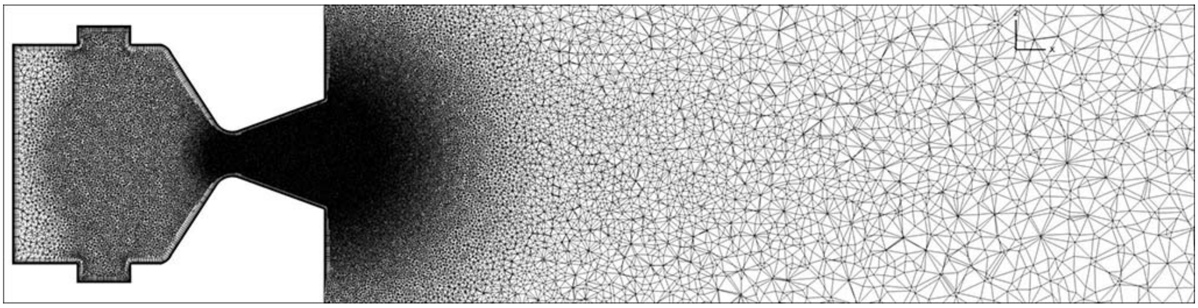

(a) Relevant Domain

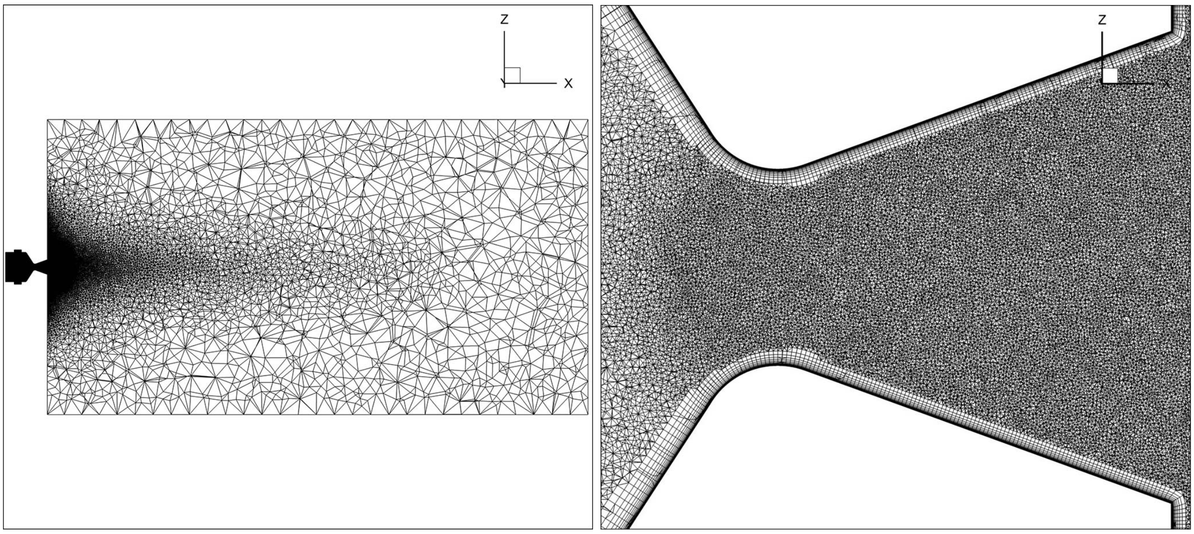

(b) Full Domain

(c) Critical Domain

Figure 4.4: Mesh Layout ZX-Plane Cut of the Reference Nozzle

The solver was setup in the same manner as described above in Section 4.1.3. However, there is one major difference. The very initial calculations performed with the reference nozzle where conducted at a 33 % increased total pressure at the inlet boundary. With this an initial first order solution was generated, using the *van Leer* scheme and a CFL number of 0.6. Based on this the a second order solution was generated, with the intended *AUSMDV* and a CFL number of 0.2. Shortly afterwards it was decided, not by the author, to lower the pressure for the tests conducted, see Chapter 5. Therefore, the pressure for all CFD calculations was lowered accordingly. The CFD calculation presented here is already at the correct pressure, it was however generated using the old calculation as the initial condition. This should not have an influence on the final solution, as these should be independent.

4.2.2. Reference Nozzle Results

The general results of the CFD simulation of the reference nozzle are presented in Table 4.2. All values are nondimensional values, as indicated in the table. Thrust and massflow have been made nondimensional using the values obtained from the 1D simulation, presented Chapter 3.2, to allow an immediate comparison. Thrust, massflow and static inlet pressure are part of the set of monitoring values and are logged for each iteration in the log file. The values shown in Table 4.2 have been averaged over the last 2500 iterations to average out the small oscillation which are present in the steady state solution. The nozzle exit pressure cannot be logged directly, its has been therefore been obtained by reading out the full solution file. The solution file exist however only for the final iteration, hence possible oscillation cannot be averaged out. Moreover, both the inlet pressure and the nozzle exit pressure are averaged over the inlet or exit area respectively.

Table 4.2: Average Nondimensionalised Results of the Reference Nozzle Case (Values have been made dimensionless according to Table A.1)

Relative (Averaged) Parameter:	**Value** [%]**:**
Thrust $\overline{T}$	0.48
Massflow $\overline{\dot{m}}$	94.04
Inlet Pressure $\overline{p}_{in}$	96.70
Nozzle Exit Pressure p_e	101.04

As the nozzle without the pintle and the nozzle with the pintle at the max. thrust/ pintle fully retracted position have the same throat area, expansion ratio, initial and ambient conditions and fluid properties, they should, according to the ideal rocket theory outlined in Chapter 2.1, have the same theoretical thrust, massflow and exit pressure. The simulated thrust in Table 4.2 is almost 10 % lower than thrust of the max. thrust in the 1D simulation and thus the theoretical loss free thrust. The mass flow is approximately 6 % below its theoretical maximum. The static pressure at the inlet is 3.3 % below the defined total pressure at the inlet boundary, which is the same as the assumed combustion/ reservoir pressure. That the static pressure at the inlet is below the total pressure indicates that the flow is not stationary but in motion. This is to be expected as the whole flow inside the post combustion chamber is moving. The nozzle expands to an exit pressure of 101.04 % of the local ambient pressure and is thus almost optimal. In comparison, the 1D simulation with the pintle fully retracted results a pressure of 97.0 % of the ambient pressure thus expands the flow a bit further. This can be explained by the viscous effects taken into account by the CFD simulation. These lead to a less optimal expansion of the flow and therefore to a somewhat higher exit pressure.

A cut for the whole flow field, showing the Mach number, pressure and temperature can be found in Figure 4.5. It was decided that to in general only show the cut through the inlet (ZX) plane. However, due to the design of the inlets the thruster is not x-axis symmetric, hence the other planes should also be analysed. For reference a XY-Plane cut of the Mach number contour is shown in Figure 4.6. When comparing the contours in Figures 4.5a and 4.6, a difference is visible. The largest difference is noticeable, when comparing the Mach lines in the nozzle exit area. However, the difference is still rather small and it thus concluded that only showing and analysing the ZX-cut is sufficient.

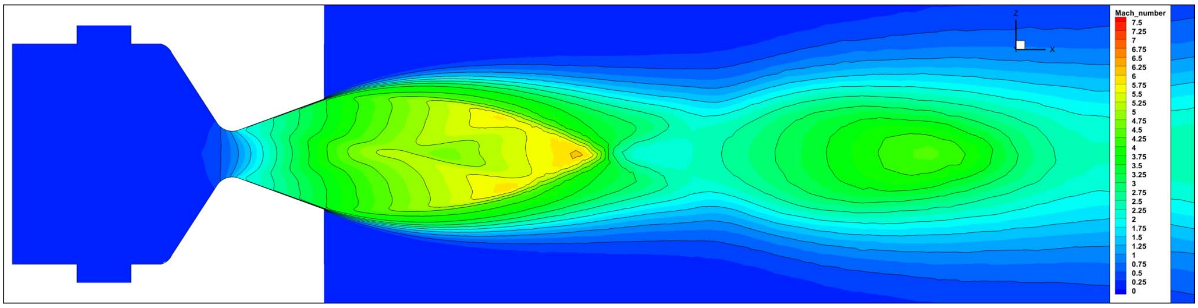

(a) Mach Number

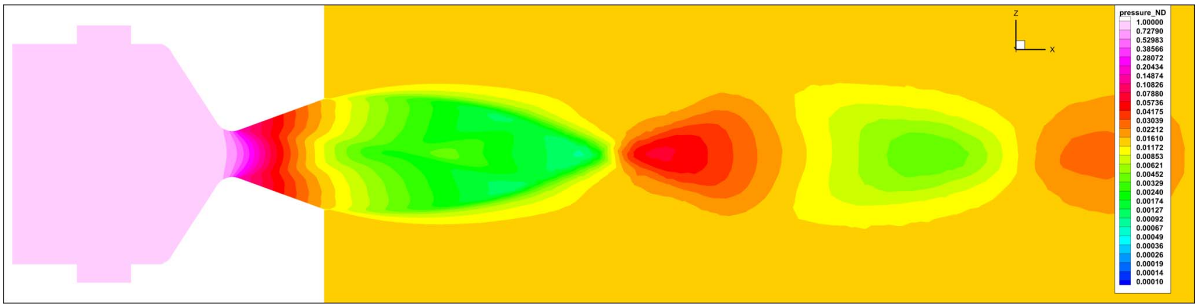

(b) Pressure

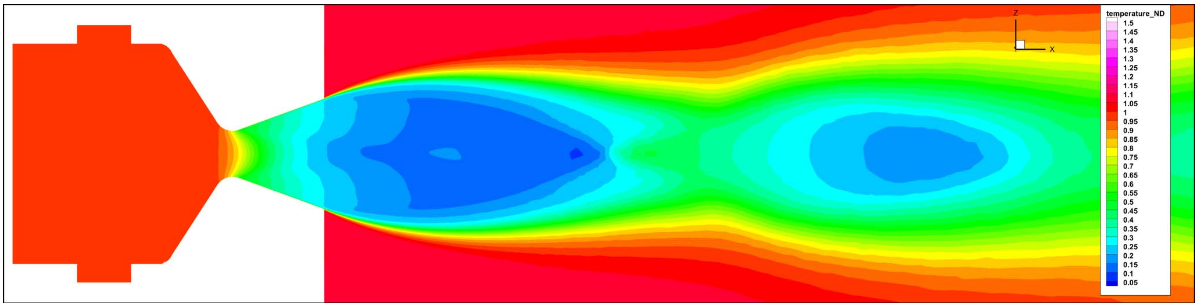

(c) Temperature

Figure 4.5: CFD Results ZX-Plane Cut Contour Plot of the Reference Nozzle (Values have been made dimensionless according to Table A.1, Mach Number ranging from $M = 0.0$ to $M = 7.5$ with $\Delta M = 0.25$ and for the lines a $\Delta M = 0.5$)

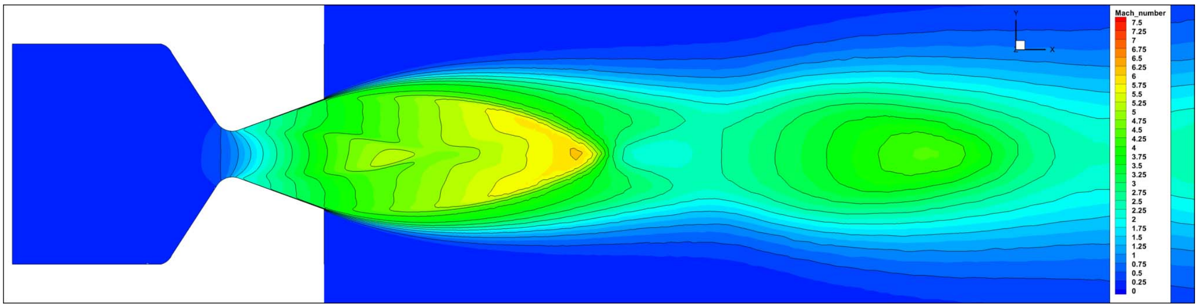

Figure 4.6: CFD Results XY-Plane Cut Contour Plot (Mach number only) of the Reference Nozzle (Mach Number ranging from $M = 0.0$ to $M = 7.5$ with $\Delta M = 0.25$ and for the lines a $\Delta M = 0.5$)

The Mach number contour in Figure 4.5a looks like a typical contour for a supersonic conical nozzle. The sonic line (the second Mach line) is slightly curved, this effect is not a viscous effect, but arises from the multi-dimensional nature of the flow. The diverging part of the nozzle also does not show any anomalies. The Mach number near the central axis is slightly higher with the pressure being lower. The expansion lines (right running characteristics) which are emitted from the initial expansion curve downstream of the throat running diagonally to he nozzle axis. Thus the flow near the axis is always a bit faster. This effect is amplified by the presence of the boundary layer at the walls. The boundary layer, even though it is very thin, is visible in Figure 4.5a, with the thickness increasing towards the nozzle exit. The flow inside the nozzle is entirely shock free, as it should be for a correctly designed nozzle. The flow downstream of the nozzle continues to expand further until it hits an oblique shock wave which is emitted from the nozzle exit inwards towards the axis with an angle of approximately 30°. The shock waves cross each other on the axis, this is nicely visible in the pressure contour (Figure 4.5b), where a strong area of compression can be seen downstream of the shock. Another smaller and short shock wave is emitted from the nozzle exit outwards away from the axis. A bit further downstream this shock weakens and eventually disappears forming the shear layer between the free-stream flow and the nozzle plume. Note, the resolution of the shocks is not as clear as one would expect. Due to the numerical dissipation, that is present in any higher order CFD solver, they tend to smear out a bit. This effect is amplified by the mesh already being a bit coarse in these regions (see Figure 4.4a), the shock is thus smeared out over multiple larger cells. Another small anomaly is that the flow field is not entirely symmetric. This can have multiple reasons. Firstly, the mesh used is unstructured and thus per definition not symmetric. Another reason, could be 3D flow effects caused by the fact that the whole setup is not axis-symmetric. Finally, the steady state solution presented here still contains small oscillations and appears to be not fully convergent. Therefore, the asymmetries in contour do look somewhat different when plotting a contour 1000 iterations later. The last aspect is a larger problem, it could indicate that the whole solution is not convergent and/ or not physical. As this issue appears in most of the static and stationary CFD simulations, it is addressed in detail in Chapter 6.1.1. However, in general it can be concluded that the solution presented here is consistent with the theory described in Chapter 2.1 and in the Literature Study [2].

4.2.3. Reference Nozzle Mesh Analysis

When simulating a flow with CFD or any other approach that discretises the calculation domain, it is common practice to verify that the level of discretisation is sufficiently refined to resemble the actual domain. In other words, the mesh needs to be checked whether it is convergent. This is usually done by in and/or decreasing the refinement of the mesh (number of cells) and to check if the modified mesh still yields in the same solution. If the solution still changes significantly, the mesh is said to be not convergent and the number of cells must be increased until the solution stays constant: There are two approaches to perform this mesh test:

1. The refinement of the mesh can be increased or decreased by changing the settings in the mesher. For example to decrease the rastering arc length of edge and face of the geometry by a fixed percentage and to also a just the sources accordingly. This way a completely new mesh with a fixed amount of extra nodes is generated. This also means that the whole calculation has to be started again from zero, therefore this approach is rather time consuming and calculation intensive.

2. An alternative is to adapt the already existing mesh, this way the calculation does not have to be restarted from scratch. TAU has an algorithm to perform a full mesh adaption. The algorithm uses an already existing mesh and solution file, which is ideally from a fully converged steady state solution. Based on the difference of a number of user defined indicator variables between neighbouring cells regions of steep gradients, such as compression or expansion waves, shocks and shear layers are identified. In these regions the mesh is locally refined by adding new cells. The total number of new cells is defined by the user. An overview of the principles of adaptation can be found in Chapter 2.2.4. This method has the advantage that it is not required to completely recreate the mesh. Moreover, the calculation can be restarted on the original solution, which saves a lot of calculation time. However, one could argue that this method might lead to a false negative test, if the solution file used for the adaption is not convergent or does not represent a physical solution.

For this project the second method was chosen. Firstly, the risk of false negative error is minimal if the solution file is checked by the user prior to the adoption. Secondly, as it is much less calculation and work intensive. The process can be automated and does not require that much user input. Moreover, cells are only added in relevant regions of the flow and the calculation can be restarted from an existing solution, thus reducing the calculation time significantly.

In the given case the difference in the three state variables density ρ, pressure p and temperature T were used as the indicator variables. Two new meshes were generated, one with a 30 % increase in the number of points and one with a 60 % increase.

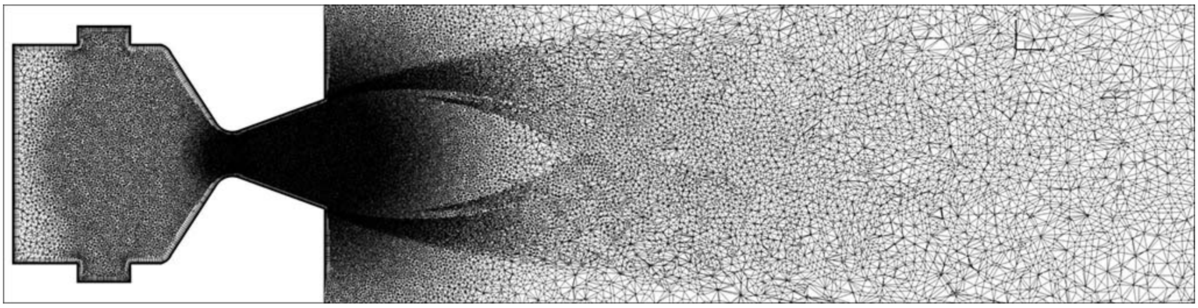

(a) 30 % increase in Points

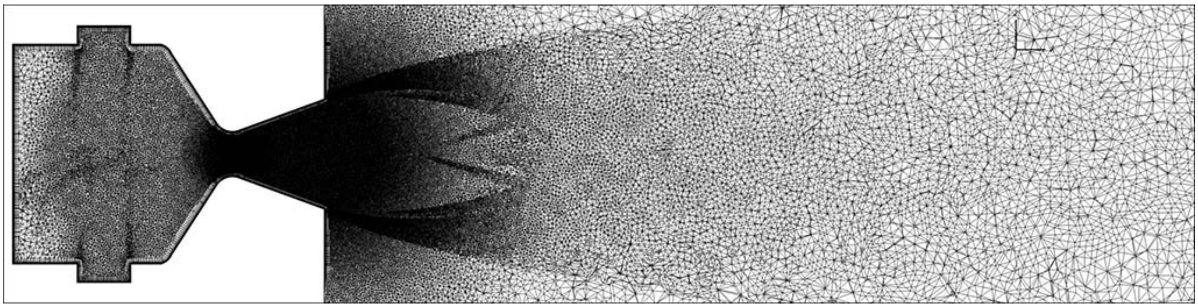

(b) 60 % increase in Points

Figure 4.7: Adapted Mesh Layout ZX-Plane Cut of the Relevant Domain of the Reference Nozzle

The procedure outlined above resulted into two new meshes, a cut-view of both can be found in Figure 4.7. Both meshes shown a significantly increased refinement around the shear layer and near the oblique shocks and a in general increased refinement in the exhaust plume region. As to be expected the mesh with the 60 % (see Figure 4.7b) extra points has an overall much higher refinement level. It however also shows additional refinement in the post combustion chamber, especially around what appears to be the shear layer of the inlet inflow.

The results of the mesh analysis can be found in Table 4.3. These results show that the chosen mesh is indeed convergent. The variation for each parameter between the different meshes is below 1 %, which is well within the accuracy of the CFD methods applied. Therefore, the original mesh is deemed sufficient

Table 4.3: Comparison of the Average Nondimensionalised Results of the Original and the Adapted Meshes of the Reference Nozzle (Values have been made dimensionless according to Table A.1)

Relative (Averaged) Parameter:	**Original Mesh**:	**Plus 30** %:	**Plus 60** %:
Thrust [%]	90.48	90.34	90.60
Massflow [%]	94.04	93.32	93.45
Inlet Pressure [%]	96.70	96.85	96.84

An analysis whether a mesh with less points/ nodes would have also been acceptable was not conducted. Firstly, it would have been very time consuming. Secondly, as discussed in the previous section, the mesh downstream of the nozzle is already rather coarse to resolve the shock waves in this area so reducing the resolution in this area is not advised. A Mach contour plot for the refined meshes is depicted in Figure 4.8. In both plots the resolution of the shock waves is better than in the original mesh, see Figure 4.5a. However, this should not have any influence on the parameters presented in Table 4.3, as these values are only dependent on the flow up to the nozzle exit and for supersonic flow information does not travel upstream. Note, the last statement does not hold for the subsonic part of the boundary layer, but the influence of that should be negligible. Finally, the original mesh has a runtime of approximately 116 s per 50 iterations, the mesh with 30 $\%$ more points of 153 s and the mesh with 60 $\%$ more points of 189 s. As a single simulation can have a couple of 100,000 iterations this is not negligible. Thus the original mesh is a good compromise between shock resolution and runtime and is therefore deemed sufficient.

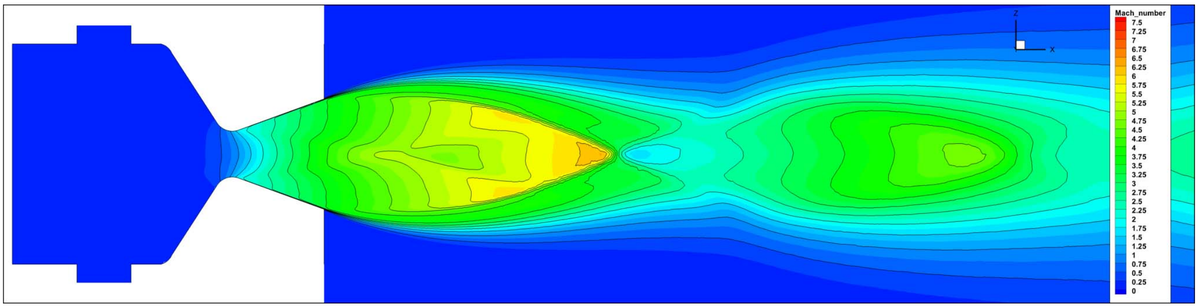

(a) 30 $\%$ increase in Points

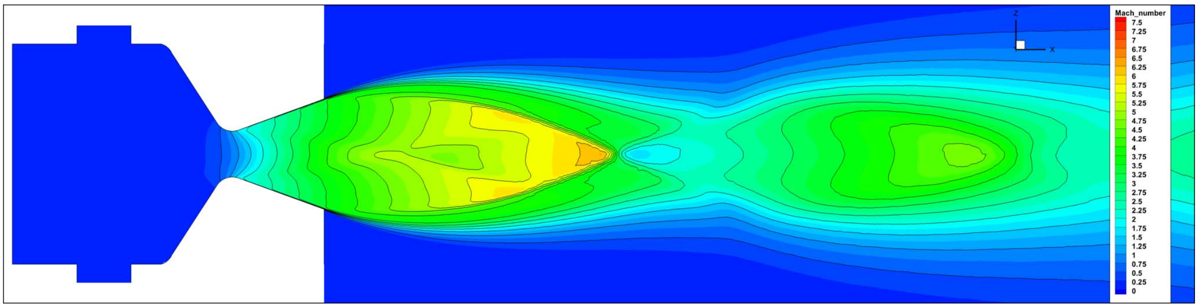

(b) 60 $\%$ increase in Points

Figure 4.8: CFD Results XY-Plane Cut Contour Plot (Mach number only) with the adapted Reference Nozzle Mesh (Mach Number ranging from $M = 0.0$ to $M = 7.5$ with $\Delta M = 0.25$ and for the lines a $\Delta M = 0.5$)

4.3. Static Nozzle-Pintle CFD Simulation

This section presents the results of the static Nozzle-Pintle CFD Simulation. The term static here refers to the movement of the pintle, which is not moving, hence static. The movement of the pintle was discretised using a min. and max. position and a certain step size, as in the 1D simulation described in Chapter 3. For each of these settings, in total thirteen different ones, a stationary CFD simulation was setup and run.

4.3.1. Static Nozzle-Pintle Setup

The setup does not vary substantially from the general setup outlined in Section 4.1 and the setup of the reference nozzle, see Section 4.2.1. In total thirteen different geometries were created with the pintle at different settings ranging from the maximum (fully open) to the minimum (fully closed) position. Note, as for the 1D simulation, the minimum (fully closed) position does not mean that the pintle completely blocks the flow through the nozzle. Therefore, the nozzle will always produce a certain minimum thrust, hence the term minimum setting.

For each of the thirteen geometries a separate mesh had to be created. Here only the minimum, maximum and mid position mesh are shown and discussed. A ZX-plane cute of these can be found in Figures 4.9, 4.11 and 4.13. All meshes have been generated using the method described in in Section 4.1.2.

Table 4.4: Number of Nodes for the different Meshes

Pintle Setting	**Number of Nodes**
100 %	7,682,045
50 %	7,715,257
0.0 %	9,897,923

For the cases where the pintle is close to or at the minimum position, such as the 0.0 % position in Figure 4.9, an additional point source was inserted into the nozzle throat, to increase the resolution in the small gap between pintle and nozzle wall. In Table 4.4 it can be seen that this has a significant influence on the total number of nodes. This also has an influence on the calculation time.

To assure that the meshes generated are in fact convergent a mesh analysis, similar to the analysis performed for the reference nozzle in Section 4.2.3 would have to be executed. As this mesh analysis is both work and computationally expensive, it was not performed for all thirteen different meshes. Instead only the three representative meshes of maximum, mid position and minimum positions, shown in Figures 4.9, 4.11 and 4.13, were analysed. This was deemed sufficient to assure that also the meshes in between are convergent. For each case two additional meshes with 30 and 60 % extra nodes were created using the TAU adaptation algorithm, with the same settings as for the reference nozzle case, see Section 4.2.3. The additional meshes are depicted in Figures 4.10, 4.12 and 4.14. The locations area in which the number of cells are increased are basically the same as for the reference nozzle, see Section 4.2.3: The shear layer and the shock and expansion waves downstream of the throat and the shear layer at the inflow zone in the post combustion chamber. The latter effect is especially visible in the configuration where the pintle is at the minimum position, see Figure 4.14. In this case the adaptation pattern downstream of the nozzle flow also looks substantially different compared to the other two positions. This is due to the difference in the actual flow pattern, skip ahead to Figure 4.17e, compared to a flow pattern of a regular nozzle.

The results of the mesh analysis are summarised in Table 4.5. As for the analysis of the reference nozzle, the thrust, massflow and inlet pressure where used as the check variables. All values shown in Table 4.5 have been made non-dimensional, as indicated and are given [%]. For all three positions the difference between the three variables for the different meshes is less than 1 %. In many cases the difference is much less. Therefore, it can be concluded that all three meshes can be assumed convergent. As discussed for the reference nozzle, see respective Section 4.2.3, an analysis to show that a mesh with less cells would possibly also suffice was not conducted.

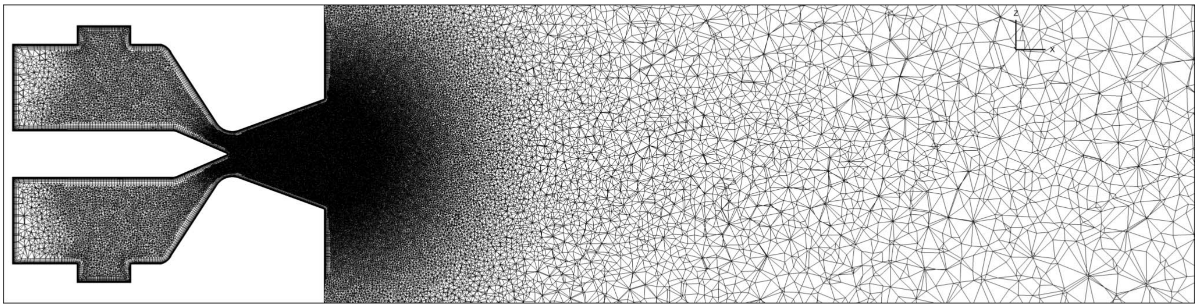

(a) Relevant Domain

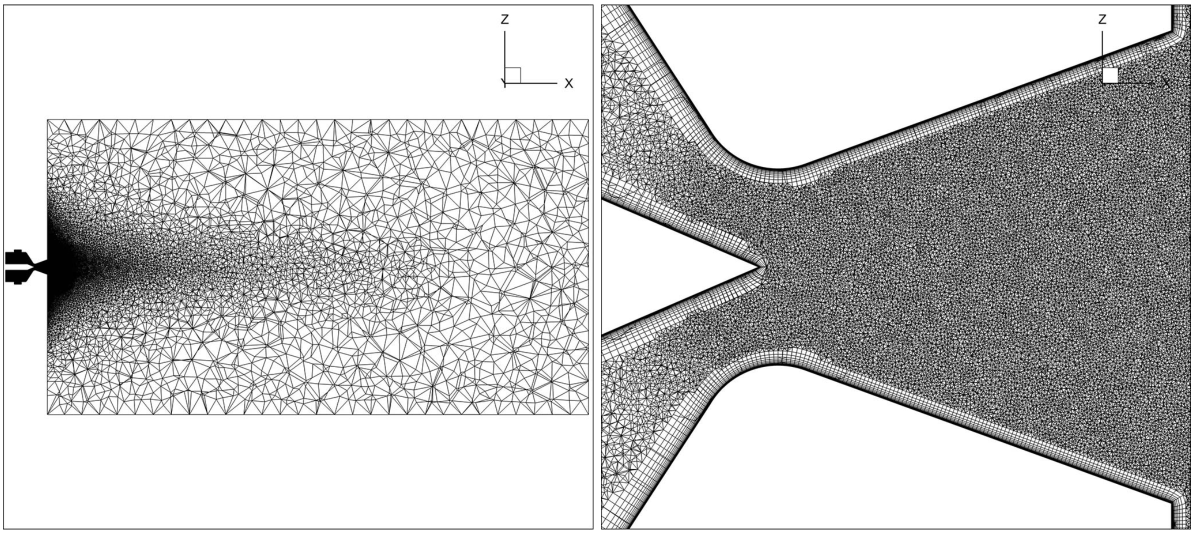

(b) Full Domain (c) Critical Domain

Figure 4.9: Mesh Layout ZX-Plane Cut at 100 % Pintle Position

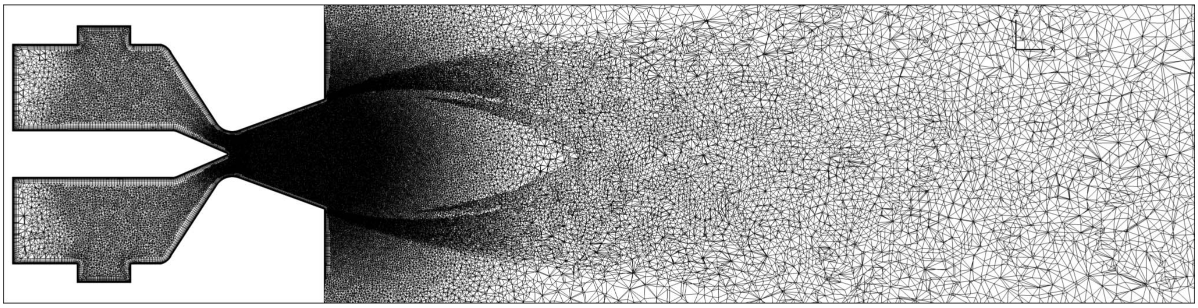

(a) 30 % increase in Points

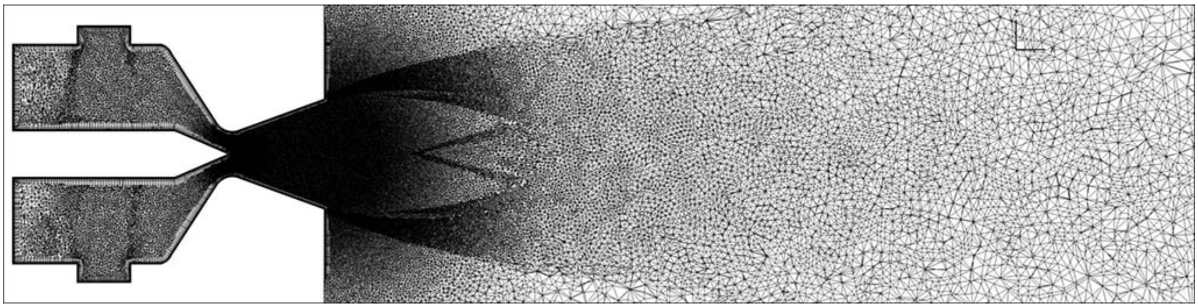

(b) 60 % increase in Points

Figure 4.10: Adapted Mesh Layout ZX-Plane Cut of the Relevant Domain at 100 % Pintle Position

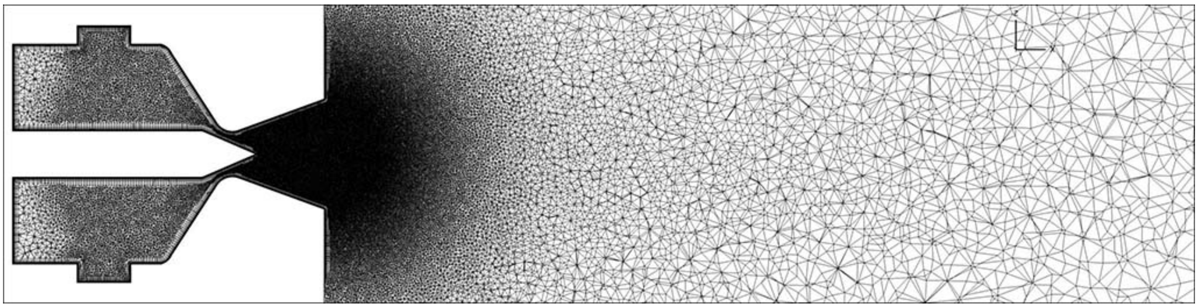

(a) Relevant Domain

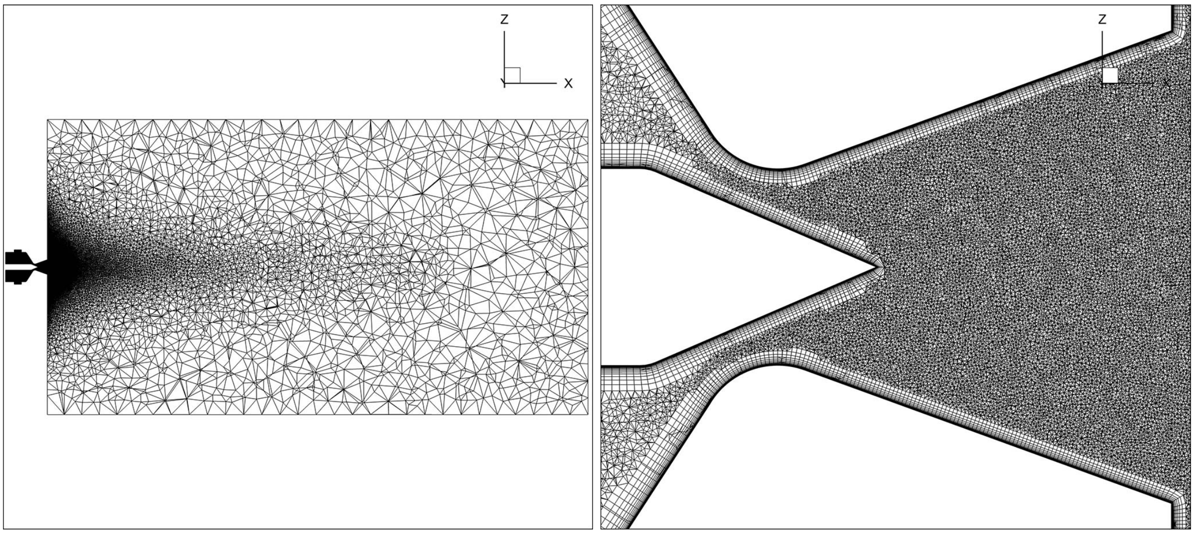

(b) Full Domain

(c) Critical Domain

Figure 4.11: Mesh Layout ZX-Plane Cut at 50 % Pintle Position

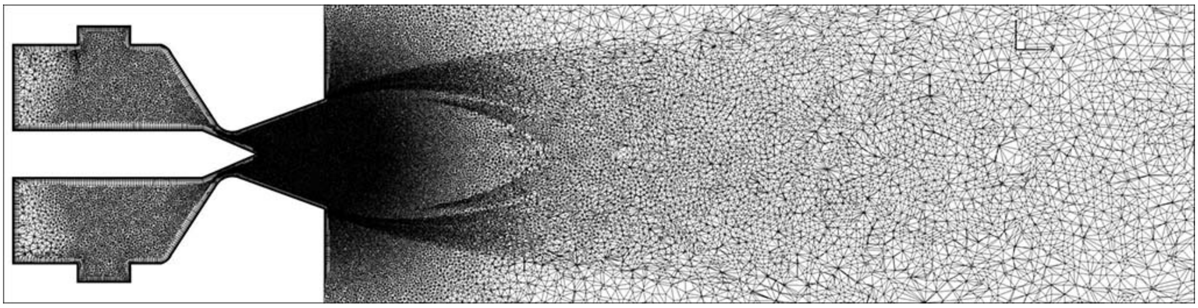

(a) 30 % increase in Points

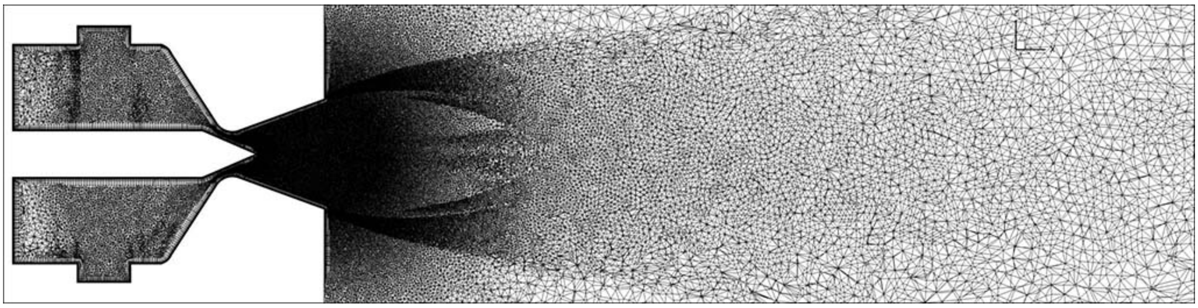

(b) 60 % increase in Points

Figure 4.12: Adapted Mesh Layout ZX-Plane Cut of the Relevant Domain at 50 % Pintle Position

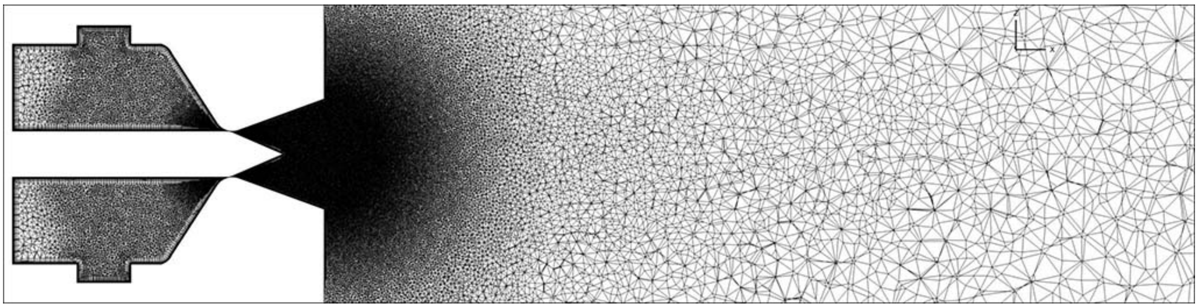

(a) Relevant Domain

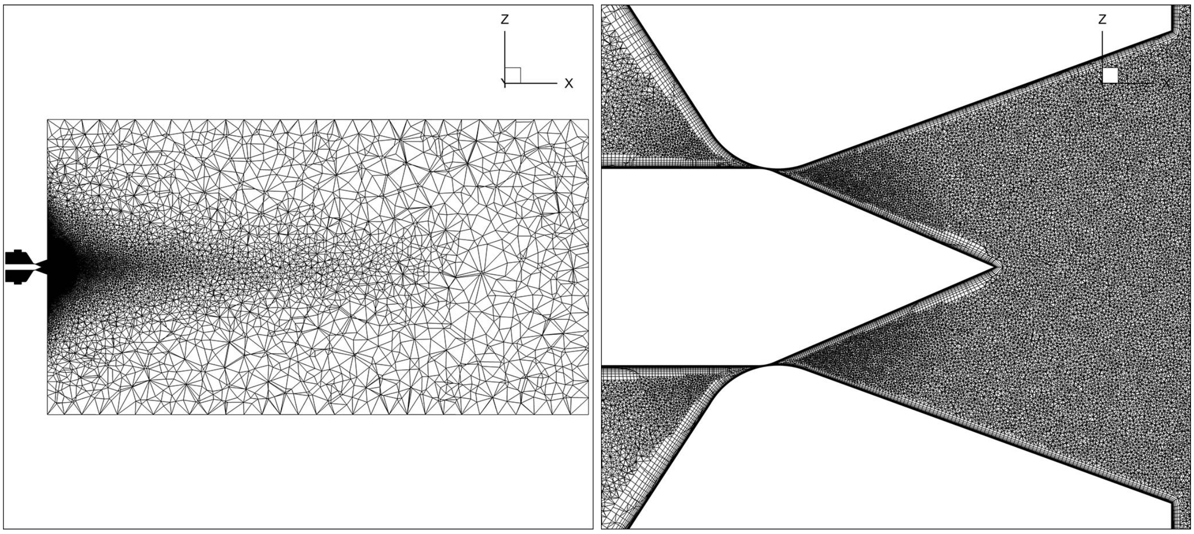

(b) Full Domain

(c) Critical Domain

Figure 4.13: Mesh Layout ZX-Plane Cut at 0 % Pintle Position

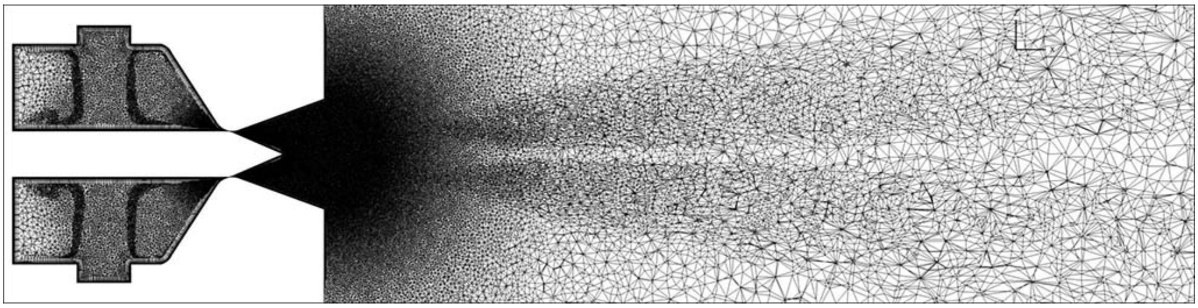

(a) 30 % increase in Points

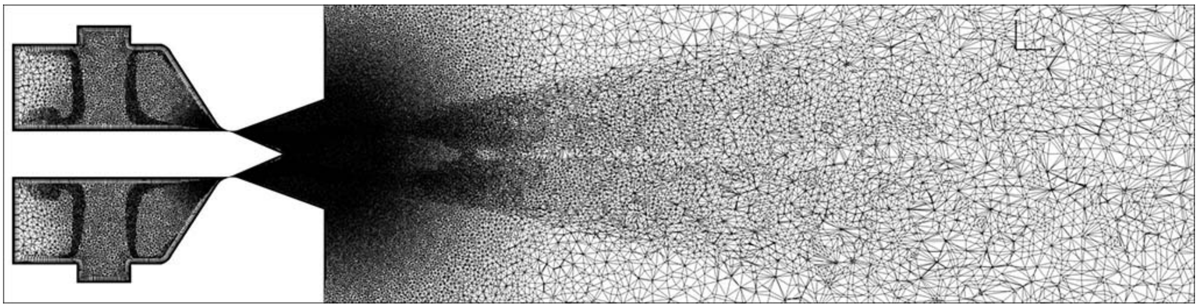

(b) 60 % increase in Points

Figure 4.14: Adapted Mesh Layout ZX-Plane Cut of the Relevant Domain at 0 % Pintle Position

Table 4.5: Comparison of the Average Nondimensionalised Results of the Original and the Adapted Meshes (Values have been made dimensionless according to Table A.1)

Relative (Averaged) Parameter:	**Original Mesh**:	**Plus 30** %:	**Plus 60** %:
	$\mathbf{x_{pi}} = \mathbf{100}\,\%$		
Thrust [%]	90.33	89.94	89.95
Massflow [%]	93.76	93.70	93.79
Inlet Pressure [%]	96.72	96.83	96.81
	$\mathbf{x_{pi}} = \mathbf{50}\,\%$		
Thrust [%]	69.91	70.13	70.05
Massflow [%]	74.53	74.75	74.63
Inlet Pressure [%]	97.95	98.01	98.02
	$\mathbf{x_{pi}} = \mathbf{0}\,\%$		
Thrust [%]	4.78	4.80	4.80
Massflow [%]	6.13	6.13	6.18
Inlet Pressure [%]	99.99	99.99	99.99

4.3.2. Static Nozzle-Pintle Results

This sections outlines the results of the static nozzle-pintle CFD simulation, at a fixed combustion/ inlet pressure as simulated with the 1D Simulation tool presented in Chapter 3.2. As outlined in Section 4.1 and as for the reference nozzle case in Section 4.2, the results presented here have been y^+ adapted.

Table 4.6: Results of the Static Nozzle-Pintle CFD Simulation (Values have been made dimensionless according to Table A.1)

x_{pi} [%]	T [%]	F_{pintle} [%]	$\dot{m}$ [%]	p_{in} [%]	p_{PCC} [%]	p_e [%]	v_e [%]
100.00	90.33	60.98	93.76	96.72	95.95	1.36	89.35
91.67	89.92	60.05	93.92	96.71	96.20	1.35	89.77
83.33	88.65	58.17	93.02	96.78	95.92	1.32	90.20
75.00	86.15	56.18	90.52	96.95	96.34	1.27	90.63
66.67	82.85	53.36	87.24	97.17	96.73	1.20	90.66
58.33	77.30	49.69	83.23	97.43	97.24	1.08	92.58
50.00	69.91	45.08	74.53	97.95	97.38	0.95	91.56
41.67	61.81	39.42	66.50	98.38	98.04	0.82	91.43
33.33	52.10	32.45	57.02	98.81	98.58	0.77	87.11
25.00	40.62	24.43	45.53	99.25	99.09	0.75	81.15
16.67	28.89	15.47	32.02	99.63	99.53	0.99	58.81
8.33	15.26	7.13	16.32	99.90	99.88	1.37	27.47
0.00	4.78	2.12	6.13	99.99	99.97	1.33	16.94

The most important result parameters for each pintle position have been summarised in Table 4.6. The thrust T, axial pintle force F_{pintle}, massflow $\dot{m}$ and static inlet pressure p_{in} have been averaged over the last couple of thousand iterations, to average out oscillations in the steady state solution. For the remaining parameters this was not possible, as TAU does not write them in the log file, but only in the overall final solution file. Therefore, those results are from the very final iteration only. Massflow, pressure and velocity values are further given as averages over the respective surface domain. The post combustion chamber (PCC) domain is defined as the cross-sectional surface of just before the nozzle contour starts to converge, so at $x = -0.78 \cdot L_{div}$ from the throat (see Figure 4.1). The nozzle exit surface domain is set to be the cross-sectional surface just upstream of the nozzle exit. The massflow presented and used here is always the massflow at the inlet domain. Note, as explained in Section 4.1, there is a small offset with respect to the massflow leaving the farfield. This offset is caused by the farfield domain moving at $M = 0.01$.

Figure 4.15 shows the thrust and axial pintle force for all simulated pintle positions. The plot has been made dimensionless by the max. thrust obtained from the 1D Simulation, in Chapter 3.2. The results of the 1D Simulation have also been included in these plots to allow for easier comparison. A detailed analysis regarding the differences of the two simulations will be presented in Chapter 6.2. For the thrust shown in Figure 4.15a the two curves follow almost the same pattern. The gradient for the CFD results is slightly lower, so are the thrust results for and close to the fully open 100 % position. However, for the 0 % the CFD simulation predicts a thrust that is slightly higher than that of the 1D Simulation.The green circle in the plot shows the thrust of the reference nozzle, which was presented in the previous Section 4.2. The thrust of the reference nozzle essentially matches the thrust at the 100 % position, which is expected. The patterns for the pintle force are also very close to each other. With the CFD simulation predicting a slightly lower force. Apart from the initial two data points both curves run almost in parallel and the difference between CFD and 1D result appear to be constant.

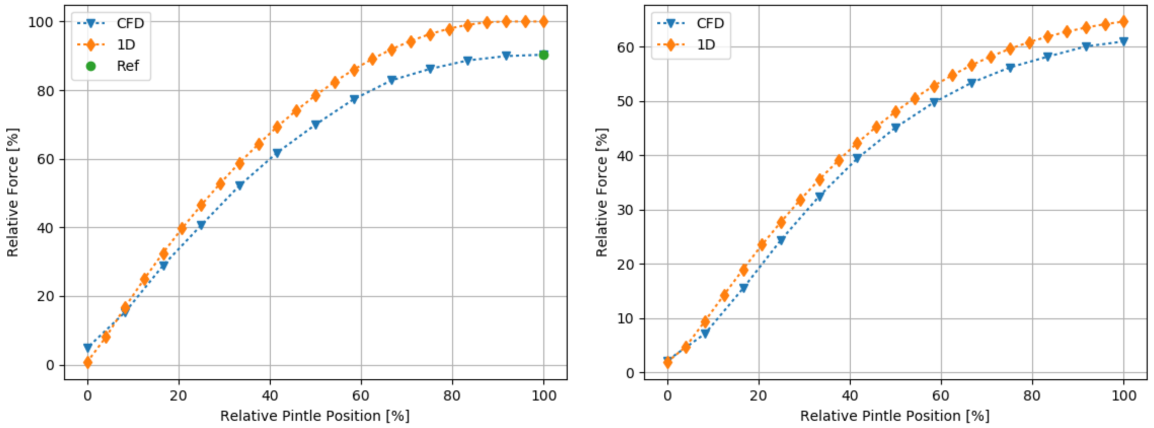

(a) Thrust

(b) Pintle X-Force

Figure 4.15: CFD Results Thrust and Pintle Force, CFD Simulation compared to 1D Simulation and CFD Reference Nozzle (Values have been made dimensionless according to Table A.1)

Figure 4.16 shows the secondary results of the CFD simulation. Also here the results are dimensionless and compared to the 1D Simulation results. The blue curve in Figure 4.16a shows average nozzle exit pressure for each pintle position. For the pintle positions above 40 % the curve corresponds almost exactly with the results obtained from the 1D simulation. Below that point both curves diverge and the blue curve with the CFD results starts to increase again. This increase results is caused by the flow separation which starts to occur for all simulated pintle positions below 33.3%. This is confirmed by the contour plots presented later in this section and in Appendix B, specifically in Figure B.9 and following. The flow separation caused the flow to detach from the nozzle wall and the ambient flow which is at a higher pressure to flow back into the nozzle in these regions. Therefore, the overall average pressure over the exit plane starts to increase again. Note, the ambient pressure corresponds to approximately 1.35% of the reference pressure used to scale the above plot. When presenting the results of the 1D Simulation in Chapter 3.2, the possibility of flow separation, due to the high expansion ratio was discussed. It was found that according to the Summerfield criterion flow separation should occur for pintle positions below 31.5 %. Therefore, the criterion comes very close to what is predicted by the CFD simulation. The exit pressure of the reference nozzle is again indicated by the green circle and matches the 100 % result.

Figure 4.16b displays the nozzle exit velocity of the two simulations. Also here the flow separation phenomena is visible for the lower pintle positions, as the average exit velocity is much lower with respect to what is predicted by the 1D Simulation. The only exception is the fully closed 0 % position where the CFD prediction turns out to be somewhat higher. For pintle positions above the separation point the exit velocity is initially a bit higher than the 1D prediction. The difference however decreases and becomes invisibly small close to the fully open position. Results of the 100 % position again match the reference nozzle case (green circle).

Figure 4.16c compares the massflow of both simulations. The plot is very comparable to the thrust plot in Figure 4.15a. However, the difference is somewhat smaller. This is to be expected as the thrust is directly depended on the massflow and the exit velocity ($T = \dot{m} \cdot v_e$). The massflow of the pintle 100 % position match the reference nozzle case (green circle). Note, there is a small kink at the 66.6 % position data point in the CFD results curve. The kink is also visible in the exit velocity plot in Figure 4.16b, but is not visible in the thrust plot in Figure 4.15a. So far there is no explanation for this phenomena.

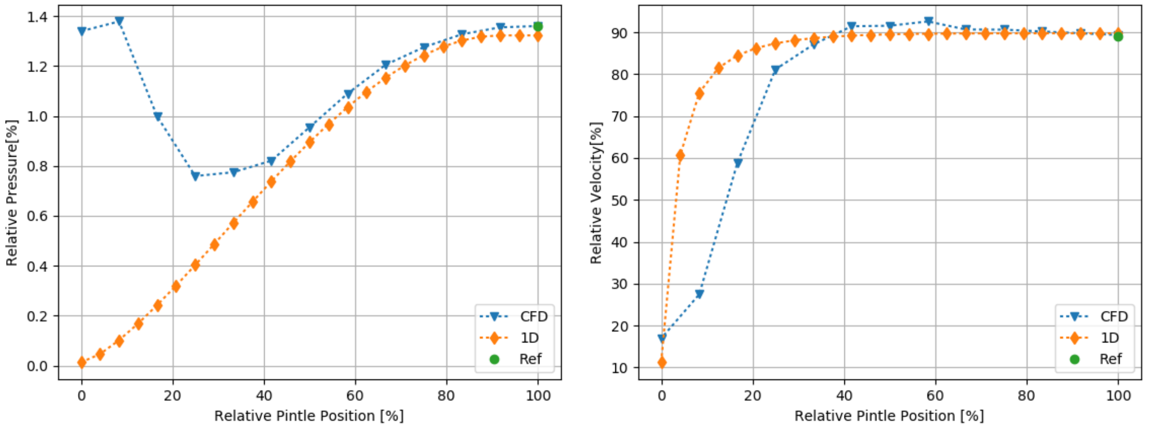

(a) Exit Pressure (b) Exit Velocity

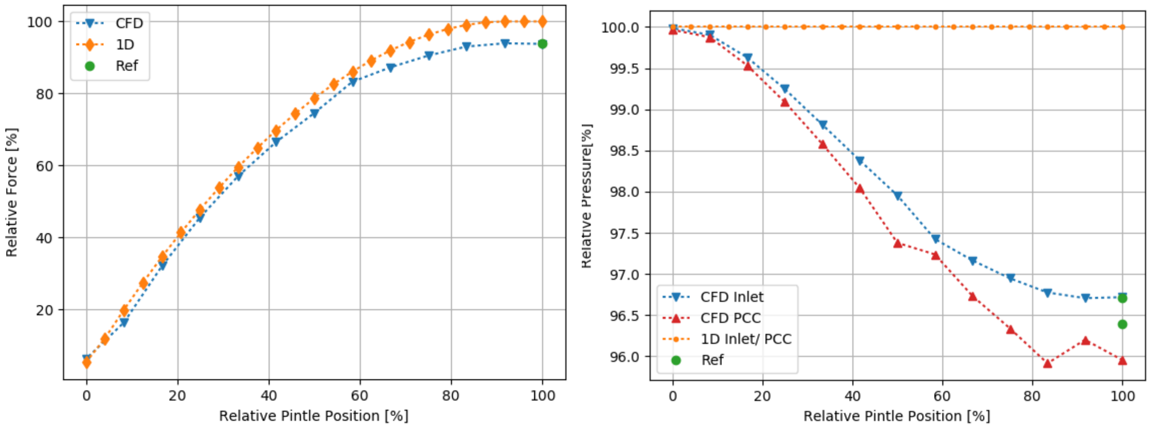

(c) Massflow (d) Inlet Pressure

Figure 4.16: CFD Results Pressure, Velocity and Massflow, CFD Simulation compared to 1D Simulation and CFD Reference Nozzle (Values have been made dimensionless according to Table A.1)

The final plot, see Figure 4.16d, compares the static inlet pressures. The static inlet pressure for the 1D Simulation is constant and equivalent to the combustion pressure. This is one of the governing assumptions of the 1D Simulation, for details see Chapter 3.1.1. In the CFD simulation only the total inlet pressure is defined as constant, as the total pressure and total density at the inlet define the inlet boundary condition. As the flow field at the inlet and in the post combustion chamber is in motion the static pressure will be lower than the total pressure. This is resembled in the blue curve in Figure 4.16d. The more the pintle is opened the more the static pressure drops, as the flow will move with a higher speed. The inlet pressure for the reference nozzle and pintle 100 % position again match. For additional comparison the average static pressure at the end of the post combustion chamber is plotted in the red curve. Note, the post combustion chamber pressure is defined as the average pressure over cross-sectional surface just before the nozzle contour starts to converge, so at $x = -0.78 \cdot L_{div}$ from the throat (see Figure 4.1). The p_{PCC} is again a bit lower than the static inlet pressure, which is expected and likely caused by a pressure loss and expansion of the flow. The discontinuities in the respective curve are however not expected and so far cannot be explained. The respective result for the reference nozzle does not exactly match the 100 % position. This is likely caused by the presence of the pintle geometry in the measurement cross-section.

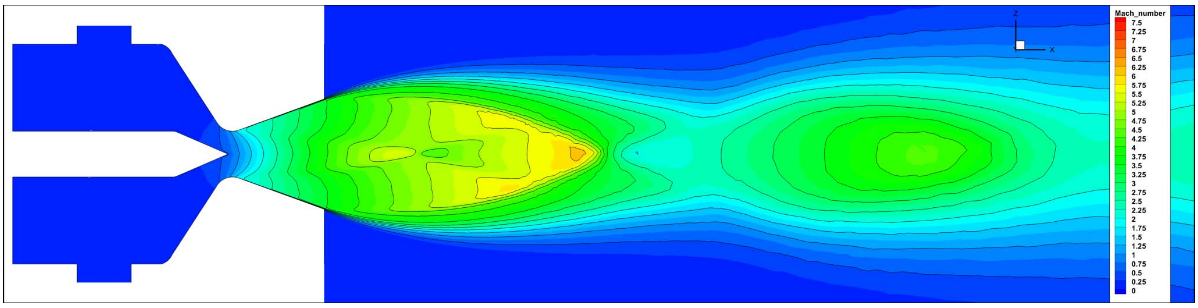

(a) 100 %

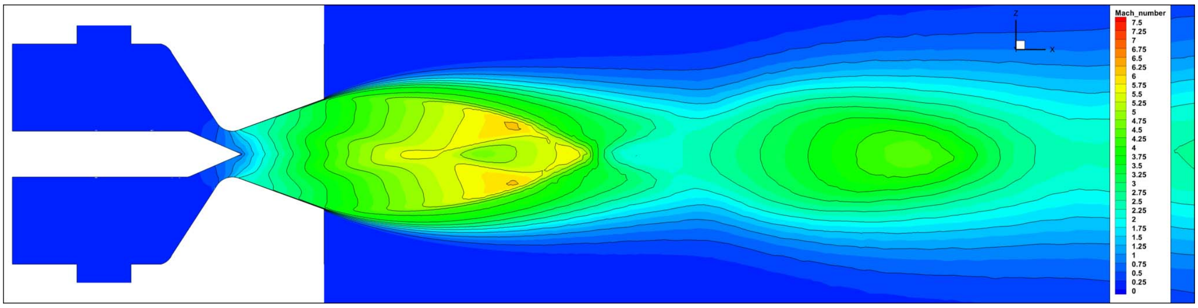

(b) 75 %

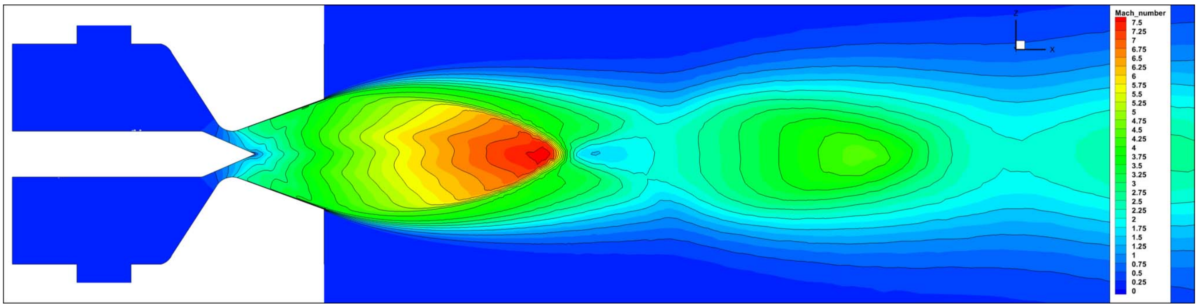

(c) 50 %

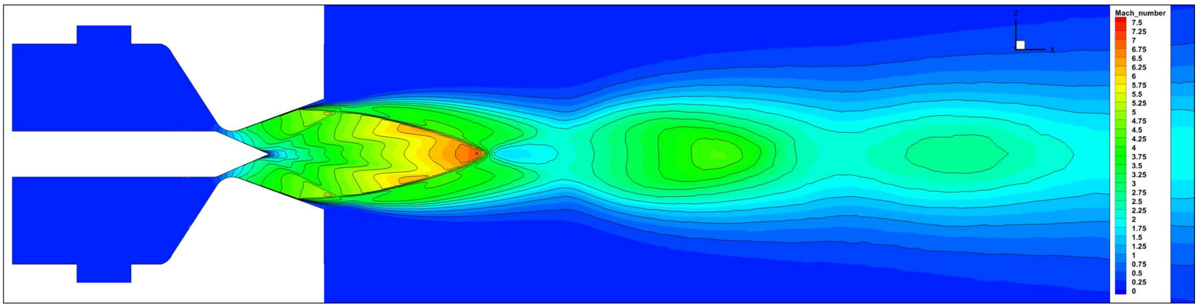

(d) 25 %

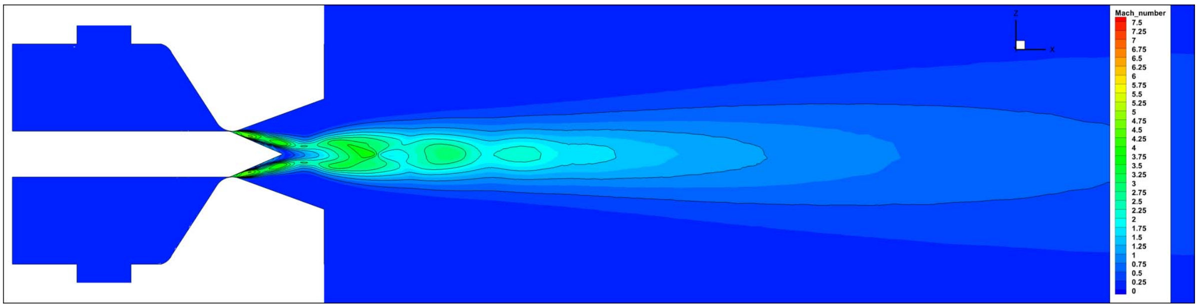

(e) 0 %

Figure 4.17: CFD Mach Number Results ZX-Plane Cut Contour Plot, (Mach Number ranging from $M = 0.0$ to $M = 7.5$ with $\Delta M = 0.25$ and for the lines a $\Delta M = 0.5$)

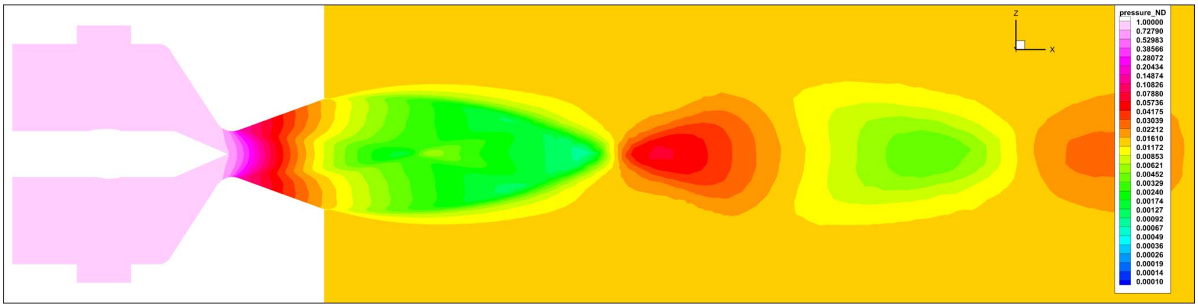

(a) 100 %

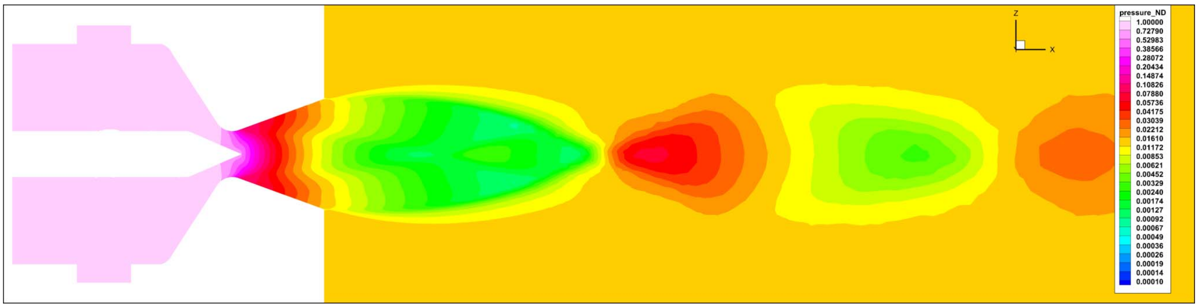

(b) 75 %

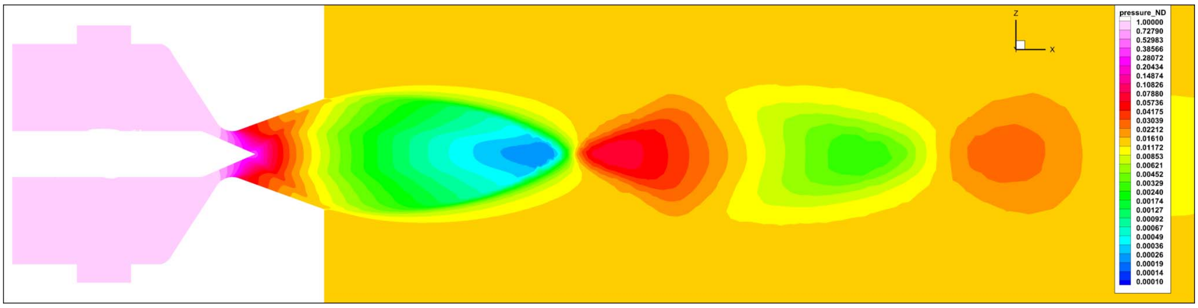

(c) 50 %

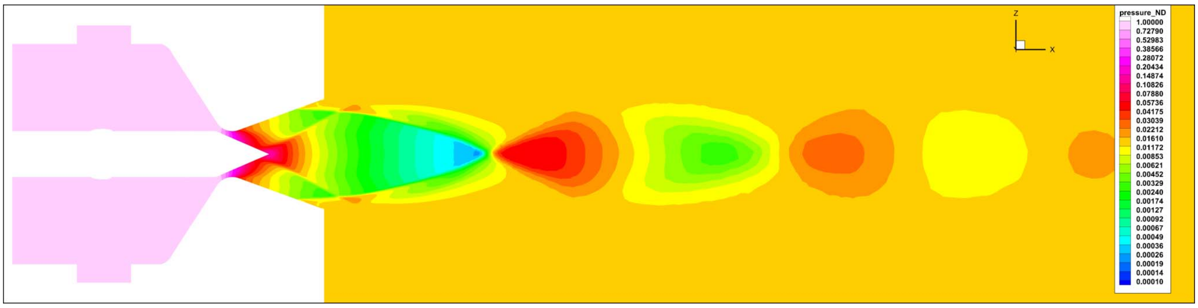

(d) 25 %

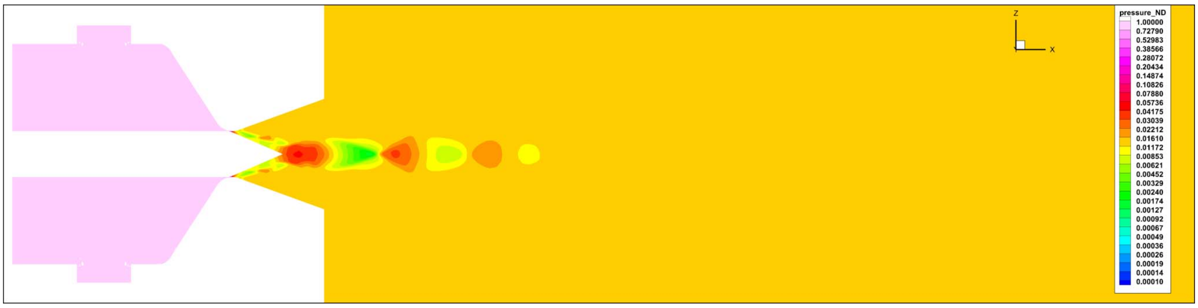

(e) 0 %

Figure 4.18: CFD Pressure Results ZX-Plane Cut Contour Plot, (Values have been made dimensionless according to Table A.1)

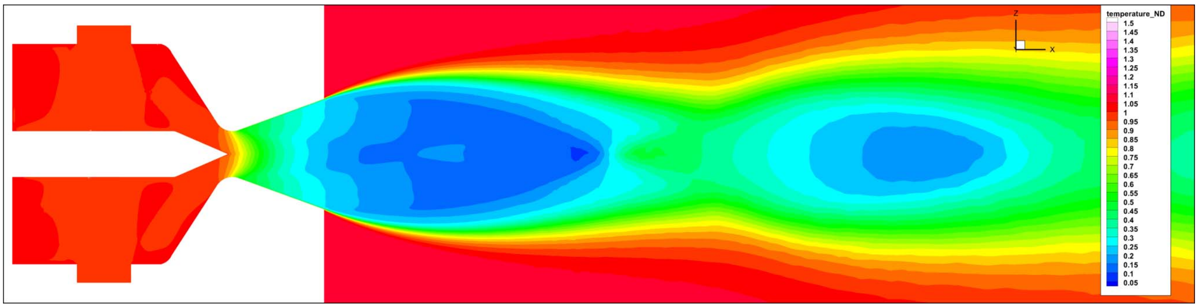

(a) 100 %

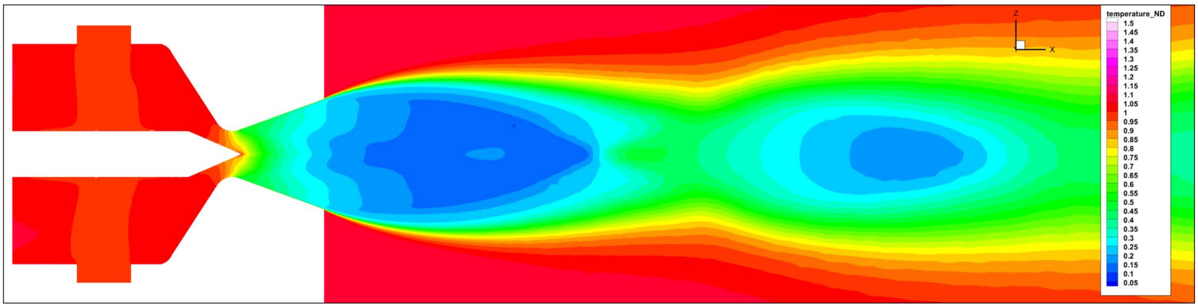

(b) 75 %

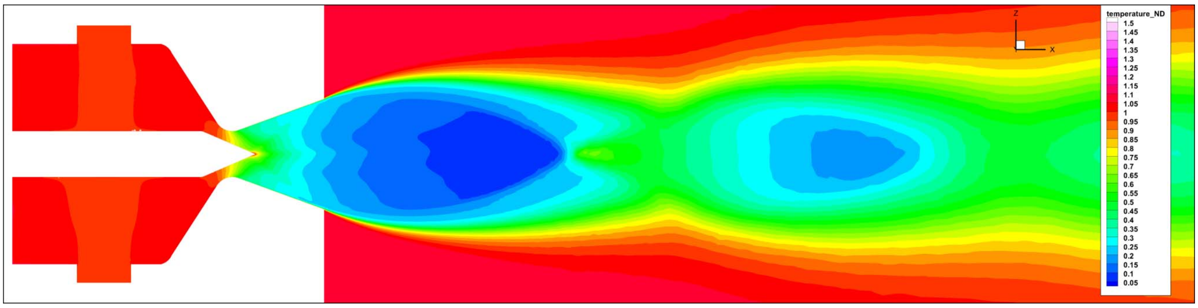

(c) 50 %

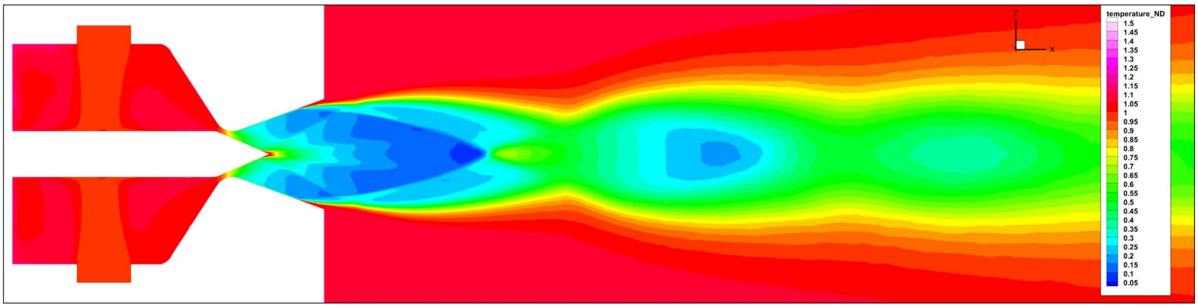

(d) 25 %

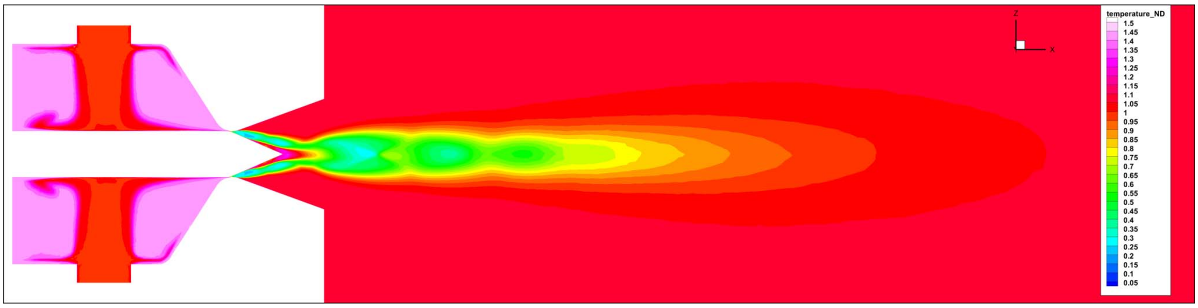

(e) 0 %

Figure 4.19: CFD Temperature Results ZX-Plane Cut Contour Plot, (Values have been made dimensionless according to Table A.1)

Contour plots of the ZX-plane cut of the Mach number, pressure and temperature for the pintle positions from min. to max. in 25 % steps are shown below in Figures 4.17,4.18 and 4.19. The contour plots for all positions are displayed in Appendix B in Figures B.1 to B.13. The pressure and temperature plots have been made dimensionless according to Appendix A. To allow an easy comparison, the colour scale for plots showing the same variable are the same for all pintle position and for the reference nozzle presented in Section 4.2.2, Figure 4.5.

For the pintle positions close to the fully open position the flow field is very similar to that of the reference nozzle. This becomes evident when comparing the contour plots in Figure 4.17a and b with the reference nozzle in Figure 4.5a, but also when comparing the respective plots for pressure and temperature. The flow field is a typical flow field for a conical nozzle. The expansion/ Mach line inside the diverging section of the nozzle have the typical shape. For cases where the pintle is already a bit inserted, a small deformation at the centre line of the neighbouring Mach lines is shown. The flow inside the nozzle remains entirely shock free. The flow field (shock-/ expansion pattern and shear layer) downstream of the nozzle exit is very similar for the respective pintle positions and also to the reference nozzle.

A notable difference in the flow field only becomes visible for pintle positions below 75 %. This first becomes visible at the 66.6 % position depicted in Figure B.5. It is clearly visible in the Mach, pressure and temperature plot for the 50 % position, shown in Figures 4.17c, 4.18c and 4.19c respectively. The Mach line/ expansion pattern in the diverging part of the nozzle is significant different and the flow is expanded further. Inside of the nozzle the expansion is still shock free. Downstream of the nozzle exit the flow is expanded more drastically and to a higher velocity or lower temperatures and pressures. Therefore, the oblique shock, that is emitted from the nozzle exit corners towards the symmetry line occurs earlier, thus further upstream. It is also much stronger.

From positions 33.3 % and lower the flow on the nozzle walls starts to separate. This is first visible in Figure B.9. As already mentioned before when discussing the nozzle exit pressure in Figure 4.16a, this is roughly what the Summerfield criterion indicated. The oblique shock that was previously emitted from the nozzle exit is now emitted from the separation point, see Figure 4.17d. The shock is also much clearer and stronger, as indicated by the high number of Mach lines very close to each other. The whole flow field pattern thus also shifts further upstream. Flow separation also starts to develop at the tip of the pintle, this is clearly visible in Figure 4.17d and Figure 4.19d. If the pintle is inserted even further the separation points both on the nozzle wall and on the pintle will move further upstream. Moreover a weak shock starts to develop at the separation point on the pintle surface, the shock is emitted outwards and intersects the other shock. Both effects can be best observed in Figure B.11a and B.12a.

Below the 25 % position and each time the pintle is inserted further into the throat, the flow pattern inside and downstream of the nozzle, looks less like the flow field of a conical nozzle. It actually starts to resemble more the flow field of an aerospike nozzle. Once the pintle is fully inserted the flow field resembles that of an aerospike nozzle with complete flow separation. The flow is no longer attached to the nozzle wall at all and also separates from the pintle surface almost immediately. This creates a circulation wake in between the shear layer and the pintle wall and just downstream of the pintle. In this wake the flow velocity is close to zero, however the pressure is rather high. It is higher than the pressure in the exhaust stream and higher than ambient. The effect is similar to the circulation zone at the base of a truncated aerospike nozzle and likely also responsible for a significant part of the small thrust, that is still produced in this configuration. This concludes the review of the above contour plots.

The axial force on the pintle, see Figure 4.15b, is one of the primary outcomes of this simulation. It is a function of the pressure distribution over the pintle. Therefore, the pressure distribution over the pintle is investigated in more detail. Figures 4.20, 4.21 and 4.22 display the pressure distributions over the pintle at the two extreme and the mid position. The distributions shown in the x/p-Plots (left side) are not the average distributions, but the distributions of the pintle top side in the ZX-plane. The CFD results in the respective plots are again compared to the results of the 1D simulation.

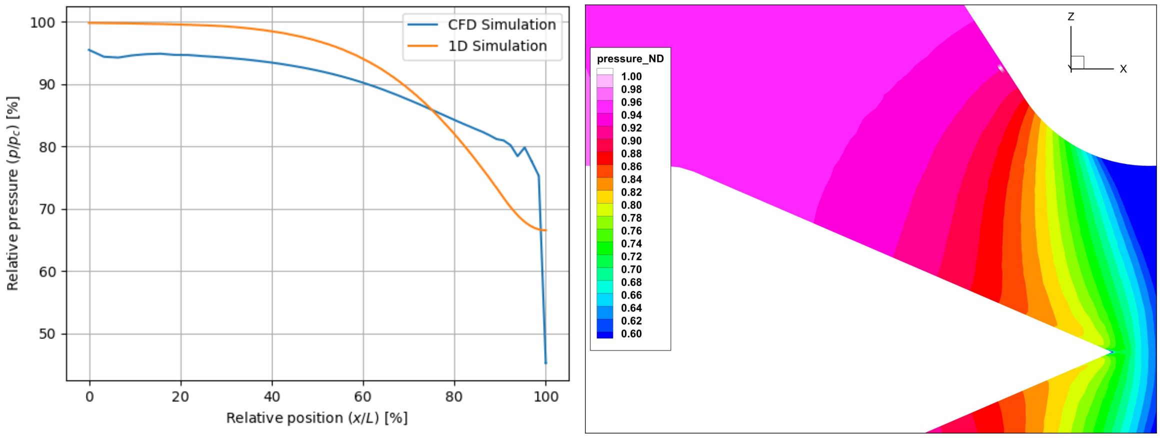

(a) x/p-Plot (b) Contour Plot

Figure 4.20: Pressure Distribution over the Pintle at the Fully Opened Position 100 %. For the CFD simulation the values of the top side in the ZX-plane are shown. (Values have been made dimensionless according to Table A.1)

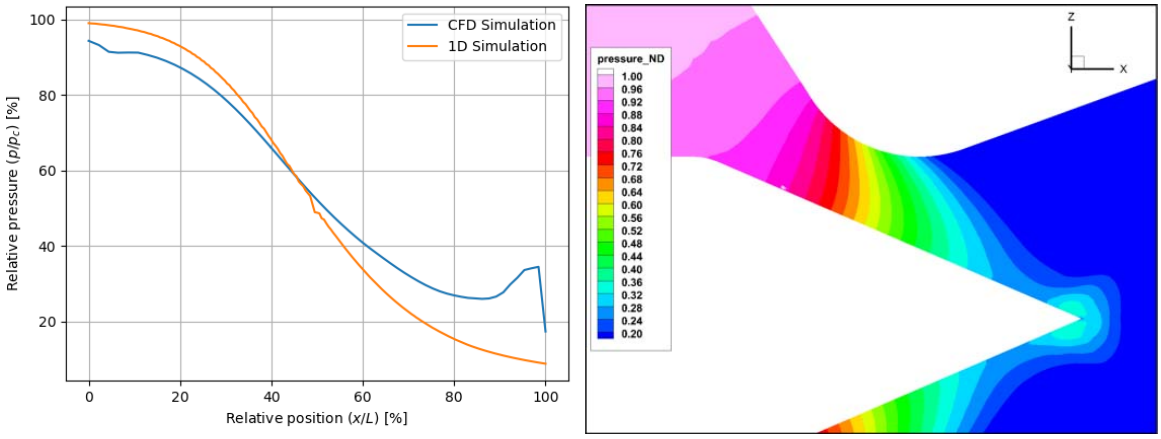

(a) x/p-Plot (b) Contour Plot

Figure 4.21: Pressure Distribution over the Pintle at the Fully Opened Position 50 %. For the CFD simulation the values of the top side in the ZX-plane are shown. (Values have been made dimensionless according to Table A.1)

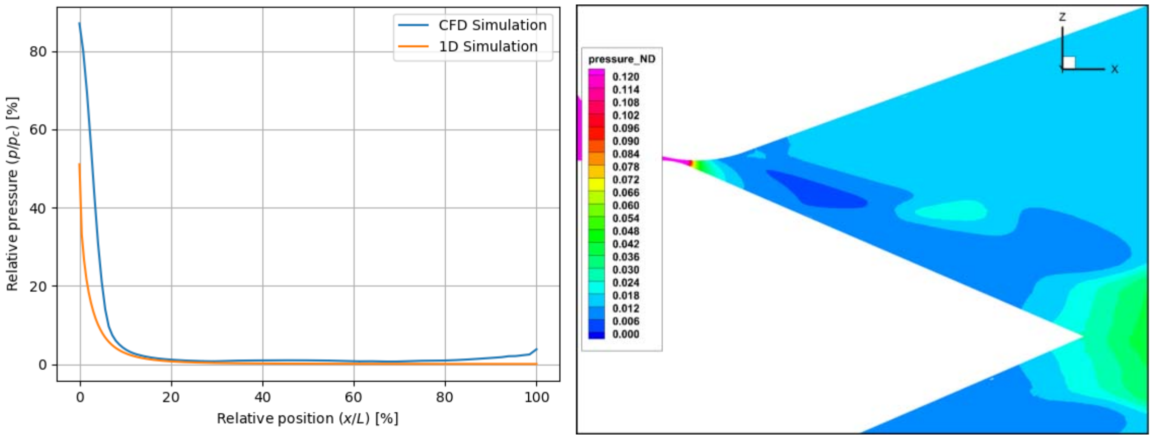

(a) x/p-Plot (b) Contour Plot

Figure 4.22: Pressure Distribution over the Pintle at the Fully Opened Position 100 %. For the CFD simulation the values of the top side in the ZX-plane are shown. (Values have been made dimensionless according to Table A.1)

Figure 4.20 displays the pressure distribution over the pintle at the 100 % position. For this positions the CFD results show a pressure that is about of 5 % below the combustion pressure at the pintle root. The results show a small initial drop in pressure followed by a small rise. This effect is believed to be caused by the small radius at the pintle corner, which causes a temporary sign change in the derivative of the area-ratio. The effect is also visible for the pintle mid position displayed in Figure 4.21. Afterwards the pressure gradually decreases to about 80 % of p_c right upstream of the tip. This is followed by a small kink in the pressure curve. The cause of this effect is not entirely understood. In theory it is possible that it is caused by a small local shock. However, this is unlikely as the flow velocity in this region and for this pintle position is still subsonic. The effect is also observed for the pintle mid position, see Figure 4.21a. Right after the kink the pressure suddenly drops by more than 30 %. This phenomenon is believed to be caused by local flow separation at the pintle tip. This results in a small low pressure circulation zone just downstream of the tip. The effect can also be observed in the contour plot in Figure 4.20b, where a very small blue area is situated right at the pintle tip. It is very well possible that the flow separation is caused by the sharp corner at the pintle tip, sharp corners generally are cause for flow separation. However, the effect can also be a numerical issue caused by the non optimal grid resolution at the pintle tip, see Figure 4.9c. The effect is also visible in the pintle mid position (see Figure 4.21), however the pressure drop is not that significant.

Figure 4.21 displays the pintle pressure distribution for its mid position. Also here the pressure at the pintle root is about 5 % below the combustion pressure or the pressure of the 1D simulation at the pintle root. This followed by the small bump, which was also observed for the previous pintle position. Thereafter, the pressure drops with an increasing gradient to roughly 60 % in the middle of the pintle. Thereafter, the gradient starts to decrease again. At the same point the result of the CFD simulation matches the 1D results. After this point their difference is reversed. Further downstream of the pintle at approximately 90 % of its length the pressure levels off at roughly 25 % of the combustion pressure. This is followed by a 10 % increase in pressure, likely caused by a small shock. At the pintle tip the pressure drops again sharply, this is the same flow separation observed for the previous pintle position.

The pressure distribution for the closed pintle position is outlined in Figure 4.22. At the pintle root the pressure is about 90 % of the combustion pressure. This is significantly above the 1D result, which predicts a value of about 50 % of the combustion pressure. Just downstream of the root the results of both simulations drop drastically to a value of below 1 % of the combustion pressure. The CFD simulation predicts a slightly higher pressure. However, both results give pressure which is below the local ambient. This is to be expected as the flow at this point is no longer attached to the pintle wall, see Figures 4.17e 4.18e and 4.19e. The pressure drop and subsequent flow separation is caused by a rapid expansion of the flow through the very small gap between pintle and nozzle wall. At about 70 % of the pintle position the pressure on the pintle wall starts to slightly increase followed by a steeper increase at the tip. This is caused by the recirculation effect that occurs just downstream of the pintles tip, which was also described above.

4.4. Dynamic/ Chimera Nozzle-Pintle CFD Simulation

The following section presents the dynamic and instationary CFD simulation where the pintle motion is included. The simulation uses the so called Chimera or Overset grid technique, which was outlined in Chapter 2.2.5. First the setup of the simulation is explained, this is followed by a presentation of the simulations results.

4.4.1. Chimera Setup

The setup of the chimera CFD simulations require some additional steps compared to the standard stationary simulations described in Sections 4.1 to 4.3. These are outlined in the following.

Geometry, Boundary Conditions and Mesh

As explained in Chapter 2.2.5 a chimera setup features multiple grids which are laid over each other. The nozzle grid is used as the background grid. A separate grid surrounding the pintle functions as the overset grid. This is depicted in Figure 4.23a, with a red nozzle or background grid and a black pintle or overset grid.

The background grid is almost exactly the same grid as used for the reference nozzle, see Figure 4.4 in Section 4.2.1. The only difference is that the cells in the rear of the combustion chamber have been refined such that they match the cell size of the pintle grid. Cells of the overlapping regions between two overset grids should be roughly of the same size to assure a good interpolation between the two grids. This was achieved by placing an additional line source in the respective region and regenerating the mesh. All boundary conditions for the nozzle mesh remain the same as before. The actual conditions and values at the inlet, at the farfield and for the medium also remain the same as for the static calculations.

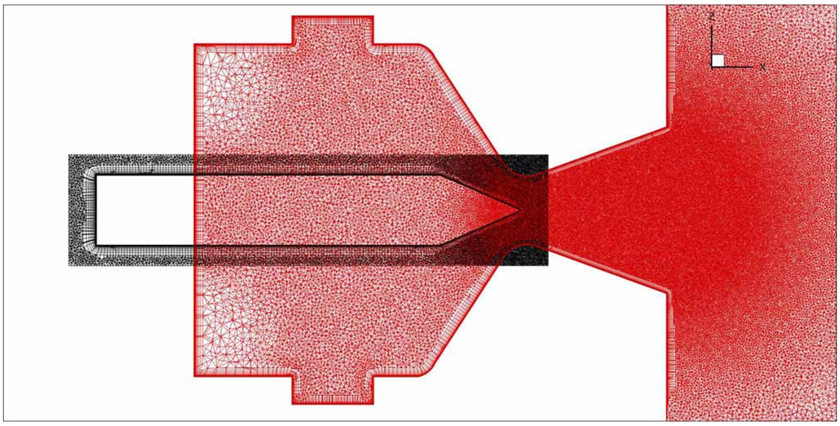

(a) Original (Intended) Version

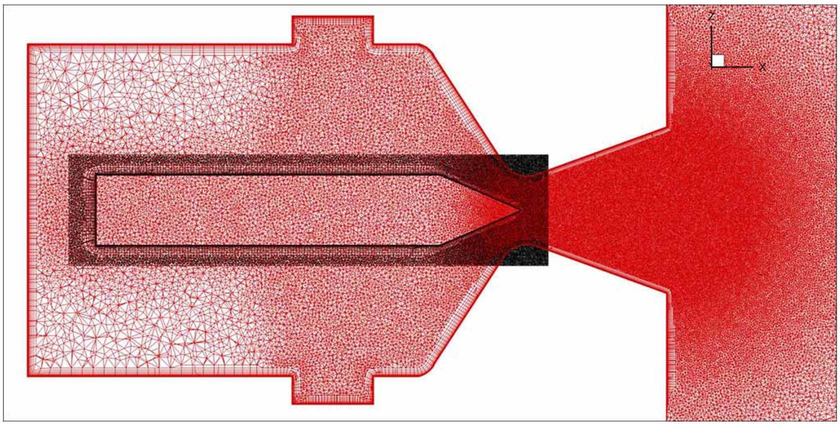

(b) Alternative (Used) Version

Figure 4.23: Chimera Geometry and Grid Setup, Red: Nozzle (Background) Grid and Black: Pintle (Overset) Grid (ZX-Cut)

The overset pintle grid had to be newly generated. The pintle geometry was elongated such that when the pintle is fully inserted a small portion at the rear will still be outside of the post combustion chamber. A cylinder was placed around the pintle to defined the farfield boundary of the pintle grid. The diameter of the cylinder was set to $1.6 \cdot d_{throat}$ to assure a sufficient overlap between the two grids. Also at the pintle tip and rear sufficient overlap was created by extending the length of the cylinder. The outer side of the cylinder was assigned a special *Chimera* boundary condition, which defines the interpolation cells for the overset pintle grid.

The setup outlined above features three locations where hole cutting will have to be applied. Firstly, a hole will have to be cut in the background mesh at the location of the pintle. Secondly, a hole will have to be cut into the overset pintle grid at the location where the overset grid leaves the background grid (near the nozzle throat). Finally, another hole is required in the pintle grid, where both grid and pintle are out of the rear of the nozzle grid. At this location two geometries or wall boundaries cross each other. Initial stationary test simulations have show that this creates an issue. This is shown in Figure 4.24a, where a significant negative velocity in x-direction, where the chamber and pintle wall intersect each other, can be observed.

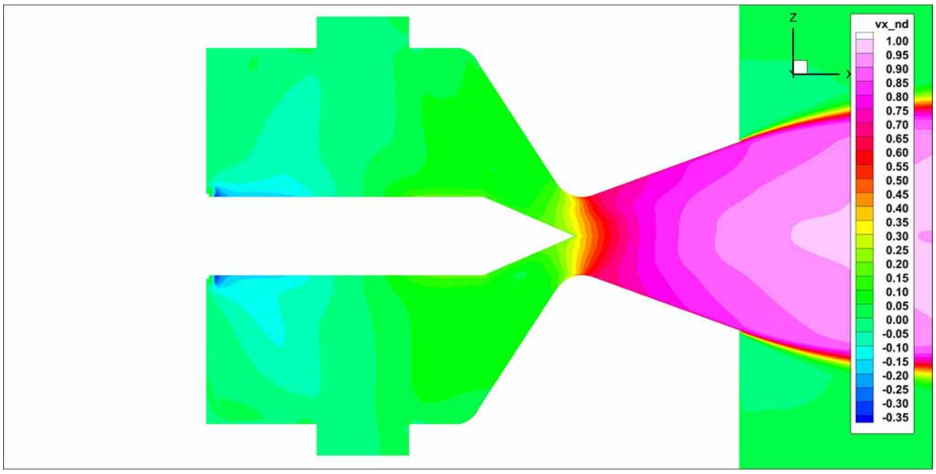

(a) Original (Intended) Version

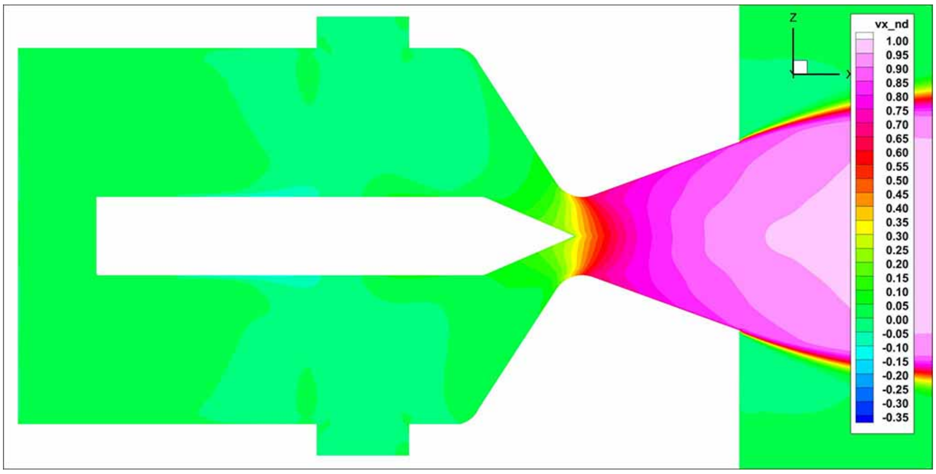

(b) Alternative (Used) Version

Figure 4.24: Chimera Initial Steady-State Results, ZX-Plane Contour of the x-Velocity (Values have been made dimensionless according to Table A.1)

There exists no physical explanation for such a high velocity in this region, therefore it is believed that this is a numerical issue. It is believed that the problem is caused by an error in the interpolation between the pintle and nozzle grid across the intersecting wall boundaries. The issue does not seem to have any visible influence on the rest of the flow field. Nevertheless it was deemed not negligible especially as it was not entirely understood. From Ref. [55] it is understood that the TAU-Code should be capable of handling these intersecting walls. However, the above results clearly indicate some kind of problem. As the issue could not be mitigated in an acceptable time it was decided to avoid any intersecting wall boundaries and the geometry was changed accordingly.

To avoid intersections the geometry has to be modified, this can be done in two ways. The first option is to shorten the pintle. However, this would result in the pintle rear side moving into the inlet zone. This is deemed infeasible, as it could influence the measured pintle force. The second option is to extend the post combustion chamber. This will lead to increase in chamber volume, which could decrease the potential dynamic effects (pressure transients and hysteresis effects). Nevertheless, this was deemed the preferred option.

As a consequence it was decided to add an additional $1.2 \cdot L_{div}$ at the rear of the post combustion chamber, while the pintle geometry and mesh remains the same. The new geometry and mesh is shown in Figure 4.23b. Also for the new geometry initial test calculations were performed, see Figure 4.24b. These do not show any abnormal velocities in the respective regions of the pintle.

Hole Cutting and Interpolation

Hole cutting, the deactivation of undesired parts of a grid, is an essential part of any chimera calculation. The TAU-Code features three different methods for hole cutting:

1. *Manual Static Hole Cutting* is the simplest form of hole cutting. Essentially a dummy geometry is placed into the respective grid at the location of the hole prior to creating the grid. This geometry is thus fixed and cannot move. This procedure would thus only be useful if the grid motion is confined to rotation only. In the given setup the method can thus not be applied.
2. *Manual Dynamic Hole Cutting* also requires manual user input. Here the geometry of the hole is specified in a dedicated separate coordinate file. The coordinates will shift with the motion of the geometry. A hole is defined by a set of dedicated grid elements. The TAU-Code allows tetrahedrons, prisms, pyramids and hexahedrons. Accurately cutting a holes of cylindrical or curved shape would thus require a large number of these shapes. Defining all these by hand in a list is an extremely laborious task. This is especially true for the given geometry where multiple small and curved holes would have to be cut. Therefore, this method is very unpractical for the given case.
3. *Automatic Hole Cutting* is a fully automated hole cutting process, as presented by Nakahashi et al [48]. The feature is only available in TAU since version 2016.2.0, see Ref. [55]. The default algorithm cuts the hole as close to the border as possible. Using a dedicated input it is possible to increase the hole size and thus reduce the overlap zone between the two grids. Moreover, for geometries where holes have to be cut in multiple grids a priority list has to be specified, as otherwise the algorithm does not know in which grid to cut the hole.

Out of the above method the third is the most convenient. Moreover, as the other two method are either inapplicable or unpractical, method three is the only viable option. When using automatic hole cutting in multiple grids a priority must be specified, such that the algorithm knows which cells to deactivate and which have to stay active. In the given case a hole has to be cut in the background or nozzle grid at the location around the pintle. A second hole is to be cut where part of the pintle grid leaves the nozzle grid (near the nozzle throat). To achieve this both grids need to be explicitly given equal and high priority. The priority is assigned by a simple number, with the higher number meaning a higher priority. Thus, in the given case both grids were assigned priority number 2.

The default hole cut will be as close as possible to the pintle geometry, however it would be beneficial to reduce the overlap region between the nozzle and pintle grids. This was attempted using the respective setting parameters within the TAU-Code, however the results were not beneficial and only a small reduction of the overlap zone near the pintle tip could be achieved. Therefore, the default settings were used. This is depicted in Figure 4.25, which shows the mesh including the cut holes and the interpolation points (red dots) for the two pintle extreme positions.

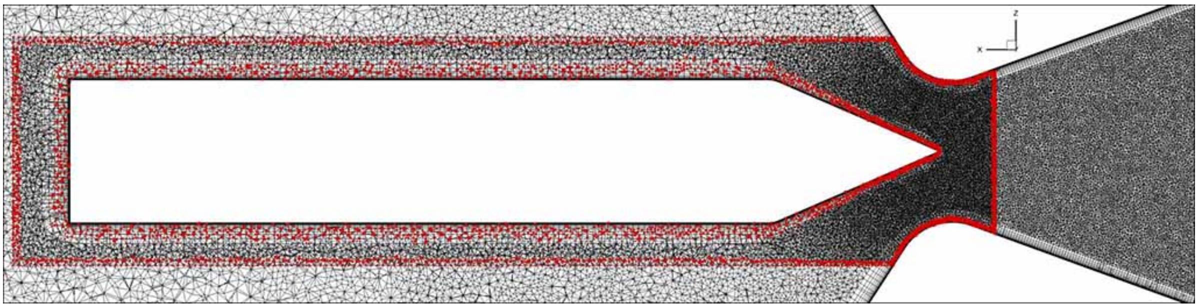

(a) Fully Opened 100 %

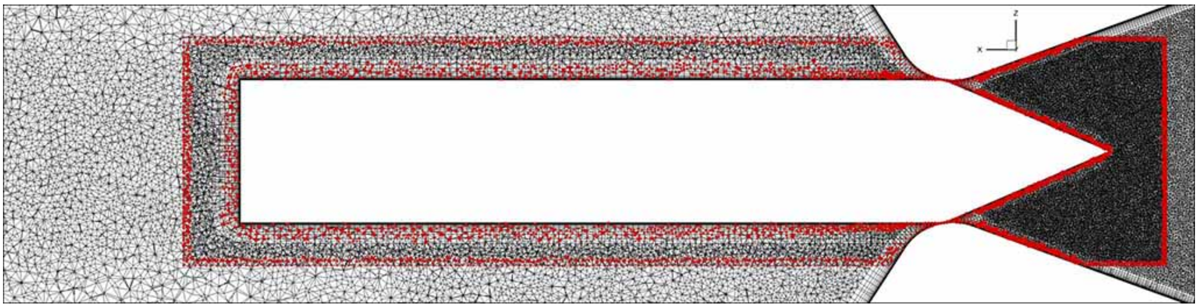

(b) Fully Closed 0 %

Figure 4.25: Chimera Holes and Interpolation Points (ZX-Cut)

Figure 4.25 displays the two holes in each of the cases. The hole in the background grid at the current pintle location and the hole in the pintle mesh where it is out of the bounds of the nozzle mesh. The outer interpolation boundary, which transfers information from the background (nozzle) grid to the pintle grid is located at the most outer cells of the pintle grid as defined by the chimera boundary condition. Only at the hole in the pintle grid (near the nozzle throat) the interpolation points shift inwards. The inner interpolation boundary, which transmits information from the pintle grid back to the nozzle grid is situated close to the hole boundary in the boundary layer of the pintle grid. However, the actual interpolation points are not within the pintle grid but lie in the background grid. Note, in Figure 4.25 it appears as if some of the interpolation points are located within the actual pintle, this is misconception and is caused by the cut through a 3D conical geometry.

The host and donor points for each interpolation zone are not shown in the above Figure 4.25. The TAU-Code determines these points automatically using an Alternating Digital Tree algorithm, see Ref. [49].

Motion Description and Time Stepping
The TAU-Code has multiple possible definitions for the grid motion. The most sophisticated method is to define the motion in an external file via the TAU-Python interface. This would also allow for a coupled motion simulation where for example the motion is simulated via an actuator that is directly depended on the simulated pintle force. This would be the most realistic setup, however it would also be the most complex and costly in terms of preparation and calculation duration. Therefore, it was chosen to use the much simpler method of prescribing a simple periodic motion.

A periodic motion definition can be done directly in the TAU-Code setup file and does not require any interfaces with external files. The motion is defined by a set of Fourier Series (one for each DOF), for details see Ref. [29]. In the given case only a single series is required, as there only exists a single DOF namely a translation in x-direction. The Fourier Series was setup as such that the motion represents a simple Sinus curve staring with a $\pi/2$ phase shift at the amplitude extreme point. The amplitude is simply the difference between the minimum and maximum pintle position. For reasons previously mentioned, the actual time period cannot be given here. All values of time mentioned here have been made non dimensional by $T_{1/2}$, see Table A.1 in Appendix A. $T_{1/2}$ is the estimated time the pintle needs to move from a fully closed to a fully open position or vis versa.

A CFD simulation involving the motion of a full or segment of a grid must per definition be an instationary simulation. Therefore, an instationary time stepping scheme must be applied. For the chimera simulations an implicit dual time stepping scheme (Euler backward-difference) with a constant time step was used. For details on dual time schemes, see Blazek [31]. The time step size was not defined directly. Instead, the number of time steps n per periodic motion was defined. The physical time step is thus defined as $\Delta t = T/n = \left(2 \cdot T_{1/2}\right)/n$. The chimera simulation was run twice, once with an $n = 120$ and once with $n = 240$. Each run was over a full period T, so with pintle insertion and retraction.

Note, initially a much higher time-step resolution (n) was planned. However, it was discovered that with their initially and preferred settings the chimera calculations would have had a run-time of approximately 90 days each, when parallelised over 64 domains/cores on the cluster computer. For these calculations only a total of 128 cores was available. Thus, there was no capacity available to increase the number of cores per calculation to shorten the run-time. As however a run-time of 90 days was unacceptable the settings had to be altered. Firstly, the number of time-steps was brought down to the values mentioned above. As this was still not sufficient, the number of inner iterations or iterations per time-step had to be reduced. This has an influence on the accuracy of the calculation as it can no longer be guaranteed that each time-step result has fully converged before moving to the next time-step. Moreover, reducing the time-step means that potential dynamic effects which are shorter than the time-step are no longer visible. In order to assure that all such effects are captured one would have to perform a detailed time-step convergence analysis. However, for such analysis neither the time nor the computational resources were available within the frame of this project.

4.4.2. Chimera Results

The results of the two chimera calculations are presented in the following section. The full tabulated results of both calculations and the Mach Number Contour for a number of selected time steps, are presented in Appendix B.2 in Tables B.1 and B.2 and Figure B.14. However, before presenting the actual results the pintle movement is analysed. This is shown in Figure 4.26a for both settings of n.

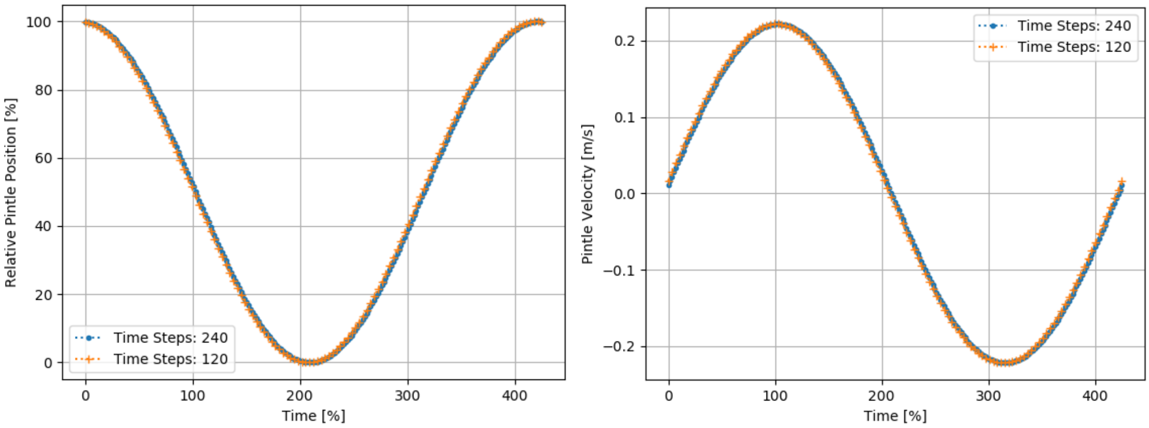

(a) Pintle Position vs. Time

(b) Pintle Velocity vs. Time

Figure 4.26: CFD Chimera Pintle Movement over Time, showing the results for both time-steps (Values have been made dimensionless according to Table A.1)

Firstly, it can be observed that the pintle motion is identical for both time step settings, which is to be expected. Secondly, the pintle motion resembles a sinus curve starting at the pintle open or 100 $\%$ thrust position. The pintle is than inserted into the nozzle throat upto the closed or 0 $\%$ thrust position. After which it is retracted again until the fully open position. So far the plot looks as expected. However, this is no longer the case when looking at the x/time-axis of the plot. The axis has been made dimensionless using the value of $T_{1/2}$, for details see Appendix A. $T_{1/2}$ is defined as the intended time it should take to move the pintle from the fully closed to the fully opened position and vice versa.

This time requirement has been derived from a preliminary assessment of the concept conducted prior to this project. Therefore, the x/time-axis of Figure 4.26a should range from 0 $\%$ to 200 $\%$, with the position minimum occurring at exactly 100 $\%$. However, it becomes obvious that this is not the case. Instead, the range of the axis is a bit more than double the intended range. This error was caused by a faulty user setting in the definition of the Fourier-Series, which governs the motion of the pintle. The error was only discovered very late into the calculation. At this point the time was not sufficient to restart the calculations with the correct settings, therefore it was decided to keep and analyse the faulty calculations. This can potentially mean that a potential dynamic effect, which only occurs at higher pintle speeds is missed or that another effects is not as strong as it would have been. However, this is considered unlikely as the intended and simulated $T_{1/2}$ are both very low already (below $1/10$ of second). Therefore, their absolute difference is still very small and the impact is deemed negligible.

In the following both the primary and secondary results of both simulations will be analysed with respect to time. Figure 4.27 shows the nozzle thrust and pintle force. The blue curves represent the calculation with $n = 240$ time steps and the orange curve with $n = 120$ time steps. Figure 4.27a displays the thrust results. Initially the thrust is at the max. level and for some time remains constant until the physical throat area actually starts to decrease. This has also been observed in the static CFD and 1D simulations. After that the thrust level rapidly decreases to its minimum value. Thereafter it increases again in the same manner. From this plot it is not possible to observe any significant differences between the inserting and retracting part of the simulation. The min. and max. thrust values are almost equivalent, with a relative deviation of $< 1\,\%$, to the results of the static CFD simulation. A small difference can be observed between the two calculations at different time steps, however only at the very beginning and end. Here the calculation with the smaller time step $n = 240$ shows very small oscillations (transient behaviour). The effect is sightly stronger in magnitude at the end of the calculation then at the beginning.

The same effects can be observed when analysing the pintle force in Figure 4.27b. Other than that the pintle force curve does not show any anomalies. Also here the min. and max. results are again almost equivalent to the static CFD simulation.

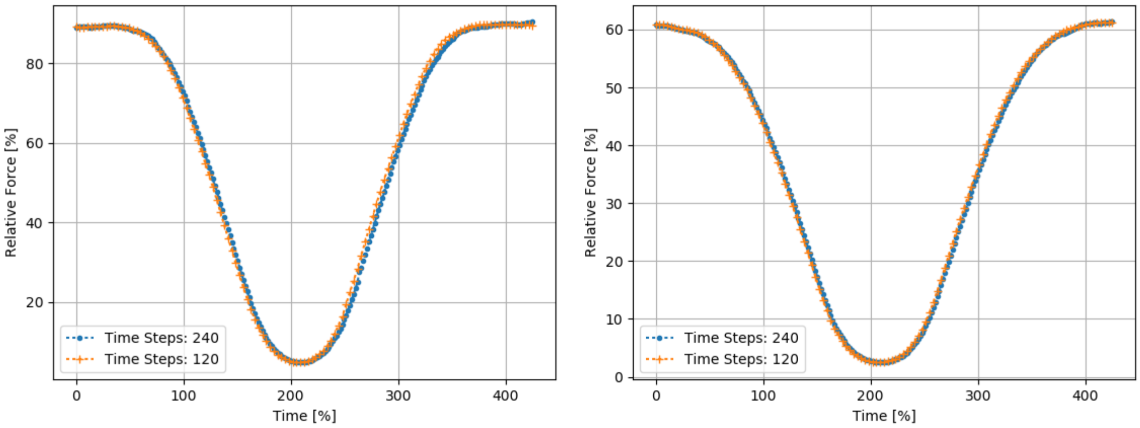

(a) Thrust (b) Pintle X-Force

Figure 4.27: CFD Chimera Results Thrust and Pintle Force versus Time (Comparing two Calculations with two different number of time-steps) (Values have been made dimensionless according to Table A.1)

The remaining results of the two calculations plotted against time are displayed in Figure 4.28. Figure **??** shows the nozzle exit pressure, off all the plots this shows the largest asymmetries. The first half of the pintle curve (inserting) looks somewhat different from the second half (pintle retracting). This interesting as the nozzle exit pressure is a driving factor for the flow separation and the asymmetries in the curve could be a potential indication for a hysteresis. Initially the exit pressure remains constant, as the thrust, until a significant change in the nozzle expansion ratio starts to take effect. Also the flow pattern does not significantly change in that period, compare Figures B.14a and B.14b. Thereafter, the pressure starts to drop. Except an initial transient, the pressure drop occurs at a constant gradient. However, after some time the pressure gradient starts to level-off. At this point the flow first starts to show separation from the nozzle wall, for reference see Figure B.14d. At the min. exit pressure point, where the gradient is zero, the flow has fully separated from the nozzle wall, see Figure B.14e. Afterwards the average exit pressure raises again. As ambient flow is at a higher pressure than the initial nozzle exit pressure it raises above the initial value. At the max. exit pressure point the flow is almost completely separated from the nozzle wall. However, except at its very tip, it is still fully attached to the pintle. Such that the flow pattern, see Figure B.14f, in this region looks very similar to that of an aerospike nozzle. After this point the flow also separates from the pintle wall. A large proportion of the flow occurs very sudden, compare the two consecutive time steps shown in Figure B.14g and B.14h. The former corresponds to the local minimum, which follows the first global maximum in the exit pressure curve. Thereafter the exit pressure again rises very shortly, followed by another small drop at another local minimum. This occurs exactly when the pintle is at the min. (0.0 %) position, the contour plot of which is shown in Figure B.14i. Thereafter the pressure curve and flow behaviour is essentially mirrored, see Figure B.14j to B.14q. However, the pressure level is slightly elevated at all important points. Moreover, it can be observed that the flow reattachment both at the pintle and at the nozzle wall occurs a little bit later, with respect to the pintle position.

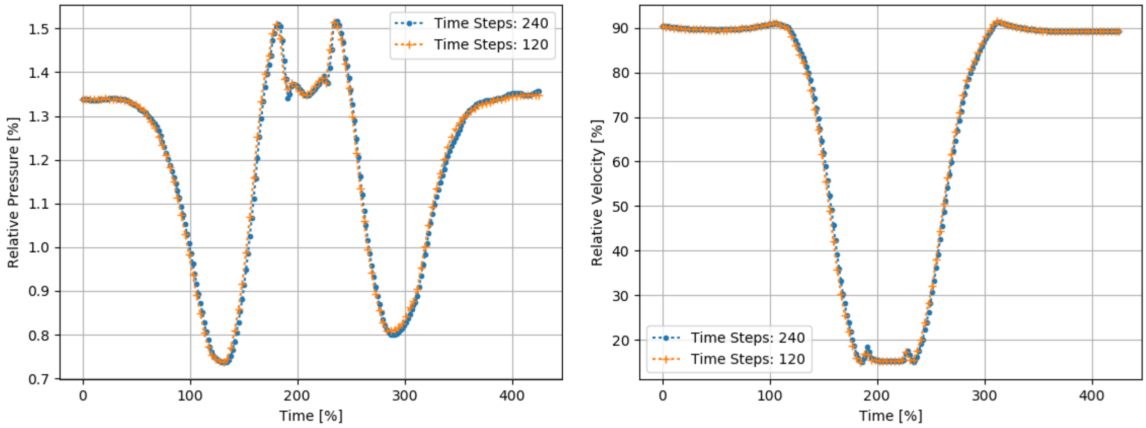

(a) Exit Pressure (b) Exit Velocity

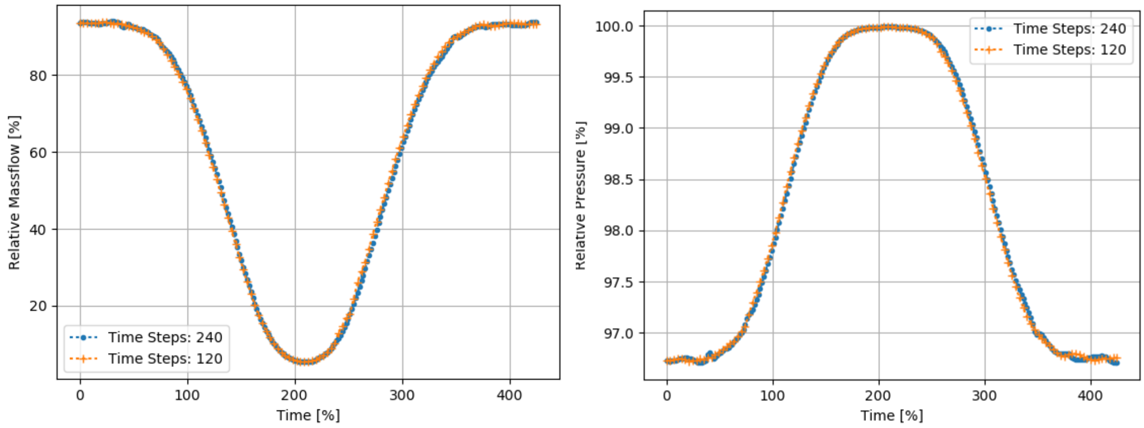

(c) Massflow (d) Inlet Pressure

Figure 4.28: CFD Chimera Results Pressure, Velocity and Massflow versus Time (Comparing two Calculations with two different number of time-steps) (Values have been made dimensionless according to Table A.1)

The nozzle exit velocity is shown in Figure 4.28b. There is no visible difference between the results of the two calculations. The nozzle exit velocity approximately stays constant for the first quarter of the simulation. It even rises slightly after the nozzle exit pressure has already dropped significantly. Only after reaching a maximum, which is only slightly elevated compared to the initially value, it starts to drop significantly. The Mach number contour plot of this point is shown in Figure B.14c. The Mach number in the nozzle exit is almost equivalent compared to the starting condition. However, the max. Mach number in the plume has increased significantly. The velocity drop ends in a minimum which corresponds with the global maximum in exit pressure (see Figure 4.28a) and the contour plot in Figure B.14f. This is followed by a short rise in the exit velocity, where the peak corresponds to the local minimum in the exit pressure and the pintle flow separation point (Figures B.14g and B.14h). Thereafter the exit velocity levels off and remains constant until the pintle 0 $\%$ position. As the pressure the plot is almost mirrored after that point, but also here the values are slightly different. However, the exit velocity is slightly lower while the exit pressure was increased. Note, the difference is so small that it is barely visible in Figure 4.28b. For confirmation check the values in Tables B.1 and B.2.

The massflow of the nozzle is displayed in Figure 4.28c. The massflow curve basically follows the same behaviour as the the thrust curve. However, here the difference between the $n =$ 120 and the $n =$ 240 calculations is more clear. While the $n = 120$ calculation does not show any anomalies, the $n =$ 240 calculation clearly shows small oscillations near the beginning and end of the simulation.

Finally, the inlet static pressure is shown in Figure 4.28d. The behaviour of the static pressure is very similar to the static CFD simulations (see Figure 4.16d). Namely, the static pressure drops towards the fully open pintle position, as the flow speed at the inlet increases. However, the plot also indicates some dynamic effects. Out of all plots shown in this section Figure 4.28d shows most clearly the small oscillations occurring at the beginning and at the end of the simulation. For all previous plots these were only visible in the calculation with $n =$ 240 time steps, here they are visible in both calculations. However, they are more distinct in the calculation with $n =$ 240 time steps.

In general the differences between the two chimera calculations are small. However, as previously described the the calculation with $n =$ 240 time steps shows stronger oscillations. Therefore, it is difficult to argue that the selected time-step size has converged. As already stated in Section 4.4.1, this would require additional calculations at a reduced time step size. For the sake of clarity and as it appears to be showing more details, all following discussion and analysis will only make use of the calculation with $n =$ 240 time steps.

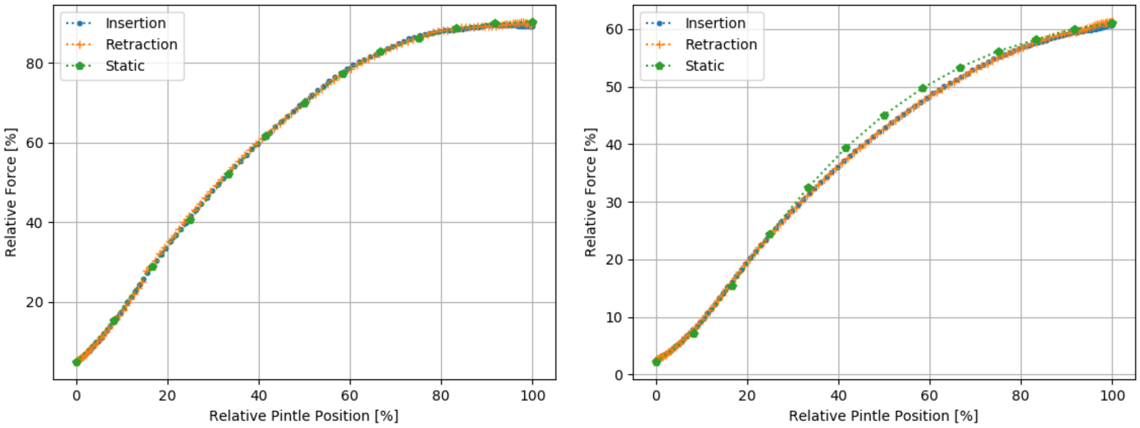

(a) Thrust

(b) Pintle X-Force

Figure 4.29: CFD Chimera Results Thrust and Pintle Force versus Pintle Position, comparing the Chimera Calculation (with $n =$ 240 time-steps) with the Static CFD Results (Values have been made dimensionless according to Table A.1)

To achieve a better comparison between the pintle inserting and retracting leg and also with the static CFD simulation it was decided to plot all results with respect to the pintle position. For this the inserting and retracting leg were separated and plotted together with the static results from Section 4.3.2. Figure 4.29a displays the thrust results. Here it can be observed that all three curves are an almost perfect match. There is no visible difference between the static and the dynamic/chimera simulation. Moreover, also the difference between the inserting and the retracting leg is almost indistinguishable. Only at the max. thrust position a very small difference can be spotted. This is likely caused by the small oscillations, which were outlined above and are present in these regions. The pintle force is depicted in Figure 4.29b. Also here the difference between the inserting and the retracting leg is indistinguishable. However, between the pintles 30 % and 80 % position the result of the static simulations is slightly higher with respect to the chimera results.

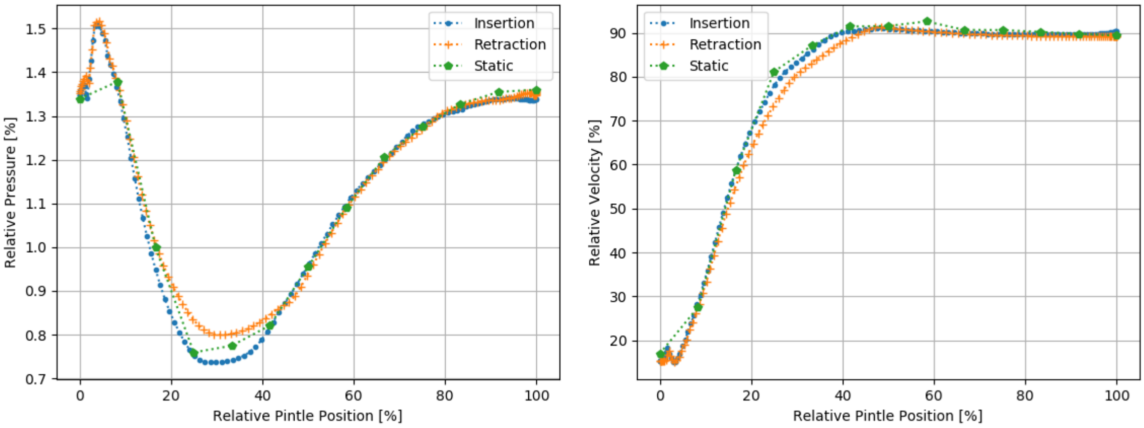

(a) Exit Pressure (b) Exit Velocity

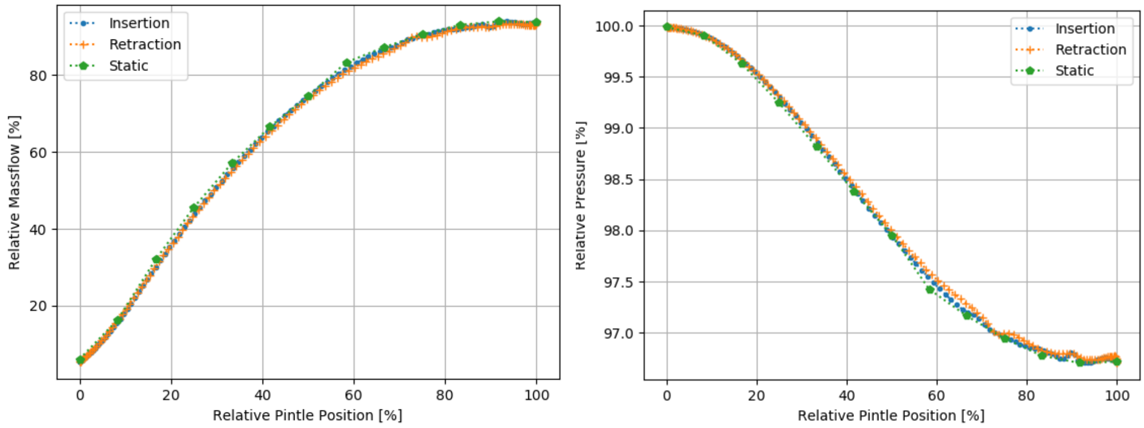

(c) Massflow (d) Inlet Pressure

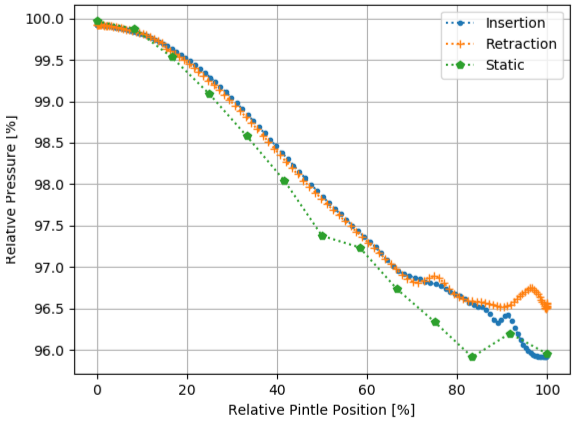

(e) PCC Pressure

Figure 4.30: CFD Chimera Results Pressure, Velocity and Massflow versus Pintle Position, comparing the Chimera Calculation (with $n = 240$ time-steps) with the Static CFD Results (Values have been made dimensionless according to Table A.1)

Figure 4.30 gives an overview of the secondary results plotted against the pintle position. The nozzle exit pressure is displayed in Figure 4.30a. It confirms the previous findings regarding the expansion and separation behaviour of the nozzle. The global minima again correspond with the point where the nozzle flow has fully separated, so to the contour plots in Figures B.14e and B.14m for the inserting and retracting leg respectively. This confirms that the flow separation occurs at a lower pintle position or in other words the flow reattachment occurs later. Moreover, does the nozzle expand to a slightly lower pressure when on the inserting leg. The pressure results of the static CFD simulation are in between the chimera results. However, the separation point matches more closely that of the inserting leg. Also as before, the pintle flow separation corresponds to the global maximum and local minimum. Here also a small difference in the x-positions can be observed, however this is hardly visible in Figure 4.30a. Moreover, it is so small that it is in the same order of magnitude as the Δx between two time steps and is therefore not conclusive.

The nozzle exit velocity is illustrated in Figure 4.30b. As to be expected in the flow separation regions, where the pressure results do not match, the velocity values also do not match, but with reversed difference. However, this time the static CFD results do not lie in between the chimera legs. Instead the static CFD results are slightly higher. The small kink, which was already described in Section 4.3.2, present in the static results at the 66.6 $\%$ pintle position does not show in the chimera results. Note, the kink is also visible in massflow and inlet pressure results (Figures 4.30c and 4.30d), but also here only in the results of the static CFD simulations. This could indicate that it is caused by a numerical issue occurring at that static pintle position only.

The massflow and static inlet pressure results shown in Figures 4.30c and 4.30d also perfectly match each other. The static inlet pressure results again show small oscillations or anomalies near the pintle max. thrust position. These effects are however best visible when looking at the PCC pressure, see Figure 4.30e. Theses effects could be caused by the moving pintle, which would cause a small pressure drop when moving forward and a small pressure increase when retracting back into the PCC. This however does not explain why the results at the very beginning and the very end (at the max. thrust position) does not match each other. This could also be an indication a numerical issue.

A more detailed analysis of the potential dynamic effects and findings of the chimera simulations will be presented in Chapter 6.1.3. This concludes the presentation of the chimera simulation results.

4.5. Static Hot-Fire CFD Simulation

All CFD simulations presented hitherto in this chapter have been conducted using a fluid at approximately ambient temperature and with the assumption that the fluid can be treated as an ideal or perfect gas. This was done to allow a comparison with the cold-gas test conducted by Metsker [16], see Chapter 5. However, in the potential application of the given principle the fluid expanded through the nozzle will most likely not be at ambient conditions, but likely will be generated by a gas generator utilising rocket fuel and thus be in excess of 1000 K. Moreover, the ideal gas assumption will no longer be entirely correct. However, the 1D simulation relies on the ideal gas assumption, see Chapter 3.1.1.

In order to find out whether this leads to an unacceptably large error a CFD simulation for a generic hot-fire case was setup. The CFD simulation will use a real gas model, thus specific heat-ratio γ and gas-constant R will no longer be constant, but will vary with pressure p and temperature T. The results of the CFD simulation will be compared against 1D simulation case using the same inlet conditions, but an ideal gas assumption. This section will describe the setup of the hot-fire CFD simulation and its results. The 1D simulation setup is basically equivalent to what was presented in Chapter 3. Only the initial inputs T_c, γ and R were changed.

4.5.1. Hot-Fire Setup

The setup of the hot-fire CFD simulation is very much similar to the original cold-gas case. For the sake of simplicity the geometry was left exactly the same, as depicted in Figure 4.1. However, the amount of simulations conducted was reduced by only simulating half of the pintle positions compared to the cold-gas case. Therefore, the grids generated in Section 4.3.1 can be reused and no new grid needs to be generated.

As stated previously, the geometry used resembles closely the geometry used by Metsker [16] for his cold-gas test, see Chapter 5. This geometry is comparably small. It is very probable that a geometry used in an actual hot-fire setup will be much larger in terms of size, massflow and thrust. These effects are thus neglected here. It is believed that they are insignificant, as boundary layer effects in a nozzle usually do not significantly vary with nozzle size. Moreover, if at all they decrease with increasing nozzle size. For details see the Literature Study [2].

The farfield boundary conditions remain unchanged compared to the cold gas setup. The inlet pressure also remains the same. Essentially only the inlet temperature is increased. This however also changes the relative gas constant R and the specific heat-ratio γ. The inlet and initial fluid conditions are shown in Table 4.7.

Table 4.7: Hot-Fire Setup Initial Fluid and Inlet Boundary Definition, assuming Perfect Gas Relations (Values have been made dimensionless according to Table A.1)

Condition:	**Value:**	
Relative Total Inlet Pressure p	1.0	[-]
Relative Temperature T	7.41	[-]
Specific gas constant R	287	[J/ (kg · K)]
Specific heat ratio γ	1.29	[-]
N_2 fraction	0.76	[-]
O_2 fraction	0.24	[-]

The fluid conditions shown in the above Table are only the initial conditions. If for the CFD simulation presented in this Section an ideal gas would be assumed those conditions would remain constant over the entire domain and with pressure temperature. As previously stated, in this case the ideal gas assumption is no longer used. The standard version of the DLR TAU-Code (2015.2.0 and 2016.2.0) used in this project hitherto are only capable of ideal gas calculations. For any real gas calculations one has to switch to separate and dedicated versions. These versions are referred to as the *TAU-Chemie* (Chemistry) versions or Spacecraft τ, see Ref.[56]. For this project the 2016 version of the TAU-Chemie-Code has been used.

The code features two possibilities of modelling the fluid. A chemical equilibrium model, where the fluid composition and pressure and temperature ranges are defined prior to the actual simulation. From this a table is generated, where the actual values are interpolated from during the CFD simulation. A non-equilibrium model is also available. For this only the initial fluid composition is defined, the new compositions and the respective fluid data is than recalculated for each iteration during the CFD simulation. Both methods are outlined in Ref. [56] and a detailed description of the principals for both methods can be found in the book of Anderson [57]. As the latter method is computationally rather expensive, it was decided to neglect any possible reaction between the different fluid components. Therefore, it would be sufficient to employ the first (chemical equilibrium) method.

There are many potential fuel combinations and an even greater amount of different exhaust compositions for a hot DACS system. As the combination for the given case is completely undetermined and for the sake of simplicity, a simplified version of hot air was used. This allows for a further simplification, as the required species for air are already contained in the standard *Tau-Code Chemistry Definition (Air, 11 species) File*. Thus no new species file had to be created. The simplified version of hot air only contains nitrogen N_2 and oxygen O_2. The compositions are shown in Table 4.7. Both nitrogen and oxygen, especially the former, represent a majority of the exhaust components of most rocket fuel combinations. The approximation is thus not unjustified.

4.5.2. Hot-Fire Results

The presentation of the results of the hot-fire case is done in a similar style as the presentation of static cold-gas results presented in Section 4.3.2. Table 4.8 presents all relevant results. The results were made dimensionless by the same reference values as before and summarised in Appendix A. Table 4.8 also contains the results for the reference nozzle geometry (without the pintle). These are designated by *NP* (for no pintle).

Table 4.8: Tabulated Results of the Hot-Fire CFD Simulation (Values have been made dimensionless according to Table A.1)

x_{pi} [%]	T [%]	F_{pintle} [%]	$\dot{m}$ [%]	p_{in} [%]	p_{PCC} [%]	p_e [%]	v_e [%]
NP	93.82	N/A	29.04	97.00	99.78	2.05	287.19
100.00	93.68	61.47	29.13	96.98	96.65	2.05	279.04
83.33	92.19	59.01	32.17	97.06	96.69	1.95	258.22
66.67	86.43	54.33	30.30	97.39	97.04	1.77	260.17
50.00	73.54	46.31	22.95	98.12	97.44	1.48	294.51
33.33	53.85	33.82	19.20	98.93	98.57	1.01	260.68
16.67	29.75	16.80	10.73	99.62	99.54	0.96	191.42
0.00	4.82	2.48	1.66	100.04	100.03	1.40	34.20

The thrust and the pintle force versus the pintle positions are plotted in Figure 4.31. The plots also show the results of the 1D simulation using the same initial conditions, but with an ideal gas assumption. The general trend of the thrust and pintle force curve is the same as for the cold-gas case, compare with Figure 4.15. Compared to the cold gas case the absolute thrust force is slightly increased by approximately 4 $\%$. This is expected due to the higher efficiency caused by the much larger exhaust velocity, which is a consequence of the much higher characteristic velocity c^* caused by a higher combustion temperature T_c (see Chapter 2.1). The max. difference in thrust between the 1D and CFD simulations is also very comparable, with 10.2 $\%$ for the hot-fire case and 9.7 $\%$ for the cold-gas case. The thrust of the reference nozzle matches the thrust of the pintle at the 100 $\%$ setting.

The difference in pintle force is even less significant, both comparing CFD and 1D simulation and when comparing the hot-fire and cold-gas cases. The difference between the hot and cold case is less than 1 $\%$. Considering that the pintle force is a function of the pressure over the pintle this is to be expected as the initial pressure for both cases is the same. The difference between CFD and 1D simulation has its maximum of 5 $\%$ at the 100 $\%$ positions. In general the differences for the primary results (thrust and pintle force) between the 1D and the CFD simulation are small and can be considered acceptable.

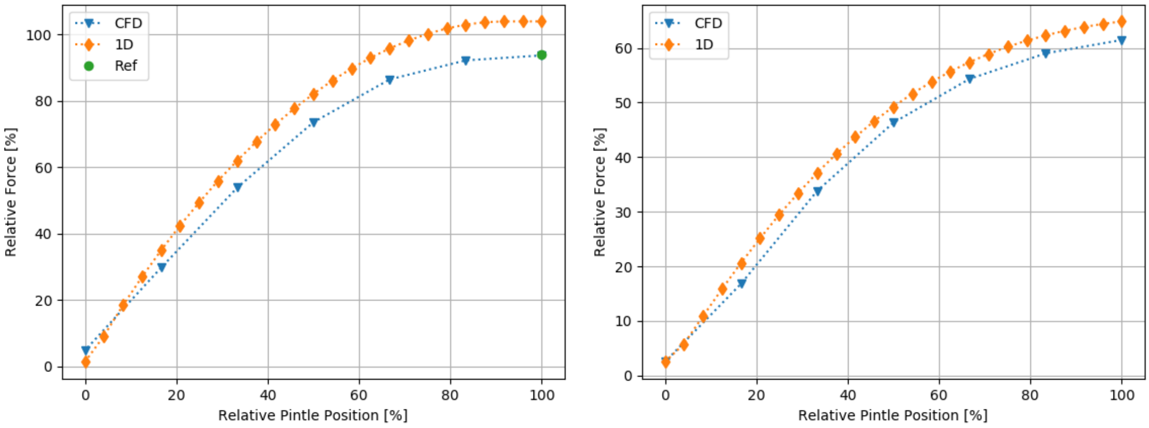

(a) Thrust

(b) Pintle X-Force

Figure 4.31: CFD Hot-Fire Results Thrust and Pintle Force, CFD Simulation compared to 1D Simulation using Hot Inlet Conditions and Hot CFD Reference Nozzle (Values have been made dimensionless according to Table A.1)

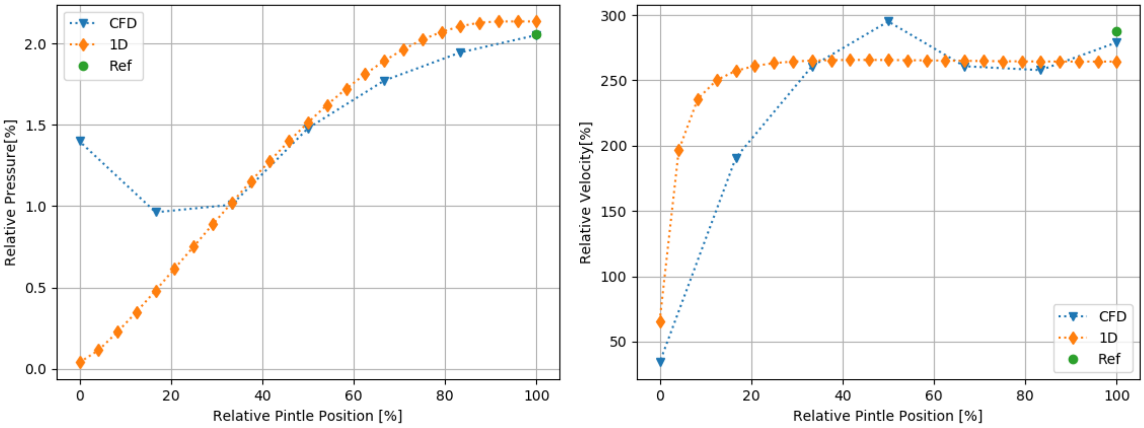

(a) Exit Pressure

(b) Exit Velocity

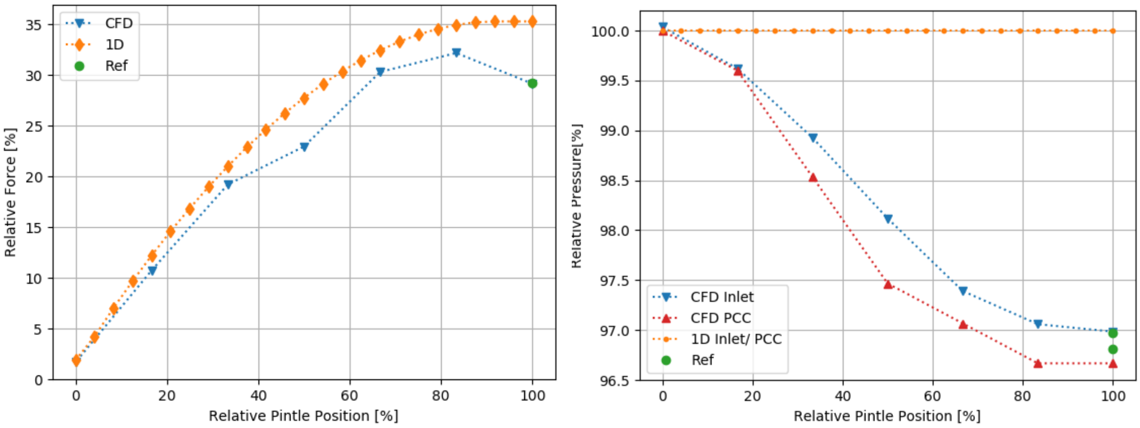

(c) Massflow

(d) Inlet Pressure

Figure 4.32: CFD Hot-Fire Results Pressure, Velocity and Massflow, CFD Simulation compared to 1D Simulation using Hot Inlet Conditions and Hot CFD Reference Nozzle (Values have been made dimensionless according to Table A.1)

The secondary results of the simulation are shown in Figure 4.32. The nozzle exit pressure is shown in Figure 4.32a. CFD and 1D simulation results are very comparable except for the two pintle positions subjected to flow separation. In contrast to the cold-gas cases, the CFD simulation returns slightly lower values than the 1D simulation. This is surprising as one would expect that the expansion process through the nozzle is less ideal and the CFD results should thus be higher than the 1D result. A possible explanation is the different specific heat-ratios γ. The 1D simulation has a constant $\gamma = 1.29$, while in the CFD simulation γ varies, for the 100 % pintle position $\gamma = 1.33$ averaged over the nozzle exit plane. Moreover, it is notable that the exit pressure is significantly higher (relatively increased by 50 %). While for the cold-gas case the nozzle is expanding the flow to roughly ambient conditions (at the pintle 100 %), for the hot-fire case the nozzle is thus under-expanding the flow. This also explains why the flow separation occurs at a latter stage. For the hot-fire case separation only occurs at the 16.6 % pintle position, for the cold-gas case separation already occurs at 33.3 %. According to the Summerfield criterion flow separation should occur for pintle position slightly below 20 %. The CFD results show that this is the case. However, to determine the exact position at which separation occurs, simulations at the in between positions should be conducted.

Figure 4.32b compares the different nozzle exit velocities. Here the differences between 1D and CFD simulation are more visible. The CFD results initially increase with a much shallower gradient. Thereafter they overshoot to a value significantly above the 1D simulation. For the two following pintle positions CFD and 1D almost match each other. For the result of the 100 % position the CFD result is again significantly higher and the CFD result for the reference nozzle is even a bit above that. The reason for the final increase of the exit velocity is not entirely understood. It is however believed that it is related to the under-expansion of the flow at that position. Compared to the results of the cold-gas case, see Figure 4.16b, the exit velocity is much higher (up to a factor 3). This is however expected, as the hot-fire case has a much higher c^* (see Eq. 2.9 and Chapter 2.1.1). This will lead to a much higher specific impulse I_{sp} and thus to a higher exit velocity.

The increase in c^* at the same time will lead to a reduction in massflow, compare Figure 4.32c and 4.16c. This effect is also expressed by Eq. 2.6 and the reduction in density. In general 1D and CFD results follow the same trend and the results initially have a good match. However, the deviations increase for higher pintle positions. The massflow results for the hot-fire case, show anomalies at the same positions as the velocity. At positions where the exit velocity has a peak the massflow has a dip. The first anomaly at the 33.3 % positions occurs where the flow is still over-expanding, but without any flow separation from the nozzle wall. At the second anomaly at the 100 % positions the flow is already significantly under-expanding. Therefore, it is believed that these effects are related to the over- and under-expansion behaviour of the nozzle. These effects are not visible in the thrust curve (Figure 4.31a) as the respective increase in velocity is always coupled to a decrease in massflow. Thus, according to Eq. 2.5 the thrust will stay constant. At the 33.3 % position a further anomaly can be observed, when skipping ahead to the respective contour plot, see Figure B.18 in Appendix B. The plots show asymmetric flow in the divergent nozzle section and downstream of the nozzle exit. These appear to be caused by asymmetric flow-separation at the pintle tip. Whether the above effects are related is not clear.

The final plot (Figure 4.32d) compares the inlet and post combustion chamber pressure. For the 1D simulation both pressures are equivalent and assumed constant with pintle position. Note, the post combustion chamber pressure is defined as the average pressure over cross-sectional surface just before the nozzle contour starts to converge, so at $x = -0.78 \cdot L_{div}$ from the throat (see Figure 4.1). For the 0 % pintle position both post combustion chamber and inlet pressure are equal to the 1D result. This is expected as in that case the flow velocity at the inlet and in the post combustion chamber are close to zero. Therefore, the static pressure will match the total pressure defined at the inlet boundary. When the pintle is opened the the flow velocity will increase this will also cause an increased pressure drop. Compared to the cold-gas results (see Figure 4.16d) the pressure drop is a little bit smaller. This is likely caused by a decrease in the specific heat ratio γ, which according to the general istentropic flow relations will reduce the pressure drop.

Figures 4.33, 4.34 and 4.35 display the Mach number, pressure and temperature for the reference nozzle, the full thrust (100 %), the mid (50 %) and min. thrust (0 %) positions. The contour plots of all hot-fire calculations can be found in Figure B.15 to B.20 in Appendix B.

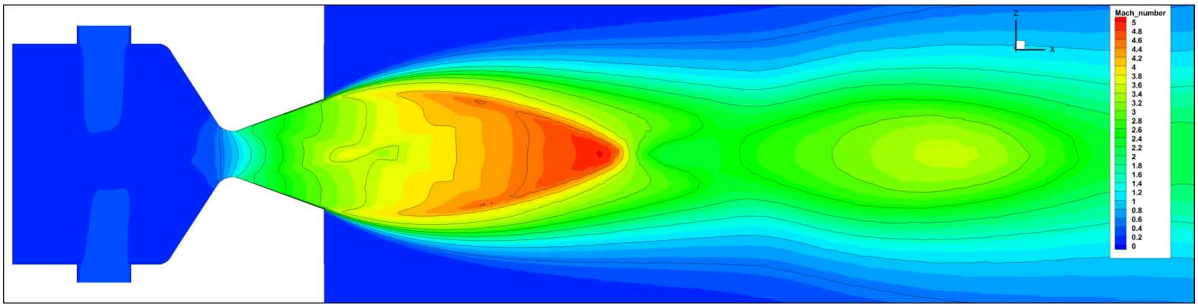

(a) No Pintle

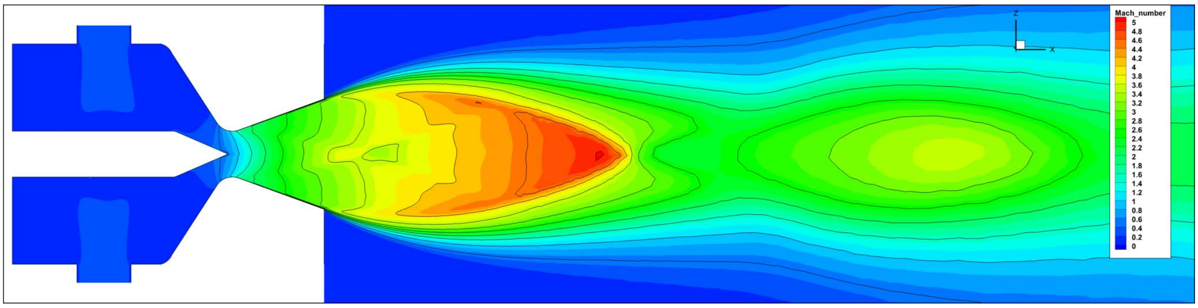

(b) 100 $\%$

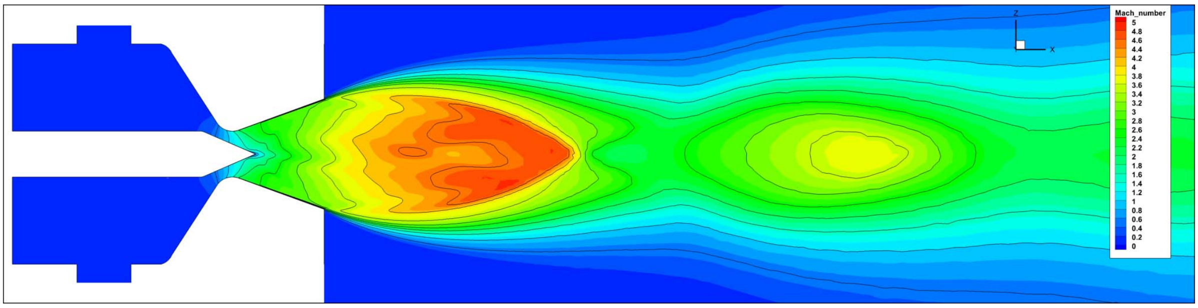

(c) 50 $\%$

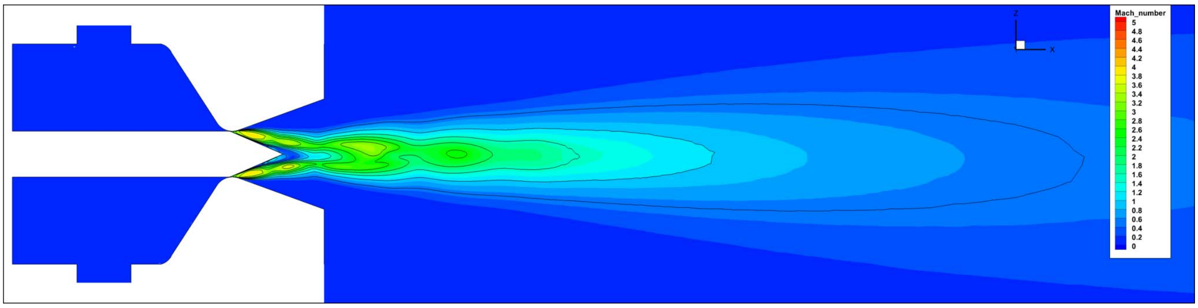

(d) 0 $\%$

Figure 4.33: CFD Mach Number Results ZX-Plane Cut Contour Plot, (Mach Number ranging from $M = 0.0$ to $M = 5.0$ with $\Delta M = 0.2$ and for the lines a $\Delta M = 0.5$)

The Mach number contours are comparably similar to the Mach number plots of the cold-gas simulation (see Figure 4.17). The maximum Mach number reached is however significantly lower, even though as discussed above the achieved velocities are much higher. However, the temperature and therefore also the speed of sound increase significantly. This results in a lower Mach number. Another notable difference is that the flow for the reference nozzle and the 100 $\%$ (see Figure 4.33a and 4.33b) is under-expanded. This can be observed by the much wider plume downstream of the nozzle exit. Also notable are the asymmetric flow-separations from the pintle wall. These can be seen in their mild form in Figures 4.33c and 4.33d, but they are most strongly visible in Figure B.18. The asymmetric flow-separation also results into asymmetric flow further downstream. It is also interesting to observe that the asymmetric flow-separation occurs for the 0 % and the 33.3 % position, for the position in between (16.6 %) it is however entirely symmetric (see Figure B.19). The reasons for the asymmetric flow-separation is not entirely understood. One possible explanation could be asymmetries in the unstructured grid at the respective separation location. The asymmetries can also be observed in the cold-flow results (see Figure 4.17) their effects further downstream are however far less severe.

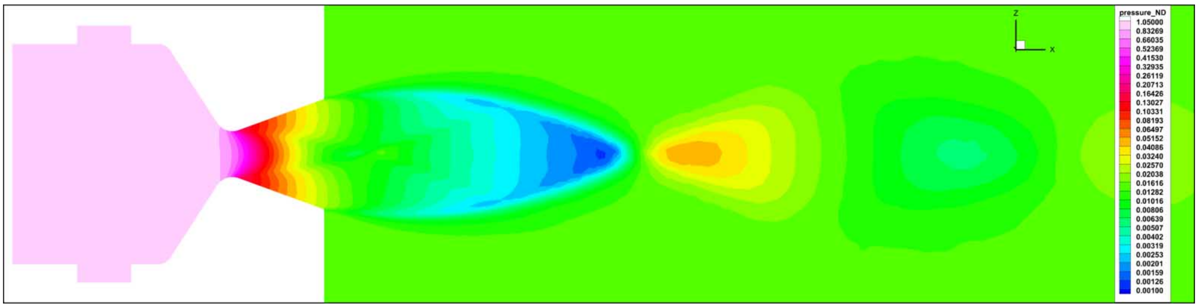

(a) No Pintle

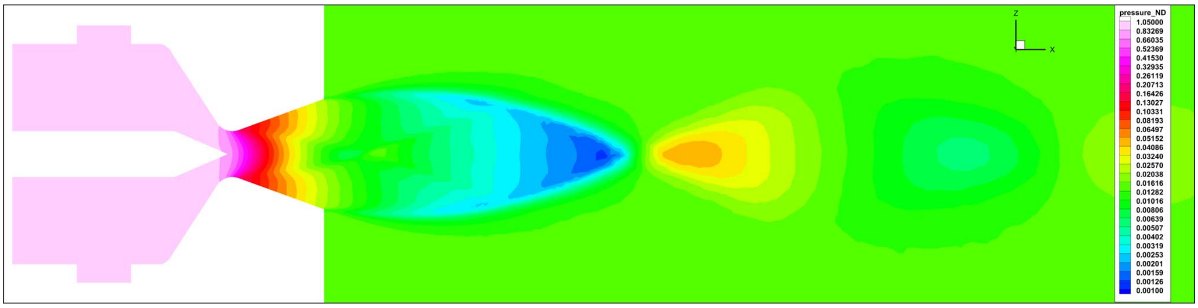

(b) 100%

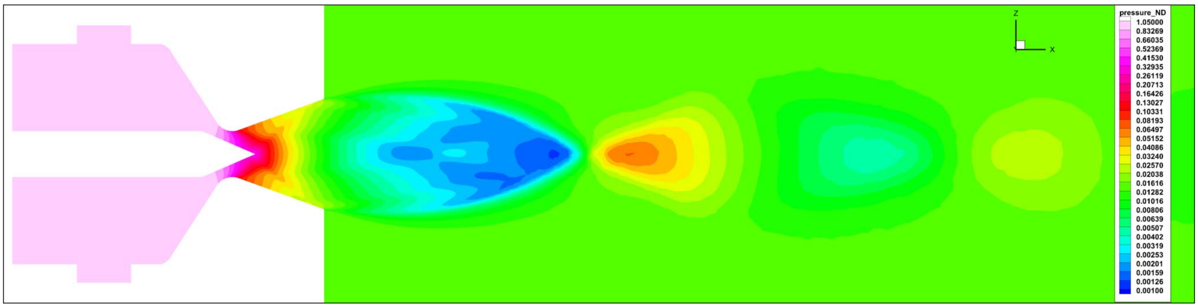

(c) 50%

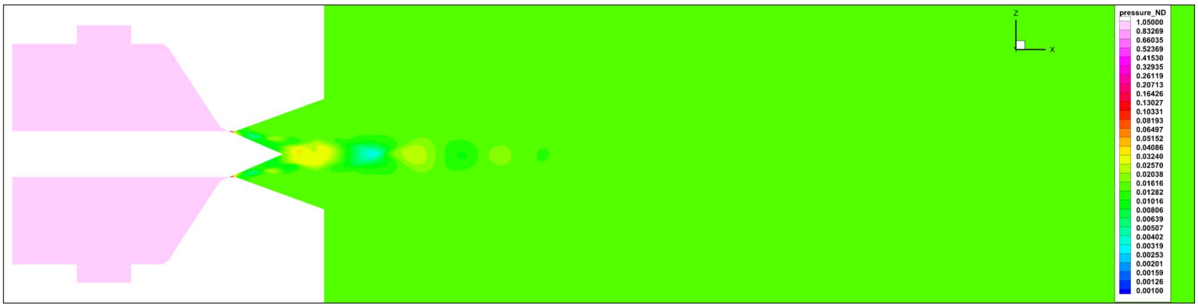

(d) 0%

Figure 4.34: CFD Pressure Results ZX-Plane Cut Contour Plot (Values have been made dimensionless according to Table A.1)

The effects described above are also visible in the pressure plots, see Figure 4.34. These also confirm the initial under-expansion for the reference nozzle at the 100% position. These effects can be observed best on the temperature plots, see Figure 4.35. These also show the plume effects downstream of the nozzle exit, such as the shear-layer or the expansion waves after the nozzle exit. These are than followed by shock, visible by a sharp increase in temperature, after which the flow expands (cools down).

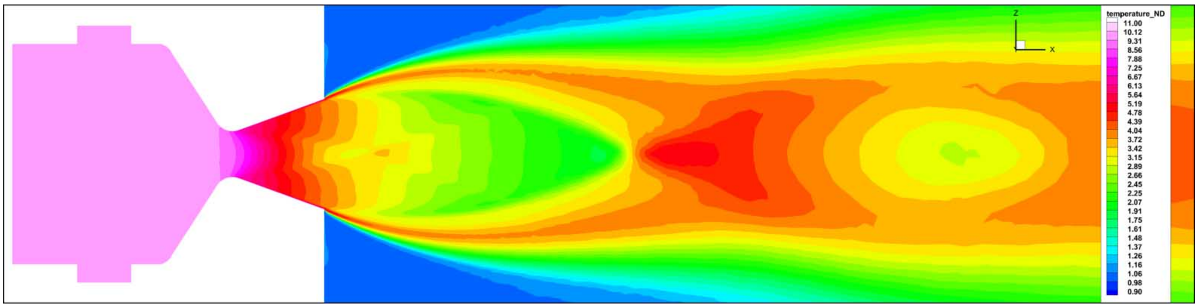

(a) No Pintle

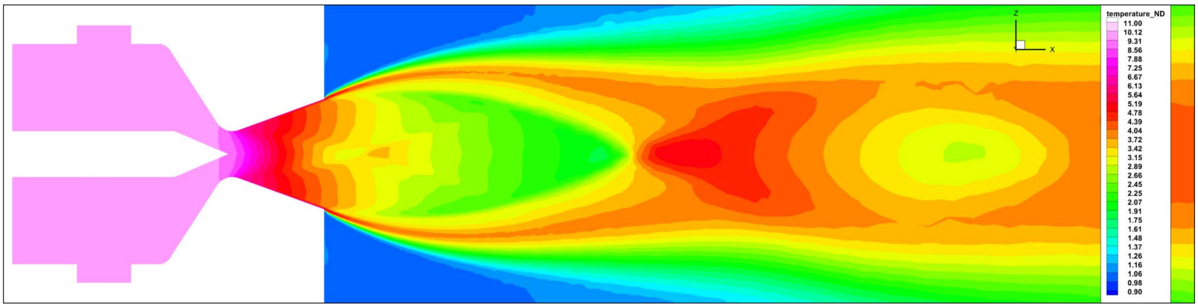

(b) 100 %

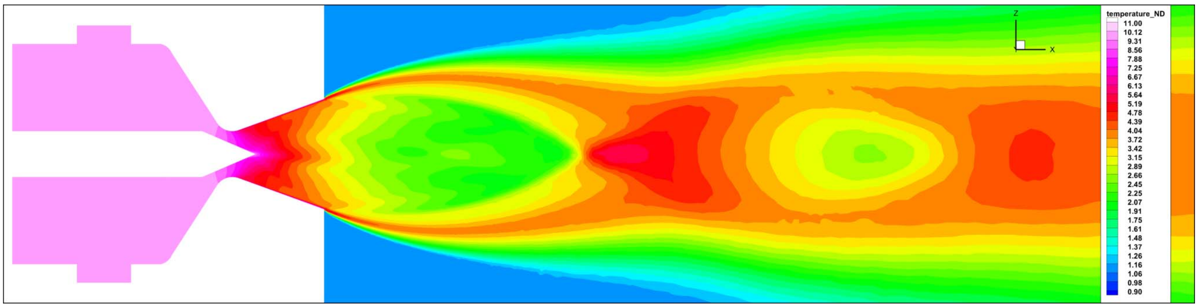

(c) 50 %

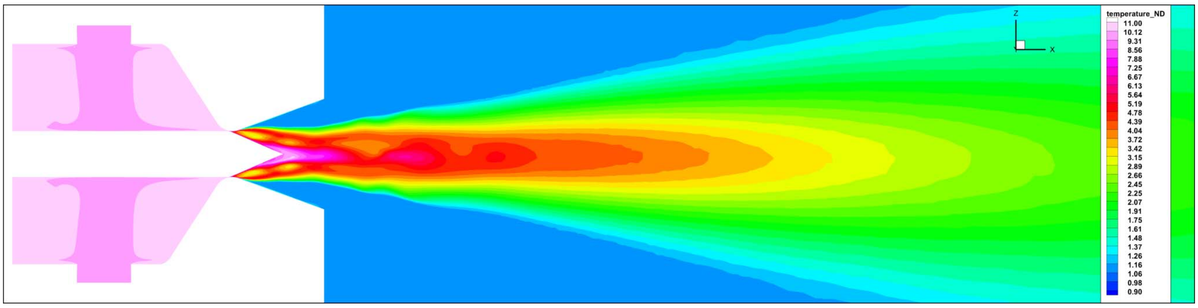

(d) 0 %

Figure 4.35: CFD Temperature Results ZX-Plane Cut Contour Plot, (Values have been made dimensionless according to Table A.1)

4.6. Summary & Conclusions

As this chapter is rather large and covers a wide variety of content a short summary and conclusion will be given here. The chapter described the setup and results of all three CFD simulations (Static Cold-Gas, Dynamic/Chimera Cold-Gas and Static Hot-Fire).

The first section dealt with the general setup, such as the solver, geometry, boundary and initial conditions and the mesh generation, which are common for all three simulations. All have been made using the DLR TAU-Code, a semi-commercial 3D solver for turbulent viscous flow from the low subsonic to the hypersonic regime and developed by DLR. The code uses semi-structured hybrid grids, featuring structured cells at the boundary layers and unstructured volume mesh.

The second section focused on the simulation of the reference nozzle. To verify the main simulations featuring the pintle a static simulation was generated for the thruster without the pintle. It was expected that this simulation should give the same results as the simulations with the fully retracted pintle. Later on in the chapter this could be confirmed.

The following section dealt with the Static Cold-Gas simulation of the thruster. The simulation was conducted at 13 different pintle positions, each requiring a separate geometry and grid. At first the setup, which also included an assessment of grids with different refinement levels was presented. The primary results (thrust and pintle force) of the static CFD simulation were found to be very comparable to the 1D simulation results. The secondary results especially nozzle exit pressure and velocity showed significant differences. These were caused by the flow separation form the nozzle and later also the pintle wall. The flow separated from the nozzle walls for the 33.3% pintle position and below. This was also confirmed by the presented contour plots, which also showed shocks inside the nozzle in coherence with the separation behaviour.

Section four deals with the setup and results of the dynamic/chimera simulations, which was created to investigate potential transient effects when moving the pintle. At first the setup of the employed chimera or overlap grid method were explained. As an overlap between the nozzle and pintle geometry created an inter-grid communication error, the PCC had to be extend such that it can house the pintle grid when fully retracted. The transient effects that could be observed in this simulations were only minor. A small hysteresis effect was observed for the flow separation and reattachment and small oscillations in chamber pressure could also be observed when the pintle was closed to its fully retracted position. The primary results for the static and dynamic simulations were found to be almost identical. However, the results of these simulations are not entirely conclusive as the selected time step and other setting might have been too crude.

The final section focused on the Static Hot-Fire simulation. It was setup to investigate the influence of real gas effects (change of specific heat-ratio) when one would simulate a hot-fire case in the 1D simulation, which is based on an ideal gas assumption. For this the CFD simulation was modified: The ideal gas model used previously was replaced by a real gas model for simplified air and the inlet conditions were changed to representative hot-fire scenario. In the 1D simulation only the inlet conditions were adapted. An initial comparison of the results did not indicate any substantial additional errors, as the results of both simulations were found to be very similar.

The chapter met all research (sub) objectives which are dealing with CFD simulations and were presented in Chapter 1. The results presented here will be analysed further and validated in Chapter 6.

5. Test Setup & Results

This chapter describes the static tests conducted with a DACS demonstrator. The geometry (Figure 4.1) previously used in the 1D and CFD simulations resembles the PCC and nozzle geometry of that demonstrator. The test results will later be used in the analysis of the simulation results, see Chapter 6. The tests were conducted by Yuriy Metsker at the TU Munich as part of his phd thesis [16]. The author assisted in two of the three tests and in the design of the tested thruster and the test setup.

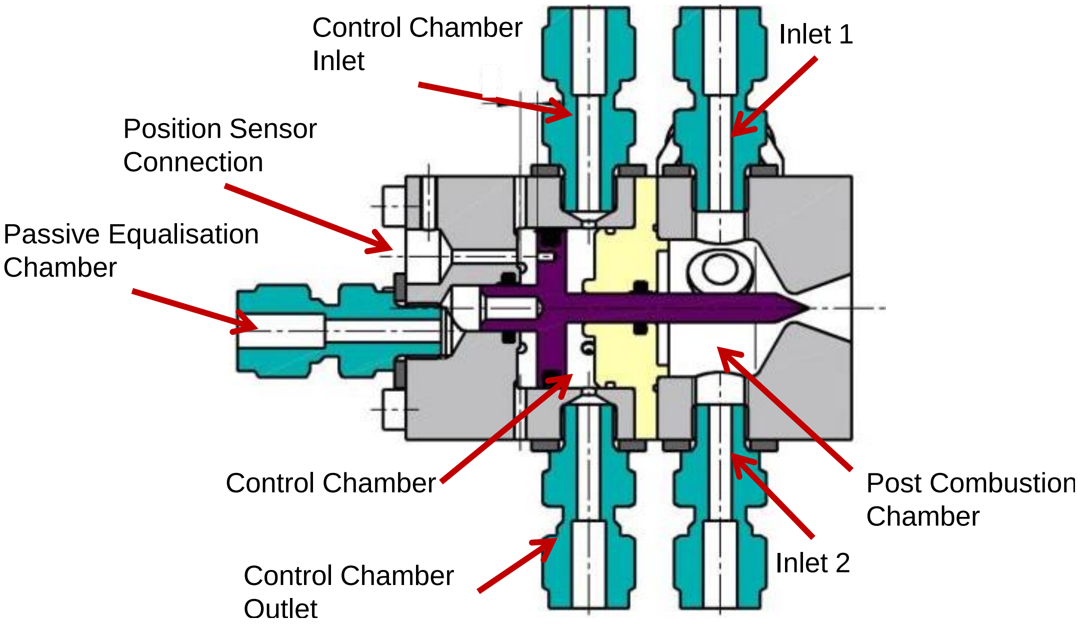

Figure 5.1: Pneumatically actuated DACS Cold-Gas Thruster (Prototype/ Demonstrator Version)

A sketch of the demonstrator is shown in Figure 5.1. The demonstrator features a pneumatic actuator which is used to move the pintle. As only the static tests are outlined in this report, the actuator will not be described any further, for details see Ref. [16]. The static test setup is outlined in the following section.

5.1. Test Setup

The static test setup does not require the pneumatic pintle actuation system, as the pintle position is fixed. These parts are thus excluded from the test setup. Figure 5.2 shows the components of the demonstrator which are required for the tests. These are the PCC/nozzle section, which is manufactured from a single piece of steel. The second required part is the pintle/poppet assembly and the last component is the wall assembly, this separates the PCC from the actuator section and consist out of multiple parts also including O-rings and seals. The PCC features four connecting ports. Two of these ports are the main gas inlets to the PCC, see Figure 5.1. The inlets are situated exactly opposite of each other, such that the pintle is not subjected to off-axis loads. The other two ports are connectors for a pressure and temperature sensor, see Figure 5.2 (left).

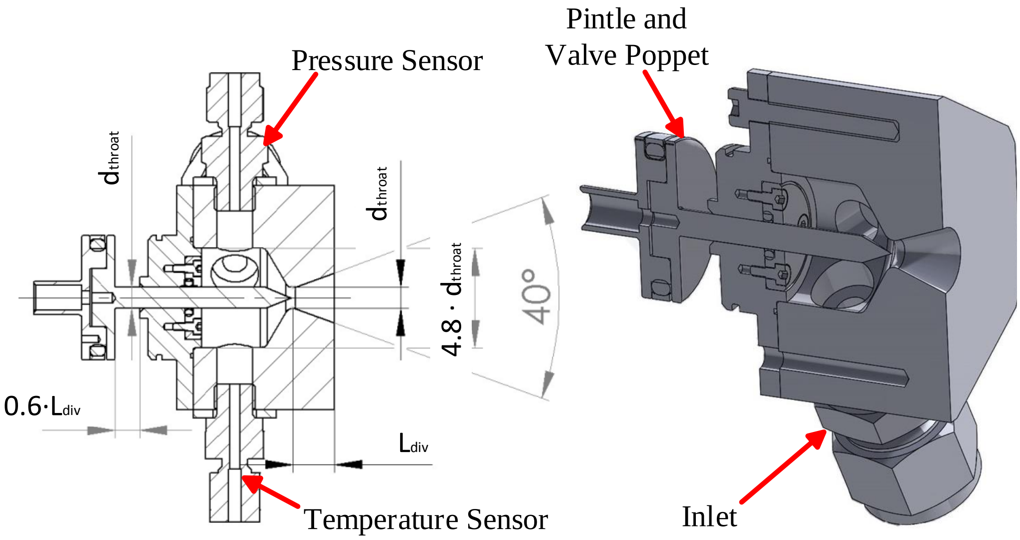

Figure 5.2: Thruster modified for Static Tests (Original Figure obtained from Metsker [16])

The assembly shown in Figure 5.2 is fixed to the vertical side of a specially manufactures L-piece. This is depicted in Figure 5.3. The rear of the pintle/poppet assembly is connected to to a load cell, via a specially made connector pin. The other end of the load cell is mounted via a screw to a block. The block is mounted to the horizontal part of the L-piece. Via the screw the pintle/poppet assembly together with the load cell can be moved backwards and forwards.

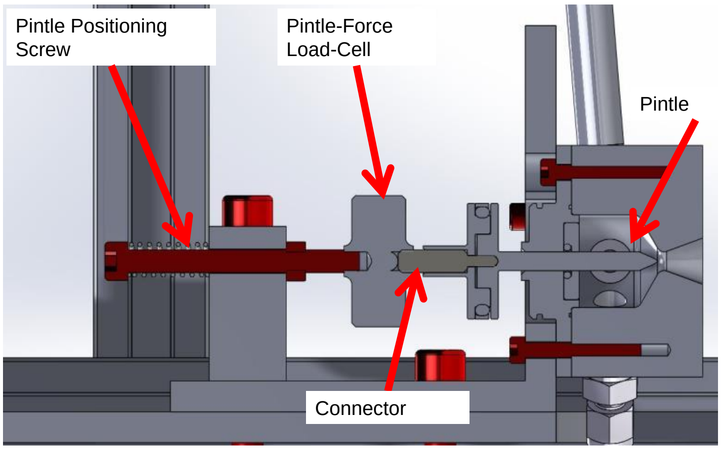

Figure 5.3: Static Test Setup Pintle Position and Measurement (Original Figure obtained from Metsker [16])

The L-piece is mounted on top of a flexible thrust-plate. The thrust plate is connected via another load cell to the frame of the thrust-bench. With this approach both the pintle force and the nozzle thrust can be measured at the same time. The full thrust bench/table assembly can be seen in Figure 5.4a.

The two inlet ports of the demonstrator are connected to a fluid supply system via Swagelok feed-pipes. The fluid supply systems consist out of three separate channels, each channel has its own remote controlled valve, regulator, bleed- and manual valve. In the static test setup only a single channel is used. The other end of the channel is connected to reservoir consisting of $16 \times 50\,\ell\ N_2$ bottles. The initial pressure of a fresh bundle is 300 bar. Valve actuation and sensor data recording is done by a measurement and actuation system. A picture of the full setup is shown in Figure 5.4b.

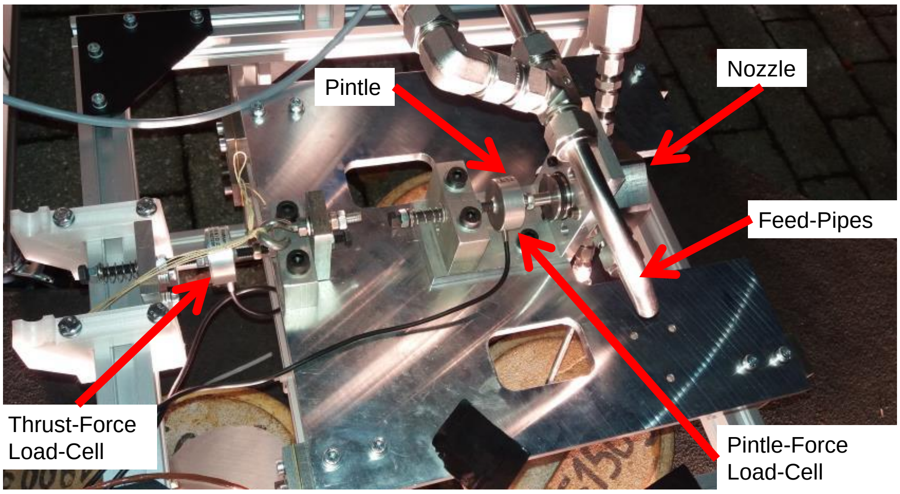

(a) Thrust Table (without Pilot-Valves)

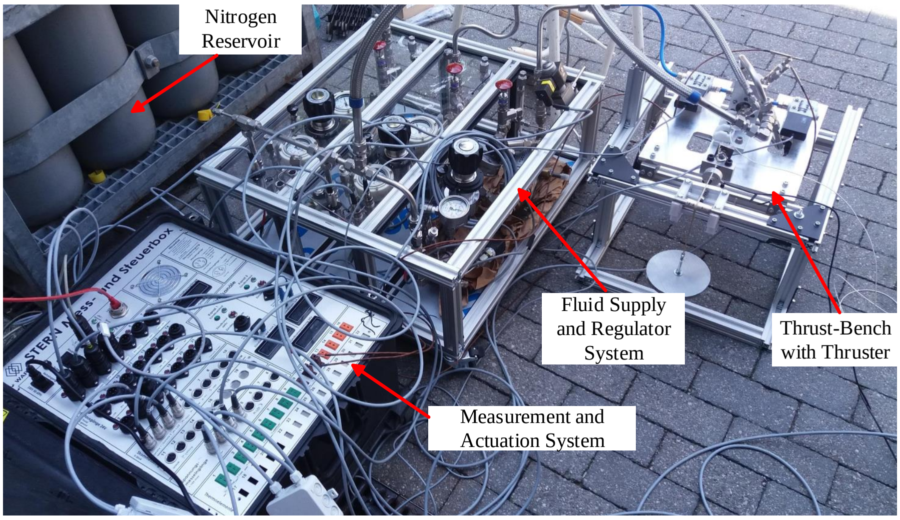

(b) Full Setup

Figure 5.4: Static Test Setup as assembled at the TU Munich

In total three test series were conducted. Each test series consists of a number of tests each at a different pintle position. The Δx is not the same for all test series and also not exactly the same throughout the test series, as it is very hard to precisely change the pintle position using the positioning screw. For the static test the pintle positions were manually measured using a vernier calliper. It should be noted that this method is not perfectly accurate and a measurement error of ± 0.02 to ± 0.03 mm is expected, see Ref. [16]. For each pintle position the automatic valve was opened and the forces and pressures were recorded for a about 1 s. The final results were obtained by computing the average over that time. As an example, the results from a single test are shown in Figure 5.5.

Table 5.1: Overview of the different Test Conditions (Values have been made dimensionless according to Table A.1)

	Test 1	Test 2 and 3
Date:	04-11-2016	01-06-2017
Gas Reservoir Pressure:	2.27 [-]	3.93 [-]
Regulator Setting:	$\approx$ 0.95 [-]	$\approx$ 1.0 [-]
Ambient Pressure:	962 hPa	966 hPa
Ambient Temperature:	8° C	25° C

The three test series were not conducted on the same day and therefore have different ambient conditions. The reservoir or bundle pressure is also substantially different. This has an effect on the pressure drop over the regulator. Moreover, a small error in the regulator setting of test series 1 was discovered, the pressure was slightly too low. The different parameters for each test series are summarised in Table 5.1.

5.2. Test Results

This section gives a brief description of the static test results of all three test series. A sample of the raw measurements for a single pintle position of the first test series can be seen in Figure 5.5. The data record starts shortly before the main valve is opened and stops shortly after closing. In total four different measurements were recorded. The thrust and pintle forces, the PCC pressure and the pressure downstream of the pressure regulator, but upstream of the automatic valve. The test setup also included a temperature sensor for the PCC, however its response time proved too slow to produce any useful response. Therefore, its data was not analysed and is not presented in this report.

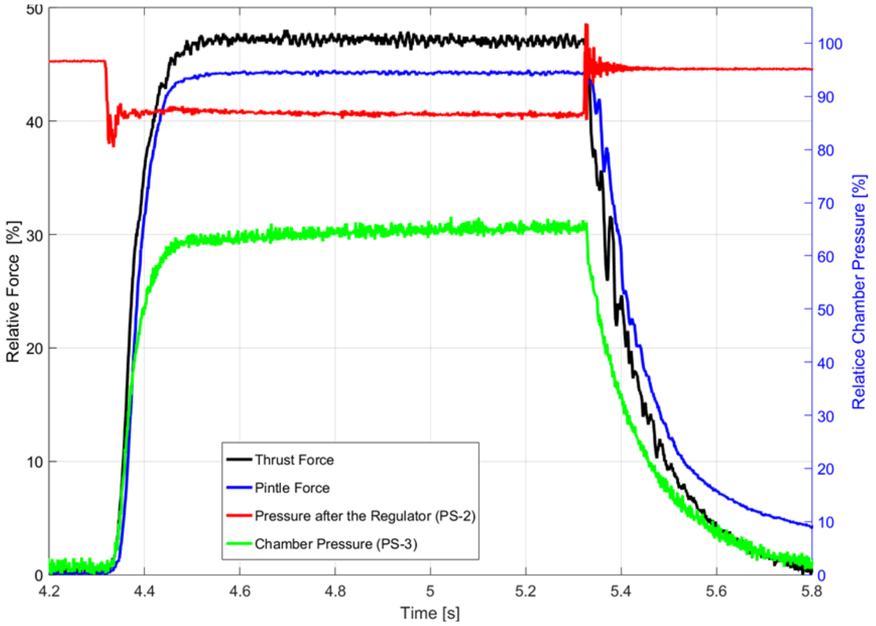

Figure 5.5: Measurement Data from Test Series 1 Test 13 (Values have been made dimensionless according to Table A.1)

The pressure just downstream of the regulator is represented by the red curve in Figure 5.5 and displays an interesting result. The curve initially shows the value that the regulator is set to (0.95 the reference pressure). Once the the main valve is opened the value drops and after a short transient settles at a value which is about 10% below the original setting. The value only jumps back to the intended setting once the automatic valve has been closed. This shows that the regulator is not capable of maintaining the static pressure, at higher massflows. The pressure drop increases the more the pintle is retracted (opened). Figure 5.5 shows the results for the fully retracted pintle position, thus the most extreme case.

Another notable anomaly is that the pressure in the PCC (green curve)is significantly below the regulator pressure (red curve). It would be expected that the PCC pressure is only slightly lower, due to the natural pressure drop in the feed-lines. However, a relative pressure drop of about 25% cannot exclusively be attributed to friction losses in the pipe. Therefore, it is believed that the flow in a single or multiple locations becomes sonic and the flow is chocked, which changes its properties. However, the diameters of the feed system have been sized such that in theory chocked flow should not occur. Prominent candidates for the chocked flow locations would be the T-piece splitting the main feed line and leading to the PCC inlets and the PCC inlets themselves. With the current setup it is however impossible to determine where exactly in the system these losses occur. As the pressure loss over the regulator, this loss increases the more the pintle is retracted (thus with increasing massflow). This is also visualised in Figure 5.6c where the combined pressure losses for all three test series are plotted.

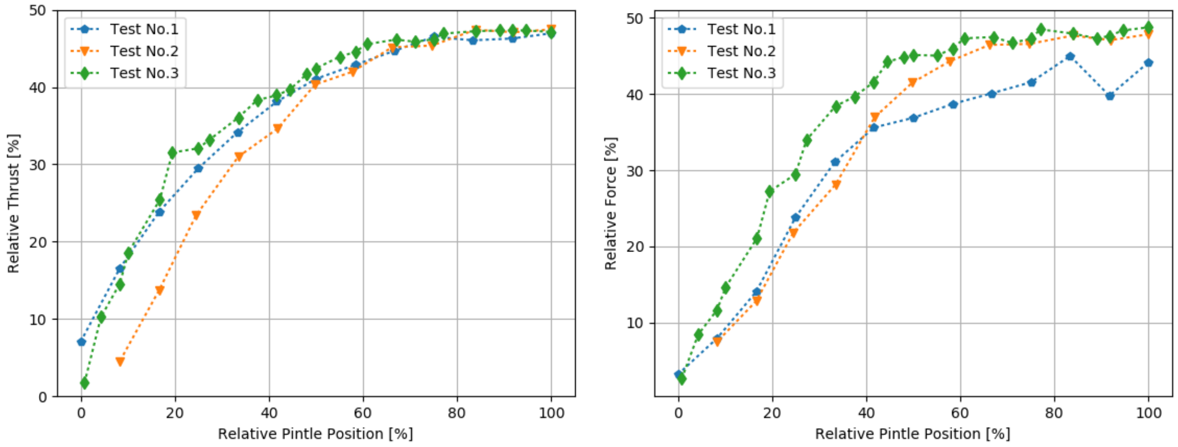

(a) Thrust (b) Pintle X-Force

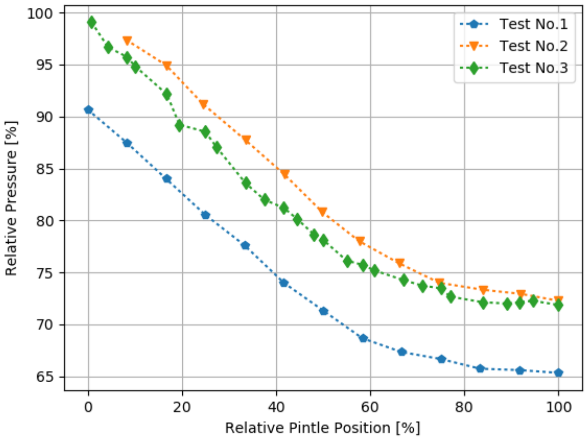

(c) PCC Pressure

Figure 5.6: Static Test Results, Series 1,2 and 3 (Values have been made dimensionless according to Table A.1)

The full results of all three static test series are displayed in Figure 5.6. Figure 5.6a shows the thrust results. As for all other force values, the results have been made dimensionless using the maximum obtained thrust of the 1D simulation, see Appendix A. The test results will later be compared to the simulation results, see Chapter 6.1.2. From this it is obvious that the results of the tests are significantly below the results of both the 1D and the CFD simulation. The maximum thrust is less then half of the 1D simulation thrust. The general shape of the test plots is the same as for all previous simulations, with the exception of a few outliers. It should be noted that for all three test-series the final/maximum thrust value is almost equivalent. This is surprising considering that for test-series one the PCC pressure is significantly lower, which should in consequence cause a reduction in thrust.

The measured axial pintle force for all three test series is plotted in Figure 5.6b. The general curve shape is again comparable to the simulation results. However, the curves features quite a number of discontinuities (zig-zag). The actual results are also lower than the simulation outputs, however their difference is far less significant compared to the thrust results.

The PCC pressure is depicted in Figure 5.6c. The results have been made dimensionless by the pressure used for the simulations inlet boundary conditions. This (for test series two and three) is the same as the pressure set at the regulator (see Table 5.1). Therefore, the results plotted in Figure 5.6c give an immediate indication of the pressure loss. As for the CFD simulations the pressure loss for the closed pintle positions is almost zero and increases the more the pintle is retracted. The test results however show a far greater pressure loss than the simulation results.

In general there are two surprising results of the static tests, firstly the significant pressure losses and secondly the low thrust values. However, it is believed that both these aspects can be attributed to the measurement and test setup and are not a property of the nozzle-pintle concept. The pressure losses have already been discussed above. It was concluded that they are mainly caused by chocked flow somewhere in the feed system of the test setup and to a smaller degree by the pressure regulator. Previously, it was observed that the thrust results seem to be independent of the pressure losses. The likely explanation for this is a problem in the thrust measurement procedure. As described in Section 5.1, the whole setup is mounted on a thrust table which is connected to a load cell. Thus in an ideal setup all axial loads would pass through the load cell and would thus be captured by it. However, a real setup usually has some additional mounting then the load cell. In the given test setup this mounting consist out of the four vertical brass flat-spring plates, which connect the thrust table and bench. These have a certain stiffness which however is compensated for by calibrating the load cell accordingly. Moreover, the stiffness is further increased by the solid pipes which connect the PCC inlets and the fluid supply system (see Figure 5.4). As these are solid circular pipes they naturally have a very high stiffness. Due to the high pressure it was however not possible to replace these pipes by more flexible hoses. Also their stiffness should in theory not matter as this is also taken into account when calibrating the load cell. However, the load cell is calibrated when the pipes are empty (at ambient conditions). Due to the nature of the chosen test setup it is not possible to perform the calibration while the system is pressurised. The high pressure in these pipes will significantly increase the stiffness of these pipes and reduce the measured force at the load cell. It is believed that this error together with the high pressure loss is responsible for a larger part of the thrust losses. It is however not possible to exactly quantify these losses or to exclude the possibility of other factors, that could potentially be responsible for these losses.

6. Analysis, Verification & Validation

This chapter contains the analysis of the simulation and test results and the verification and validation of the former. The chapter is split into two sections. The first section deals with the analysis of the CFD results and makes a comparison with the test data. The second part focuses on the analysis, verification and validation of the 1D simulation.

6.1. CFD Simulations

This section presents the analysis of the three separate CFD simulations. Firstly, the convergence issue will be discussed. Thereafter the cold-gas static CFD simulations will be analysed and the compared to the respective test result. Finally, the chimera simulation will be discussed and potential dynamic effects will be analysed.

6.1.1. Convergence Assessment and Verification

The DLR TAU-Code, which was used for all CFD simulations within this project, is a modern FVM viscous Navier-Stokes CFD solver. As most modern CFD codes it can be applied to a wide variety of flow types ranging from low-speed incompressible to compressible super- and hypersonic flows and has been verified by it creators for these flow types (see Refs. [29, 56]). Even though, the codes primary application is aerodynamics, so external flows, its has been successfully applied to internal flow problems. An example is a nozzle flow study carried out by the DLR, see Ref. [53]. Therefore a complete and independent verification, as part of this project is not necessary and will not be conducted.

However, within the course of this project multiple issues with the convergence of the CFD simulations have occurred. It is not believed that these issues are a major problem, nevertheless they should not be neglected. Therefore, they will be presented and discussed in the flowing sub-section. The problems mainly occurred in the static cold-gas and hot-fire simulations and will be presented in that order.

Cold-Gas Calculations

Anomalies were first discovered during the static cold-gas chimera calculations, the setup and results of which were presented in Chapter 4.3. The first notable anomaly is that all calculations had an unusual long run time. This was due to the high number of iterations required. Prior to this project the author conducted a number of CFD simulations with the DLR TAU-Code of an external flow problem. These simulations had an equally sized grid (similar number of nodes) and were also in the high supersonic flow regime. Compared to these simulations the nozzle-pintle simulations required between 10 to 100 times the number iterations. The long run time in itself is not a major issue. Nevertheless, it is notable especially considering the increase in the simulations run time from the usual couple of thousands or ten-thousands to a couple of hundred-thousand iterations. For reference 50 iterations required approximately 90 s of computation time. There are two reasons which are believed to be responsible for this issue:

1. As stated previously the DLR TAU-Code was primarily designed for external flow problems. Therefore, it is less robust than regular commercial codes (eg. Ansys Fluent), which are designed for both internal and external flows.
2. The suboptimal Mach number ($M = 0.01$) that was used to initialise the flow field. For details see Chapter 4.1.1. The velocity used to initialise the flow field is identical with the farfield boundary condition. Therefore large parts of the flow field are initialised with a Mach number very much different from the final solution.

The high number of iterations is not a real problem, only non-practical as each calculation takes much longer. More problematic is however when the simulations do not properly converge. To asses the convergence of a CFD simulations one usually monitors a couple of variables. Here the density residual, the force vector components plus the x-component of the pintle force, the massflows of the inlet and farfield boundary and the static pressure at the inlet boundary were used. For the definition of the density residual see Eq. 2.28 in Chapter 2.2.2. These are shown in Figure 6.1 for the 83.3 $\%$ pintle position, which is used as an example here.

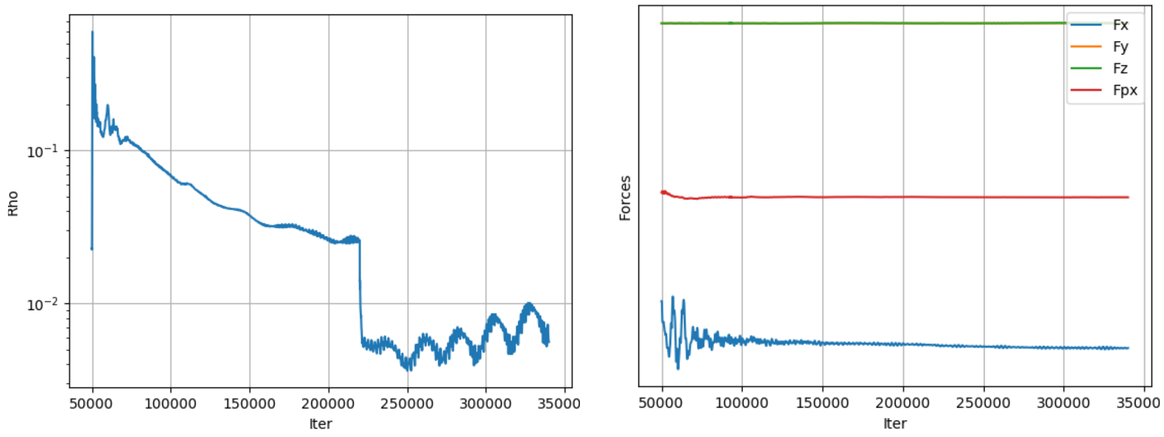

(a) Global Density Residual

(b) Forces

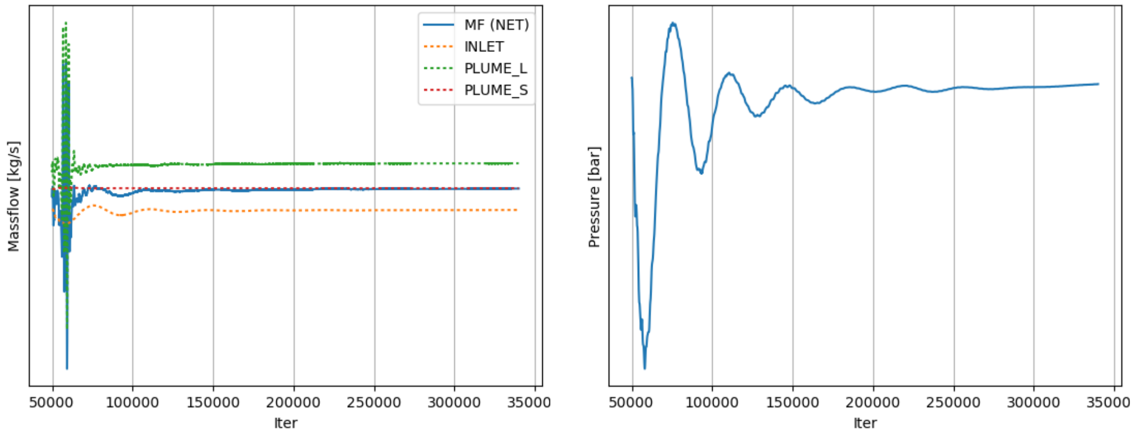

(c) Massflows

(d) Static Inlet Pressure

Figure 6.1: Convergence Behaviour Example of a Cold-Gas Static CFD Calculation (Dimensions have been removed from the Plot)

As stated in the solver setup description (Chapter 4.1.3), all steady state CFD simulations were first initialised using a first order upwind (van Leer) solver. After the results had sufficiently converged the simulation was restarted using the intended second order upwind AUSMDV solver. This took between 50,000 to 100,000 iterations. Figure 6.1 only shows the convergence behaviour for the second order calculations, hence the iteration number does not start at zero. Figure 6.1a shows the density residual on a log-scale. It initially starts to slowly decrease. At iterations 220,000 a sudden drop occurs, this is caused by the y^+ adaptation of the mesh. Thereafter it continues to decrease, however later it starts to oscillate with an increasing amplitude and increasing average. This is not desirable, as it potentially indicates that the numerical solution of the simulation (here specifically the solution of the continuity equation) is not converging or possibly even diverging for some parts of the solution.

However, while the density residual is slowly starting to diverge in an oscillating manner all solution monitors stay constant. The forces in Figure 6.1b are all unperturbed and at their intend values. The non-axial force components F_y (orange) and F_z (green) are both zero. F_x (blue) which is equivalent to the nozzle thrust has converged to a value which is within an acceptable offset to the 1D simulation result and to an additional verification calculation. The same holds true for the pintle x-force (red).

Inlet and outlet massflow have also converged to a verified value which further corresponds to the thrust result. Note, the outlet or farfield massflow is split in two components referred to as *PLUME L(arge)* and *PLUME S(mall)*. The latter defined as the inner half of the left hand side of the blue farfield cylinder shown in Figure 4.2. The former is the remainder of the farfield. The net massflow is also approximately zero. The static pressure at the inlet (see Figure 6.1d) has also converged to an acceptable value, which is slightly lower than the set total pressure boundary condition. Therefore, it can be concluded that all physical values have converged to an acceptable value. Only the density residual has not converged entirely. A similar behaviour was observed for the other pintle positions, a few positions did not show any issue and non had diverging physical monitoring values.

Initially, it was believed that the behaviour is due to suboptimal settings of the solver. Therefore, a number of test calculations were run with changed settings. Multiple different second order upwind methods were tested, all of them with an equal or worth results than the original AUSMDV method. The time discretisation method was changed from an implicit Backward-Euler scheme to an explicit Runge-Kutta scheme. This caused the performance to deteriorate further, which was to be expected as explicit schemes are in general less stable. The turbulence model was changed from the two-equation Menter-SST to the one-equation Spalart–Allmaras model. This had no effect. Moreover, some additional setting in the TAU-Code were altered, explaining those in further detail would go beyond the scope of this section. Nothing had any decisive effect. The only modification that would improve the behaviour of the density residual, was a change back to a first-order upwind solver. However, this was not acceptable as it has a potentially large influence on the accuracy of the solution.

The reasons for this behaviour are not entirely understood. A couple of theories which could explain this behaviour were developed:

1. Initially it was believed that the strong gradients present in the exhaust plume, especially in the shear layer, could be responsible. This would also explain why there is no visible influence on the chosen physical monitoring values. To confirm this theory the farfield cylinder was removed and the domain was terminated at the nozzle exit using a pressure outlet boundary, which was set to ambient conditions. However, this did not improve the density residual convergence.

2. Strong pressure gradients also exist in the entire nozzle, starting from its convergent section. The gradient is further increased in the presence of shocks. This high gradient will have negative influence on the density residual. The theory could neither be confirmed nor rejected. However, the fact that the convergence behaviour deteriorates the more the pintle is inserted does support this theory.

3. In the current setup the inlets directly oppose each other. This causes the high pressure inlet-streams to both imping with each other and on to the pintle. This could also lead to a very dynamic flow behaviour with strong gradients and could thus negatively influence the residual. Also this theory could not be confirmed or rejected.

The theories two and three could both explain the behaviour of the residual. However, it was not possible to find a single cause or mitigate the problem. Eventually, it was concluded that the issue can be neglected as long as the residual does not completely diverge and the physical solution values are not affected and converge to a verified value. This was the case for all regular cold-gas static CFD simulations. Therefore, there results were accepted as verified steady-state solutions.

Later on in the project further cold-gas static simulations were performed. They are essentially the same as the simulations presented in Chapter 4.3. The only difference is that the total pressure defined at the inlet boundary was lowered. The full results have not been presented hitherto. They were used in the detailed analysis and validation of the static CFD simulations and will be presented in the respective section in this chapter (see Section 6.1.2). During these simulations it was discovered that when the total inlet pressure at the boundary is reduced, additional instabilities in the convergence behaviour occur. As an example the monitoring values for the results of the static CFD simulation for the pintle mid position at reduced inlet pressure are presented in Figure 6.2. The inlet pressure was reduced to 0.713 that of the reference (original) pressure.

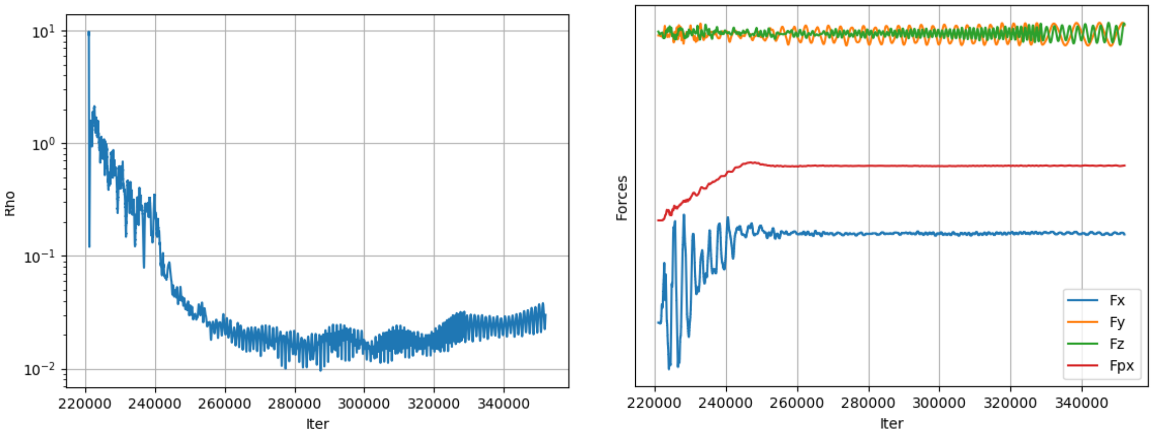

(a) Global Density Residual (b) Forces

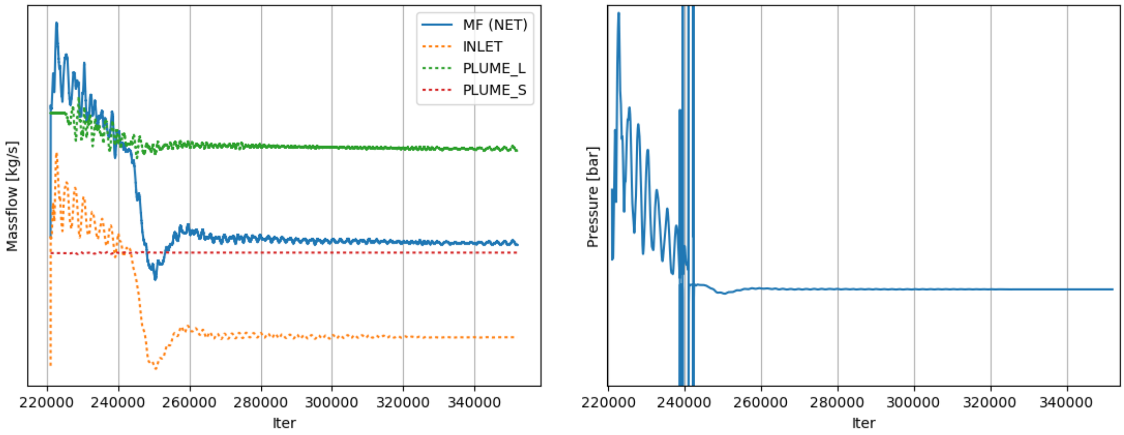

(c) Massflows (d) Static Inlet Pressure

Figure 6.2: Convergence Behaviour Example of a Cold-Gas Static CFD Calculation at lower Inlet Pressure (at approximately 0.713 of reference pressure) (Dimensions have been removed from the Plot)

The behaviour of the density residual (see Figure 6.2a) is similar to the previous case. It converges to a certain level, thereafter it slowly starts to increase again. As concluded above, this alone would be no reason for concern. However, now also the physical solution monitors are affected. The off-axis forces in Figure 6.2b start to oscillate with increasing amplitude around zero. The thrust force (blue curve) also oscillates around its solution value, but with a much lower amplitude. The same is true for the massflow values, see Figure 6.2c.

This means that the condition developed above, namely that the physical solution values should remain unaffected, no longer holds true. Therefore, an additional analysis was conducted. Based upon theories two and three presented above it was thought that the simulation might be too dynamic to be approximated by a steady-state CFD method. Moreover, it is common practice in CFD to switch to unsteady method if convergence cannot be achieved with a steady-state one. Hitherto, this had not been attempted, as it causes a severe increase in calculation time. For this the time stepping scheme was changed to an implicit dual time stepping scheme (Euler backward-difference) with a constant time step. In total 5 physical time steps were simulated, with a $\Delta t = 1$ ms. Each time step had 5000 inner iterations. The simulation was initialised using the final iteration of the steady-state results, shown in Figure 6.2.

The results of the unsteady CFD simulation are shown in Figure 6.3. The density residual (see Figure 6.3a) now converges and decreases without any major oscillations. Note, the residual shown here has been scaled by the starting value (final iteration of the previous steady-state results: 0.03002). Thus, the actual residual is much smaller than shown here. The oscillations previously present in the force values die out within two physical time steps, see Figure 6.3b. The same is true for the massflow values, see Figure 6.3c. The static pressure converges to a new value. However, this can be neglected as the absolute difference between initial and final value is extremely small (less than 0.01 bar).

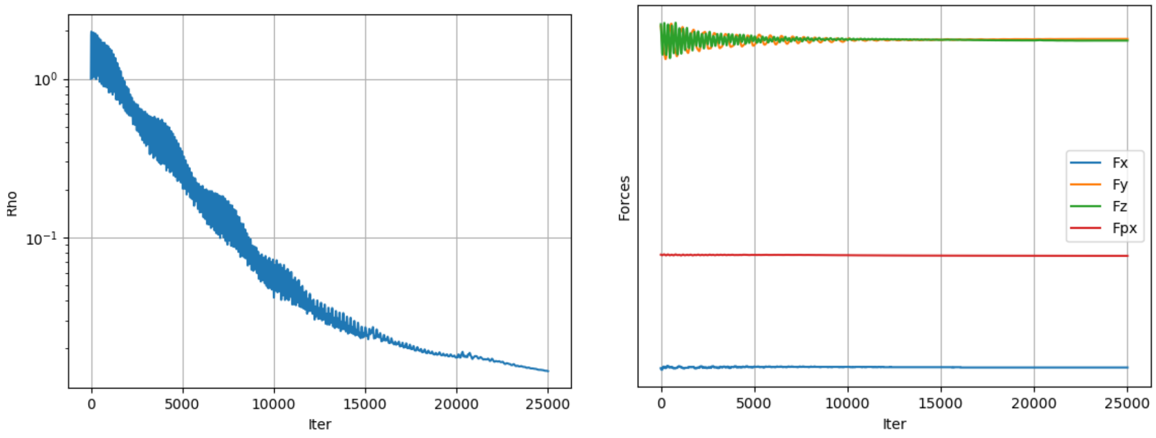

(a) Global Density Residual (b) Forces

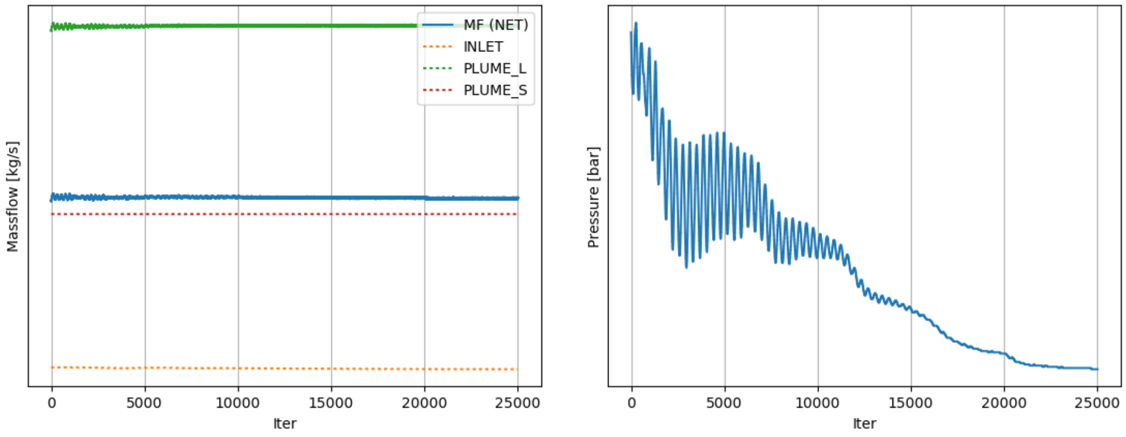

(c) Massflows (d) Static Inlet Pressure

Figure 6.3: Convergence Behaviour Example of an Instationary Cold-Gas Static CFD Calculation, initialised using the Final Iteration in Figure 6.2 (Dimensions have been removed from the Plot)

These results confirm the hypothesis made above. Essentially they confirm that the convergence issues do not represent any physical behaviour of the flow. They might be caused by a single or multiple physical aspect of the flow (see points two and three above), which one exactly is not understood but also not relevant. These aspects cannot be properly represented by the numerics of a steady-state solution and thus lead to numerical errors. The results in Figure 6.3 further show that the steady-state simulation will still give a good results as long as the oscillations are averaged out. Therefore, it is not necessary to use the more expensive unsteady approach for all calculations.

Hot-Fire Calculations

During the hot-fire calculations presented in Chapter 4.5 an additional anomaly in the convergence behaviour was discovered. The massflow at the large farfield section (PLUME L) converges to a value that is physically impossible. Normally the value should be approximately the same magnitude as the inlet massflow, but of opposite sign. In case of the original hot-gas simulation, it was more than ten times the magnitude and had the same sign as the inlet massflow. For reference, see the initial value of the green curve in Figure 6.4b.

To investigate the phenomena it is advisable to take a closer look at the flow in the farfield of an example case. This is shown in Figure 6.5a. Here three noteworthy effects can be observed:

1. Close to the left hand border of the farfield in Figure 6.5a something which looks like a rotating source pair can be observed. Of course this is not an actual source, but the 2D cut through a 3D flow phenomena. A similar phenomena, with only a single source, has been observed when looking at the inlet flow in the XY-plane. It indicates a strong flow in the direction perpendicular to the viewed plane. As the pair is rotating in an opposite directions, the plume is possibly surrounded by some kind of ring flow.

2. A vortex pair is visible in the right part of the farfield section in Figure 6.5a. Such effects have been observed previously within this project, but were not shown in this report as they had no effect on other solution variables. Therefore, it is believed that they are not in direct relation to the strange outlet massflow.

3. The nozzle exhaust plume in Figure 6.5a is distorted. It shows unusual bulges. These are likely caused by the effects described in point one.

It is highly likely that the offset in the outlet massflow is due the phenomena described in point one. The phenomena causes flow sucked in from outside the farfield boundary and would thus be responsible for the large massflow into the domain.

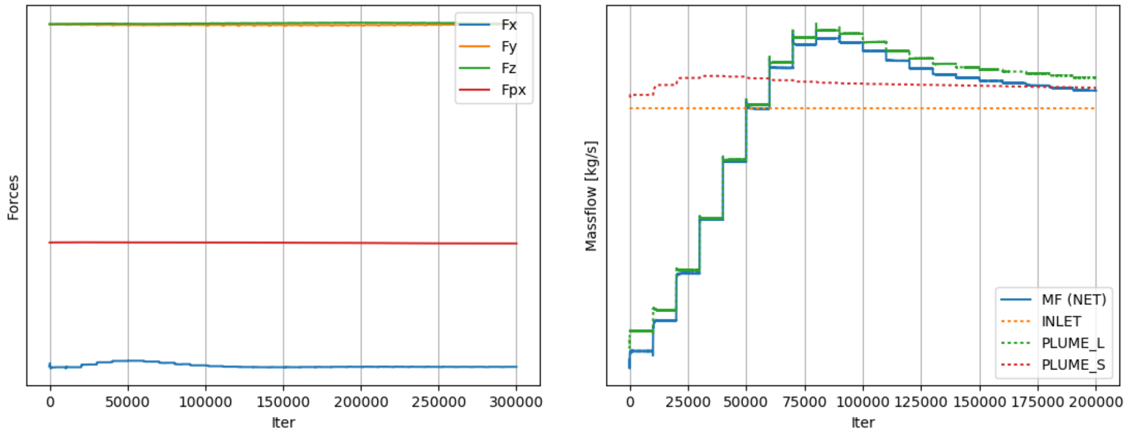

(a) Forces

(b) Massflows

Figure 6.4: Convergence Behaviour Example of an Instationary Hot-Fire Static CFD Calculation, initialised on an instable Stationary Calculation (Dimensions have been removed from the Plot)

The above explanation does not answer whether the effect is an actual physical effect or only a numerical error in the steady-state solution. The former is believed to be unlikely. To verify this theory a similar procedure as before was used. Using the final iteration of the steady-state simulation as the initial starting condition an unsteady simulation was created. The simulation was run for a total of 30 physical time-steps, each with a $\Delta t = 0.05$ ms and with 10,000 inner iterations each. A contour plot of the final results is shown in Figure 6.5b. The source pair has disappeared entirely. The exhaust plume is no longer distorted and the vortex pairs has moved a little bit downstream. The other results are shown in Figure 6.4. The massflow eventually normalises and converges to a plausible value, see Figure 6.4b. The initial and final force values are equivalent, see Figure 6.4a. Therefore, the effect seems to be purely numerical. Moreover, it does not seem to influence the primary results of the CFD simulation (thrust and pintle-force).

The cause for this numerical error is unknown. One possible explanation is that the farfield domain was not big enough. This could cause interactions between the hot plume expanding into the ambient and the farfield boundary. Due to time constraints this theory was not investigate further. Even though the error does not influence the primary results of the simulation, it still distorts the exhaust plume. Therefore, all hot-gas results presented in Chapter 4.5 and B.3 have been generate using an unsteady time stepping scheme.

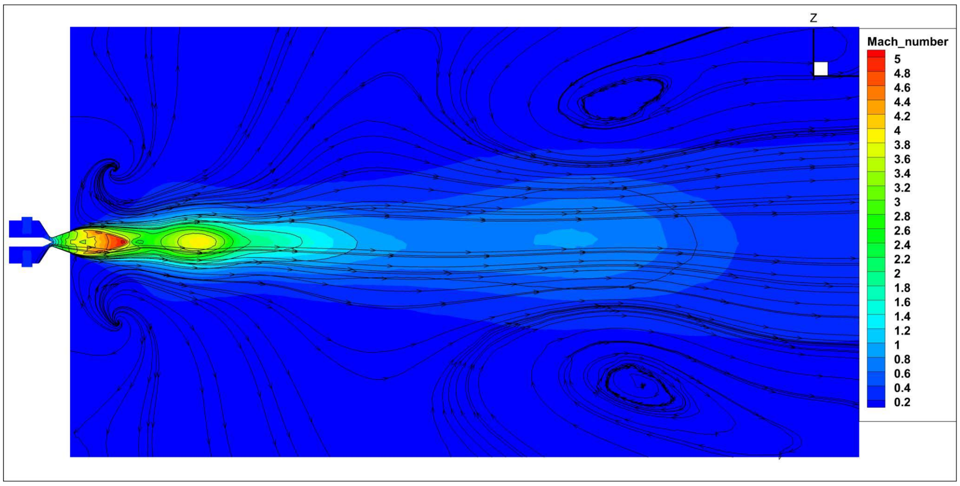

(a) Stationary (Oscillating)

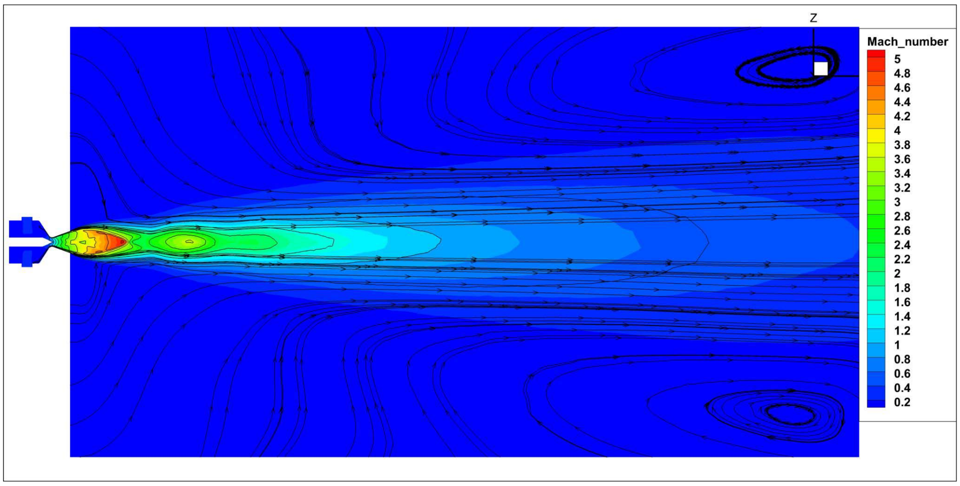

(b) Instationary (Converged)

Figure 6.5: Mach Number Contour Plot (XZ-Cut) including Streamlines, to visualise Eddies in the Nozzle Plume

6.1.2. Static Simulation

The goal of this section is to compare and validate the cold-gas static CFD simulations with the test results presented in Chapter 5. The hot-gas simulation cannot be validated in this way as no test data exist. Therefore, it is excluded in this section.

As the test data from series 1 was conducted with a faulty regulator setting and has an error in the pintle force measurement, it will be excluded in the initially analysis. Figure 6.6 compares the CFD results (thrust and pintle force) with the test data from series 2 and 3. Figure 6.7 compares the relative and absolute differences of the CFD and test results. From 0 % to about 20 % the thrust test results of test 3 are a good match (both relative and absolute) with the results of the CFD simulation (see Figure 6.7b). The results of test 2, see Figure 6.7a do not match that well. Above the 20 % pintle position the thrust test results start to level of while the CFD results keep increasing. Therefore, the differences between the two results keep increasing until the thrust max. position. Here the relative difference with both test results is almost 50 %, which is very high.

In general the pintle forces are a better match, see Figure 6.6b. However, here the tendency is reversed and test 2 is a better match than test3. For test 2 the relative difference has a maximum of approximately 20%. For test 3 the relative differences in the first half is much worse, as the test results actually lie above the CFD results. In the second half both test results have a comparable difference to the CFD results. Also the absolute difference for both test results is comparable. Note, both for thrust and pintle force the relative difference near the 0 % pintle positions is very high. This is due to the fact that the absolute difference is very small and one of the two results is close to zero. This is negligible as long as the absolute difference remains small.

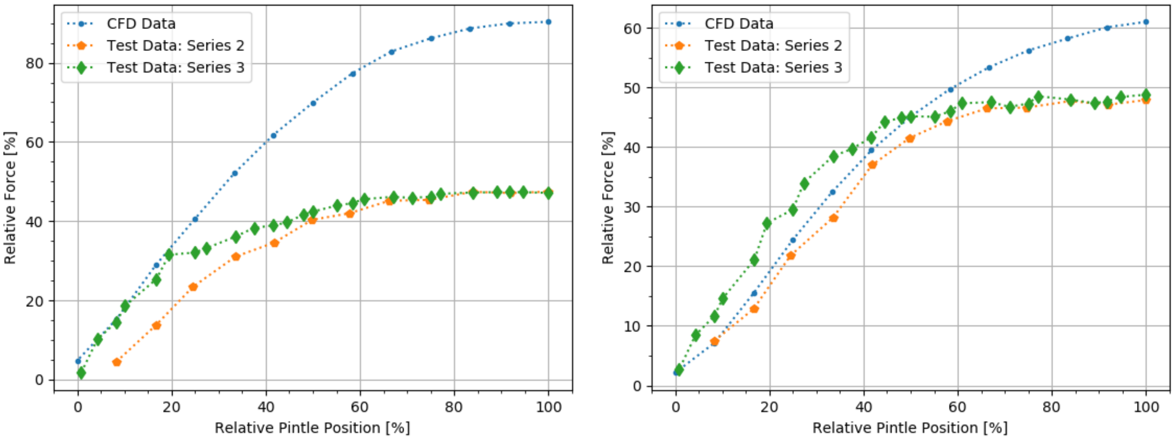

(a) Thrust (b) Pintle X-Force

Figure 6.6: Direct Comparison between Static CFD Results and Test Results from Series 2 and 3 (Values have been made dimensionless according to Table A.1)

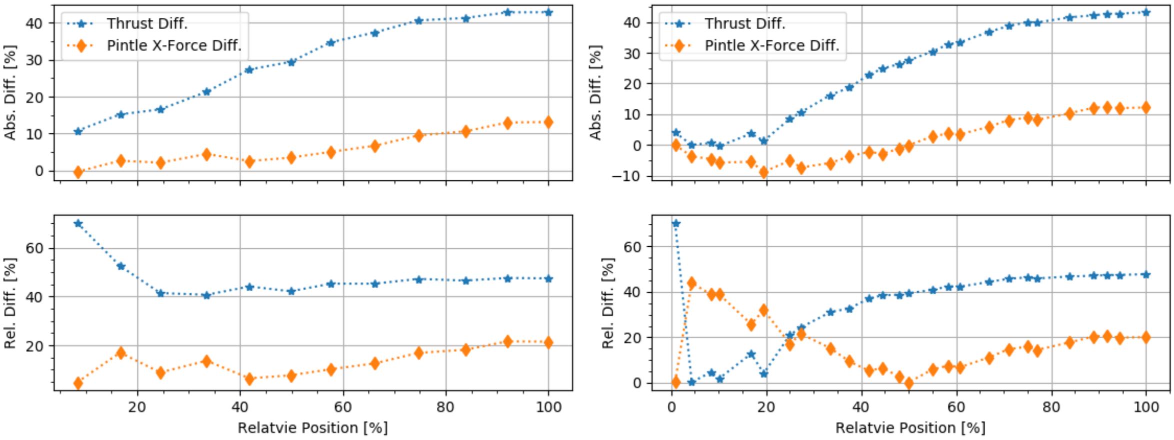

(a) CFD vs. Test Series 2 (b) CFD vs. Test Series 3

Figure 6.7: Relative and Absolute Differences between Static CFD Results and Test Results from Series 2 and 3 (Values have been made dimensionless according to Table A.1)

The difference between the test and CFD results is significant. This is especially true for the thrust results. It is believed that a large portion of these differences are caused by two errors in the measurement and test setup. These were already discussed at the end of Chapter 5.2 and are briefly repeated here:

1. The solid pipes feeding the gas from the fluid supply system into the PCC have a certain stiffens. This stiffens is accounted for by calibrating the system with a series of known loads. The stiffens of these pipes is further increased as soon as they are pressurised. However, due to the nature of the test setup it is impossible to calibrate the system while under pressure. Therefore, the pressure component of the stiffens leads to an error in the thrust measurement. The magnitude of this error is unknown. This would also explain why the measured pintle force is partially higher than the measured thrust. Normally the pintle force should be lower as it is component of the thrust. The error has no effect on the pintle force measurement. It is believed that this is the reason why the thrust error is much larger than the pintle force error.

2. There exist a severe pressure drop in the fluid supply system. Its believed that the drop is caused by loses in the regulator and chocked flow further downstream. Therefore, the static pressure at the PCC inlet in the test is significantly lower than in the CFD simulations. The max. relative difference in inlet pressure for tests 2 and 3 is approximately 25 %, for test 1 it is even larger. For details compare Figures 5.6c and 4.16d. This will greatly reduce both the thrust and pintle forces in the test.

The issue outlined under point 1 cannot be resolved without reconstructing the test setup such that it can be calibrated while pressurised. This is not possible as part of this project. However, the issue described under point 2 can be accounted for by modifying the static CFD simulation. The inlet boundary condition of the CFD simulation can be modified such that they are equivalent to the measured PCC pressure in the test. Thereafter, the simulation is rerun for each pintle position with the modified pressure setting. This was done for the imperfect test series 1 only. Test Series 2 and 3 where only completed on the 01-06-2017. However, thereafter no sufficient time and computational resources were available to repeat the simulations to match the test series 2 and 3 conditions.

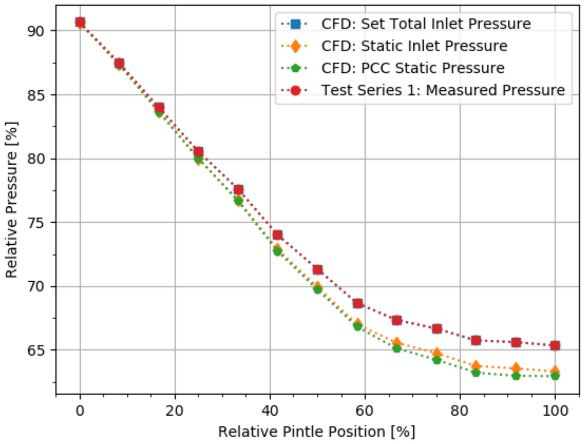

Figure 6.8: Pressure Settings for CFD Results with modified Total Inlet Pressure, to match Pressures measured in Test Series 1 (Values have been made dimensionless according to Table A.1)

The pressure settings for the modified CFD simulations are shown in Figure 6.8. Here the red curve represents the measured test data and the blue curve the set total pressure at the inlet boundary. The two curves match each other. The orange and green curves show the actual static pressure achieved during the simulation at the inlet and the PCC respectively.

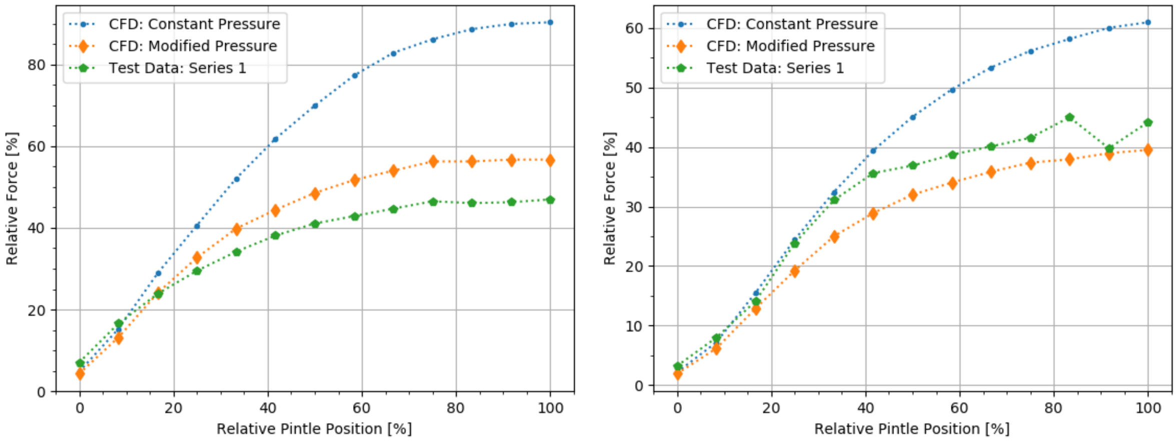

(a) Thrust (b) Pintle X-Force

Figure 6.9: Direct Comparison between Static CFD Results with modified Total Inlet Pressure and Test Results from Series 1 (Values have been made dimensionless according to Table A.1)

The primary results of the CFD simulation with modified pressure are plotted together with the test series 1 results and the regular simulation in Figure 6.9. The thrust results of the modified simulation are a much better match with the test results. The results are however still not perfect as the test results still level of earlier. The pintle force match is also significantly improved, see Figure 6.9b. However, the CFD results are below the test results and between the 20 % and 40 % pintle position the regular CFD simulation gives a better match.

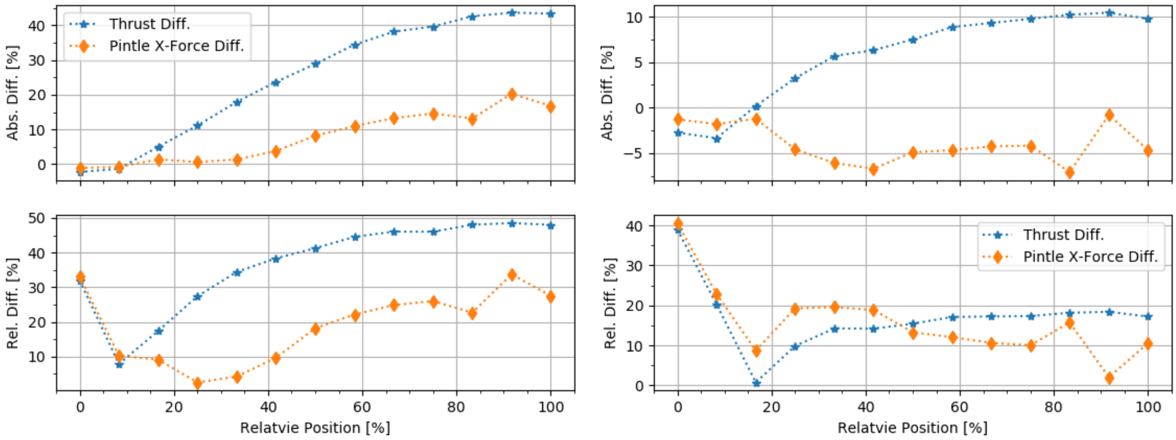

(a) Regular Pressure (b) Modified Pressure

Figure 6.10: Relative and Absolute Difference of Static CFD Results with modified and regular Total Inlet Pressure and Test Results from Series 1 (Values have been made dimensionless according to Table A.1)

The above is confirmed when analysing the absolute and relative differences for the regular (Figure 6.10a) and modified (Figure 6.10b) with the test results. The differences for the CFD simulation with regular pressure are only a little bit worse compared to the differences with test 2 and 3 (see Figure 6.7). This is to be expected, due to the lower inlet pressure in test 1. The differences for the CFD simulation with the modified inlet pressure are significantly reduced. Except for the first two data points the relative differences for the thrust and pintle forces are below 20%. This is an improvement by about 30 % and thus confirms the issue presented under point 2 above, namely that the pressure drop in the fluid supply system of the test setup is responsible for a major part of the differences between test and CFD results. The difference for the pintle force was also reduced, however only for pintle positions above 50 %. For pintle positions below that the relative difference has actually increased. The reason for this behaviour is unclear. One possibility is an error in the CFD simulation which causes an under-prediction of the pintle force. A second possibility is an unknown problem (not point 1 or 2 above) of the test and measurement setup that influence the pintle force measurement of test 1. The second option is very plausible. When comparing the pintle force measurement of all three tests (see Figure 5.6b), it can be seen that only the results of test 1 show a strange behaviour beyond the 40 % pintle position.

In general the comparison of the test and CFD data is not entirely satisfactory. The test data confirms the overall behaviour of the pintle force. Both thrust and pintle force initially increase in an almost linear fashion and after some time the gradient starts to level-off. For the thrust curve the gradient eventually becomes zero, while the pintle force gradient keeps increasing. Therefore, the tests confirm the overall theory and the general behaviour of the CFD results. However, the actual test results differ significantly from the CFD simulation, both relatively and on an absolute scale. This difference is too significant to claim that the static CFD simulation is validated with these test results. It is very likely that the differences are largely caused by problems in the test setup. To fully confirm this the test setup would have to be completely redesigned and a series of new test to be conducted. Moreover, the CFD simulations with modified pressure should be repeated for the measured pressures of test 2 and 3, especially considering the strange behaviour of the pintle force in test 1 (see Figure 5.6b). Until then it is not possible to claim full validation of the static CFD simulation.

6.1.3. Chimera Simulation & Dynamic Effects

This section deals with a further analysis of the chimera simulation and potential dynamic effects that might occur when inserting or retracting the pintle, which cannot be capture by the static CFD simulation. The method and results of the chimera simulation have already been presented in Chapter 4.4.

A separate verification of the chimera methods is not required as the general approach has already been verified by numerous other researchers and institutions. Also the implementation of the concept within the TAU-Code has already been verified. For details on the Chimera method, see Chapter 2.2.5. A dedicated validation of the simulation is not possible as no corresponding test data exists. Therefore, the analysis here can only be based on an assessment of results presented in Chapter 4.4.2.

A preliminary analysis during the presentation of the chimera result found two potential dynamic effects:

1. There exist a clear difference in terms of pintle positions for the flow separation and subsequent reattachment. When the pintle is inserted the flow separates from the nozzle at a lower pintle position and expands to a lower pressure. In contrast, when it is retracted it reattaches only at a higher position and at a higher pressure. This effect is best visible in Figure 4.30a. The same effect can be observed for flow separation and reattachment from the pintle wall, see the middle section Figure 4.28a. However, here the difference in position is very small such that it is indistinguishable in the position plot in Figure 4.30a. In fact, the difference is so small that it is of the same order of magnitude as the pintle Δx between two time-steps. Therefore, no definitive conclusion can be drawn on the pintle flow separation effects.
2. Transient behaviour can be observed at the beginning and at the end of the chimera simulation, so when the pintle is near its maximum position and is just starting or about to stop its movement. The effects are most strongly visible in the static inlet pressure (see Figures 4.28d and4.30d) and the PCC pressure (see Figure 4.30e), but also in all other primary and secondary results. The effects are visible in both chimera simulations, however they are more distinct in the calculation with the smaller time step. For the calculation with the wider time step they only show properly in the inlet and PCC pressure and are hardly visible in the other variables (see Figures 4.27 and 4.28).

The effect described under point 1 is a hysteresis effect. Such effects are not uncommon in aero- and fluid-dynamics. Most aerofoils show this behaviour for flow separation and stall. When the angle of attack is increased the flow stays attached until a certain angle of attack. However, when the angle is again decreased the flow only reattaches much later. Mathematically speaking, there exists no unique solution of the Navier-Stokes equation for such flows. The solution is bifurcated. This can be the case when backward flow and/or flow separations occur. For the mathematical details of this effect see Schlichting [42]. In the analysed case the effect is very small, the difference in pintle position for separation and reattachment is only between 1 - 2 $\%$. For reference see Figure 4.30a and compare the contour plots of the separation points in Figure B.14d versus B.14n and Figure B.14d versus B.14m.

The transient effects described in point 2 are less clear. The transients are most visible in the inlet and PCC pressure readings. Therefore, one possibility is that they are caused by the moving pintle. Once the pintle starts to move forward the volume in the PCC starts to increase this would cause a pressure drop at the inlet and in the PCC. At the same time the throat diameter is being reduced. However, according to ideal rocket theory (see Chapter 2.1.1 Eq. 2.6), this causes an increases in combustion pressure. These two effects oppose each other and could therefore be responsible for the small initial oscillations in inlet and PCC pressure. The oscillation in chamber pressure will also cause an oscillation in the massflow and in consequence will also influence the thrust and all other parameters. It is notable that the oscillations only occur at the very beginning and at the very end of the simulation. In both cases the pintle velocity is slow, see Figure 4.26b. This can be explained in two ways. It could be possible that the oscillations dampen out after some time or simply do not occur at higher pintle speeds. The second option is that the time step in the simulation is not sufficiently small to resolve any oscillations at higher pintle speeds. The latter option is supported by the fact that the oscillations are stronger in the simulation with the smaller time step ($n =$ 240). However, non of the above explains why the the initial PCC pressure in different than the final PCC pressure (see Figure 4.30e).

The issue of the time step size was already highlighted during the discussion of the chimera setup and results, see Chapter 4.4. The fact that the results of the two simulations at different time step size indicate that the time step might be too large. To assure that all dynamic effects are captured the time step should be reduced further until two consecutive simulations match each other. Only than one can claim that the time step selection is sufficiently small. This could not be done in the project due to a lack of time and the high computational resources that such calculations demand. For the same reasons the number of iterations per time steps were reduced possibly even below an acceptable level. The number of iterations per time step should be increased to a level at which it can be assured that each time step has sufficiently converged before jumping to the next time step. Only after these two requirements have been achieved it is possible to give a definitive answer regarding the transient effects described above. Moreover, only then one can be sure that no other dynamic effects, which possibly have not shown themselves here, are present. Furthermore, only then the possibility that the transient effects under point 2 are actually physical effects and not a numerical error caused by an un-converged solution can be excluded.

However, it should also be kept in mind that the effects described above are all comparably small. The hysteresis effect only alters the separation and re-attachment position for the nozzle by about $1-2\%$. Moreover, the effect is completely invisible when only looking at the primary results. The conciliations in the inlet and PCC pressures are also very small especially when viewed on an absolute scale and also they have hardly any influence on the primary results. Therefore, one could conclude that the dynamic effects observed are sufficiently small to be neglected and a static simulation of the thruster would have been entirely sufficient. However, this can only be concluded with absolute certainty when the time-step issue described in the paragraphs above have been successfully resolved.

6.2. 1D Simulation

This section deals with the analysis of the 1D simulation and its results originally presented in Chapter 3. To verify the results of the 1D simulation, the results of the CFD simulation will be utilised. The 1D simulation approximates the flow in the nozzle as quasi-one-dimensional inviscid flow. It therefore neglects all viscous losses, flow separation and multidimensional effects etc., for details see Chapter 3.1.1. To asses whether the 1D simulation is sufficiently accurate for a future preliminary design of a nozzle-pintle application it is compared to the results of the static CFD simulation. This is done for both the cold-gas and the hot-fire case, starting with the former.

6.2.1. Cold-Gas Case

The results of the cold-gas 1D simulation were originally presented in Chapter 3.2 and again together with the static CFD simulation in Chapter 4.3.2. For better and quantitative comparison the absolute and relative differences for the thrust and pintle force results of the 1D simulation and the static CFD simulation have been plotted in Figure 6.11.

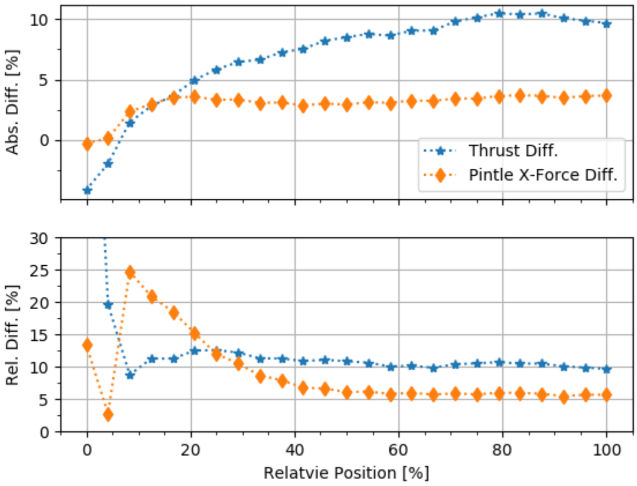

Figure 6.11: Relative and Absolute Difference of Static CFD and 1D Simulation Results(Values have been made dimensionless according to Table A.1)

The absolute difference in thrust ranges from approximately -4 % at the pintle min. position (the 1D simulation is under-predicting the thrust, hence the minus) to +10 % at the max. pintle position (here the thrust is over-predicted). The absolute difference in pintle force is less and ranges from approximately ±0 % to slightly below +4 %. The relative differences of thrust and pintle force for the positions close to the minimum positions are much larger. The initial relative difference is with ca. 86 % of the chart in Figure 6.11. This is due to the fact the thrust predicted by the 1D simulation is very close to zero, while the the CFD simulations still predicted a small thrust. The high relative difference can however be neglected considering that the absolute difference is still very small. The same, but less extreme holds for the relative difference of the pintle force. Beyond the pintles 40 % positions both relative differences remain roughly constant. The relative thrust difference is between 10-11 % and the relative pintle force difference approximately 6 %. Note, the points from which the relative differences remain constant corresponds to the point beyond which no more flow separation occurs.

The differences between the 1D simulation and the CFD simulation is partly caused by various viscous losses, such as friction and the effectively narrower throat due to the presence of the boundary layer. However, in addition to that their exist a certain pressure loss. The 1D simulation assumes a constant PCC pressure. The CFD simulation also predicts the pressure loss inside the PCC. The pressure loss or drop is shown in Figure 4.16d, which shows the static pressure at the inlet and the PCC for all pintle positions. For the pintle max. position this pressure loss is approximately 4%. To characterise the error in the 1D simulation that occurs due to the neglect of this pressure loss, a pressure correction method was implemented in the 1D simulation. The pressure correction was set as such that it resembles the pressure loss of the CFD simulations. The full results of this 1D simulation with modified pressure together with the original CFD results are shown in Figure 6.12. The pressure correction is depicted in Figure 6.12f, where the 1D inlet/PCC pressure exactly matches the CFD PCC pressure. In general it can be seen that the match between the CFD results and the updated 1D results is much closer, compared Figures 4.15 and 4.16 versus Figure 6.12. The thrust, pintle force and massflow results are now an almost perfect match. However, the nozzle exit pressure now matches less well, as the 1D simulation now under-predicts the exit pressure even further.

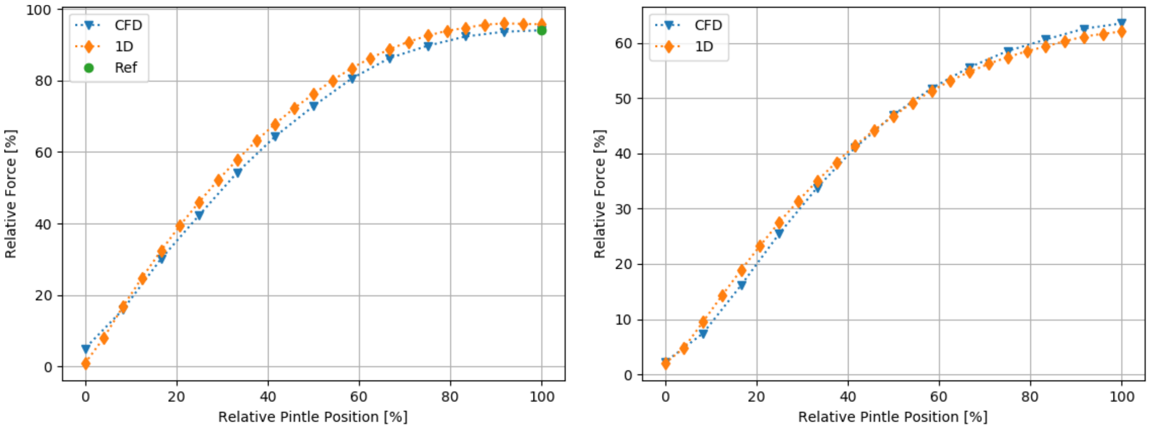

(a) Thrust (b) Pintle X-Force

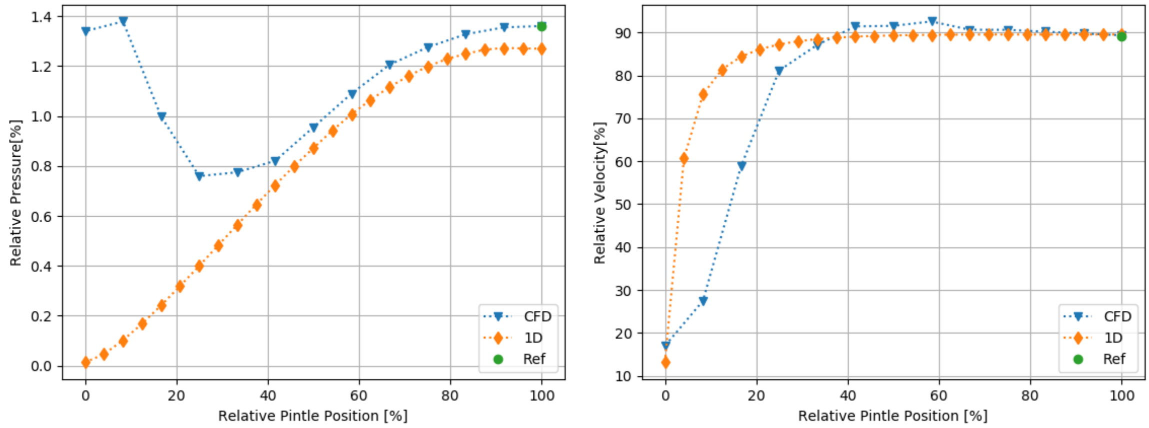

(c) Exit Pressure (d) Exit Velocity

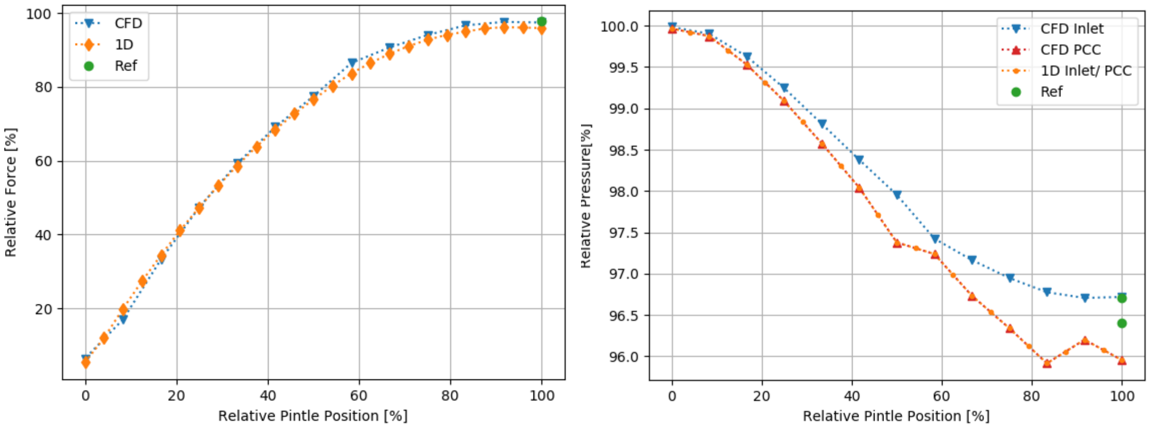

(e) Massflow (f) Inlet Pressure

Figure 6.12: Cold-Gas CFD Results versus 1D Simulation Results with adapted Inlet Pressure (Values have been made dimensionless according to Table A.1)

To asses the absolute and relative difference between the primary results of the modified 1D simulation and the static CFD simulation, the values were plotted in the same manner as previously, see Figure 6.13. The absolute differences have decreased. The thrust difference now ranges form -4 % to a little above +6 %. The pintle force difference is initially approximately $\pm 0\%$ than it rises quickly to around +4 % and thereafter drops slowly to around +1 % at the pintle max. position. The relative differences from the 0 % to the 40 % pintle position, where flow separation occurs is very similar to the previous case. However, thereafter they do no longer stay constant but keep declining until the pintle max. position. The relative thrust difference declines from ca. 10 % to ca. 5.7 % and the relative pintle force difference from about 5 % to 1.7 %.

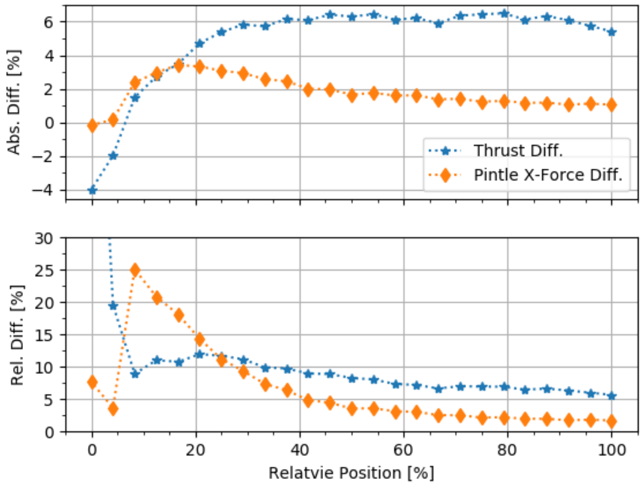

Figure 6.13: Relative and Absolute Difference of Static CFD Results and 1D Simulation with adapted Inlet Pressure (Values have been made dimensionless according to Table A.1)

From the above it is possible to draw a number of conclusion regarding the errors in the 1D simulation:

1. From 0 % to the 40 %, so at the pintle position where the flow is partly or entirely separated from the nozzle and in parts also the pintle wall, the error of the 1D simulation is quite high. In this area the error caused by the neglect of the flow separation effects is defiantly dominant.
2. Beyond the 40 % pintle positions other factors dominate the error (pressure and viscous losses). Around the 40 % positions the relative differences between the static CFD and the 1D simulation with and without pressure correction are almost equal. Thus the error due to the pressure loss is small in this region (compare Figure 6.11 vs. 6.13). This is to be expected as the pressure loss at this pintle position is still small, see Figure 4.16d. However, at the pintle max. position the pressure loss is responsible for about half of the error in the original 1D simulation.
3. The remaining error in the 1D simulation is largely caused by the viscous losses. The viscous loss appears to be decreasing towards the higher pintle positions. It can be split into two components:
    (a) The loss due to friction. This reduces the exit velocity and thus reduces the thrust. It should reduce the further the pintle is retracted beyond the throat.
    (b) The loss due to the presence of the boundary layer. This causes an effective reduction in the nozzle throat diameter and thus the cross-sectional area. This reduces the massflow and thus the thrust. This error reduces with increasing throat area and thus also as the pintle is retracted.

    The final viscous loss in thrust when the pintle is fully retracted is 5.7 %. This is about twice the viscous thrust loss of an ordinary nozzle, which is around 2 % see Ref. [2]. The higher viscous loss can however be explained by the presence of the pintle. Moreover, the nozzle-pintle configuration simulated for this project is rather small. Smaller nozzles usually have an increased viscous loss, as the loss due to the boundary layer is much greater for nozzles with small throats (see Ref. [2]).

In general the errors in the 1D simulation are at an acceptable level. Beyond the 40 % pintle position the error in thrust lies between 10 to 11 % without pressure correction. If pressure correction is introduced the error can be halved. The error for the predicted pintle force is significantly less. Therefore, the 1D simulation can be considered verified and there is no objection with respect to its use for the preliminary design of a DACS or any other nozzle-pintle application. Moreover, the simulation almost always over-predicts the thrust and pintle force. This is actually an advantage when using it to size the pintle actuator or the structure and materials of the system.

The 1D simulation could be improved by implementing a more permanent approach of taking into account the pressure loss. Furthermore, a criterion to predict the flow separation position should be included. For the current case the Summerfield criterion, which is the most rudimentary one, gave a decent prediction of the separation position,see Chapter 4.3.2. This way the pintle position below which the 1D simulation becomes less accurate can be immediately predicted without the need for an expansive CFD simulation.

6.2.2. Hot-Fire Case

When using the 1D tool to simulate an application using rocket propellant (hot-fire) to generate the necessary thrust. Two additional errors occur. A hot-gas can have a significant variation in its specific heat-ratio γ and gas-constant R. Therefore, it no longer behaves like an ideal-gas, but has to be treated as a real-gas. It is also possible that the hot exhaust gases keep reacting in the PCC and the nozzle. This would cause an additional error. However, this latter error cannot analysed here, as the CFD simulation also neglects any chemical reactions.

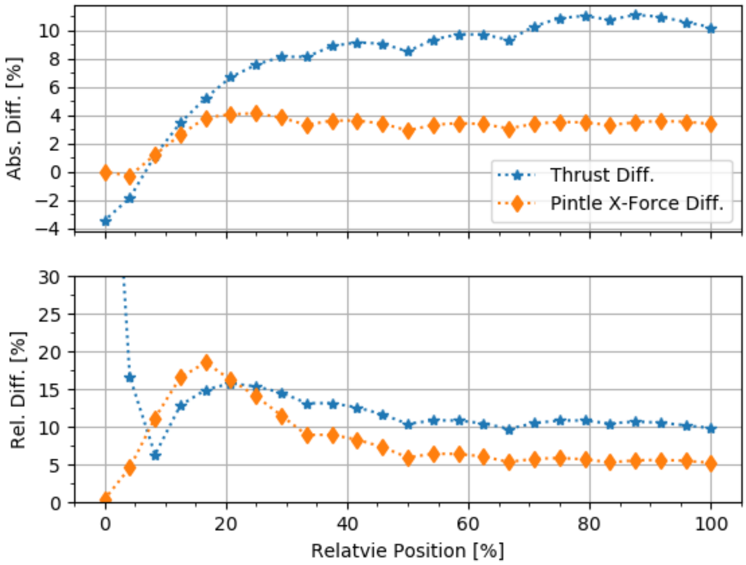

Figure 6.14: Relative and Absolute Difference of Static Hot-Fire CFD and 1D Simulation Results(Values have been made dimensionless according to Table A.1)

To asses the error, which is caused by the neglect of the real-gas effects in the 1D simulation, the absolute and relative differences between CFD and 1D simulation are compared in the same style as previously (see Figure 6.14). The full hot-gas results for both simulations have been presented previously in Chapter 4.5.2 in Figures 4.31 and 4.32. Essentially the differences are almost the same as previously, compare Figures 6.14 vs. 6.11. The difference is only marginal and can basically be neglected. In parts of the flow separation region the relative differences is even lower than for the cold-gas case.

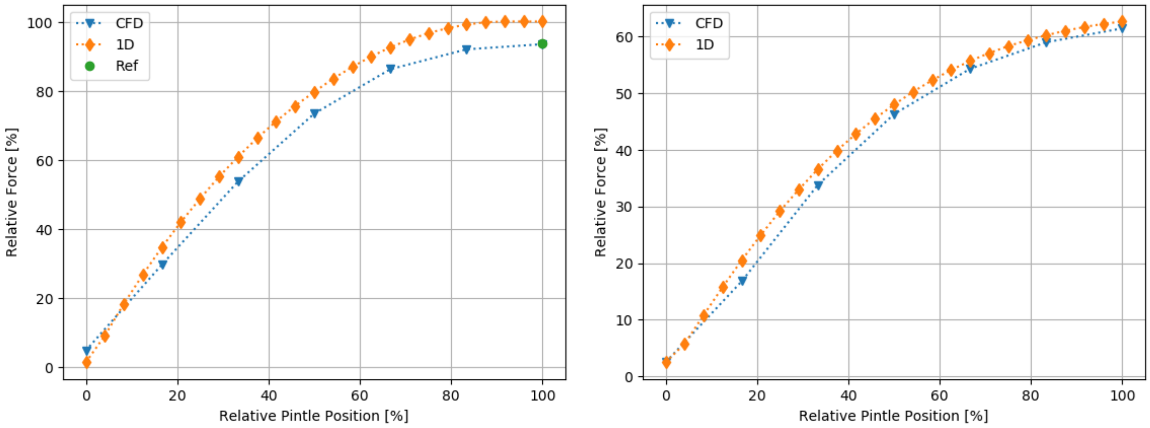

(a) Thrust

(b) Pintle X-Force

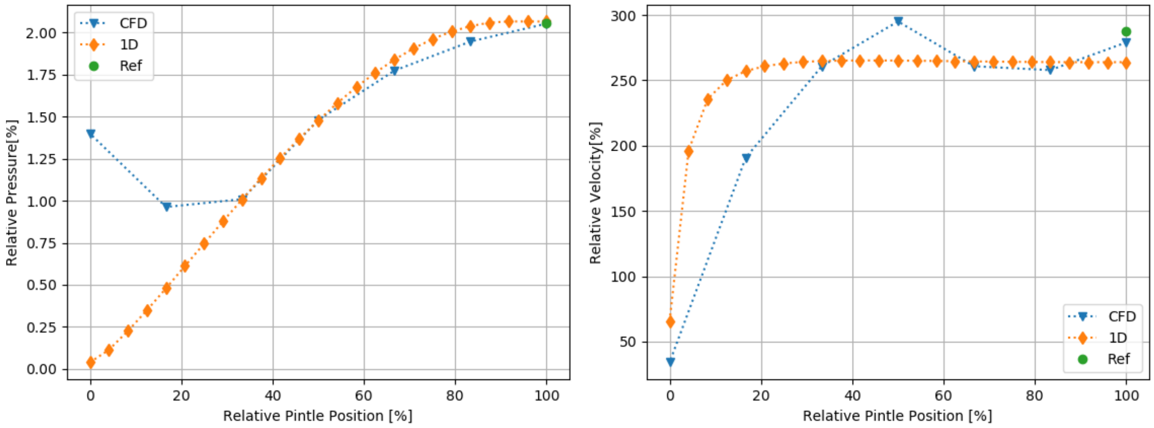

(c) Exit Pressure

(d) Exit Velocity

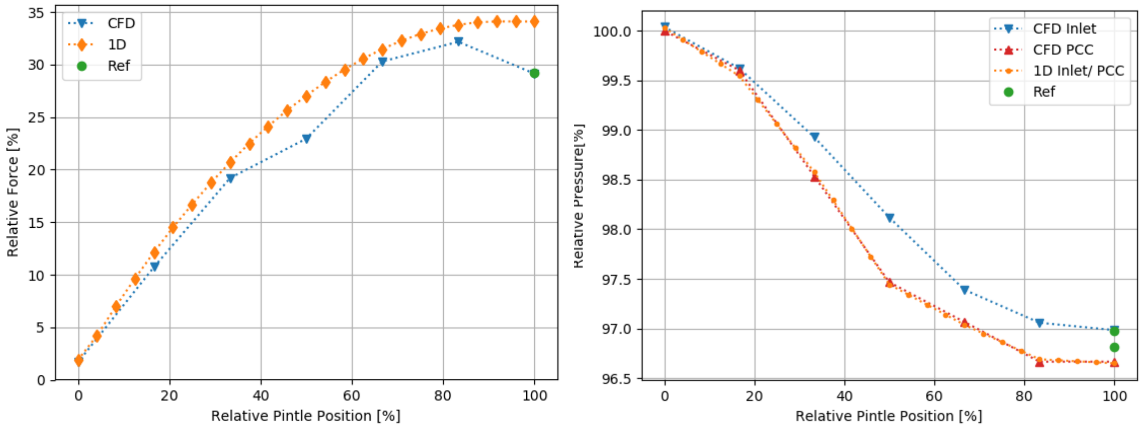

(e) Massflow

(f) Inlet Pressure

Figure 6.15: Hot-Fire CFD Results versus 1D Simulation Results with adapted Inlet Pressure (Values have been made dimensionless according to Table A.1)

To factor out the error caused by the pressure loss in the PCC the same procedure was applied as for the cold-gas case. The results of the updated/modified 1D simulation together with the CFD simulations have been plotted in Figure 6.15. In general the differences between the two results have decreased. Unlike the cold-gas case now also the exit pressure is a closer match, as here the 1D simulation underpredicts. This is attributed to the variation in the specific heat-ratio, which decreases from the inlet towards the exit, but in the 1D simulation remains constant at the inlet value.

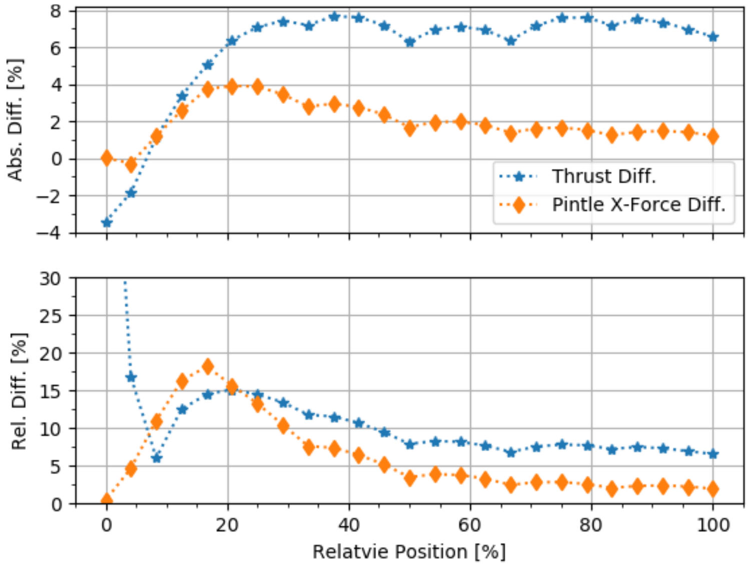

Figure 6.16: Relative and Absolute Difference of Static Hot-Fire CFD Results and 1D Simulation with adapted Inlet Pressure (Values have been made dimensionless according to Table A.1)

To asses the absolute and relative difference between the primary results of the modified 1D simulation and the hot-fire static CFD simulation, the values were plotted in the same manner as previously, see Figure 6.16. The plot looks very similar to the plot for the modified cold-gas case, see Figure 6.13. However, the differences are marginally higher for the hot-fire case. This is to be expected, as an additional error is introduced in the 1D simulation. The final relative error in thrust is about 6.6%. For the cold-gas case it was 5.7%. The additional error is thus only 0.9 %.

As the additional error is very small and all differences both relative and absolute are at an acceptable level, there is no objection against using the 1D tool to simulate a hot-fire nozzle pintle configuration. The 1D tool is therefore also verified for the simulation of hot-fire cases. To mitigate the additional error it would also be possible to directly couple the 1D tool with a Chemical Equilibrium tool, that predicts the gas parameters for certain propellant combination at a certain pressure. An example for such a tool is NASA's Chemical Equilibrium with Applications (CEA) tool, for details see Ref. [58]. However, whether the small improvement is worth the effort is doubtful.

7. Conclusions & Recommendations

The aim of this project was to gain a better understanding of the flow behaviour inside and downstream of a pintle controlled rocket thruster. This requires the existence or development of a flow simulation for such a thruster. Therefore, the following objective was given out (for the detailed sub-objectives see Chapter 1):

To develop the capability of analysing the flow field in a pintle controlled rocket thruster, by developing a three-dimensional CFD simulation of the thruster, which is validated by experimentally obtained test results.

With the simulations developed under the above objectives, the following general research question was to be answered:

How do different positions of the pintle influence the flow characteristics inside and downstream of the pintle controlled thruster?

The research question was split into three sub-questions, which focus on different aspects of the flow. The first questions is as follows: *What are the performance characteristics of the thruster at different pintle settings?* This question was answered, amongst others, with the help of the developed 1D simulation tool. The tool was supposed to provide a reasonable estimate of the thrust and the axial pintle force as a function of the pintle setting and given fixed initial conditions inside the PCC. The setup and results of this simulation tool were outlined in Chapter 3. Its primary results have been shown in Figure 3.3. The advantage of this simulation is that the geometry and flow conditions to be simulated can be quickly altered and the simulations run-time only takes a couple of minutes per case. This would make the 1D simulation an ideal tool for the preliminary design of any system using this thruster concept. However, the 1D simulation has numerous disadvantages. Due to its simplifications (for details see Chapter 3.1.1) it neglects all viscous and multi-dimensional effects of the flow. Furthermore, it neglects any pressure drop inside the PCC. These simplifications could potentially lead to a significant error in the prediction of the thruster performance.

Therefore, the 1D simulation results were compared with the results of the static CFD simulation, with the objective of verifying the former. The setup details can be found in Chapter 4.1 to 4.3. The primary results (thrust and pintle force, see Figure 4.15) were very comparable. The secondary results (see Figure 4.16) showed the differences somewhat more significantly. Especially the exit pressure significantly deviates. This was caused by flow separation from the nozzle wall and occurs for all pintle positions below 33.3%, which was also confirmed by the contour plots of the flow. Moreover, a significant pressure drop occurs at the inlet and inside the PCC. During the analysis performed in Chapter 6.2.1 it was discovered that this pressure drop is responsible for approximately half of the difference between CFD and 1D simulation. The other half was caused by the viscous losses (friction and the reduction of the throat by the boundary layer). The overall differences between the two simulations was about 10%. However, this was only true as long as the flow remains attached to the nozzle wall. For the pintle positions where the flow is separated the relative error is much larger, but the absolute difference is still acceptable. From this it was concluded that the 1D simulation is a reasonably good approximation for the actual flow and can be used as a preliminary design tool. The results of the 1D model also give a satisfactory answer to the first research sub-question.

The second research sub-question was as follows: *What are the different characteristics of the flow field (flow separation, shocks, sub-/supersonic boundary), do they occur and how do they change with different pintle settings?* This question can only be answered by analysing the contour plots of the CFD simulation. Above, it was already concluded that flow separation from the nozzle wall occurs for all pintle positions below 33.3% in the static CFD simulation. Moreover, it was discovered that this matches the prediction by the Summerfield flow separation criterion. Flow separation also occurs for the pintle wall. Already at high pintle positions 66.6% and below a very small separation was visible at the tip of the pintle. However, the majority of the flow stayed attached to the pintle for all pintle positions, except for the fully inserted 0% position. Here the flow was almost completely separated from pintle and nozzle walls. It was also found that the flow inside the nozzle remains shock free for pintle positions above 33.3%. Below that positions shocks started to form first at the separation points along the nozzle wall and later also from the pintle tip. As for a regular nozzle shocks also occurred in the exhaust plume of the nozzle.

The final research sub-question of this project was: *What are the transient effects of the pintle moving inside the thruster?* This required the setup of an additional dynamic/chimera CFD simulation, which is also one of the project objectives. To simulate the moving pintle the Chimera or Overset Grid Method was used, see Chapter 2.2.5. The setup and the results of the dynamic CFD simulation were presented in Chapter 4.4. It was found that the primary results (thrust and pintle force), are basically equivalent to the results of the static CFD simulation. The difference in the secondary results were more significant. There was a visible difference in the exit pressure curve for the insertion and retraction leg of the movement. The differences were attributed to a hysteresis effect for flow separation (when inserting the pintle) and re-attachment (when retracting it). For the inserting leg the flow remained attached a little longer and expanded to a lower pressure. Such phenomenons can also be observed for the flow separation on a wing or airfoil. Here difference in pintle position was however very small (below 2%) and there was no visible influence on the primary results, such that the effect could be neglected. Next to the hysteresis effect another possible dynamic effect was discovered. This was best visible in the static inlet and PCC pressures. These oscillated at the beginning and the end of the chimera simulation, when the pintle is close to the maximum thrust position and moving at a slower speed. These oscillations in pressure also influenced the massflow and all other results. It was concluded that these oscillations effects are caused by the initial and final pintle movement. If the pintle was inserted, this increased the PCC volume, which resulted in a small temporary pressure drop. However, at the same time the throat radius was decreased which caused an increase in chamber pressure, causing an initial transient effect in the PCC. Both of the dynamic/transient effects discovered here are comparably small and will not have any major effect on the operation of the thruster. The magnitudes of those effects were not comparable to the effects described in the paper of by Heo et al. [15], which were much more drastic. However, in Chapter 6.1.3, where all dynamic effects were analysed, it was also concluded that the results are not fully conclusive. This was due to the chosen time-step and number of iterations per time step. It was suspected that the former was too large and the latter too small. To confirm this one would have to conduct a detailed convergence analysis of multiple calculations at different settings. This was not possible within the time frame of this project. However, until that has not been done it is impossible to exclude that there are any additional dynamic effects or that the effects discussed here are more or less extreme or that these effects are not only the consequence of a numerical issue. Therefore, the respective results are not fully conclusive and additional work would be required before they can be fully confirmed.

In addition to the three question it was decided to investigate the hot-gas flow through the thruster using the 1D and CFD simulations. The details of the setup and the results have been presented in Chapter 4.5. Besides the initial conditions, the major difference is that the ideal gas assumption is no longer valid, as the specific heat ratio varies with temperature. Therefore, hot-gas CFD simulation models the combustion gas as a real gas. In the 1D simulation only the input conditions have been modified accordingly. The results of both simulations were shown in Figures 4.31 and 4.32. In general the primary results are very similar to the cold-gas cases. However, due to the high temperature the massflow is much lower and in return the exit velocity is significantly higher. Therefore, the thrust level remains very similar. Even though the hot-fire 1D simulation assumes an ideal gas, it still provides a reasonable approximation of the actual flow. It was found that the additional error is below 1%. Therefore, it was concluded that the 1D simulation can also be used to simulate a hot-gas thruster.

The above paragraphs have addressed all research questions and almost all objectives. Apart from the objective to validate the simulation using the test data from Metsker [16] (see Chapter 5). The validation attempt was presented in Chapter 6.1.2. It was found that the test data confirms the general trend of the thrust and the pintle force, however the values measured were substantially lower than the simulated values, see Figure 6.6. This is especially true for values close to the maximum trust position, where the relative difference in thrust is almost 50%. It was concluded that the reasons for these significant discrepancies likely lie in the measurement and test setup. Firstly, a large pressure drop in the fluid supply system was found, this is responsible for a significant reduction in thrust and pintle force. This was confirmed by a CFD simulation at adapted pressures, which gave a much closer match to the test results. Secondly, a problem with the calibration of the thrust measurement setup is believed to have been responsible for a larger part of the thrust data offset. It was however not possible to characterise these errors. Therefore, the objective of validating the simulation using test data could not be entirely met.

In general it can be concluded that all objectives and research question have been assessed, almost all of them successfully. The validation objective was not fully complied with, this would require additional test data which as of yet does not exist. Moreover, the research question regarding the dynamic effects could not be answered conclusively without additional calculations.

From the conclusions drawn above a number of recommendations concerning the different simulations and the test data can be drawn. These are listed below:

- **Recommendations regarding the 1D simulation:**
  - In the analysis in Chapter 6.2 it was found that the relative error in the 1D simulation, for the region where the flow is not attached to the nozzle wall, is both rather large and varies significantly. After the flow is attached the error stays approximately constant at 10%. It was also discovered that empirical flow separation criteria, such as the Summerfield criterion, give a reasonably good approximation of the separation pintle positions. Therefore, it is recommended to incorporated this in the 1D simulation. This way the user can immediately determine, below which point the results decrease in accuracy.
  - In the analysis in Chapter 6.2 it was also found that when correcting for the pressure losses inside the PCC the accuracy of the 1D simulation can be significantly improved. Therefore, it is recommended to develop a more permanent method to approximate the pressure loss and include that in the 1D simulation.
- **Recommendations regarding the dynamic CFD simulation:**
  - The dynamic simulations contained an error in the definition of the pintle movement, which was too slow. For details see the beginning of Chapter 4.4.2. It is recommended to repeat the simulations with the error corrected.
  - Due to time constraints and limited computational resources the number of time steps n and the number of iterations per time step was significantly reduced. It is very probable that both values were reduced too much. It is recommended to conduct a convergence analysis and systematically increase the values until the results for two consecutive simulations match each other. Only than it can be concluded that all dynamic effects have been correctly captured.
- **Recommendations regarding the simulation validation and test data:**
  - It is recommended to modify the test setup such that the thrust load cell can be calibrated while the full system is pressurised. This could be achieved by modifying the nozzle piece such that the nozzle exit can be temporarily plugged.
  - It is recommended to decrease the overall stiffness of the thrust measurement setup. One possibility is to exchange the feed pipes by more flexible hoses.
  - It is recommended to redesign the fluid supply system, such that it can be assured that the flow is not chocked prior to entering the thruster. This way the pressure drop inside the PCC can be analysed more accurately.
  - It is further recommended to try and minimise the pressure drop over the regulator.
  - After the above points have been settled it is recommended to conduct multiple test series and using that data repeat an attempt in validating the CFD simulation.

Bibliography

[1] Barrere, M., Jaumotte, A., Fraeijs De Veubeke, B., and Vandenkerckhove, J., *Raketenantriebe*, Elsevier Publishing Company, Liege, Belgium, 1961, German Translation from the French Original.

[2] Ehlen, J., "Investigation of the Flow Characteristics in a Pintle Controlled Rocket Motor Nozzle," Tech. rep., TU Delft, Faculty of Aerospace Engineering, December 2016, Assignment: AE4020 Literature Study.

[3] Jones, D. S., Brooks, S. J., and Barnes, M. B., "Executive Summary of Propulsion on the Orion Abort Flight-Test Vehicles," Tech. Rep. NASA/TM—2012–216049, NASA, December 2012, `http://ntrs.nasa.gov/search.jsp?R=20130010949`.

[4] Bocam, K., Escalera, P., and Sullivan, B., "Development of the Orion PA-1 Launch Abort System - From Conception to Demonstration ," *AIAA SPACE 2011 Conference & Exposition*, September 2011, AIAA 2011-7129.

[5] Williams-Hayes, P. S., "Crew Exploration Vehicle Launch Abort System Flight Test Overview," *AIAA Guidance, Navigation and Control Conference and Exhibit*, NASA Dryden Flight Research Center, AIAA, Hilton Head, South Carolina, USA, August 2007.

[6] Coon, J. and Yasuhara, W., "Solid Propulsion Approaches For Terminal Steering," *AIAA / SDIO 2nd Annual Interceptor Technology Conference*, AIAA / SDIO, Albuquerque, US, 1993, AIAA 93-2641.

[7] Robinson, S. D., "Navy Theater-Wide Defense AEGIS LEAP Intercept (ALI)/STANDARD Missile Three (SM-3) Flight Test Program Overview," *6th Annual AIAA/BMDO Technology Readiness Conference and Exhibit*, San Diego, Ca, August 1997, `http://www.dtic.mil/dtic/tr/fulltext/u2/a329084.pdf`.

[8] W. Prins, A. S. and Roberts, J., "SM-3 SDACS Flight Test Successes," *39th AIAA/ASME/SAE/ASEE Joint Propulsion Conference and Exhibit*, Huntsville, Alabama, USA, July 2003, AIAA 2003-4664.

[9] Cover, C. L. and Drendel, A. S., "Rocket thruster assembly comprising load-balanced pintle valve," Patent US 8215097 B2, July 2012, `http://www.google.com/patents/US8215097`.

[10] Rock, S., Habachi, S., and Marquette, T., "Numerical simulation of controllable propulsion for advanced escape systems ," *15th Applied Aerodynamics Conference*, CFD Research Corp. and U.S. Navy, Naval Air Warfare Center, AIAA 97-2254, Atlanta, GA, USA, 1997.

[11] McDonald, A. B., "4th Generation Escape System Technologies Demonstration Phase," Tech. Rep. AFRL-HE-WP-TR-1998-0130, United States Air Force Research Laboratory and Boeing, February 1998.

[12] IHS Global Limited Jane's Weapons: Naval, "RIM-66/-67/-156 Standard SM-1/-2, RIM-161 Standard SM-3, and RIM-174 Standard SM-6," Online Database, August 2015, Last Accesed: 13-11-15.

[13] Dumortier, A., "Hot-Gas Valve Development using a simple Numeric Code," *30th AIAA/ASME/SAE/ASEE Joint Propulsion Conference*, Societe Europeenne de Propulsion (SEP), Indianapolis, IN, June 1994, AIAA 1994-3185.

[14] Lafond, A., "Numerical Simulation of the Flowfield Inside a Hot Gas Valve," *37th Aerospace Science Meeting & Exhibit*, SEP Division de SNECMA, AIAA, Reno, NV, January 1999, 99-1087.

[15] Heo, J., Jeong, K., and Sung, H.-G., "Numerical Study of the Dynamic Characteristics of Pintle Nozzles for Variable Thrust," *AIAA Journal of Propulsion and Power*, Vol. 31, No. 1, 2015, pp. 230–237.

[16] Metsker, Y., *Untersuchung von Querschub- und Lageregelungstriebwerken für den Betrieb mit Festtreibstoffen im Endo- und Exo-Atmosphärischen Bereich*, Ph.D. thesis, Technische Universität München, Lehrstuhl für Flugantriebe, 2018, To-be-published.

[17] Anderson Jr., J. D., *Fundamentals of Aerodynamics*, McGraw-Hill, 5th ed., 2011.

[18] Zandbergen, B., *Thermal Rocket Propulsion*, TU Delft Faculty of Aerospace Engineering, 2nd ed., February 2010.

[19] Anderson Jr., J. D., *Modern Compressible Flow With Historical Perspective*, McGraw-Hill, 3rd ed., 2003.

[20] Sauer, R., "General Characteristics of the Flow through Nozzles at Near Critical Speed," Tech. Rep. 1147, NACA, June 1947, Translation of: "Allegemeine Eigenschaften der Strömungen durch Düsen in der Nähe der kritischen Geschwindigkeit", Deutsche Luftfahrtforschung, Bericht Nr. 1992, Berlin 1944.

[21] Rao, G. V. R., "Approximation of Optimum Thrust Nozzle Contour," *ARS Journal*, Vol. 30, No. 6, June 1960, pp. 561.

[22] Frey, M. and Hagemann, G., "Restricted Shock Separation in Rocket Nozzles," *Journal of Propulsion and Power*, Vol. 16, No. 3, 2000, pp. 478–484.

[23] Hagemann, G., Immich, H., Nguyen, T., and Dumnov, G. E., *Liquid Rocket Thrust Chambers: Aspects of Modeling, Analysis, and Design*, Vol. 200 of *Progress in Astronautics and Aeronautics*, chap. Chapter 12: Rocket Engine Nozzle Concepts, AIAA, 1801 Alexander Bell Drive, Reston, Virginia, 2004.

[24] Summerfield, M., Forster, C., and Swan, W., "Flow separation in overexpanded supersonic exhaust nozzles," *Jet Propulsion*, Vol. 24, September 1954, pp. 319–320.

[25] Schmucker, R. H., "Stroemungsvorgaenge beim Betrieb ueberexpandierter Duesen chemischer Raketentriebwerke, Teil 1: Stroemungsabloesungen," Tech. rep., Technische Universitaet Muenchen, 1975, TUM-LRT-TB-7, NASA-CR-143044.

[26] Stark, R. H., "Flow Separation in Rocket Nozzles - An Overview," *49th AIAA/ASME/SAE/ASEE Joint Propulsion Conference and Exhibit*, San Jose, CA, USA, July 2013, AIAA-2013-3840.

[27] Anderson Jr., J. D., *Computational Fluid Dynamics The Basics with Applications*, McGraw-Hill, 1995.

[28] Cebeci, T., *Analysis of Turbulent Flows with Computer Programs*, Butterworth-Heinemann, Oxford, UK, 3rd ed., 2013.

[29] Deutsches Zentrum für Luft- und Raumfahrt e.V., "Documentation and User Guide of the DLR TAU-Code Release 2015.2.0," Tech. rep., Institute of Aerodynamics and Flow Technology, Brunswick, Germany, 2015.

[30] Hirsch, C., *Numerical Computation of Internal and External Flows, The Fundamentals of Computational Fluid Dynamics*, Elsevier Ltd., 2nd ed., 2007, ISBN: 978-0-7506-6594-0.

[31] Blazek, J., *Computational Fluid Dynamics: Principles and Applications*, Elsevier, 2001.

[32] van Leer, B., "Towards the Ultimate Conservative Difference Scheme. V. A Second-Order Sequel to Godunov's Method," *Journal of Computational Physics*, Vol. 32, 1979, pp. 101–137.

[33] Wada, Y. and Liou, M.-S., "A Flux Splitting Scheme With High-Resolution and Robustness for Discontinuities," *AIAA 32nd Aerospace Sciences Meeting and Exhibit*, NASA, ICOMP, AIAA, Reno, NV, USA, January 1994, Published three times as: NASA TM-106452, ICOMP-93-50 and AIAA-94-0083.

[34] Liou, M.-S. and Steffen, C. J., "A New Flux Spillting Scheme," *Journal of Computational Physics*, Vol. 107, 1993, pp. 23–29.

[35] Reynolds, O., "On the Dynanmical Theory of Incompressible Viscous Fluids and Determination of the Criterion," *Philosophical Transactions of the Royal Society of London*, Vol. 186, Royal Society, 1895, pp. 123–164.

[36] Favre, A. J., "The equations of compressible turbulent gases," Tech. rep., Aix-Marseille University, January 1965.

[37] Spalart, P. R. and Allmaras, S. R., "A One Equation Turbulence Model for Aerodynamic Flows," *30th Aerospace Science Meeting and Exhibit*, Reno, NV, USA, January 1992, AIAA-92-0439.

[38] Jones, W. P. and Launder, B. E., "The prediction of laminarization with a two-equation model of turbulence," *International Journal of Heat and Mass Transfer*, Vol. 15, No. 2, February 1972, pp. 301–314.

[39] Wilcox, D. C., "Reassessment of the Scale-Determining Equation for Advanced Turbulence Models," *AIAA Journal*, Vol. 26, No. 11, November 1988, pp. 1299–1310.

[40] NASA Langley Research Center, "Turbulence Modeling Resource," Website, March 2016, `https://turbmodels.larc.nasa.gov/` (Last Accessed: 07-10-2016).

[41] Menter, F. R., "Zonal Two Equation k-ω, Turbulence Models for Aerodynamic Flows," *24th Fluid Dynamics Conference*, Orlando, FL, USA, July 1993, AIAA-93-2906.

[42] Schlichting, H. and Gersten, K., *Boundary-Layer Theory*, Springer, 9th ed., 2017.

[43] Benek, J. A., Steger, J. L., and Dougherty, F. C., "A Flexible Grid Embedding Technique with Application to the Euler Equations," *AIAA 6th Computational Fluid Dynamics Conference*, Danvers, Massachusetts, USA, July 1983, pp. 373–382.

[44] Benek, J. A., Buning, P. G., and Steger, J. L., "A 3-D Chimera Grid Embedding Technique," *AIAA 7th Computational Physics Conference*, Cincinnati, Ohio, USA, July 1985, pp. 322 – 331.

[45] Dougherty, F. C., Benek, J. A., and Steger, J. L., "On Applications of Chimera Grid Schemes To Store Separation," Tech. rep., NASA, October 1985, NASA-TM-88193.

[46] Meakin, R. L. and Suhs, N. E., "Unsteady Aerodynamic Simulation of multiple Bodies in relative Motion," *AIAA 9th Computational Fluid Dynamics Conference*, Buffalo, New York, USA, June 1989, pp. 643–657, AIAA-89-1996-CP.

[47] Hadžić, H., *Development and Application of a Finite Volume Method for the Computation of Flows Around Moving Bodies on Unstructured, Overlapping Grids*, Ph.D. thesis, Technischen Universität Hamburg-Harburg, 2005.

[48] Nakahashi, K., Togashi, F., and Sharov, D., "Intergrid-Boundary Definition Method for Overset Unstructured Grid Approach," *AIAA Journal*, Vol. 38, No. 11, November 2000, pp. 2077–2084.

[49] Bonet, J. and Peraire, J., "An Alternating Digital Tree (ADT) Algorithm for 3D Geometric Searching and Intersection Problems," *International Journal for Numerical Methods in Engineering*, Vol. 31, 1991, pp. 1–17.

[50] D'Errico, J., "distance2curve," MathWorks File Exchange, February 2013, `https://de.mathworks.com/matlabcentral/fileexchange/34869-distance2curve` (Last Accessed: 29-05-2017).

[51] DLR Institute of Aerodynamics and Flow Technology, "Hompage of the DLR TAU Code," Website, 2010, `http://tau.dlr.de/startseite/` (Last Accessed: 23-08-2016).

[52] EADS - MAS, "Mesher User Guide," Tech. rep., 2006, Unpublished.

[53] Stich, G.-D., Wagner, B., and Schlechtriem, S., "Numerical Investigation of Flow Phenomena in a Planar Expansion-Defletion Nozzle," Presentation, December 2015.

[54] Östlund, J., Damgaard, T., and Frey, M., "Side-Load Phenomena in Highly Overexpanded Rocket Nozzles," *Journal of Propulsion and Power*, Vol. 20, No. 4, 2004, pp. 695–704.

[55] Deutsches Zentrum für Luft- und Raumfahrt e.V., "TAU-Code User Guide Release 2016.2.0," Tech. rep., Institute of Aerodynamics and Flow Technology, Brunswick, Germany, 2016.

[56] German Aerospace Center, "Additional User Guide - Spacecraft τ," Tech. rep., Institute of Aerodynamics and Flow Technology, Brunswick, Germany, 2017.

[57] Anderson Jr., J. D., *Hypersonic and High-Temperature Gas Dynamics*, AIAA, 2nd ed., 2006.

[58] McBride, B. J. and Gordon, S., "Computer Program for Calculation of Complex Chemical Equilibrium Compositions and Applications II. User's Manual and Program Description," Tech. Rep. NASA RP-1311-P2, NASA Lewis Research Center, Cleveland, Ohio, June 1996, `http://www.grc.nasa.gov/WWW/CEAWeb/RP-1311.htm`.

A. Data Post Processing Information

Most of the results presented in this thesis are given in dimensionless form and as a percentage of a reference value or reference result. Sometimes certain values are also designated as n/a (Not-available). In this case it may be assumed that the value is the respective reference value. This procedure was necessary to comply with the MBDA guidelines on exporting possibly sensitive material and to avoid possible conflicts with German export law. The procedure on how certain results have been made dimensionless in this report can be found in Table A.1. The table is valid for all results presented in the report, except if mentioned otherwise in the respective section.

Table A.1: Procedure to make results dimensionless

Result	**Reference Value**	**Equation**
Thrust/ Force Values	Max. simulated thrust 1D Simulation	$\left[F/T_{1D_{max}}\right]$
Pressure Values	Assumed inlet or combustion pressure	$[p/p_c]$
Temperature Values	Assumed inlet temperature of cold gas cases	$[T/T_c]$
Density Values	Assumed inlet conditions, using Ideal Gas Law	$[\rho/\left(p_c/\left(T_c \cdot R_c\right)\right)]$
Massflow Values	Max. simulated massflow 1D Simulation	$\left[\dot{m}/\dot{m}_{1D_{max}}\right]$
Velocity Values	Max. simulated vacuum exit velocity 1D Simulation	$\left[v/v^{vac}_{e_{1D_{max}}}\right]$
Time/ Duration Values	Predefined pintle half-period $T_{1/2}$	$\left[t/T_{1/2}\right]$

The actual reference value can of course not be mentioned in the external version of this report, for the reasons explained above. However, some of the reference values might be found in the PHD thesis of Metsker [16], which should be freely available.

Not presenting these reference values in this report naturally has an influence on the scientific value of this project. Absolute values are important for a full understanding of any scientific or engineering problem. This especially true for rocket motors which do not scale easily or linear. However, the main objective of this report is to investigate the performance changes of a nozzle-pintle thruster when the pintle position is altered. For this it is not essential to know the exact absolute force or pressure values, as the focus point is the change of these values and not their absolute magnitude. Therefore, it is believed that making these values dimensionless and only giving relative quantities is justifiable.

B. Additional CFD Data

B.1. Full Static CFD Results

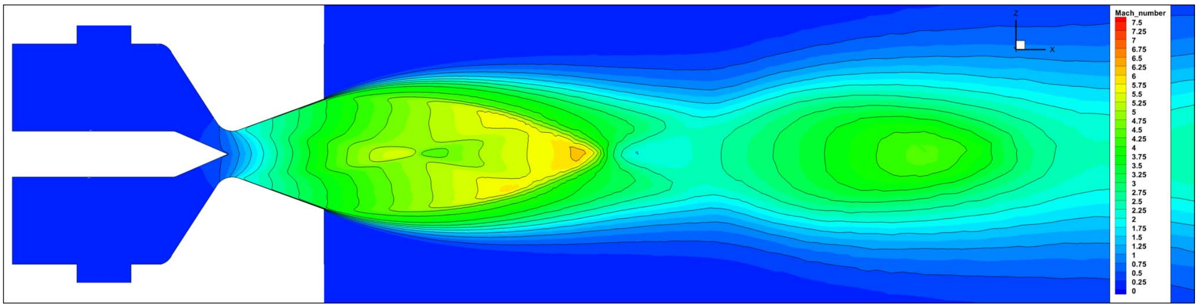

(a) Mach Number

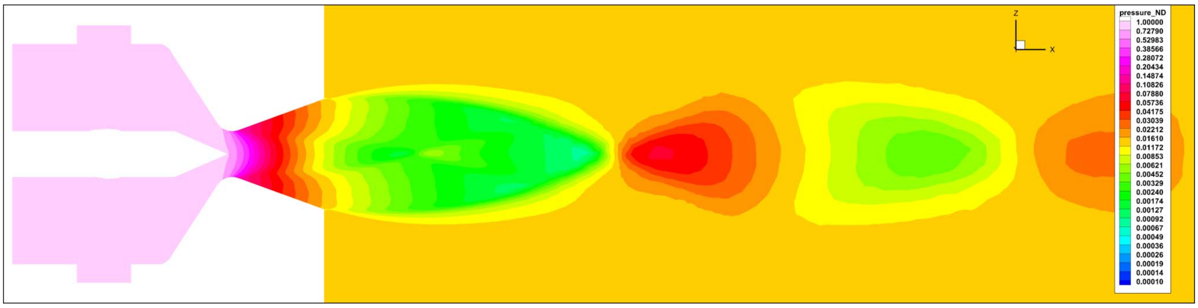

(b) Pressure

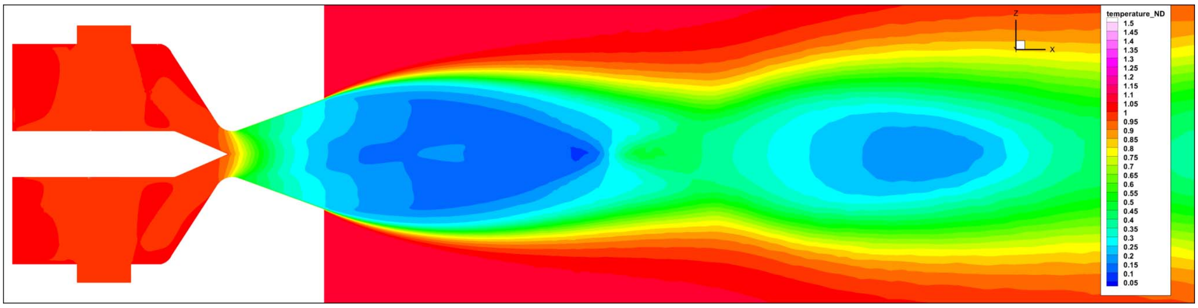

(c) Temperature

Figure B.1: CFD Results ZX-Plane Cut Contour Plot at the 100% position (Values have been made dimensionless according to Table A.1, Mach Number ranging from $M = 0.0$ to $M = 7.5$ with $\Delta M = 0.25$ and for the lines a $\Delta M = 0.5$)

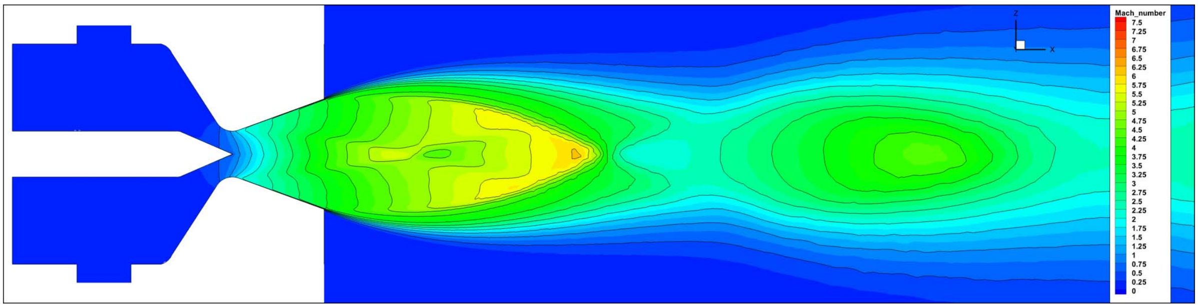

(a) Mach Number

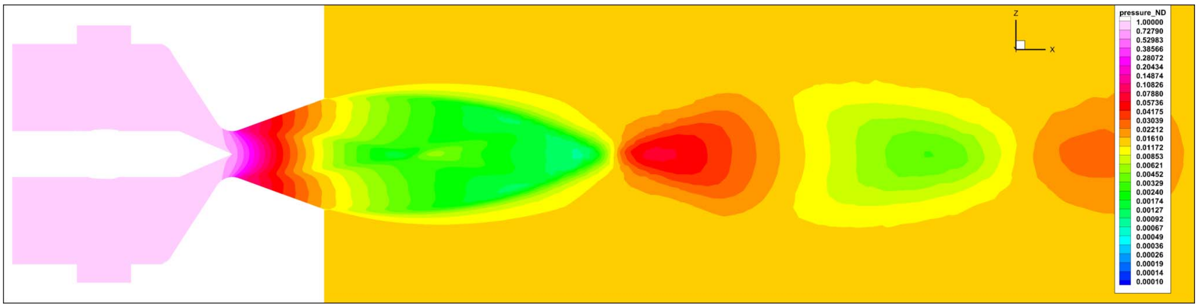

(b) Pressure

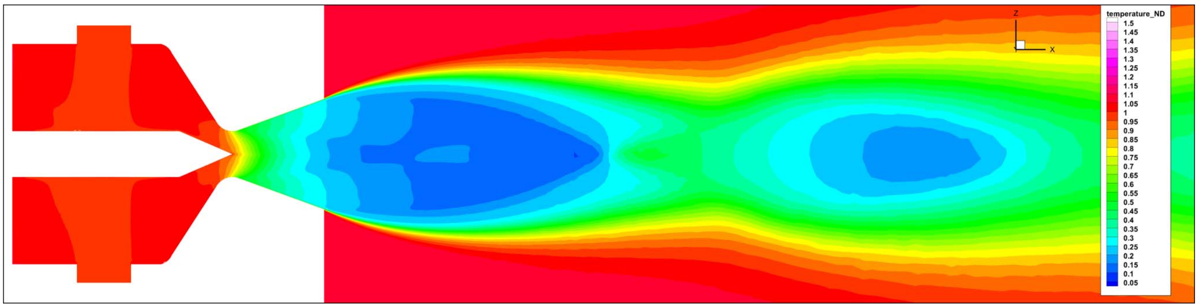

(c) Temperature

Figure B.2: CFD Results ZX-Plane Cut Contour Plot at the 91.66% position (Values have been made dimensionless according to Table A.1, Mach Number ranging from $M = 0.0$ to $M = 7.5$ with $\Delta M = 0.25$ and for the lines a $\Delta M = 0.5$)

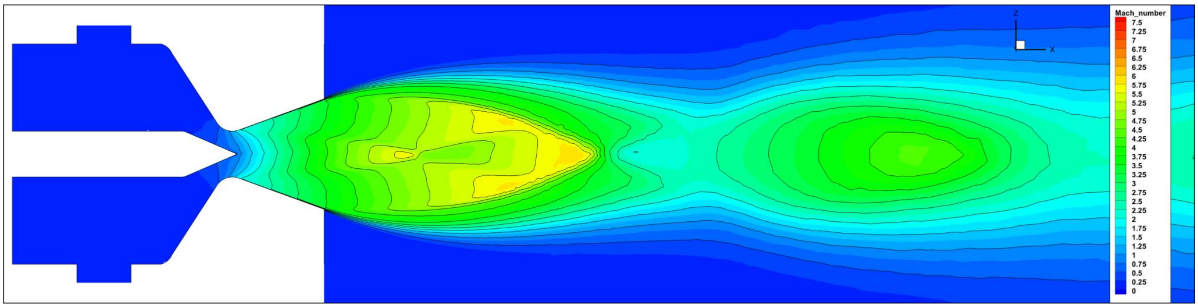

(a) Mach Number

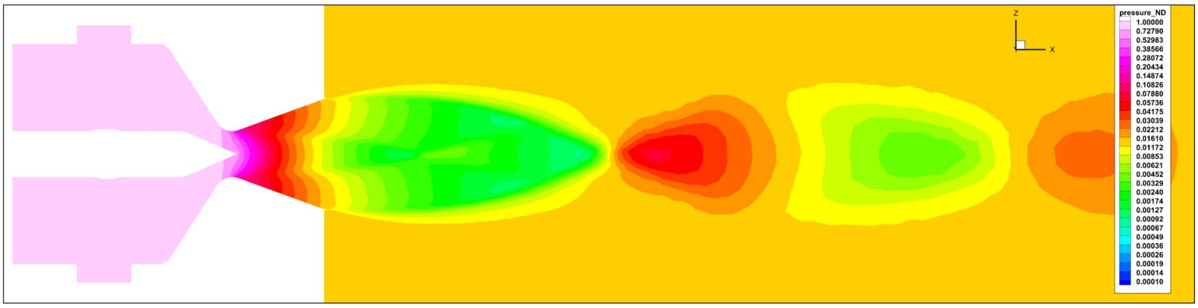

(b) Pressure

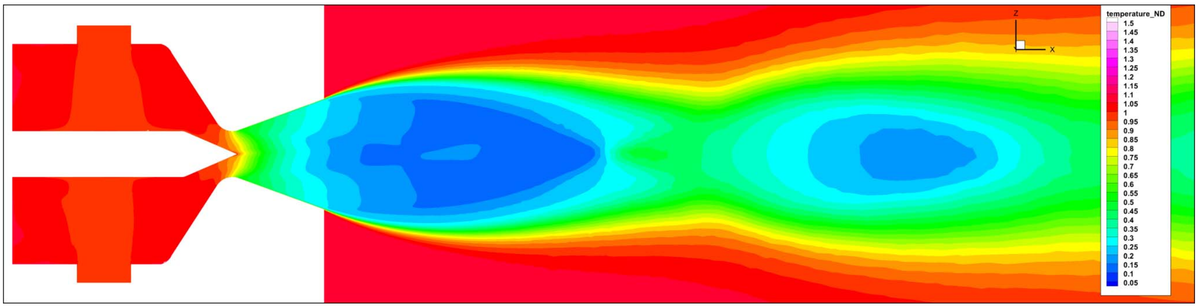

(c) Temperature

Figure B.3: CFD Results ZX-Plane Cut Contour Plot at the 83.33% position (Values have been made dimensionless according to Table A.1, Mach Number ranging from $M = 0.0$ to $M = 7.5$ with $\Delta M = 0.25$ and for the lines a $\Delta M = 0.5$)

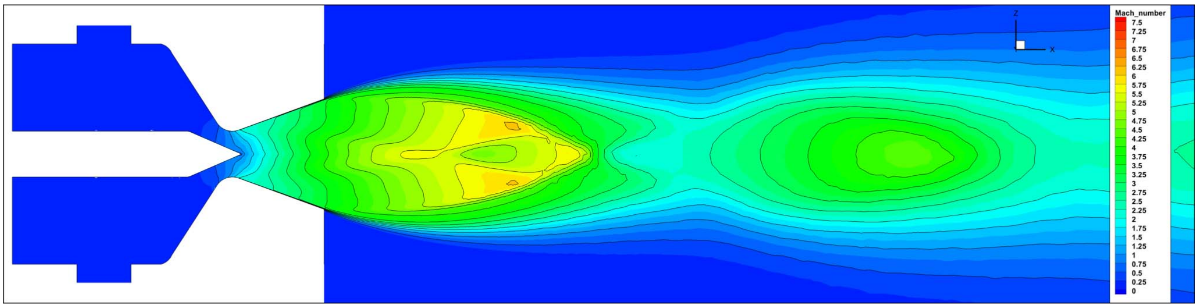

(a) Mach Number

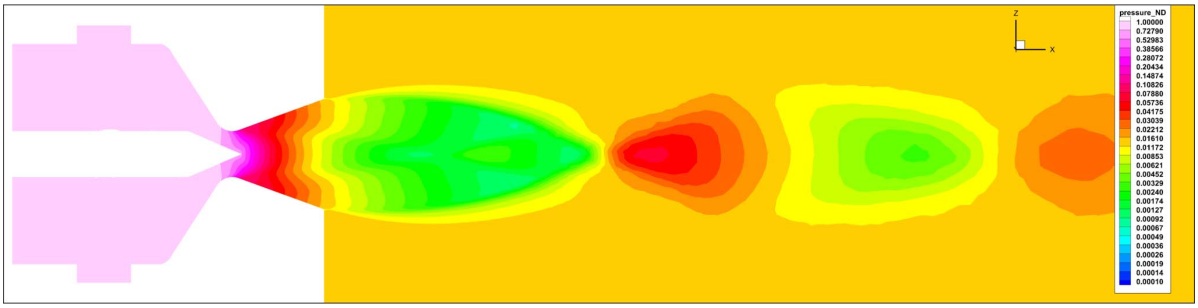

(b) Pressure

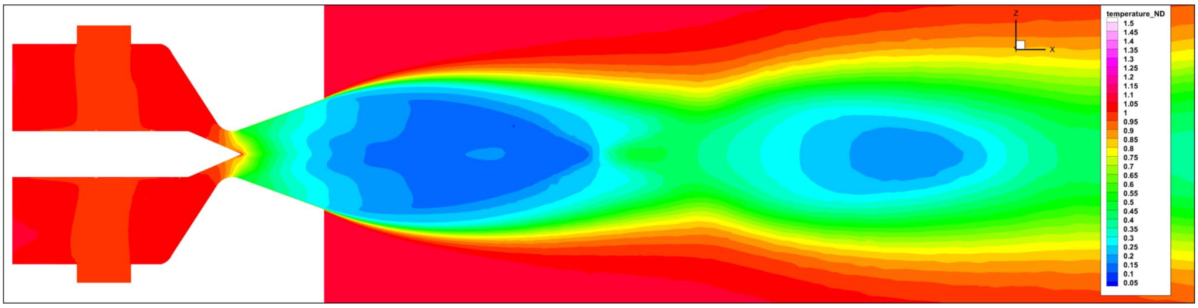

(c) Temperature

Figure B.4: CFD Results ZX-Plane Cut Contour Plot at the 75.00% position (Values have been made dimensionless according to Table A.1, Mach Number ranging from $M = 0.0$ to $M = 7.5$ with $\Delta M = 0.25$ and for the lines a $\Delta M = 0.5$)

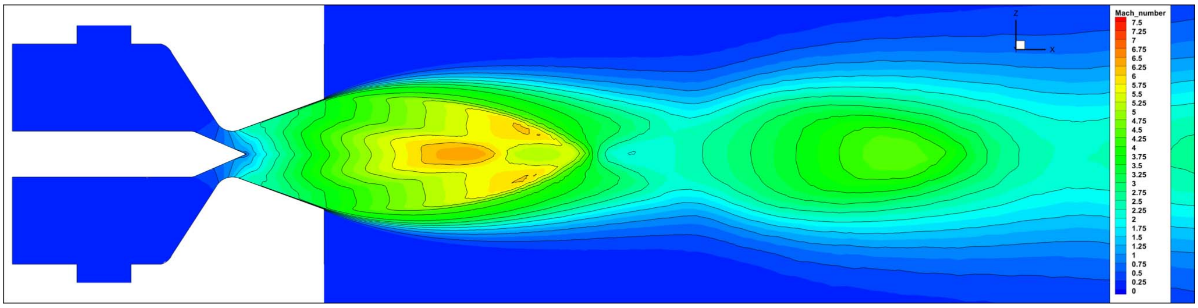

(a) Mach Number

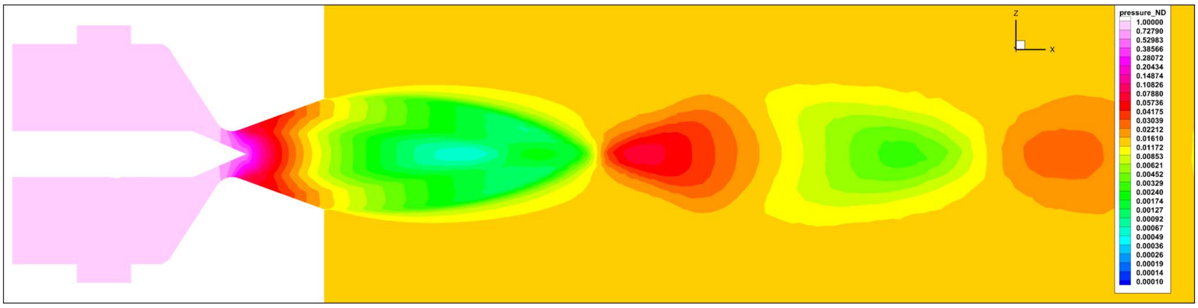

(b) Pressure

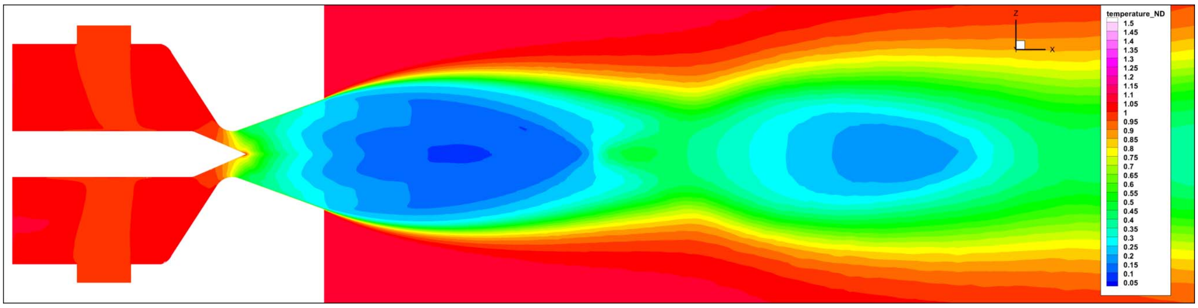

(c) Temperature

Figure B.5: CFD Results ZX-Plane Cut Contour Plot at the 66.66% position (Values have been made dimensionless according to Table A.1, Mach Number ranging from $M = 0.0$ to $M = 7.5$ with $\Delta M = 0.25$ and for the lines a $\Delta M = 0.5$)

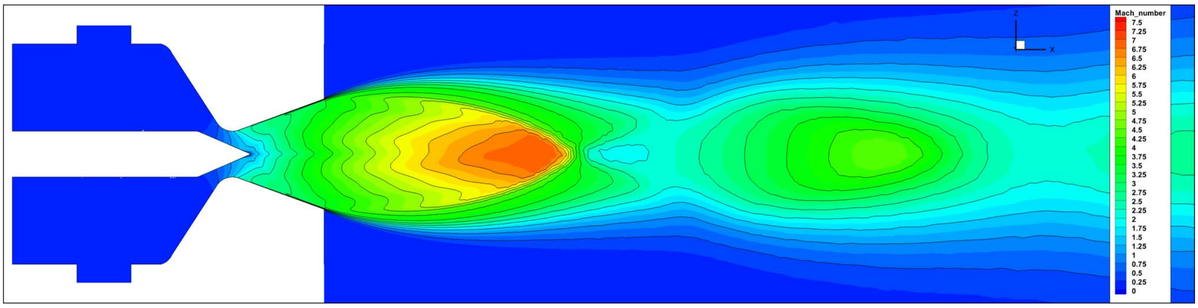

(a) Mach Number

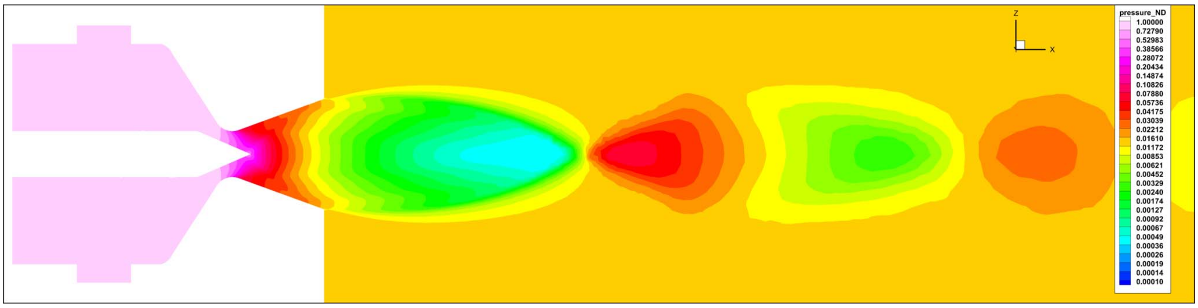

(b) Pressure

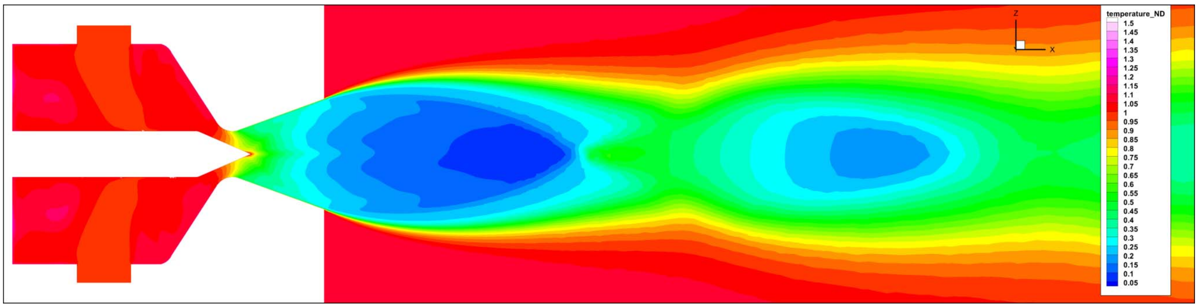

(c) Temperature

Figure B.6: CFD Results ZX-Plane Cut Contour Plot at the 58.33% position (Values have been made dimensionless according to Table A.1, Mach Number ranging from $M = 0.0$ to $M = 7.5$ with $\Delta M = 0.25$ and for the lines a $\Delta M = 0.5$)

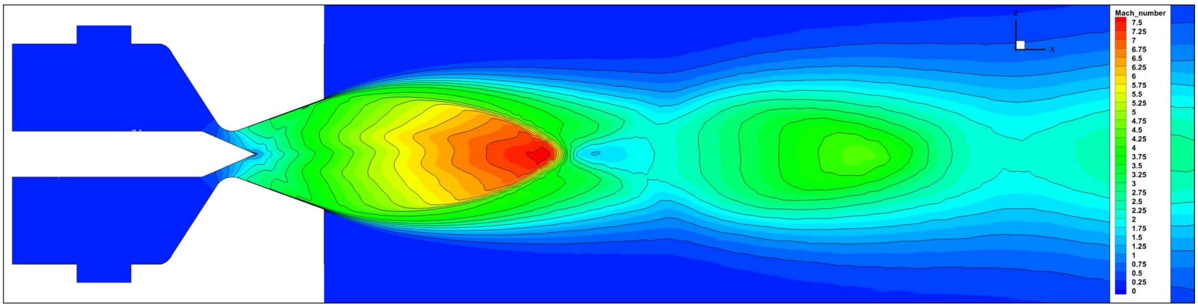

(a) Mach Number

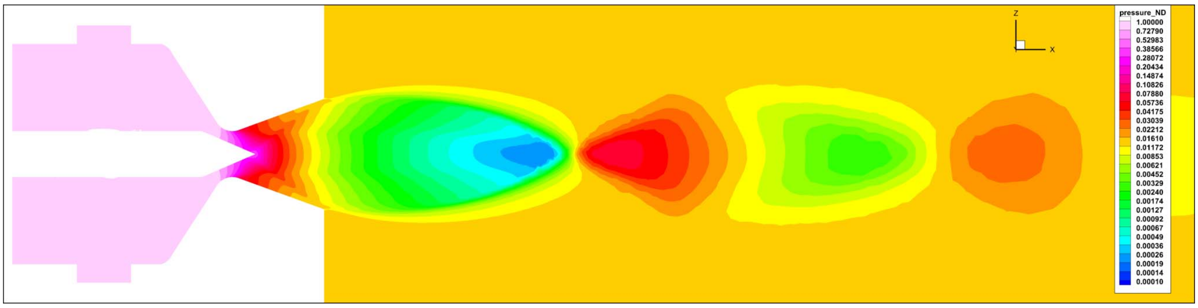

(b) Pressure

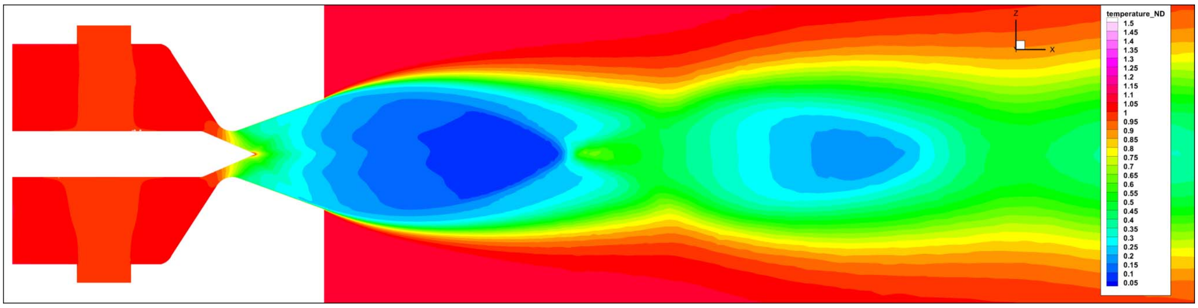

(c) Temperature

Figure B.7: CFD Results ZX-Plane Cut Contour Plot at the 50.00% position (Values have been made dimensionless according to Table A.1, Mach Number ranging from $M = 0.0$ to $M = 7.5$ with $\Delta M = 0.25$ and for the lines a $\Delta M = 0.5$)

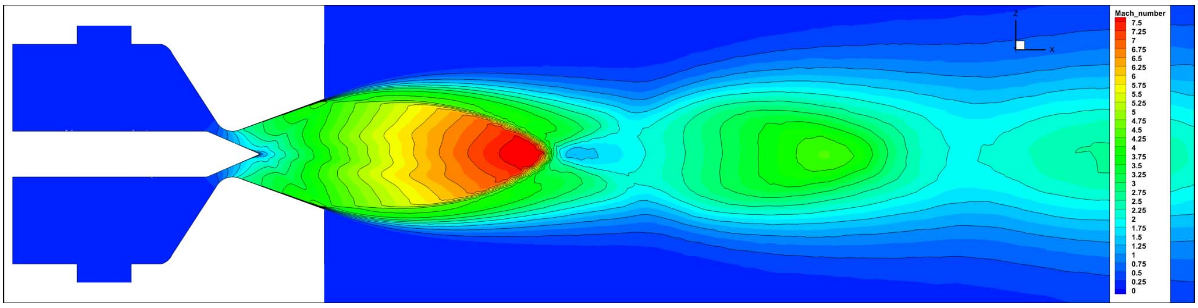

(a) Mach Number

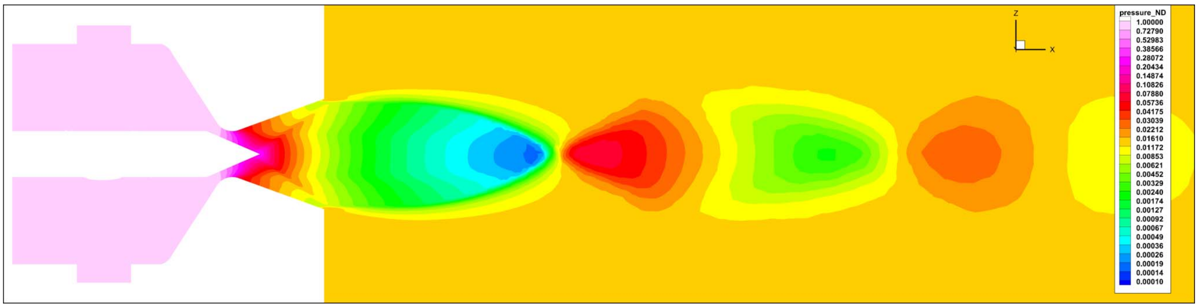

(b) Pressure

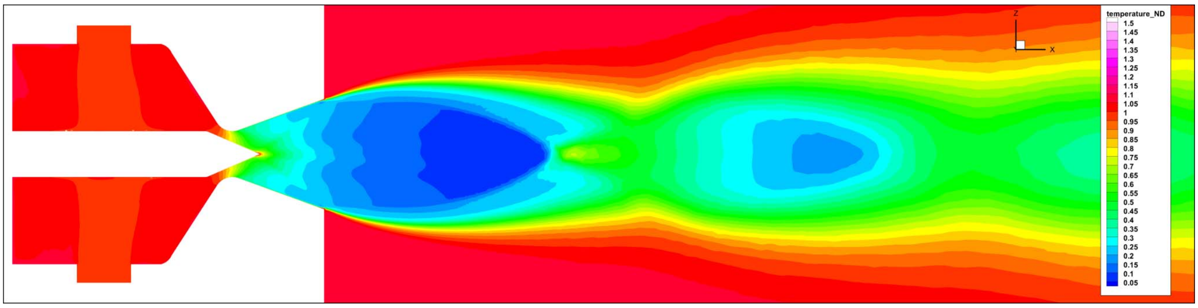

(c) Temperature

Figure B.8: CFD Results ZX-Plane Cut Contour Plot at the 41.66% position (Values have been made dimensionless according to Table A.1, Mach Number ranging from $M = 0.0$ to $M = 7.5$ with $\Delta M = 0.25$ and for the lines a $\Delta M = 0.5$)

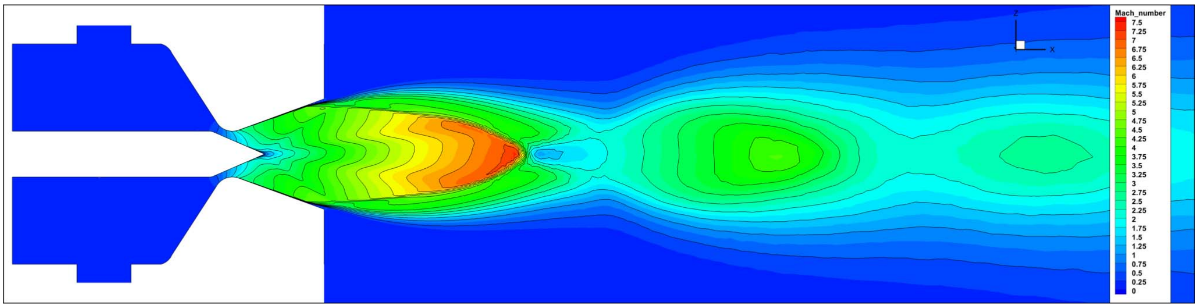

(a) Mach Number

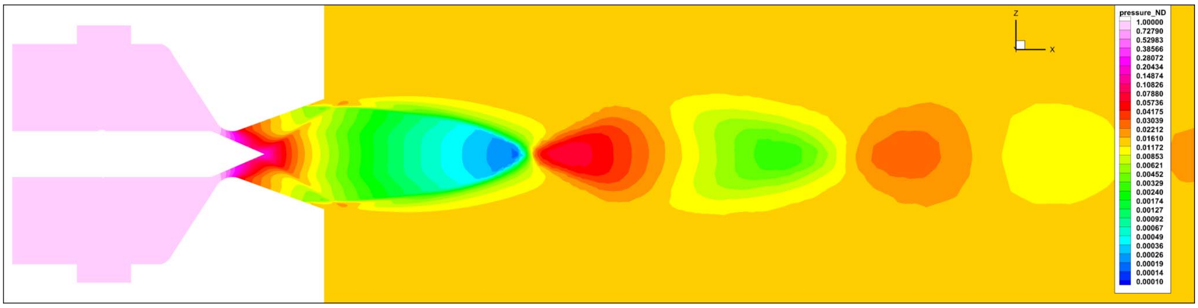

(b) Pressure

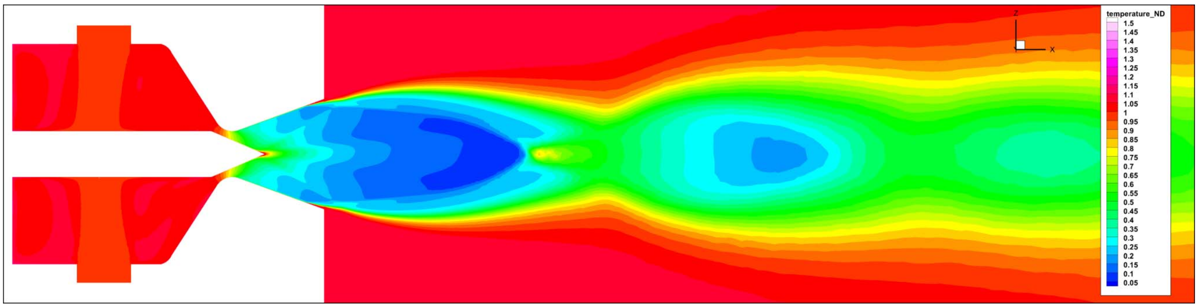

(c) Temperature

Figure B.9: CFD Results ZX-Plane Cut Contour Plot at the 33.33% position (Values have been made dimensionless according to Table A.1, Mach Number ranging from $M = 0.0$ to $M = 7.5$ with $\Delta M = 0.25$ and for the lines a $\Delta M = 0.5$)

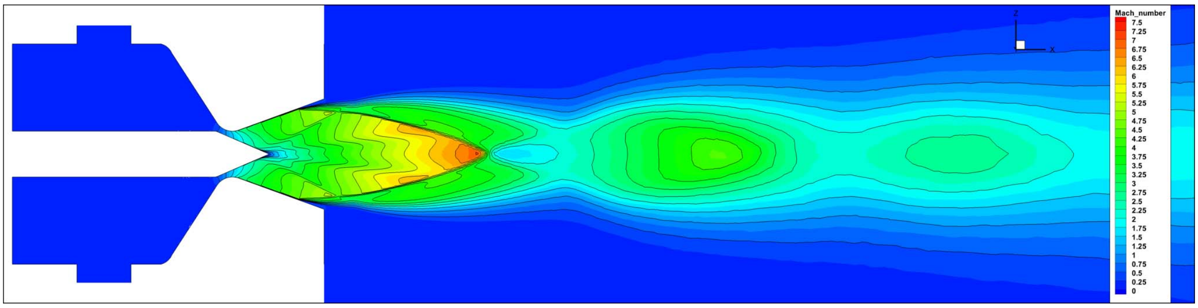

(a) Mach Number

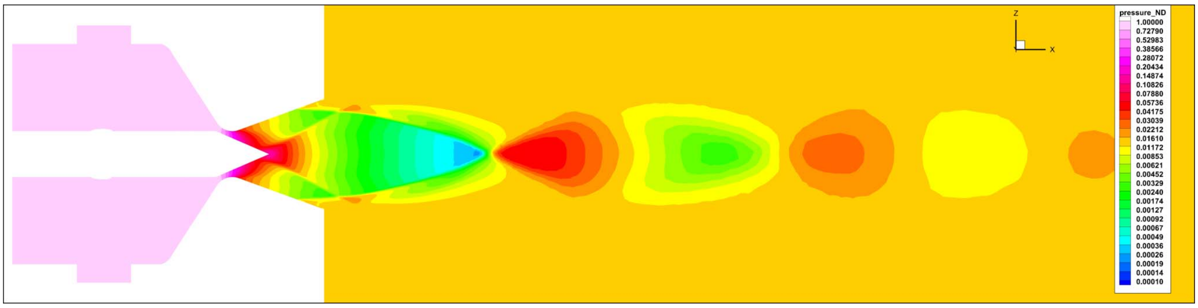

(b) Pressure

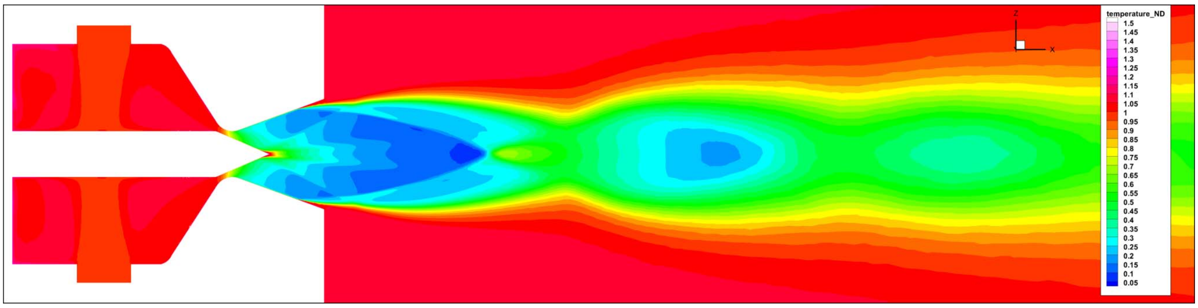

(c) Temperature

Figure B.10: CFD Results ZX-Plane Cut Contour Plot at the 25.00% position (Values have been made dimensionless according to Table A.1, Mach Number ranging from $M = 0.0$ to $M = 7.5$ with $\Delta M = 0.25$ and for the lines a $\Delta M = 0.5$)

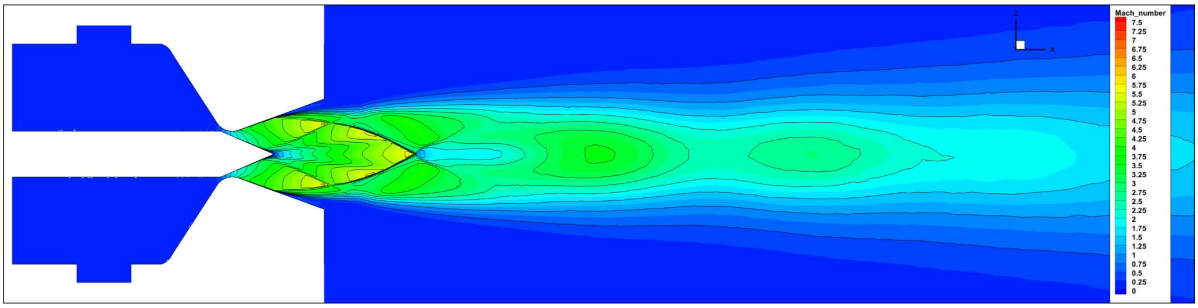

(a) Mach Number

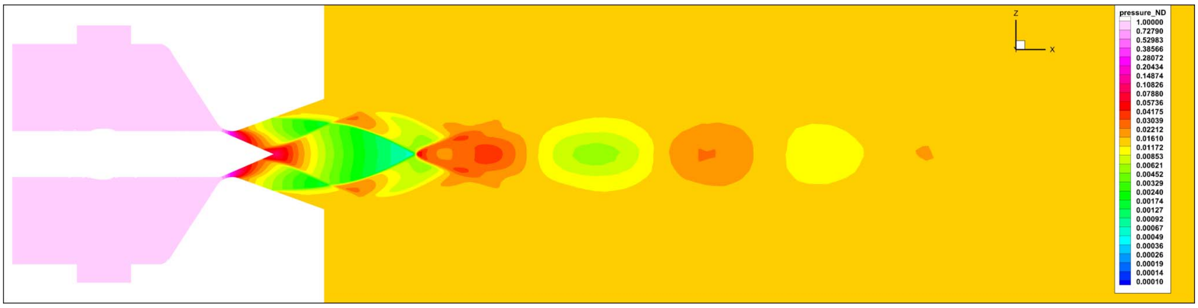

(b) Pressure

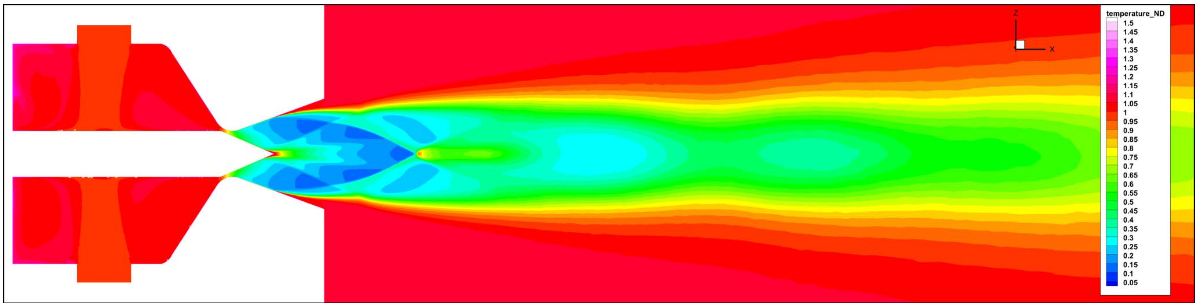

(c) Temperature

Figure B.11: CFD Results ZX-Plane Cut Contour Plot at the 16.66% position (Values have been made dimensionless according to Table A.1, Mach Number ranging from $M = 0.0$ to $M = 7.5$ with $\Delta M = 0.25$ and for the lines a $\Delta M = 0.5$)

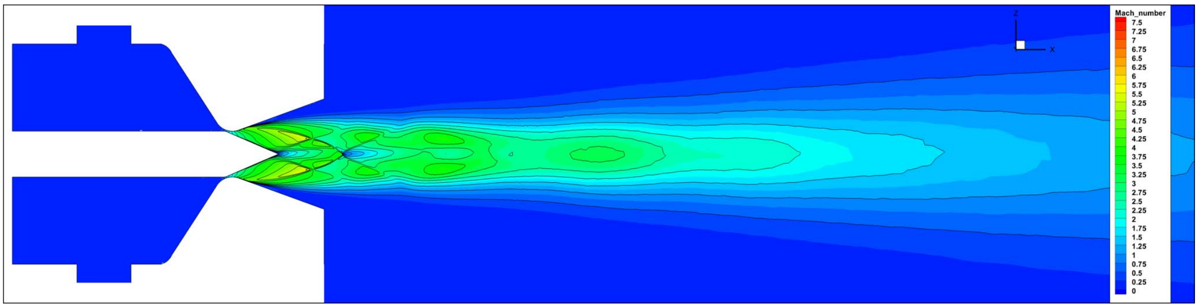

(a) Mach Number

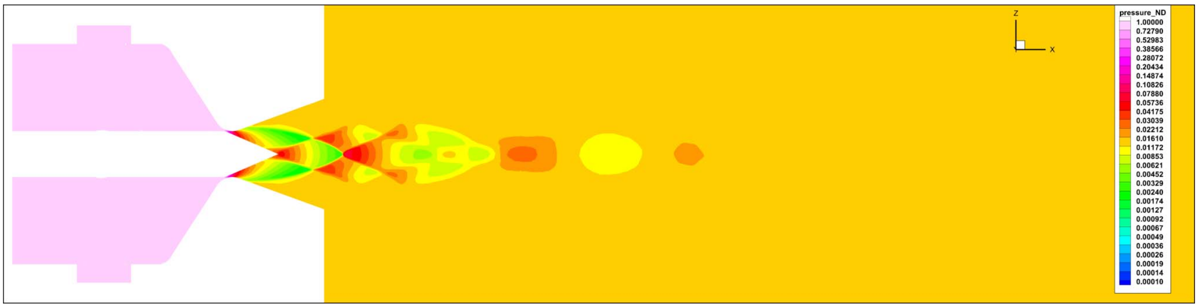

(b) Pressure

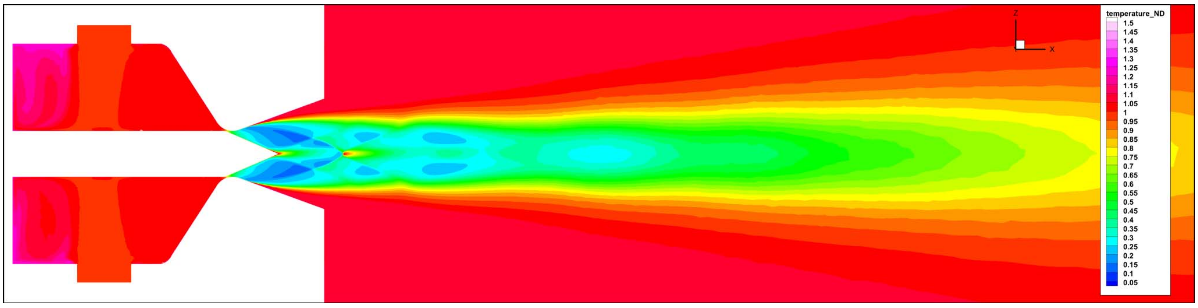

(c) Temperature

Figure B.12: CFD Results ZX-Plane Cut Contour Plot at the 8.33% position (Values have been made dimensionless according to Table A.1, Mach Number ranging from $M = 0.0$ to $M = 7.5$ with $\Delta M = 0.25$ and for the lines a $\Delta M = 0.5$)

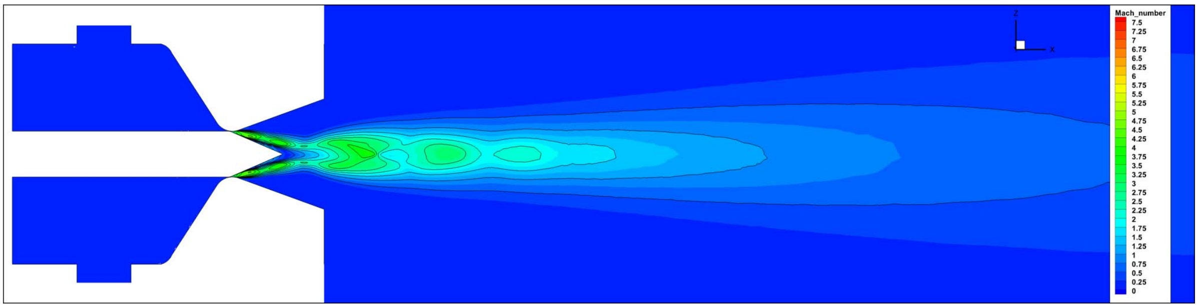

(a) Mach Number

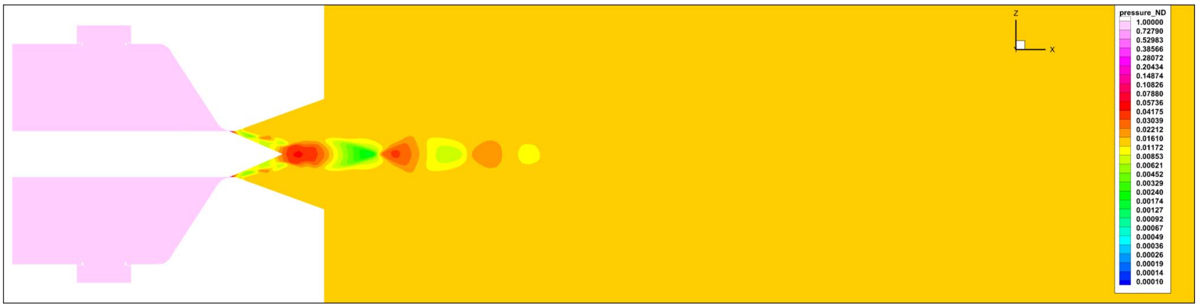

(b) Pressure

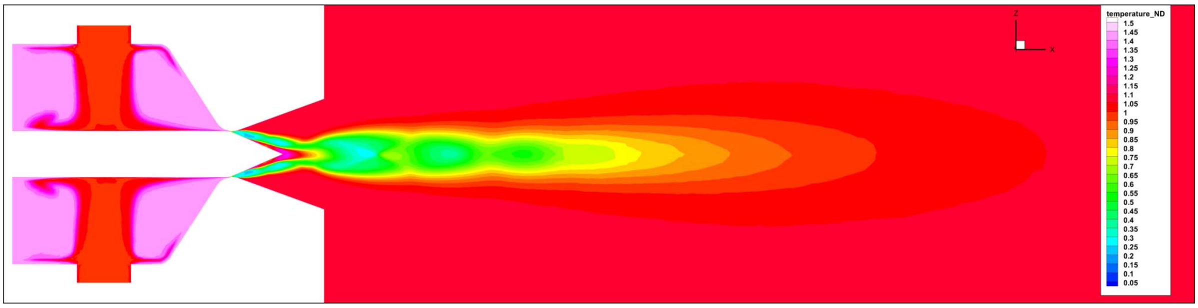

(c) Temperature

Figure B.13: CFD Results ZX-Plane Cut Contour Plot at the 0% position (Values have been made dimensionless according to Table A.1, Mach Number ranging from $M = 0.0$ to $M = 7.5$ with $\Delta M = 0.25$ and for the lines a $\Delta M = 0.5$)

B.2. Chimera CFD Results

Table B.1: Results of the Chimera CFD Simulation with $n = 240$ Time Steps (Values have been made dimensionless according to Table A.1)

No.	t [%]	x_{pin} [%]	T [%]	F_{pin} [%]	$\dot{m}$ [%]	p_{in} [%]	p_{PCC} [%]	p_e [%]	v_e [%]
4	0.0	99.94	89.15	60.84	93.59	96.73	95.96	1.338	90.44
5	1.8	99.86	89.24	60.77	93.67	96.73	95.94	1.338	90.38
6	3.5	99.75	89.24	60.74	93.69	96.72	95.92	1.338	90.32
7	5.3	99.60	89.19	60.72	93.68	96.73	95.92	1.337	90.27
8	7.1	99.42	89.19	60.72	93.63	96.73	95.92	1.337	90.22
9	8.9	99.20	89.19	60.71	93.58	96.73	95.91	1.337	90.17
10	10.6	98.95	89.19	60.67	93.51	96.74	95.92	1.337	90.11
11	12.4	98.66	89.15	60.59	93.44	96.75	95.92	1.337	90.06
12	14.2	98.35	89.15	60.50	93.39	96.75	95.92	1.337	90.01
13	15.9	98.00	89.19	60.41	93.35	96.75	95.92	1.337	89.96
14	17.7	97.61	89.19	60.32	93.30	96.76	95.93	1.338	89.92
15	19.5	97.20	89.24	60.23	93.30	96.76	95.93	1.338	89.88
16	21.2	96.75	89.28	60.15	93.36	96.75	95.94	1.338	89.85
17	23.0	96.27	89.37	60.06	93.45	96.75	95.96	1.339	89.81
18	24.8	95.76	89.47	59.94	93.55	96.74	95.99	1.340	89.78

No.	t [%]	x_{pi} [%]	T [%]	F_{pin} [%]	$\dot{m}$ [%]	p_{in} [%]	p_{PCC} [%]	p_e [%]	v_e [%]
19	26.6	95.22	89.51	59.83	93.65	96.73	96.03	1.340	89.75
20	28.3	94.64	89.56	59.78	93.79	96.72	96.07	1.341	89.73
21	30.1	94.04	89.56	59.74	93.90	96.71	96.13	1.341	89.70
22	31.9	93.40	89.51	59.67	93.90	96.71	96.20	1.340	89.69
23	33.6	92.74	89.47	59.58	93.86	96.71	96.27	1.339	89.69
24	35.4	92.04	89.47	59.50	93.80	96.72	96.35	1.338	89.69
25	37.2	91.32	89.47	59.42	93.56	96.73	96.42	1.338	89.69
26	39.0	90.57	89.37	59.29	92.74	96.79	96.42	1.337	89.68
27	40.7	89.79	89.37	59.12	92.34	96.81	96.37	1.336	89.66
28	42.5	88.98	89.24	58.92	92.72	96.78	96.33	1.334	89.64
29	44.3	88.15	89.10	58.76	93.18	96.75	96.37	1.331	89.63
30	46.0	87.29	89.01	58.55	93.10	96.75	96.44	1.329	89.61
31	47.8	86.41	88.92	58.32	92.72	96.78	96.49	1.327	89.60
32	49.6	85.50	88.79	58.12	92.50	96.80	96.52	1.325	89.58
33	51.3	84.56	88.51	57.89	92.37	96.81	96.52	1.322	89.56
34	53.1	83.60	88.38	57.67	92.14	96.83	96.54	1.316	89.58
35	54.9	82.63	88.29	57.47	91.90	96.85	96.58	1.313	89.60
36	56.7	81.62	88.24	57.24	91.86	96.85	96.61	1.310	89.61
37	58.4	80.60	88.10	57.00	91.80	96.86	96.65	1.308	89.62
38	60.2	79.55	87.92	56.71	91.59	96.87	96.68	1.304	89.63
39	62.0	78.49	87.70	56.37	91.32	96.89	96.71	1.299	89.64
40	63.7	77.40	87.42	56.01	91.02	96.91	96.74	1.294	89.66
41	65.5	76.30	87.20	55.65	90.68	96.93	96.77	1.288	89.67
42	67.3	75.17	86.92	55.25	90.33	96.96	96.79	1.283	89.69
43	69.0	74.03	86.56	54.81	90.00	96.98	96.81	1.275	89.70
44	70.8	72.88	86.11	54.37	89.67	97.00	96.83	1.266	89.73
45	72.6	71.71	85.52	53.89	89.20	97.04	96.86	1.255	89.77
46	74.4	70.52	84.88	53.39	88.53	97.08	96.88	1.242	89.81
47	76.1	69.32	84.25	52.86	87.71	97.14	96.89	1.229	89.86
48	77.9	68.11	83.61	52.29	87.05	97.18	96.91	1.216	89.90
49	79.7	66.88	82.89	51.70	86.63	97.20	96.96	1.202	89.95
50	81.4	65.64	82.16	51.14	86.13	97.23	97.02	1.187	90.02
51	83.2	64.39	81.48	50.62	85.48	97.27	97.09	1.173	90.09
52	85.0	63.13	80.89	50.06	84.69	97.33	97.17	1.160	90.17
53	86.8	61.87	80.21	49.47	83.90	97.38	97.24	1.145	90.23
54	88.5	60.59	79.44	48.82	83.13	97.43	97.31	1.130	90.28
55	90.3	59.31	78.49	48.08	82.27	97.49	97.37	1.113	90.34
56	92.1	58.02	77.49	47.37	81.33	97.55	97.44	1.094	90.41
57	93.8	56.73	76.44	46.67	80.33	97.61	97.50	1.073	90.49
58	95.6	55.43	75.36	45.95	79.29	97.67	97.57	1.052	90.57
59	97.4	54.12	74.22	45.23	78.23	97.74	97.64	1.030	90.65
60	99.1	52.82	73.09	44.48	77.12	97.80	97.71	1.008	90.74
61	100.9	51.51	71.86	43.72	75.98	97.87	97.78	0.985	90.82
62	102.7	50.20	70.59	42.94	74.78	97.94	97.85	0.962	90.89
63	104.5	48.89	69.28	42.14	73.54	98.00	97.92	0.938	90.95
64	106.2	47.58	67.96	41.32	72.27	98.07	98.00	0.915	90.97
65	108.0	46.28	66.65	40.49	70.94	98.14	98.07	0.893	90.92
66	109.8	44.97	65.33	39.64	69.58	98.22	98.15	0.873	90.76
67	111.5	43.67	63.97	38.77	68.16	98.29	98.23	0.852	90.59
68	113.3	42.38	62.61	37.89	66.73	98.36	98.31	0.829	90.47
69	115.1	41.09	61.20	37.00	65.27	98.43	98.38	0.807	90.36
70	116.9	39.80	59.79	36.09	63.76	98.51	98.46	0.787	90.16
71	118.6	38.52	58.39	35.18	62.23	98.58	98.54	0.772	89.76
72	120.4	37.25	56.94	34.25	60.67	98.65	98.61	0.760	89.11
73	122.2	35.99	55.44	33.31	59.08	98.72	98.69	0.752	88.25
74	123.9	34.74	53.99	32.37	57.46	98.79	98.77	0.746	87.29
75	125.7	33.50	52.49	31.42	55.82	98.86	98.84	0.741	86.28
76	127.5	32.27	50.95	30.45	54.15	98.93	98.91	0.739	85.21
77	129.2	31.05	49.41	29.48	52.47	98.99	98.98	0.738	84.17
78	131.0	29.85	47.86	28.49	50.78	99.06	99.05	0.737	83.25

No.	t [%]	x_{pi} [%]	T [%]	F_{pin} [%]	$\dot{m}$ [%]	p_{in} [%]	p_{PCC} [%]	p_e [%]	v_e [%]
79	132.8	28.66	46.28	27.49	49.08	99.12	99.11	0.737	82.29
80	134.6	27.48	44.69	26.48	47.36	99.18	99.18	0.738	81.18
81	136.3	26.32	43.09	25.46	45.63	99.24	99.23	0.742	79.84
82	138.1	25.17	41.49	24.44	43.90	99.30	99.29	0.751	78.22
83	139.9	24.05	39.90	23.41	42.15	99.35	99.34	0.766	76.30
84	141.6	22.94	38.30	22.38	40.44	99.40	99.39	0.785	74.21
85	143.4	21.85	36.70	21.35	38.69	99.45	99.44	0.805	72.02
86	145.2	20.77	35.11	20.32	36.93	99.50	99.48	0.828	69.73
87	147.0	19.72	33.51	19.28	35.17	99.55	99.53	0.854	67.30
88	148.7	18.69	31.94	18.26	33.47	99.59	99.56	0.881	64.74
89	150.5	17.68	30.34	17.22	31.75	99.63	99.60	0.913	61.91
90	152.3	16.69	28.76	16.20	30.09	99.67	99.63	0.948	58.89
91	154.0	15.73	27.20	15.21	28.44	99.70	99.67	0.985	55.76
92	155.8	14.79	25.67	14.22	26.81	99.74	99.69	1.024	52.47
93	157.6	13.87	24.15	13.25	25.19	99.77	99.72	1.066	49.13
94	159.3	12.98	22.66	12.32	23.59	99.79	99.75	1.110	45.76
95	161.1	12.11	21.20	11.41	22.09	99.82	99.77	1.157	42.31
96	162.9	11.27	19.80	10.59	20.62	99.84	99.79	1.204	39.11
97	164.7	10.46	18.46	9.78	19.19	99.86	99.80	1.252	35.96
98	166.4	9.67	17.19	9.08	17.91	99.88	99.82	1.293	33.17
99	168.2	8.91	16.00	8.39	16.68	99.89	99.83	1.333	30.41
100	170.0	8.18	14.89	7.79	15.54	99.91	99.84	1.365	28.18
101	171.7	7.47	13.82	7.18	14.47	99.92	99.85	1.397	25.59
102	173.5	6.80	12.86	6.70	13.48	99.93	99.86	1.417	23.95
103	175.3	6.16	11.95	6.19	12.59	99.94	99.87	1.439	21.94
104	177.0	5.54	11.12	5.76	11.74	99.95	99.88	1.474	20.12
105	178.8	4.96	10.34	5.35	10.95	99.95	99.88	1.490	18.74
106	180.6	4.41	9.61	4.93	10.26	99.96	99.89	1.506	16.88
107	182.4	3.88	8.97	4.63	9.60	99.96	99.90	1.510	15.96
108	184.1	3.39	8.37	4.30	9.00	99.97	99.90	1.506	15.19
109	185.9	2.94	7.80	3.97	8.48	99.97	99.91	1.473	15.13
110	187.7	2.51	7.32	3.73	7.99	99.97	99.91	1.426	16.09
111	189.4	2.12	6.88	3.52	7.52	99.98	99.91	1.385	16.88
112	191.2	1.76	6.50	3.34	7.16	99.98	99.92	1.340	18.39
113	193.0	1.43	6.18	3.17	6.83	99.98	99.92	1.350	17.42
114	194.8	1.13	5.93	3.05	6.53	99.98	99.92	1.369	16.06
115	196.5	0.87	5.69	2.95	6.23	99.98	99.92	1.373	15.69
116	198.3	0.65	5.48	2.84	5.99	99.98	99.92	1.371	15.53
117	200.1	0.46	5.29	2.74	5.77	99.98	99.93	1.368	15.44
118	201.8	0.30	5.14	2.65	5.64	99.99	99.93	1.362	15.40
119	203.6	0.17	5.02	2.58	5.53	99.99	99.93	1.358	15.36
120	205.4	0.08	4.92	2.52	5.44	99.99	99.93	1.353	15.34
121	207.1	0.02	4.87	2.49	5.41	99.99	99.93	1.349	15.40
122	208.9	0.00	4.85	2.47	5.39	99.99	99.93	1.347	15.41
123	210.7	0.01	4.86	2.48	5.41	99.99	99.93	1.348	15.40
124	212.5	0.06	4.91	2.51	5.44	99.99	99.92	1.351	15.39
125	214.2	0.14	5.01	2.55	5.52	99.99	99.92	1.356	15.37
126	216.0	0.25	5.12	2.62	5.61	99.99	99.92	1.362	15.40
127	217.8	0.40	5.28	2.70	5.77	99.98	99.92	1.369	15.36
128	219.5	0.58	5.46	2.80	5.94	99.98	99.92	1.374	15.37
129	221.3	0.80	5.68	2.91	6.20	99.98	99.92	1.380	15.37
130	223.1	1.05	5.93	3.01	6.50	99.98	99.92	1.386	15.40
131	224.9	1.34	6.21	3.14	6.79	99.98	99.92	1.392	15.52
132	226.6	1.65	6.53	3.33	7.11	99.98	99.92	1.380	16.80
133	228.4	2.00	6.86	3.50	7.48	99.98	99.91	1.375	17.54
134	230.2	2.39	7.26	3.67	7.93	99.97	99.91	1.411	16.56
135	231.9	2.80	7.73	3.88	8.44	99.97	99.91	1.453	15.48
136	233.7	3.25	8.28	4.19	8.95	99.97	99.90	1.507	14.98
137	235.5	3.73	8.87	4.52	9.52	99.96	99.90	1.516	15.58
138	237.2	4.24	9.50	4.83	10.20	99.96	99.90	1.516	16.31

No.	t [%]	x_{pi} [%]	T [%]	F_{pin} [%]	$\dot{m}$ [%]	p_{in} [%]	p_{PCC} [%]	p_e [%]	v_e [%]
139	239.0	4.79	10.21	5.21	10.91	99.95	99.89	1.507	17.66
140	240.8	5.36	10.98	5.62	11.64	99.95	99.89	1.490	19.10
141	242.6	5.96	11.64	6.02	12.47	99.94	99.87	1.468	20.18
142	244.3	6.60	12.48	6.52	13.53	99.93	99.87	1.432	22.39
143	246.1	7.26	13.42	7.01	14.46	99.92	99.86	1.415	24.04
144	247.9	7.96	14.45	7.58	15.49	99.91	99.85	1.388	26.15
145	249.6	8.68	15.54	8.18	16.66	99.90	99.84	1.360	28.26
146	251.4	9.43	16.70	8.83	17.89	99.88	99.83	1.326	30.76
147	253.2	10.21	17.95	9.54	19.15	99.87	99.82	1.289	33.39
148	255.0	11.02	19.26	10.29	20.51	99.85	99.80	1.249	36.21
149	256.7	11.85	20.63	11.11	21.99	99.82	99.78	1.206	39.28
150	258.5	12.71	22.08	11.99	23.47	99.80	99.76	1.162	42.52
151	260.3	13.59	23.54	12.92	25.00	99.77	99.73	1.121	45.66
152	262.0	14.50	25.05	13.88	26.60	99.74	99.71	1.082	48.80
153	263.8	15.44	27.75	14.83	27.95	99.72	99.63	1.051	51.36
154	265.6	16.40	28.74	15.83	29.71	99.68	99.60	1.017	54.30
155	267.3	17.38	30.36	16.85	31.46	99.64	99.57	0.986	57.13
156	269.1	18.38	32.07	17.88	33.07	99.60	99.53	0.958	59.81
157	270.9	19.40	33.59	18.92	34.65	99.56	99.50	0.933	62.35
158	272.7	20.45	35.21	19.97	36.32	99.52	99.45	0.910	64.76
159	274.4	21.52	36.78	21.00	38.03	99.47	99.40	0.889	67.02
160	276.2	22.60	38.39	22.03	39.76	99.43	99.35	0.870	69.20
161	278.0	23.71	39.96	23.06	41.48	99.37	99.30	0.852	71.27
162	279.7	24.83	41.54	24.07	43.19	99.32	99.25	0.836	73.27
163	281.5	25.97	43.11	25.08	44.92	99.27	99.19	0.822	75.20
164	283.3	27.12	44.68	26.08	46.63	99.21	99.14	0.811	76.98
165	285.1	28.29	46.23	27.08	48.29	99.15	99.08	0.805	78.56
166	286.8	29.48	47.77	28.07	49.93	99.09	99.02	0.801	79.91
167	288.6	30.68	49.31	29.05	51.57	99.03	98.95	0.800	81.08
168	290.4	31.90	50.86	30.04	53.19	98.97	98.88	0.800	82.08
169	292.1	33.12	52.35	31.01	54.80	98.91	98.81	0.802	82.99
170	293.9	34.36	53.85	31.98	56.41	98.84	98.74	0.805	83.92
171	295.7	35.61	55.35	32.94	57.98	98.77	98.67	0.808	84.90
172	297.4	36.87	56.76	33.90	59.53	98.71	98.59	0.813	85.85
173	299.2	38.13	58.21	34.84	61.06	98.64	98.51	0.820	86.71
174	301.0	39.41	59.57	35.76	62.57	98.57	98.43	0.829	87.53
175	302.8	40.69	60.93	36.67	64.07	98.50	98.35	0.837	88.29
176	304.5	41.98	62.24	37.56	65.54	98.43	98.27	0.848	88.97
177	306.3	43.28	63.52	38.43	66.97	98.36	98.20	0.858	89.60
178	308.1	44.58	64.79	39.29	68.37	98.29	98.12	0.867	90.26
179	309.8	45.88	66.01	40.14	69.74	98.22	98.05	0.874	90.88
180	311.6	47.18	67.24	40.97	71.07	98.15	97.97	0.888	91.19
181	313.4	48.49	68.51	41.79	72.36	98.08	97.90	0.910	91.22
182	315.1	49.80	69.78	42.60	73.62	98.01	97.83	0.935	91.12
183	316.9	51.11	71.05	43.39	74.84	97.94	97.76	0.960	90.99
184	318.7	52.42	72.27	44.16	76.01	97.87	97.69	0.985	90.86
185	320.5	53.72	73.45	44.92	77.15	97.81	97.63	1.009	90.73
186	322.2	55.03	74.63	45.66	78.23	97.74	97.56	1.032	90.61
187	324.0	56.33	75.72	46.38	79.27	97.68	97.49	1.054	90.50
188	325.8	57.62	76.81	47.09	80.25	97.62	97.43	1.076	90.39
189	327.5	58.92	77.81	47.78	81.17	97.57	97.36	1.096	90.30
190	329.3	60.20	78.67	48.45	82.03	97.51	97.30	1.115	90.21
191	331.1	61.48	79.48	49.07	82.81	97.46	97.23	1.132	90.12
192	332.9	62.75	80.26	49.67	83.54	97.42	97.17	1.148	90.04
193	334.6	64.01	81.03	50.26	84.22	97.37	97.10	1.164	89.96
194	336.4	65.26	81.75	50.84	84.87	97.33	97.04	1.179	89.88
195	338.2	66.50	82.48	51.42	85.52	97.29	96.98	1.194	89.81
196	339.9	67.73	83.16	51.99	86.19	97.25	96.91	1.208	89.74
197	341.7	68.95	83.79	52.54	86.91	97.20	96.86	1.220	89.67
198	343.5	70.15	84.34	53.06	87.66	97.15	96.82	1.232	89.62

No.	t [%]	x_{pi} [%]	T [%]	F_{pin} [%]	$\dot{m}$ [%]	p_{in} [%]	p_{PCC} [%]	p_e [%]	v_e [%]
199	345.2	71.35	84.84	53.57	88.46	97.09	96.81	1.242	89.57
200	347.0	72.52	85.38	54.08	89.69	97.01	96.84	1.250	89.55
201	348.8	73.68	85.97	54.55	90.06	96.99	96.88	1.260	89.54
202	350.6	74.83	86.34	54.99	89.94	96.99	96.89	1.269	89.52
203	352.3	75.96	86.74	55.40	89.89	97.00	96.87	1.278	89.48
204	354.1	77.06	87.20	55.75	90.09	96.98	96.81	1.288	89.45
205	355.9	78.16	87.65	56.14	90.47	96.96	96.74	1.299	89.41
206	357.6	79.23	87.92	56.51	90.89	96.93	96.68	1.307	89.36
207	359.4	80.28	88.15	56.84	91.29	96.90	96.64	1.312	89.33
208	361.2	81.31	88.33	57.14	91.63	96.87	96.62	1.316	89.31
209	363.0	82.32	88.56	57.43	91.94	96.85	96.60	1.320	89.29
210	364.7	83.31	88.74	57.71	92.22	96.83	96.59	1.323	89.28
211	366.5	84.27	88.92	57.99	92.43	96.81	96.58	1.327	89.27
212	368.3	85.21	89.01	58.25	92.55	96.80	96.58	1.330	89.26
213	370.0	86.13	89.06	58.49	92.58	96.80	96.57	1.331	89.25
214	371.8	87.02	89.10	58.72	92.58	96.80	96.56	1.332	89.24
215	373.6	87.89	89.15	58.94	92.59	96.80	96.55	1.334	89.23
216	375.3	88.73	89.24	59.10	92.57	96.80	96.54	1.336	89.22
217	377.1	89.55	89.28	59.23	92.52	96.80	96.53	1.337	89.20
218	378.9	90.33	89.24	59.30	92.58	96.79	96.52	1.337	89.19
219	380.7	91.09	89.24	59.37	92.75	96.78	96.53	1.336	89.19
220	382.4	91.82	89.28	59.50	92.97	96.76	96.55	1.337	89.21
221	384.2	92.53	89.42	59.69	93.14	96.74	96.58	1.338	89.22
222	386.0	93.20	89.56	59.88	93.19	96.74	96.62	1.340	89.24
223	387.7	93.85	89.69	60.06	93.19	96.74	96.65	1.341	89.25
224	389.5	94.46	89.74	60.23	93.21	96.74	96.68	1.341	89.25
225	391.3	95.04	89.78	60.42	93.27	96.74	96.71	1.343	89.26
226	393.1	95.60	89.92	60.59	93.33	96.74	96.73	1.345	89.26
227	394.8	96.12	90.01	60.73	93.32	96.74	96.75	1.347	89.26
228	396.6	96.61	90.06	60.83	93.24	96.75	96.75	1.349	89.25
229	398.4	97.07	90.10	60.92	93.15	96.76	96.73	1.351	89.23
230	400.1	97.49	90.15	60.98	93.09	96.76	96.71	1.352	89.22
231	401.9	97.88	90.15	61.04	93.03	96.77	96.68	1.352	89.21
232	403.7	98.24	90.10	61.08	92.99	96.77	96.64	1.352	89.20
233	405.4	98.57	90.01	61.11	92.96	96.77	96.61	1.352	89.19
234	407.2	98.87	89.96	61.13	92.94	96.77	96.58	1.351	89.18
235	409.0	99.13	89.87	61.14	92.91	96.77	96.55	1.350	89.18
236	410.8	99.35	89.83	61.13	92.87	96.77	96.53	1.349	89.18
237	412.5	99.55	89.78	61.11	92.88	96.77	96.51	1.347	89.18
238	414.3	99.70	89.87	61.11	92.99	96.77	96.50	1.347	89.20
239	416.1	99.83	90.01	61.14	93.19	96.75	96.51	1.348	89.21
240	417.8	99.92	90.15	61.19	93.43	96.73	96.52	1.351	89.21
241	419.6	99.98	90.28	61.25	93.64	96.72	96.53	1.353	89.20
242	421.4	100.00	90.37	61.30	93.77	96.71	96.55	1.356	89.19

Table B.2: Results of the Chimera CFD Simulation with $n = 120$ Time Steps (Values have been made dimensionless according to Table A.1)

No.	t [%]	x_{pin} [%]	T [%]	F_{pin} [%]	$\dot{m}$ [%]	p_{in} [%]	p_{PCC} [%]	p_e [%]	v_e [%]
4	0.0	99.86	89.19	60.92	93.61	96.73	95.94	1.338	90.36
5	3.5	99.60	89.15	60.88	93.59	96.73	95.92	1.337	90.24
6	7.1	99.20	89.15	60.83	93.50	96.74	95.91	1.337	90.13
7	10.6	98.66	89.19	60.68	93.42	96.75	95.91	1.338	90.02
8	14.2	98.00	89.24	60.48	93.45	96.75	95.92	1.339	89.92
9	17.7	97.20	89.33	60.27	93.59	96.74	95.98	1.339	89.83
10	21.2	96.27	89.37	60.12	93.82	96.72	96.08	1.340	89.77
11	24.8	95.22	89.37	60.05	93.68	96.73	96.21	1.340	89.72

No.	t [%]	x_{pi} [%]	T [%]	F_{pin} [%]	$\dot{m}$ [%]	p_{in} [%]	p_{PCC} [%]	p_e [%]	v_e [%]
12	28.3	94.04	89.33	60.00	93.61	96.73	96.34	1.338	89.71
13	31.9	92.74	89.56	59.89	93.32	96.75	96.41	1.339	89.69
14	35.4	91.32	89.51	59.70	93.40	96.74	96.46	1.338	89.65
15	39.0	89.79	89.33	59.41	93.13	96.75	96.52	1.336	89.59
16	42.5	88.15	89.19	59.13	93.07	96.76	96.58	1.333	89.55
17	46.0	86.41	88.97	58.74	92.71	96.79	96.67	1.329	89.55
18	49.6	84.56	88.97	58.32	92.41	96.81	96.69	1.327	89.52
19	53.1	82.63	88.65	57.72	92.11	96.83	96.66	1.320	89.51
20	56.7	80.60	88.24	57.11	91.63	96.87	96.64	1.312	89.53
21	60.2	78.49	87.70	56.43	91.17	96.90	96.64	1.301	89.55
22	63.7	76.30	87.06	55.67	90.72	96.92	96.71	1.288	89.60
23	67.3	74.03	86.29	54.80	89.96	96.96	96.81	1.272	89.66
24	70.8	71.71	85.34	53.78	89.15	97.01	96.93	1.253	89.74
25	74.4	69.32	84.43	52.77	88.52	97.06	97.11	1.234	89.83
26	77.9	66.88	83.30	51.81	87.00	97.18	97.23	1.211	89.91
27	81.4	64.39	81.93	50.77	85.28	97.30	97.21	1.184	89.99
28	85.0	61.87	80.12	49.58	83.84	97.39	97.24	1.150	90.11
29	88.5	59.31	78.26	48.27	82.16	97.50	97.32	1.113	90.26
30	92.1	56.73	76.26	46.87	80.31	97.61	97.43	1.074	90.43
31	95.6	54.12	74.00	45.39	78.32	97.73	97.57	1.031	90.60
32	99.1	51.51	71.55	43.88	76.23	97.85	97.74	0.984	90.79
33	102.7	48.89	68.96	42.29	73.86	97.98	97.92	0.937	90.95
34	106.2	46.28	66.24	40.60	71.24	98.13	98.11	0.891	90.95
35	109.8	43.67	63.52	38.84	68.44	98.27	98.28	0.850	90.61
36	113.3	41.09	60.70	37.05	65.50	98.42	98.45	0.805	90.36
37	116.9	38.52	57.84	35.25	62.42	98.57	98.62	0.773	89.63
38	120.4	35.99	54.94	33.40	59.27	98.71	98.76	0.754	88.08
39	123.9	33.50	51.99	31.50	56.08	98.85	98.90	0.743	86.15
40	127.5	31.05	48.95	29.54	52.85	98.98	99.03	0.740	84.08
41	131.0	28.66	45.78	27.54	49.57	99.10	99.15	0.738	82.22
42	134.6	26.32	42.58	25.49	46.25	99.22	99.26	0.744	79.74
43	138.1	24.05	39.35	23.44	42.84	99.33	99.37	0.769	76.11
44	141.6	21.85	36.14	21.38	39.43	99.43	99.46	0.809	71.82
45	145.2	19.72	32.96	19.31	36.00	99.53	99.55	0.857	67.05
46	148.7	17.68	29.82	17.25	32.63	99.61	99.63	0.917	61.64
47	152.3	15.73	26.74	15.24	29.38	99.69	99.69	0.988	55.53
48	155.8	13.87	23.75	13.28	26.22	99.75	99.75	1.069	48.99
49	159.3	12.11	20.85	11.42	23.17	99.80	99.79	1.159	42.23
50	162.9	10.46	18.15	9.80	20.29	99.85	99.82	1.253	35.88
51	166.4	8.91	15.74	8.40	17.71	99.88	99.85	1.334	30.34
52	170.0	7.47	13.61	7.19	15.43	99.91	99.87	1.397	25.51
53	173.5	6.16	11.77	6.20	13.44	99.93	99.89	1.439	21.95
54	177.1	4.96	10.21	5.36	11.71	99.95	99.90	1.490	18.76
55	180.6	3.88	8.88	4.63	10.24	99.96	99.91	1.511	16.02
56	184.1	2.94	7.73	3.97	9.02	99.97	99.92	1.477	15.10
57	187.7	2.12	6.83	3.52	7.99	99.97	99.92	1.386	16.85
58	191.2	1.43	6.16	3.18	7.19	99.98	99.92	1.361	16.86
59	194.8	0.87	5.68	2.94	6.54	99.98	99.93	1.375	15.64
60	198.3	0.46	5.27	2.73	6.02	99.98	99.93	1.368	15.45
61	201.8	0.17	5.01	2.58	5.68	99.98	99.93	1.358	15.37
62	205.4	0.02	4.87	2.49	5.48	99.99	99.93	1.349	15.37
63	208.9	0.01	4.86	2.48	5.42	99.99	99.93	1.348	15.35
64	212.5	0.14	5.00	2.56	5.47	99.99	99.93	1.356	15.31
65	216.0	0.40	5.28	2.70	5.65	99.99	99.92	1.368	15.26
66	219.5	0.80	5.70	2.91	5.99	99.98	99.92	1.380	15.29
67	223.1	1.34	6.23	3.14	6.51	99.98	99.92	1.387	15.60
68	226.6	2.00	6.90	3.50	7.14	99.98	99.91	1.375	17.39
69	230.2	2.80	7.79	3.89	7.99	99.97	99.90	1.452	15.49
70	233.7	3.73	8.96	4.52	9.01	99.97	99.90	1.515	15.47
71	237.2	4.79	10.33	5.22	10.29	99.96	99.88	1.506	17.53

No.	t [%]	x_{pi} [%]	T [%]	F_{pin} [%]	$\dot{m}$ [%]	p_{in} [%]	p_{PCC} [%]	p_e [%]	v_e [%]
72	240.8	5.96	12.16	6.03	12.97	99.94	99.89	1.475	20.12
73	244.3	7.26	14.12	7.03	14.66	99.92	99.86	1.419	24.00
74	247.9	8.68	16.33	8.20	16.91	99.90	99.85	1.364	28.30
75	251.4	10.21	19.44	9.53	18.00	99.88	99.73	1.300	32.07
76	255.0	11.85	22.52	11.11	21.83	99.82	99.61	1.216	38.13
77	258.5	13.59	25.41	12.92	26.11	99.75	99.58	1.135	44.34
78	262.0	15.44	28.46	14.83	28.95	99.69	99.57	1.059	50.56
79	265.6	17.38	31.78	16.79	31.43	99.64	99.49	0.996	56.44
80	269.1	19.40	35.17	18.88	34.81	99.56	99.38	0.941	61.82
81	272.7	21.52	38.35	20.99	38.58	99.46	99.29	0.894	66.61
82	276.2	23.71	41.59	23.07	41.93	99.36	99.21	0.856	70.94
83	279.7	25.97	44.81	25.14	45.01	99.26	99.11	0.827	74.88
84	283.3	28.29	47.86	27.16	48.30	99.15	98.99	0.810	78.34
85	286.8	30.68	50.81	29.13	51.74	99.03	98.86	0.809	80.76
86	290.4	33.12	53.67	31.03	55.08	98.90	98.73	0.811	82.63
87	293.9	35.61	56.39	32.89	58.24	98.76	98.60	0.815	84.55
88	297.4	38.13	59.16	34.76	61.17	98.63	98.45	0.825	86.44
89	301.0	40.69	61.97	36.62	64.00	98.50	98.29	0.842	88.04
90	304.5	43.28	64.74	38.46	66.91	98.36	98.13	0.862	89.42
91	308.1	45.88	67.42	40.25	69.72	98.22	97.98	0.876	90.77
92	311.6	48.49	69.91	41.96	72.31	98.08	97.83	0.903	91.41
93	315.1	51.11	72.32	43.56	74.75	97.94	97.68	0.952	91.22
94	318.7	53.72	74.68	45.09	77.07	97.81	97.53	1.002	90.93
95	322.2	56.33	76.90	46.53	79.25	97.68	97.39	1.050	90.65
96	325.8	58.92	78.94	47.89	81.24	97.56	97.26	1.093	90.40
97	329.3	61.48	80.71	49.19	83.05	97.45	97.14	1.134	90.19
98	332.9	64.01	82.34	50.42	84.71	97.34	97.03	1.169	90.00
99	336.4	66.50	83.75	51.58	86.21	97.25	96.94	1.201	89.84
100	339.9	68.95	84.97	52.65	87.51	97.16	96.85	1.229	89.70
101	343.5	71.35	85.97	53.63	88.59	97.09	96.77	1.252	89.58
102	347.0	73.68	86.79	54.52	89.46	97.03	96.69	1.271	89.48
103	350.6	75.96	87.33	55.29	90.13	96.98	96.62	1.285	89.40
104	354.1	78.16	87.88	56.01	90.69	96.94	96.55	1.296	89.34
105	357.6	80.28	88.33	56.68	91.22	96.91	96.50	1.304	89.29
106	361.2	82.32	88.74	57.31	91.68	96.87	96.46	1.312	89.25
107	364.7	84.27	89.06	57.90	92.11	96.84	96.43	1.318	89.22
108	368.3	86.13	89.37	58.44	92.62	96.80	96.42	1.323	89.20
109	371.8	87.89	89.60	58.95	93.01	96.78	96.43	1.327	89.18
110	375.3	89.55	89.69	59.37	93.10	96.77	96.45	1.329	89.19
111	378.9	91.09	89.78	59.72	92.90	96.79	96.46	1.332	89.20
112	382.4	92.53	89.78	60.02	92.79	96.79	96.45	1.336	89.20
113	386.0	93.85	89.78	60.23	92.81	96.79	96.43	1.338	89.19
114	389.5	95.04	89.78	60.42	92.90	96.79	96.42	1.339	89.19
115	393.1	96.12	89.78	60.60	93.11	96.77	96.42	1.341	89.20
116	396.6	97.07	89.83	60.75	93.35	96.75	96.42	1.343	89.20
117	400.1	97.88	89.83	60.89	93.54	96.74	96.44	1.345	89.20
118	403.7	98.57	89.83	61.00	93.59	96.73	96.46	1.346	89.20
119	407.2	99.13	89.78	61.09	93.48	96.74	96.48	1.347	89.21
120	410.8	99.55	89.74	61.17	93.33	96.75	96.49	1.347	89.21
121	414.3	99.83	89.69	61.24	93.27	96.75	96.50	1.348	89.21
122	417.8	99.98	89.69	61.29	93.30	96.75	96.51	1.348	89.22
123	421.4	99.99	89.69	61.30	93.31	96.75	96.52	1.347	89.22

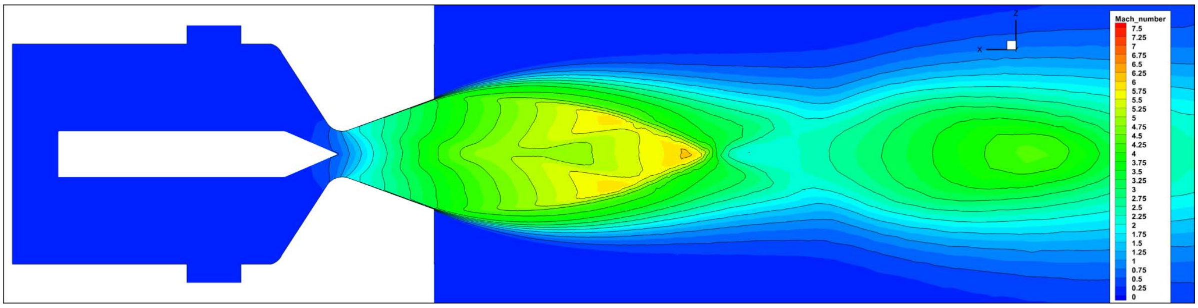

(a) At: $t = 0.0\%$ and $x_{pin} = 99.9\%$

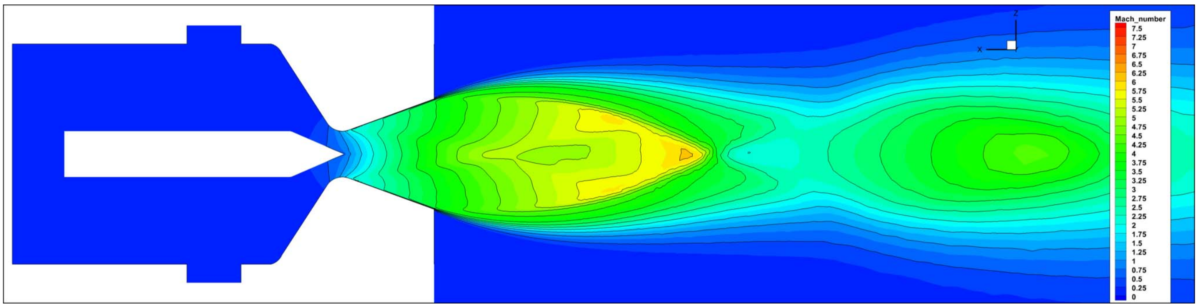

(b) At: $t = 42.49\%$ and $x_{pin} = 89.0\%$

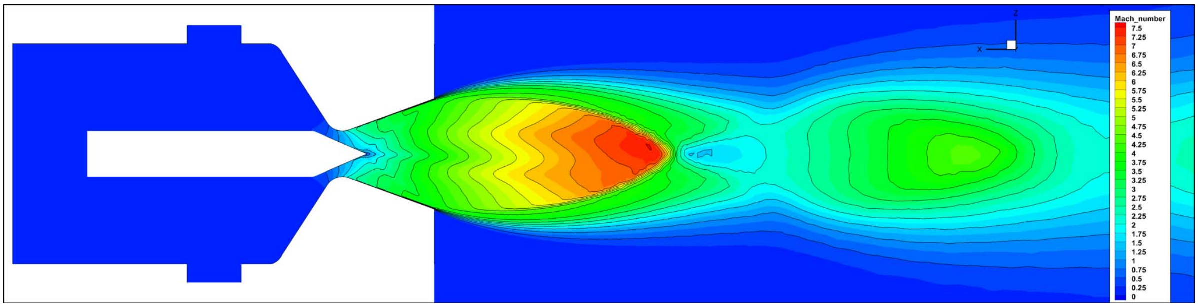

(c) At: $t = 106.23\%$ and $x_{pin} = 47.6\%$

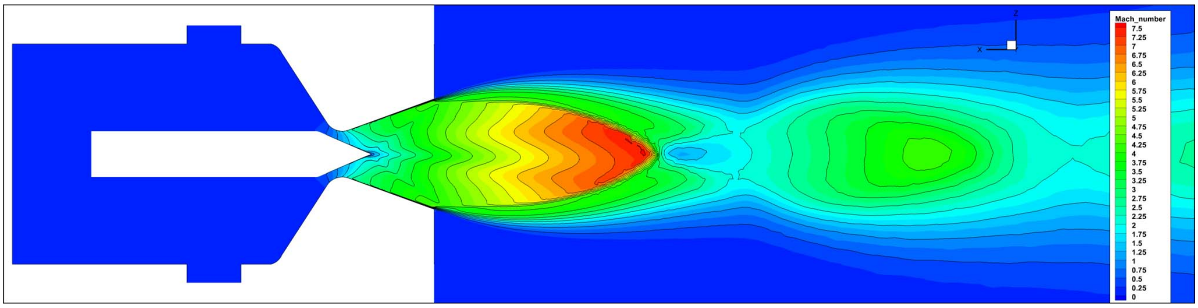

(d) At: $t = 116.85\%$ and $x_{pin} = 39.8\%$

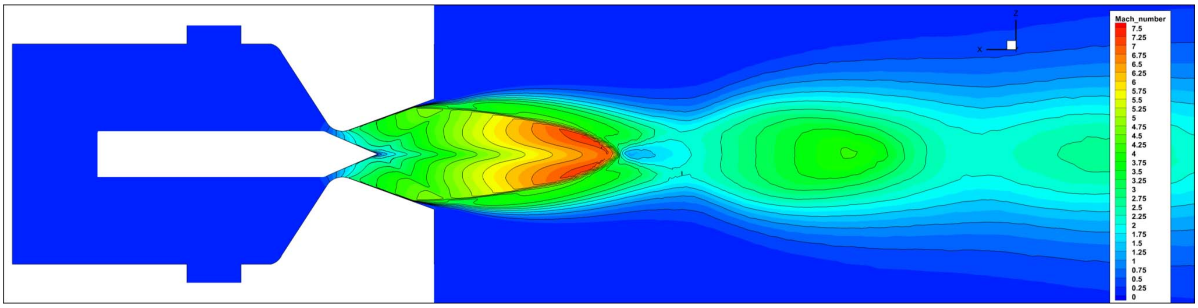

(e) At: $t = 132.79\%$ and $x_{pin} = 28.7\%$

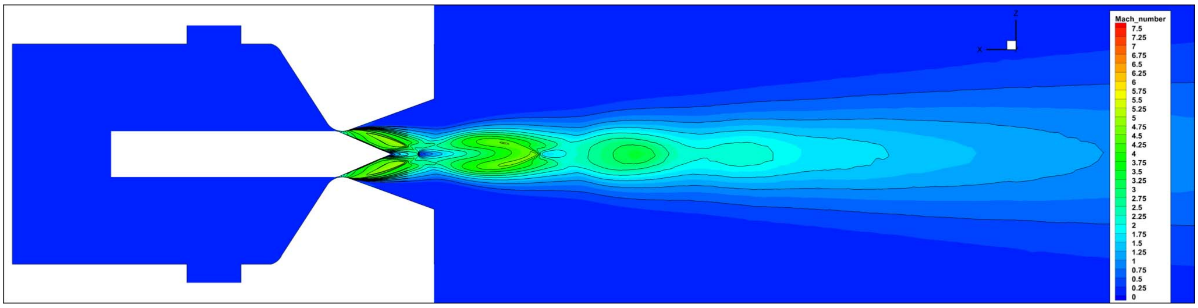

(f) At: $t = 182.36\%$ and $x_{pin} = 3.9\%$

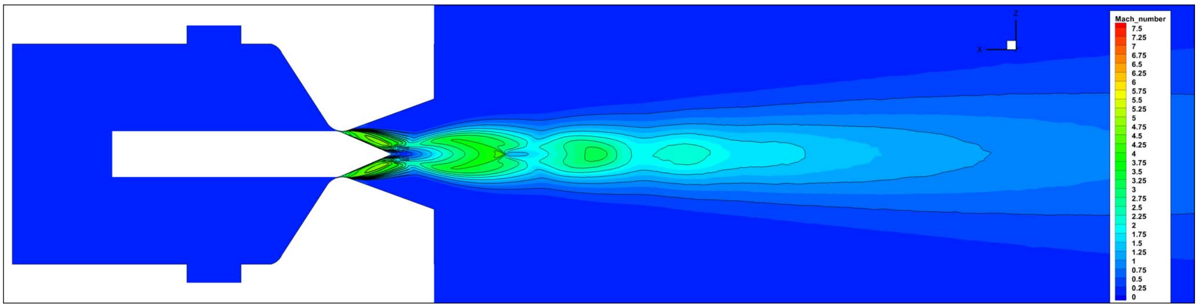

(g) At: $t = 191.21\%$ and $x_{pin} = 1.8\%$

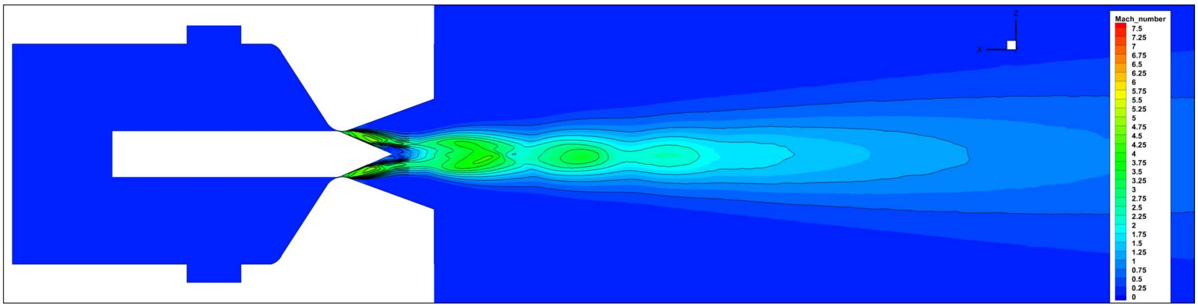

(h) At: $t = 192.98\%$ and $x_{pin} = 1.4\%$

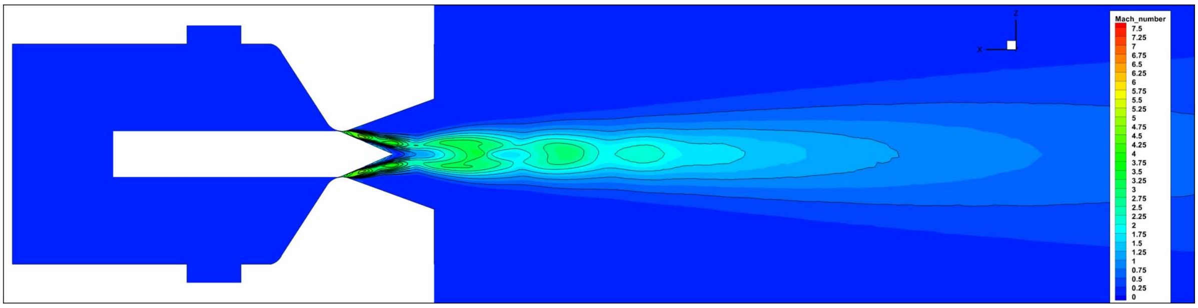

(i) At: $t = 208.92\%$ and $x_{pin} = 0.0\%$

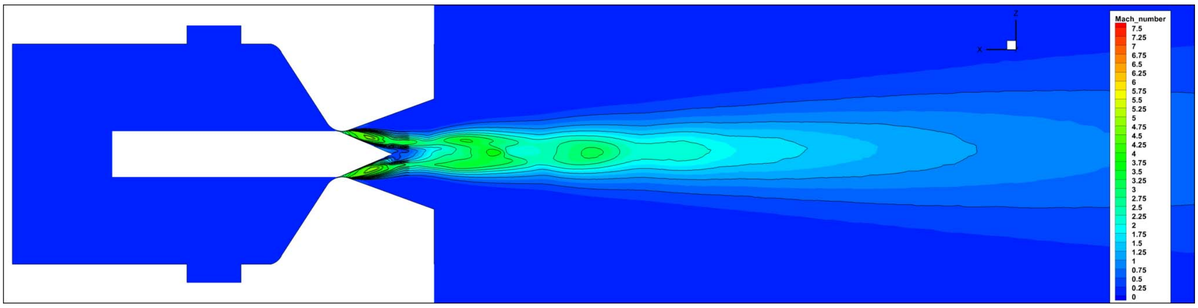

(j) At: $t = 226.62\%$ and $x_{pin} = 1.7\%$

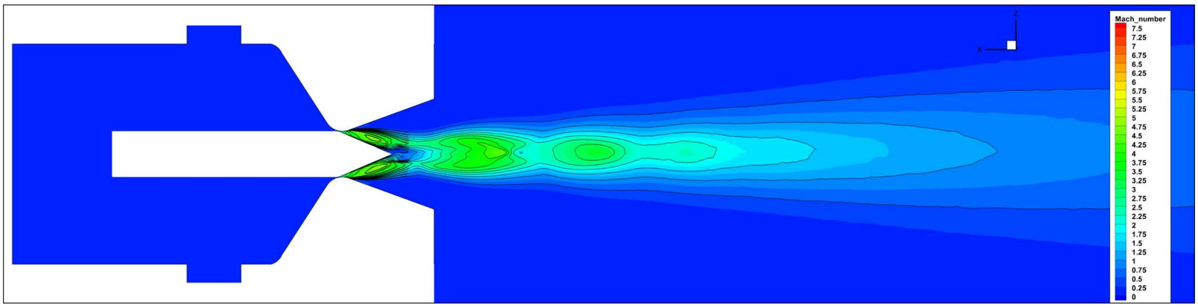

(k) At: $t = 228.40\%$ and $x_{pin} = 2.0\%$

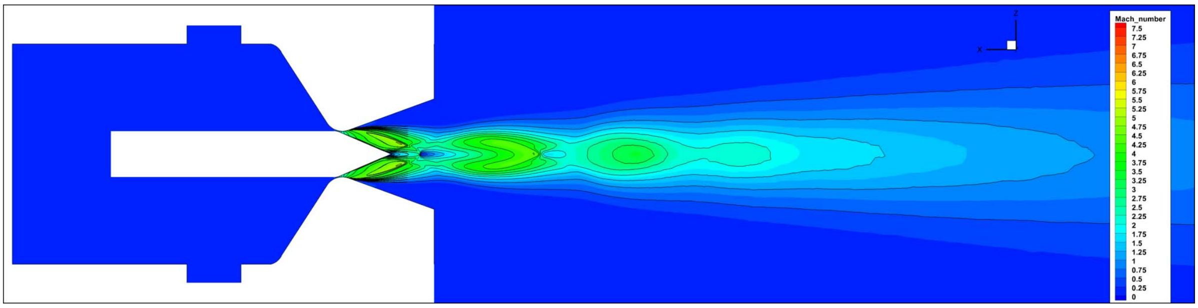

(l) At: $t = 237.25\%$ and $x_{pin} = 4.2\%$

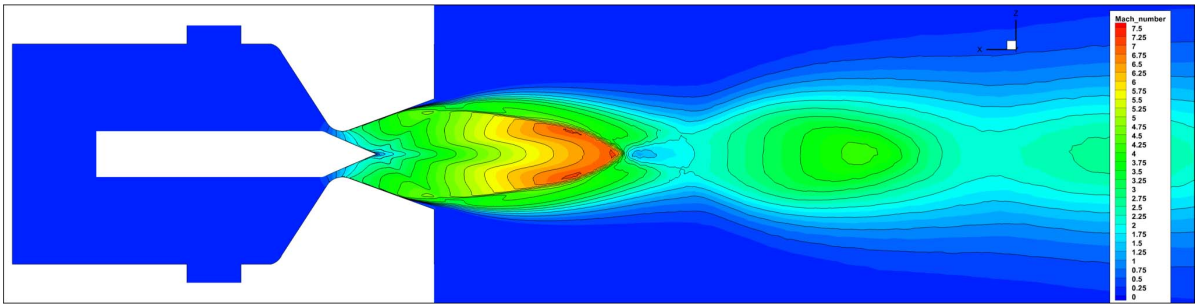

(m) At: $t = 288.60\%$ and $x_{pin} = 30.7\%$

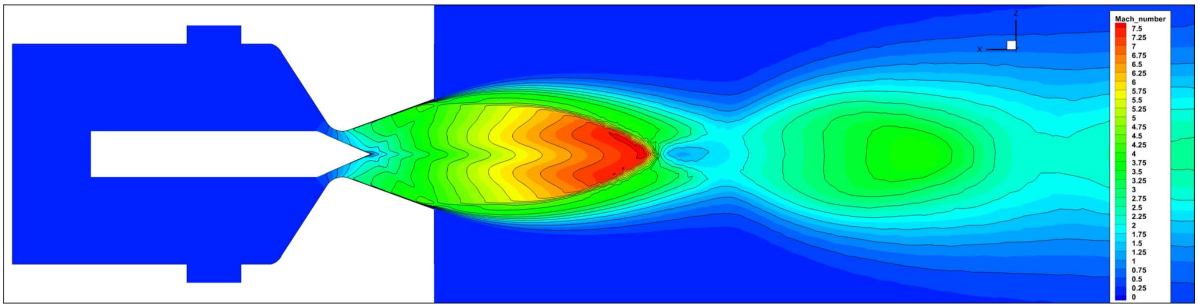

(n) At: $t = 302.75\%$ and $x_{pin} = 40.7\%$

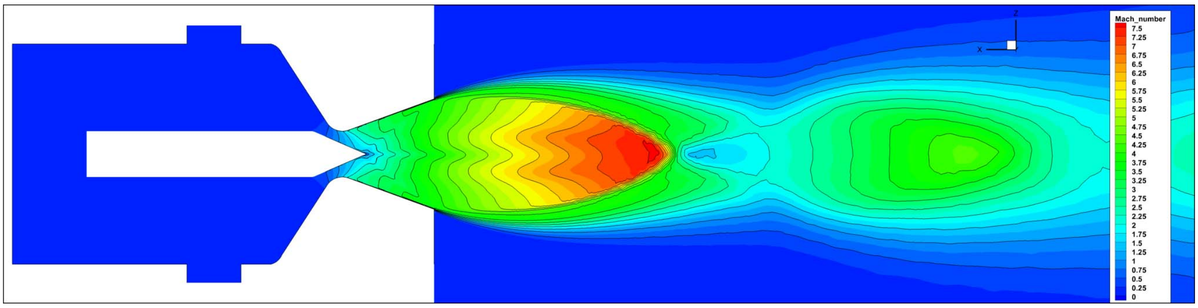

(o) At: $t = 313.38\%$ and $x_{pin} = 48.5\%$

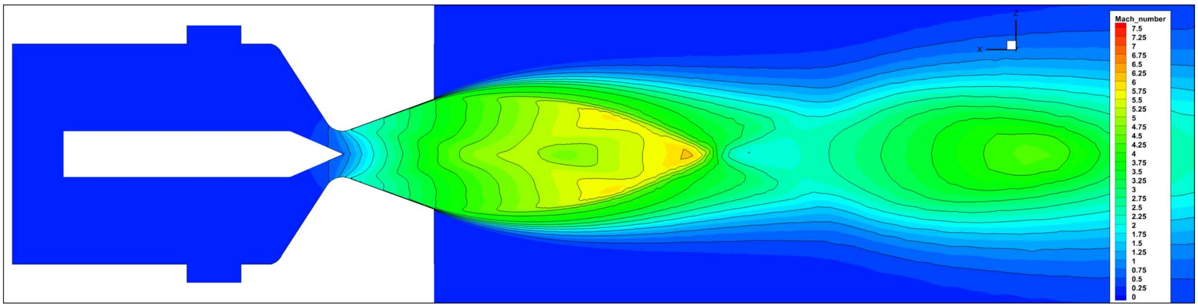

(p) At: $t = 378.89\%$ and $x_{pin} = 90.3\%$

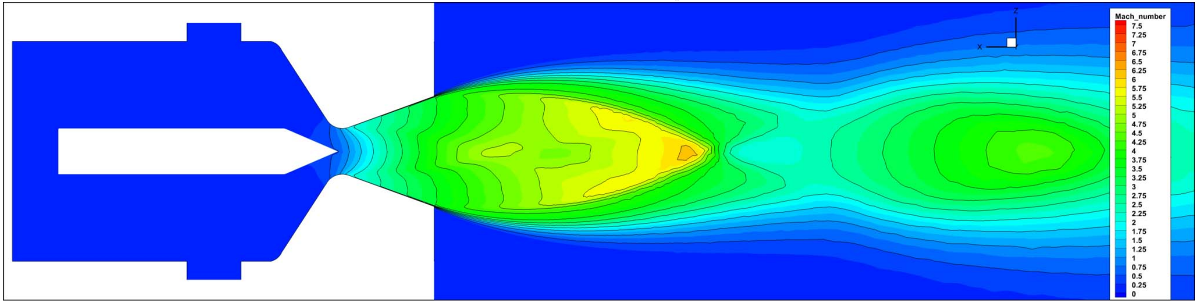

(q) At: $t = 421.40\%$ and $x_{pin} = 100.0\%$

Figure B.14: CFD Chimera Mach-Number Contours (ZX-Plane Cut) of selected Time-Steps, showing the $n = 240$ time-steps calculation only (Mach Number ranging from $M = 0.0$ to $M = 7.5$ with $\Delta M = 0.25$ and for the lines a $\Delta M = 0.5$. Note, in certain regions of some plots the Mach Lines appear to be unusually thick/ bold. This occurs due to a visualisation error in the region where the two chimera grids overlap.)

B.3. Hot-Fire CFD Results

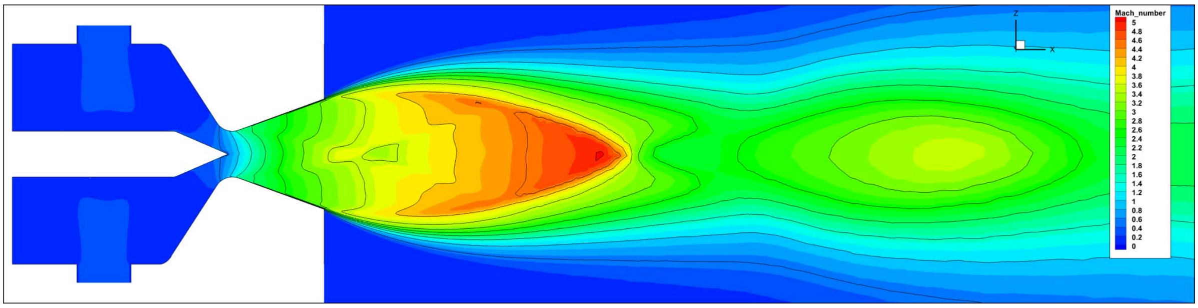

(a) Mach Number

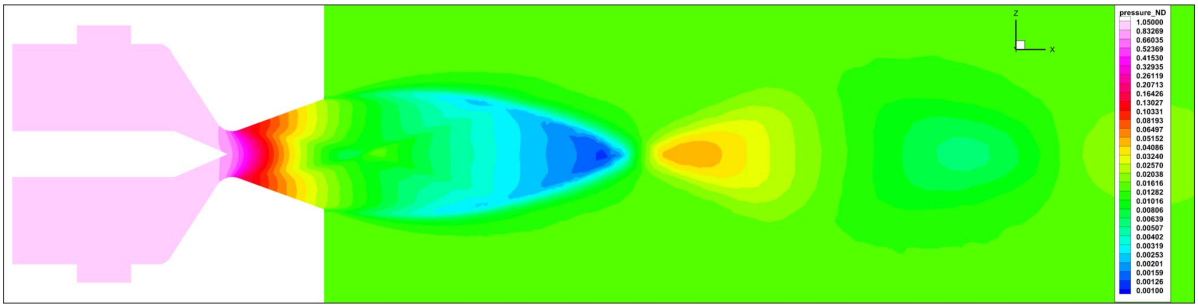

(b) Pressure

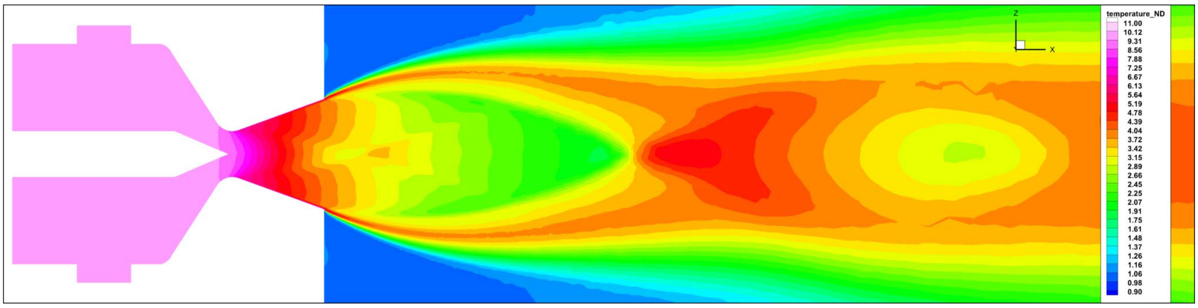

(c) Temperature

Figure B.15: CFD Results ZX-Plane Cut Contour Plot at the 0.0% position (Values have been made dimensionless according to Table A.1, Mach Number ranging from $M = 0.0$ to $M = 5.0$ with $\Delta M = 0.2$ and for the lines a $\Delta M = 0.5$)

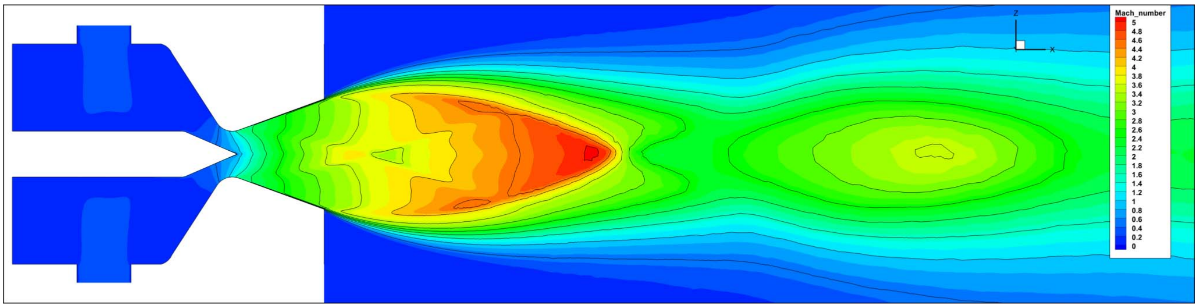

(d) Mach Number

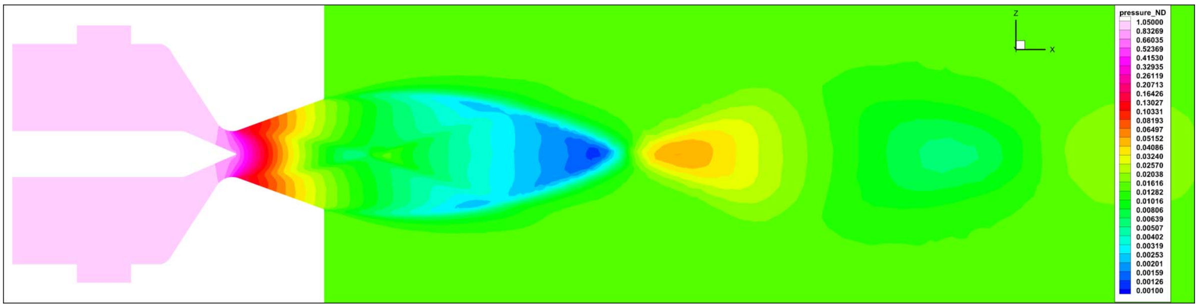

(e) Pressure

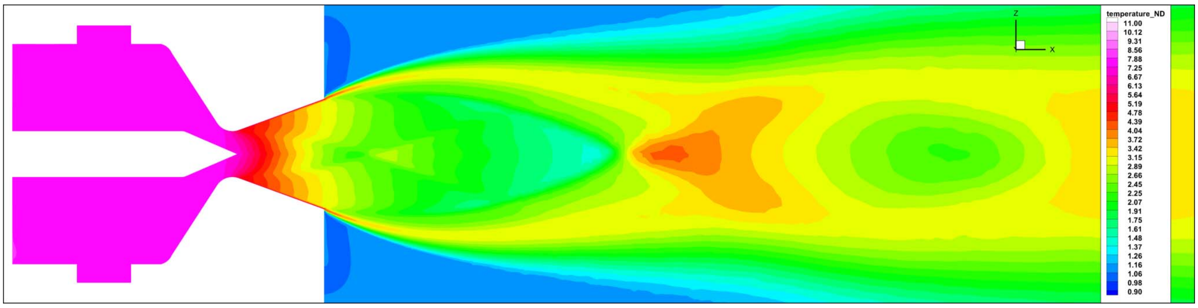

(f) Temperature

Figure B.15: CFD Results ZX-Plane Cut Contour Plot at the 83.33% position (Values have been made dimensionless according to Table A.1, Mach Number ranging from $M = 0.0$ to $M = 5.0$ with $\Delta M = 0.2$ and for the lines a $\Delta M = 0.5$)

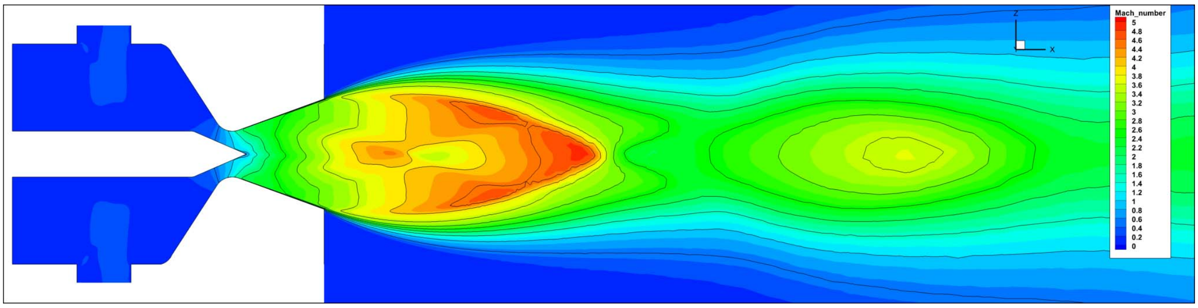

(a) Mach Number

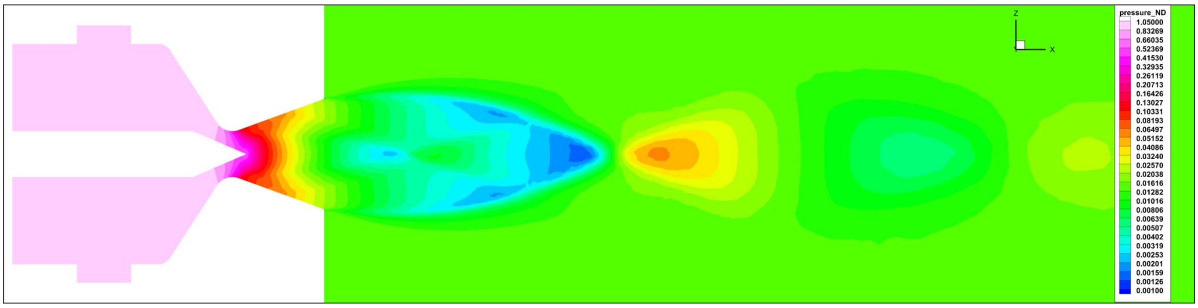

(b) Pressure

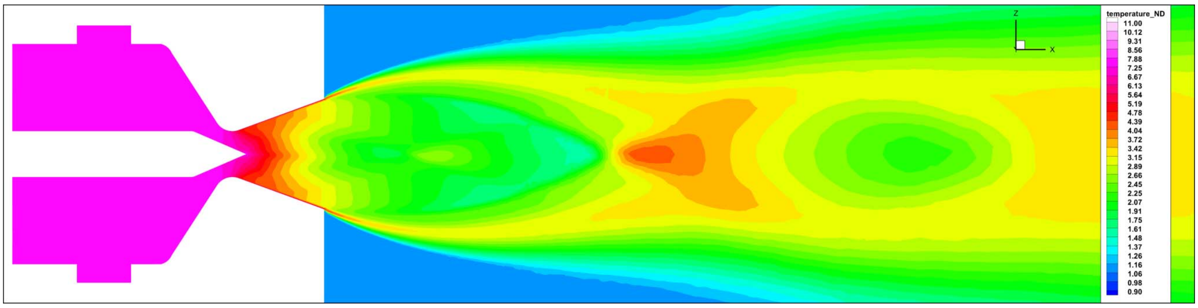

(c) Temperature

Figure B.16: CFD Results ZX-Plane Cut Contour Plot at the 66.67% position (Values have been made dimensionless according to Table A.1, Mach Number ranging from $M = 0.0$ to $M = 5.0$ with $\Delta M = 0.2$ and for the lines a $\Delta M = 0.5$)

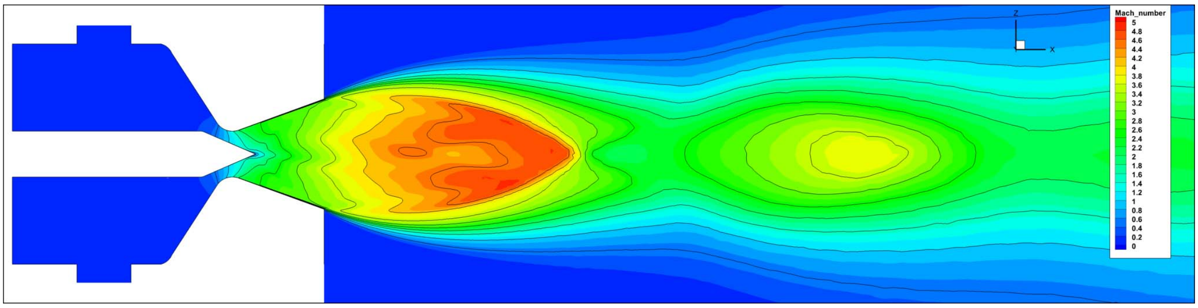

(a) Mach Number

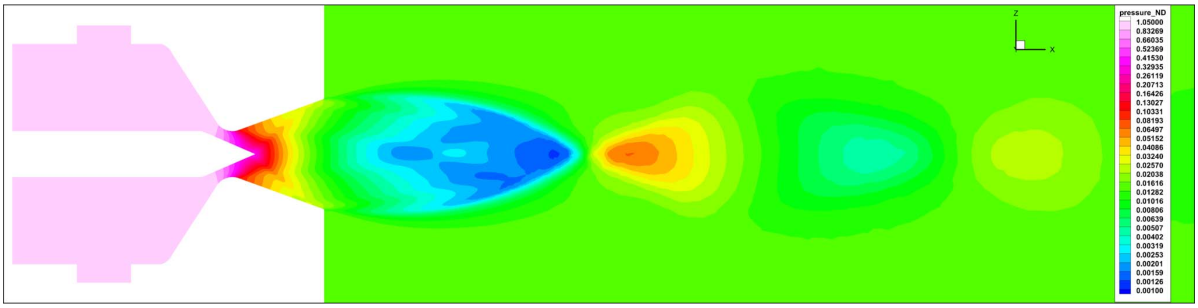

(b) Pressure

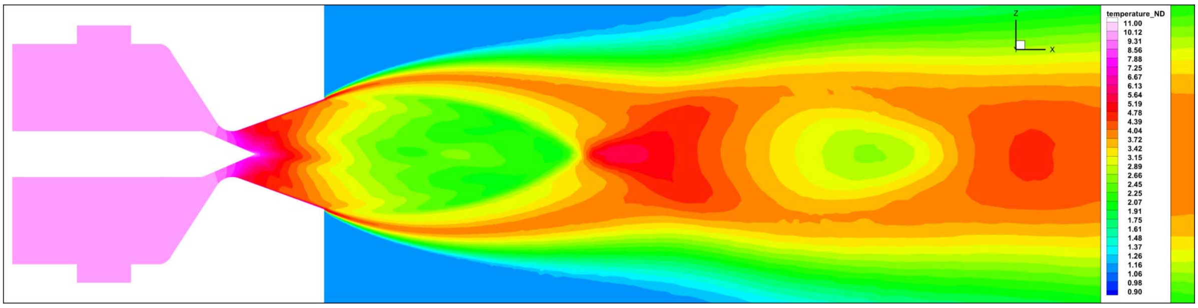

(c) Temperature

Figure B.17: CFD Results ZX-Plane Cut Contour Plot at the 50.0% position (Values have been made dimensionless according to Table A.1, Mach Number ranging from $M = 0.0$ to $M = 5.0$ with $\Delta M = 0.2$ and for the lines a $\Delta M = 0.5$)

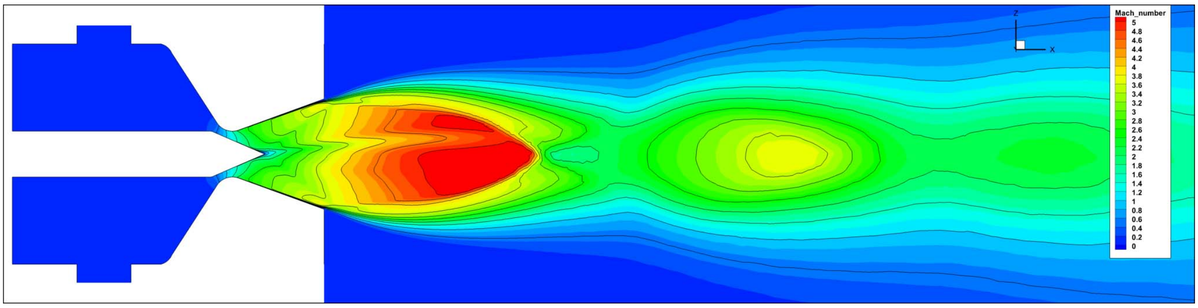

(a) Mach Number

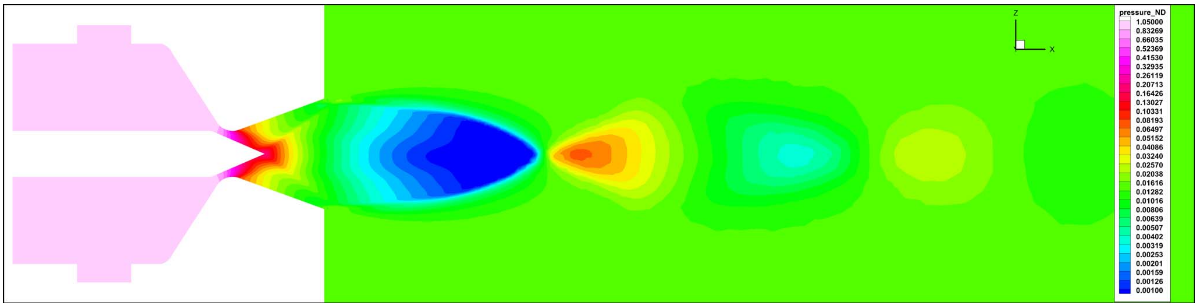

(b) Pressure

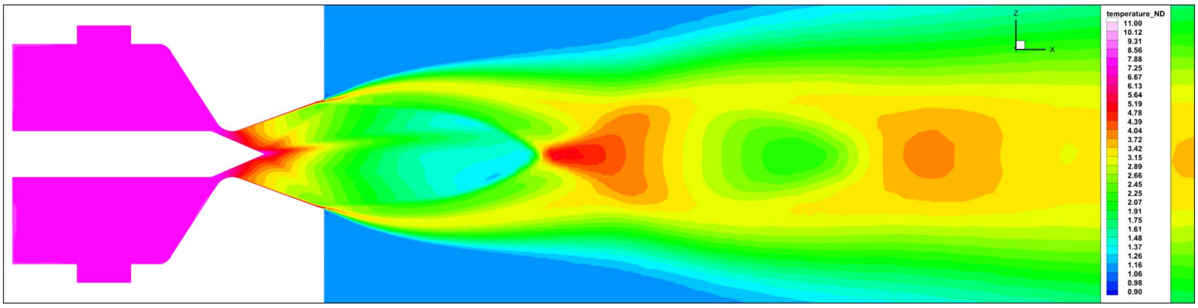

(c) Temperature

Figure B.18: CFD Results ZX-Plane Cut Contour Plot at the 33.33% position (Values have been made dimensionless according to Table A.1, Mach Number ranging from $M = 0.0$ to $M = 5.0$ with $\Delta M = 0.2$ and for the lines a $\Delta M = 0.5$)

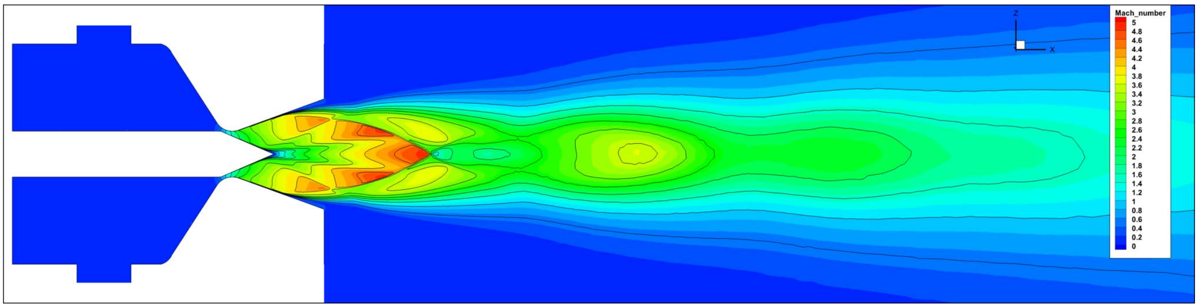

(a) Mach Number

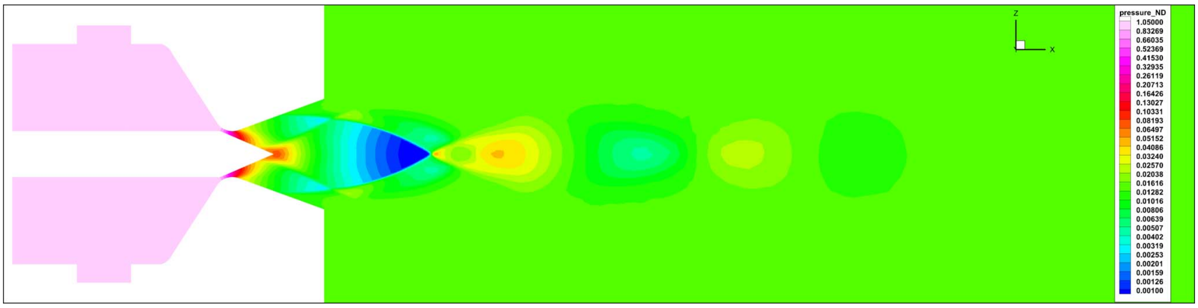

(b) Pressure

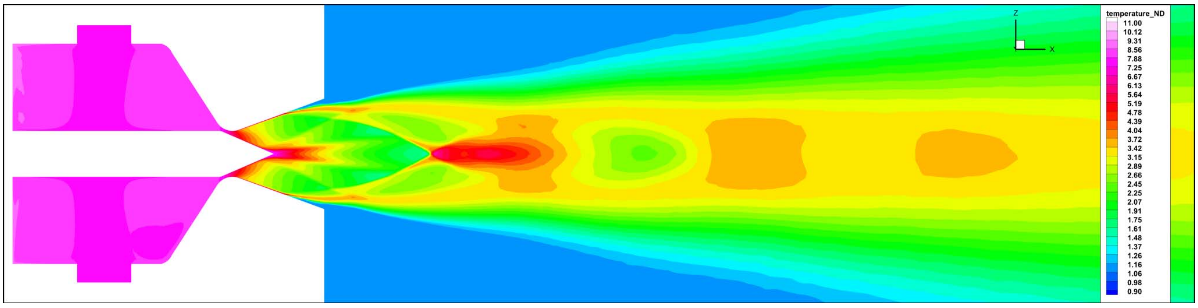

(c) Temperature

Figure B.19: CFD Results ZX-Plane Cut Contour Plot at the 16.67% position (Values have been made dimensionless according to Table A.1, Mach Number ranging from $M = 0.0$ to $M = 5.0$ with $\Delta M = 0.2$ and for the lines a $\Delta M = 0.5$)

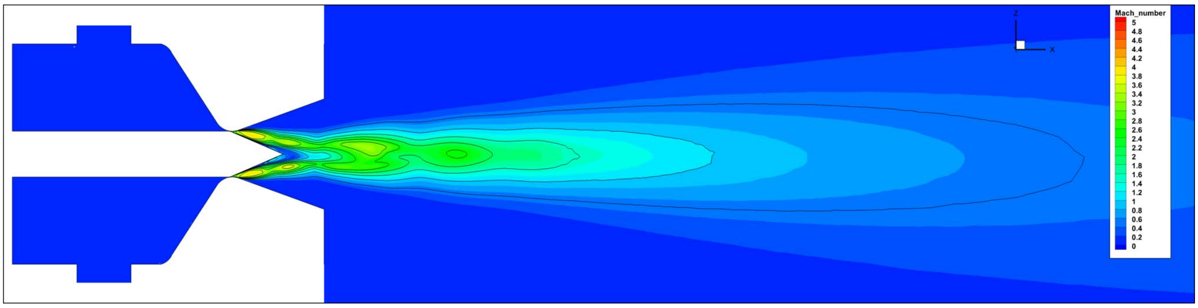

(a) Mach Number

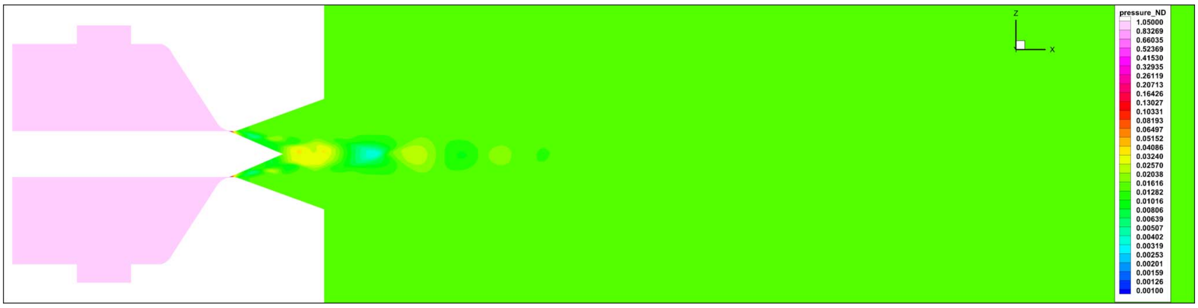

(b) Pressure

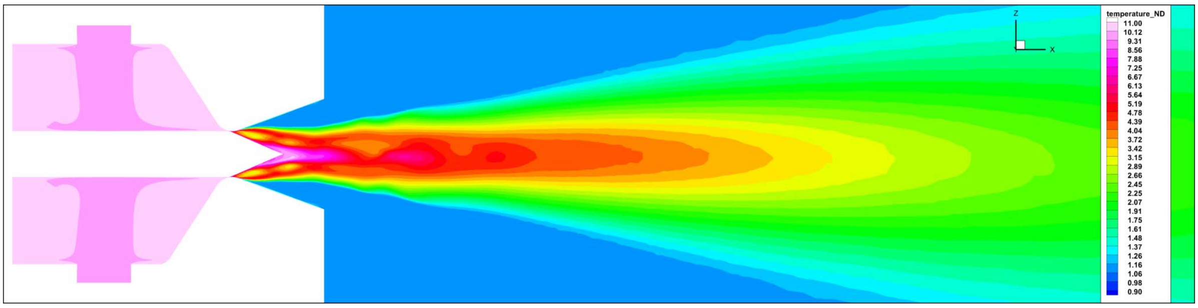

(c) Temperature

Figure B.20: CFD Results ZX-Plane Cut Contour Plot at the 0% position (Values have been made dimensionless according to Table A.1, Mach Number ranging from $M = 0.0$ to $M = 5.0$ with $\Delta M = 0.2$ and for the lines a $\Delta M = 0.5$)